INTERMOLECULAR INTERACTIONS AND MECHANICAL PROPERTIES OF MOLECULAR CRYSTALS—APPLICATIONS TO CRYSTAL ENGINEERING

A Thesis
Submitted for the Degree of
Doctor of Philosophy

By
C. MALLA REDDY

School of Chemistry
University of Hyderabad
Hyderabad 500 046
India

April 2006

Dedicated to
Amma & Nanna

STATEMENT

I hereby declare that the matter embodied in this thesis entitled **"Intermolecular Interactions and Mechanical Properties of Molecular Crystals–Applications to Crystal Engineering"** is the result of investigations carried out by me in the School of Chemistry, University of Hyderabad under the supervision of Prof. Gautam R. Desiraju and Prof. K. Anantha Padmanabhan.

.

In keeping with the general practice of reporting scientific observations due acknowledgements have been made wherever the work described is based on the findings of other investigators.

Hyderabad
April 2006

C. Malla Reddy

CERTIFICATE

Certified that the work **"Intermolecular Interactions and Mechanical Properties of Molecular Crystals–Applications to Crystal Engineering"** has been carried out by **C. Malla Reddy** under our supervision and that the same has not been submitted elsewhere for a degree.

Prof. Gautam R. Desiraju **Prof. K. Anantha Padmanabhan**

(Thesis Supervisors)

Dean

School of Chemistry

ACKNOWLEDGEMENT

It is indeed a great fortune to express my deep sense of gratitude and sincere thanks to my supervisors, **Prof. Gautam R. Desiraju** and **Prof. K. Anantha Padmanabhan** for introducing me to this fascinating multi-faceted field of research. I have been able to learn a great deal from them and consider my association with them a rewarding experience.

It gives me an immense pleasure to thank Prof. Ashwini Nangia for his encouragement on various occasions. It has been my privilege to work with him in a project that was carried out in the earlier part of my tenure which is included in this thesis in Appendix 1.

I would like to acknowledge the assistance of Prof. T.C.W. Mak and Dr. C.-K. Lam, The Chinese University of Hong Kong, China, Prof. R. Boese, University of Essen, Germany, Dr. V.M. Lynch, University of Texas, USA and Dr. Mohan Badbhade, National Chemical Laboratory, Pune for collecting the X-ray diffraction data on various compounds studied in this thesis. I thank Dr. R.C. Gundakaram and R. Meenakshi for collecting the nanoindentation data. A special note of thanks to Dr. Michael Kirchner for his help in solving some of disordered structures and helpful discussions and Dr. Srinivas Basavoju for cooperation in the survey of bending crystals, which are discussed in Chapters 2 and 3.

I thank Dean, School of Chemistry and former Deans of the School for their co-operation in providing facilities in the School. I extend my sincere thanks to all the faculty members of the School for help in various occasions. I am thankful to all the teachers and lecturers, who taught me throughout my career.

I am very thankful to my M.Sc. teachers Drs. P. Pratap Reddy, A. Ram Reddy and Vijjulatha for their encouragement to join Ph.D. programme.

I am grateful to CSIR, New Delhi for fellowship support. I thank all the non-teaching staff of the School of Chemistry and COSIST building for their assistance on various occasions. I thank Mr. Raghavaiah for his help with X-ray data collection.

I wish to thank all my friendly and cooperative labmates Drs. S.S. Kuduva, R. Thaimattam, R.K.R. Jetti, P. K. Thallapally, V.S.S. Kumar, V.R. Vangala, S. George, P. Vishweshwar, S. Basavoju, Narendar, Srinivasulu, and Mr. Sairam, Balu, Rahul, Dinu, Sreenivas Reddy, Binoy, Archan, Aparna, Sunil, Saikat, Prashant, Tejendar, Jagadeesh, Sreekanth, Bipul, Pati, Sandeep, Nabakamal, and Ranjeet for creating a cheerful working atmosphere in the lab. My stay on this campus has been pleasant with the association of all the research scholars at the School of Chemistry. I am thankful to Alchemie 99, Vamsee, Sreevardhan, Pavan, Gupta, Ravikanth, Venu, Phanipavan, Satish, Devender, Chandu, Ramesh Reddy, K.V. Rao, Raju, Aravind, Sekhar Reddy, Phani, Nari, Mahipal, Ramji, Bagavanth, Santu, Venkatram and Shashi.

It would be too formal to thank my bosom friends Ravi, Rajaseker, Basker, Prasad, SM, Rajender, Rajesh, Sagar, Nayeem, Neelima, Sangeetha, Sanath, Rajnikanth, Srinivas Reddy, Venu, Sudhakar, Ifthekar and Kittu for their unreserved encouragement. I also thank Manthriji, Narenderji, Gopi, Sailaja, Pradeep, Sathish, Navolina, Bapi Reddy, Santhosh, Nihar and Ansuman.

I thank my brothers, sisters, brothers-in-law and sisters-in-law for their support and encouragement. I thank my nieces, nephews and all the children in my family for their smiles and wishes. I also extend my thanks to my cousin brothers and brothers-in-law for their encouragement.

The blessings and best wishes of my parents keep me active throughout my life. They made me what I am and I owe everything to them. Dedicating this thesis to them is a minor recognition for their invaluable support and encouragement.

C. Malla Reddy

PREFACE

Crystal engineering, the design of organic solids with specified architectures and desired physical and chemical properties, continues to fascinate chemists. Supramolecular synthon concept simplifies the retrosynthesis and subsequent non-covalent synthesis of crystal structures. The work presented in this thesis is an attempt at establishing reliable structure-property relationships by considering mechanical response. Chapter 1 gives an overview of the streams in the development of (a) crystal engineering from solid state organic chemistry, and (b) mechanophysical aspects of materials from the viewpoint of physical metallurgy/materials science. Chapter 1 also deals with the importance of mechanical properties in materials science and crystal engineering and a glossary of terms used in this thesis. Numbering of molecules is specific to each chapter of this thesis.

Crystals of 1,3,5-trichloro-2,4,6-triiodobenzene (**135C246I**) show layered packing with strong I···I interactions within the planar layers and weak van der Waals interactions between the layers. Successive planar layers are inversion related and are stacked so that bumps in one layer fit into the hollows of the next. Application of a mechanical stress to the crystal parallel to the layers leads to shearing because of sliding of layers against one another. Twinning was observed in all the shearing crystals because of the creation of stacking faults. Shearing, twinning and anisotropy of intermolecular interactions in layered structures are described in Chapter 2.

Chapter 3 demonstrates the structural basis for the mechanical bending of organic crystals. The bending phenomenon was first observed in crystals of hexachlorobenzene which has a 4 Å short axis. A survey of around 60 crystals revealed that 17 of them could be bent. A model for bending has been proposed using descriptions obtained through X-ray diffraction, face indexing and nanoindentation techniques. These studies reveal that bending is possible when the packing is anisotropic in such a way that strong and weak interaction patterns are present in nearly perpendicular directions.

Nanoindentation and near-exhaustion creep behaviour of bending (samples 1 to 5) and shearing (sample 6) molecular crystals are presented in Chapter 4. The crystals

show near-exhaustion creep behaviour at room temperature on nanoindentation, which has been accounted for quantitatively but in phenomenological terms. It was possible to find out some differences in the mechanical behaviour of a few polymorphic crystals. It is also concluded that further studies in greater depth are necessary to acquire a more accurate and detailed understanding of the mechanical properties of molecular crystals.

Chapter 5 deals with mechanical and crystallographic properties of some halogenenated benzenes and the relevance of these properties to the elucidation of the nature of halogen···halogen interactions. These compounds appear in two broad structural groups, (a) monoclinic packing that is isostructural with C_6Cl_6, (b) layered triclinic packing with a repeated appearance of X_3 synthons.

An extended Appendix describes the engineering of a weak N–H···π interaction and a method to control it *via* guest selection in 4-(triphenylmethyl)benzamide solvates. The work in Appendix 1 is an independent study carried out in an earlier part of my tenure and was supervised by Prof. A. Nangia.

C. Malla Reddy

CONTENTS

CHAPTER 1

MATERIALS SCIENCE, MECHANICAL PROPERTIES OF MATERIALS AND CRYSTAL ENGINEERING

1.1 Introduction

Materials science is an interdisciplinary subject and combines many areas of science [1.1]. Materials science draws from chemistry, physics, and engineering to make better, more useful, more economical and more efficient materials (Scheme 1).

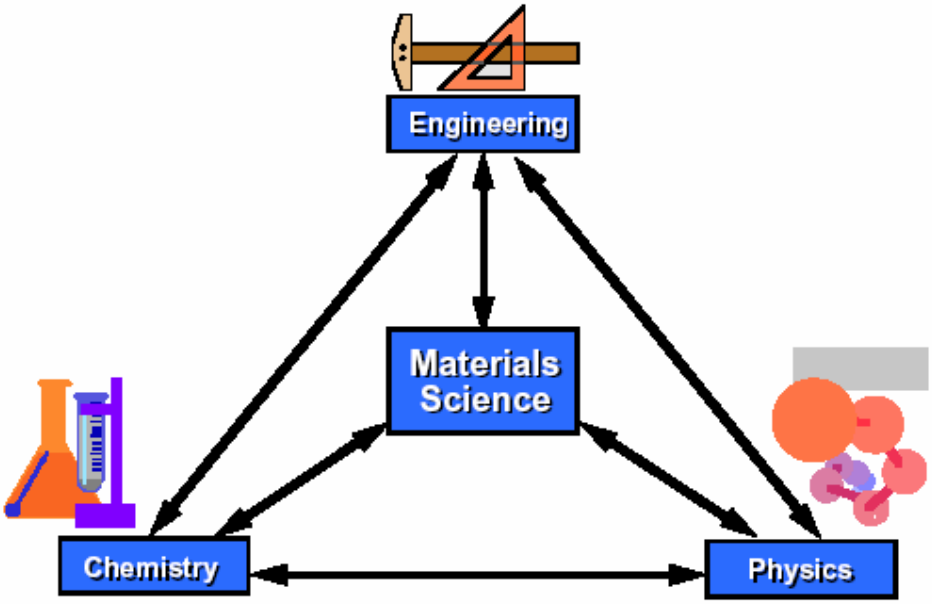

Scheme 1

In the broadest sense, what chemists do is to understand the physical and chemical properties of matter in terms of atomic and molecular level structures [1.2]. Although solution and solid state methods emerged simultaneously, the solution state played a crucial role in the continuous evolution of chemistry. Organic solid state chemistry (intersection of organic chemistry and materials science) [1.3] is nearly as old as solution organic chemistry, but the development of the subject was delayed due to

several factors and the renewals in its intersecting subjects. The developmental period of organic solid state chemistry may be viewed as flowing along three main streams: Stream I (1880s to 1970), evolution of organic solid state chemistry from organic chemistry; Stream II (1970s to recent times), rapid evolution of crystal engineering [1.2] from organic solid state chemistry which now continues towards applications of crystal engineering to various fields, mainly towards pharmaceutical applications [1.4]. Stream III (towards the future) combination of top down and bottom up approaches to understand and engineer materials in a more efficient way.

1.2.1 Stream I (1880s to 1970): Organic Solid State Chemistry

The molecular concept in organic chemistry, which originated with Wöhler's synthesis of urea in 1828, influenced the perception of chemists a great deal to adopt the bottom up approach in understanding the macro-level properties of materials by constructing them from the micro (molecular) level [1.2]. The history of chemistry suggests that thermal reactions of organic solids were known since the beginning of organic chemistry. For example, studies on light-induced reactions such as photodimerization of solid cinnamic acids and other solid-state reactions began between the end of the 19^{th} and the beginning of the 20^{th} century [1.5]. After the 1920s the growth of solid-state chemistry suffered due to a lack of proper physical methods to provide an insight into the molecular structure of organic solids. The study of physical properties of materials, say polymorphism and phase transitions, had not moved from the thermodynamic to the molecular level. It is here that the importance of X-ray crystallography was realized by the solid state chemists and crystallographers of the time who believed that the solid state properties are definitely dependent upon the molecular packing. But crystallography was not mature enough in the 1930s and the 1940s to provide important and sufficient information about the molecular structure of solids. When the power of X-ray crystallography increased during the 1960's and the 1970s, organic solid state chemistry grew rapidly into a distinct discipline [1.3, 1.6].

Solution reactivity largely depends on molecular properties, while solid state reactivity is a supramolecular property which is characteristic of an assembly of

molecules. (An analogy would be the distinction between physics and physical metallurgy.) The important link between the structure of a molecular assembly and its solid state chemical reactivity was established by Schmidt [1.7] while working on the photochemical reactivity of crystalline cinnamic acids. Schmidt found that for a series of photodimerisable olefins, the spatial arrangement of molecules in the crystalline state plays the key role on the initiation and progress of the solid state reaction. Such reactions were termed as topochemical reactions since they were considered to occur with a minimum of molecular movement [1.7-1.9]. The photochemical reaction proceeded only when the geometry of the molecules favoured in the reactant crystal. In these topochemical reactions the structure of the product was closely related to the crystal symmetry of the reactant and only a small number of products resulted.

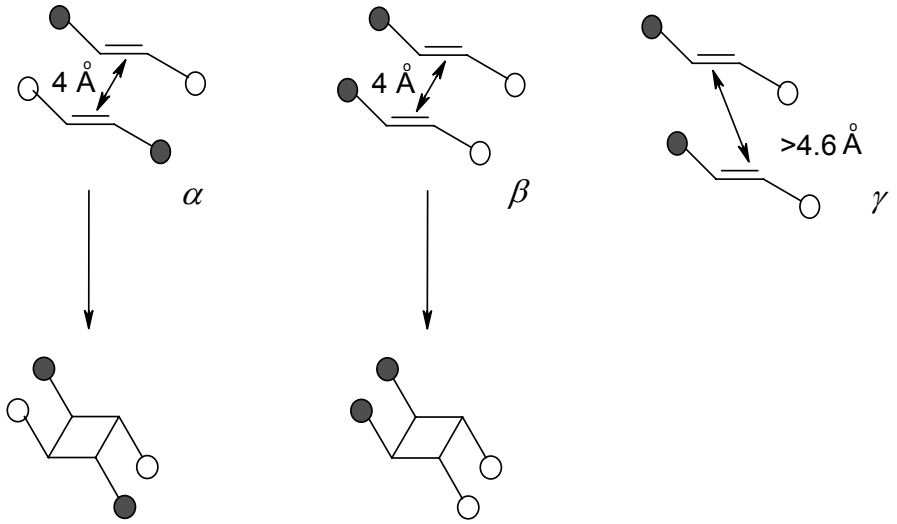

Scheme 2

Schmidt systematically studied the *trans*-cinnamic acids (Scheme 2). He found in his study that substituted cinnamic acids crystallize in one of three structural types α, β and γ. The α and β forms react in a 2 + 2 fashion to give rise to cyclobutane dimers when irradiated in the solid state, while crystals of the γ form are photostable. The topochemical principle was proposed after establishing the close relationships between the molecular packing in the crystalline state and the formation of mirror symmetry

products from the β -acids and inversion symmetry products from the α -acids. In both α and β forms, the reactive double bonds in the monomer crystal are closer than *ca.* 4.2. Å. In contrast, in crystals of the γ form, the double bond separations are around 4.9 Å, which is too far apart to involve them in photochemical reactions.

The identification of the remarkable structure-property correlations in cinnamic acid crystals by Schmidt was very successful in predicting and understanding the path of many solid state reactions and motivated one to control the crystal packing. But, this was found to be a difficult task since the understanding of crystal structures was very poor and there were no rules to predict the self assembly of molecules. At this point in time, the concept of crystal engineering was brought in to deal with these issues. The term was first suggested by Pepinsky [1.10] in 1955 and Schmidt denoted further rules which could be used to generalize and predict molecular packing [1.7]. Schmidt suggested that the systematic development of the subject would be possible by understanding the intermolecular forces which are responsible for the stability of the crystalline array [1.7]. During the later stages of this stream of activity, dislocation theory was proposed to explain the mechanisms of solid state reactions that are controlled by defect topochemistry [1.9]. Dislocation theory had already been used to explain deformation in metal crystals [1.11].

1.2.2 Stream II (1970s to the Present Time): Crystal Engineering

After Schmidt's emphasis on the importance of crystal engineering in the context of organic solid-state photochemical reactions, pioneering research work was undertaken by Desiraju [1.2], which led to the modern subject that goes far beyond organic solid state reactivity. The scope of the term crystal engineering was extended by Desiraju who defined crystal engineering as "*the understanding of intermolecular interactions in the context of crystal packing and the utilization of such understanding in the design of new solids with desired physical and chemical properties"*. Organic solids with specified architectures and desired physical and chemical properties continue to fascinate chemists [1.12]. The subject of crystal engineering is not restricted only to the design part of crystal structures, but it also includes the learning of rules of crystal packing [1.2]. This

is because the practice of 'engineering' itself is a process of learning the crystal packing rules and many of the rules developed today have been learned while attempting to engineer crystal structures. Hence, structure determination, packing mode analysis and crystal design are considered to be the key elements in crystal engineering. In this context, the supramolecular synthon [1.13] concept simplifies the retrosynthesis and the subsequent non-covalent synthesis of crystal structures. Difficulties in crystal engineering stem from the complex behaviour of intermolecular interactions and the unpredictable effects of remote functional groups (interaction interference). Interference is more of an issue for weak intermolecular interactions because of the inherent ambiguity in their geometrical and chemical recognition factors [1.14]. Understanding the exact nature of these interactions is of utmost importance in establishing reliable structure-property relationships in solids [1.15]. Efficient design and the prediction of crystal structure are the main issues in today's crystal engineering and are still to be resolved in the future by improving the approaches.

1.2.3 Stream III (Towards the Future)

The future of crystal engineering belongs to this stream. The importance of this subject is increasing and its scope is expanding with the improvisation of approaches and the engineering-down (macro to micro/top down) and the synthesis-up (micro to macro/bottom up) technologies. Today, crystal engineering is an interdisciplinary subject dealing with the self-assembly of molecular crystals, metal-organic architectures, nanostructures, and coordination polymers using hydrogen bonding, electrostatic and van der Waals interactions, and metal coordination bonding [1.16]. It brings together chemists of different specialization (synthetic, physical, computational, theoretical and analytical) to work in collaboration with crystallographers, physicists and materials scientists for the design of organic, inorganic, and hybrid systems. To deal with the future problems in all these interdisciplinary sections, the balancing of both the bottom-up and the top-down approaches will be crucial. Getting this balance correct will lead to the design of materials of pre-defined physical and chemical properties.

1.3 Metallurgy

Metallurgy is presently considered to be a part of materials science (although the former is a much older discipline), which has always been closely linked to chemistry, physics and engineering. Metallurgy may be divided into chemical metallurgy (the chemical preparation of metals) [1.17], physical metallurgy (the physical—including mechanical—behaviour of metals) [1.18] and metals engineering (the engineering of metals and alloys for different practical purposes) [1.18]. The most important property of a metal is its ductility (ability to suffer heavy deformation without breaking). While practical knowledge of the preparation of metals extends backwards for thousands of years (~16000 BC), the understanding of the actual physical phenomena underlying deformation has only developed recently, starting from the 1930s [1.18a]. In 1910 Andrade developed a technique of growing large individual crystals from the melt and later Bridgman elaborated on this technique [1.19]. Thus, the availability of suitable metal crystals made the detailed studies of plastic deformation of metal crystals possible. In the beginning of the 20^{th} century, Andrade did some classical experiments on the deformation of the metals and established the rules for creep behaviour, which led to the development of the subject of mechanical metallurgy (regarded today to be a part of physical metallurgy) [1.18a, 1.19].

Since in the early days there were no physical techniques to look into the microstructure of the deformed metals, metallurgists mainly depended on theoretical physics [1.20]. In those investigations, the atoms in a metal were visualized simply as structureless spheres that attract one another and cohere together. But the experimentally determined mechanical properties were generally about a thousand times less than the theoretical estimates. In 1934 Orowan, Polanyi and Taylor independently introduced the concept of a dislocation [1.18, 1.21], a crystal line-defect which was necessary to account for the differences between the actual and the theoretical values of the mechanical properties. The physical basis for the deformation of metals was established starting from the 1940s with the help of new physical techniques [1.18]. The studies on dislocation proved it to be the most important development in metal physics and the

dislocation theory has gained considerable importance in metallurgy because it has provided many useful ideas to solve problems like work hardening (the ability of a metal to become stronger with deformation), precipitation hardening, solid solution strengthening and origin of ductility. The dislocation or the defect provides the vital link between the atomic/molecular structure and the plastic behaviour of a crystal. The dislocation theory, with suitable modifications, was also used to understand the mechanical behaviour of other materials like ceramics, thin films and coatings.

Developments in physical metallurgy influenced other areas of materials science and led to an understanding of the mechanical properties of other materials like ceramics, coatings, polymers and thin films on a common physical basis. Advances in physical measurement techniques like scanning electron microscopy (SEM), transmission electron microscopy (TEM), (micro-, nano-) indentation and atomic force microscopy (AFM) led to remarkable developments in the measurement and understanding of mechanical properties of materials with great accuracy.

1.4 Glossary of Terms

The glossary of terms given below is aimed at familiarizing the reader with the terminologies used in crystal engineering and mechanical metallurgy. The present glossary concentrates on terms used in this thesis.

1.4.1 Crystal Engineering

The nomenclature in crystal engineering given in this section is to enable the reader to follow the discussions in the next chapters. Recently, crystal engineering nomenclature was reviewed by Nangia [1.22].

Disorder

In some crystals, parts of molecules or in some extreme cases whole molecules are found in more than one crystallographically independent orientation. This is known as disorder. This may be viewed to be two types: (1) static disorder, and (2) dynamic disorder.

In the case of static disorder, the orientations of the molecules differ randomly in different unit cells. The structure determined from the diffraction pattern is the spatial average over the whole crystal. This is not temperature dependent and can be postulated as the existence of two (or occasionally more) different types of unit cells. Here, disorder arises during crystal growth and it may be avoided by growing the crystals at lower temperatures and/or slower rates.

In case of dynamic disorder, some parts of the molecules, like organic side chains or $SiMe_3$ and tert-butyl groups are almost free to rotate (thermal motion). This is also observed commonly in case of free solvent molecules located in holes in the crystal structure. This type of disorder may vanish below certain temperatures, and this can be interpreted as a real movement in the crystal, which has been frozen. In some cases, freezing can convert the dynamic to static disorder.

Entropy considerations are important when a molecule adopts more than one orientation at any given crystallographic site. In crystals which exhibit the phenomenon of static or dynamic disorder, the entropy increases, thereby lowering the free energy [1.2].

Hydrogen Bond

A hydrogen bond D−H···A is formed when the electronegativity of a donor D relative to H in the D–H covalent bond is such as to withdraw electrons and leave the proton partially unshielded so that it can interact with the lone pair or polarizable π electrons on the acceptor A [1.14a]. Hydrogen bonds are of three types: strong or conventional H-bonds (O–H···O, O–H···N, N–H···O) with energy of 4–15 kcal mol^{-1}, weak or unconventional H-bonds (C–H···O, C–H···N, O–H···π) with energy of 2–4 kcal mol^{-1}, and very strong or ionic H-bonds ($O–H···O^-$, O^+–H···O) with partial covalent character and energy of 15–40 kcal mol^{-1}. The total energy of the hydrogen bond may be divided into electrostatic, charge transfer, polarization, dispersion, and electron repulsion with the major contribution varying, depending on whether the H-bond is strong (mostly

electrostatic), weak (electrostatic), or very strong (mostly covalent). The strongest hydrogen bond is comparable in strength to the weakest covalent bond.

Desiraju and Steiner [1.14a] defined the weak hydrogen bond as 'an interaction D−H···A wherein a hydrogen atom forms a bond between two structural moieties D and A, of which one or even both are only of moderate to low electronegativity'.

Herringbone Motif and $\pi\cdots\pi$ Interactions

Recognition between phenyl groups is mediated by numerous interactions that have two extreme geometries: edge-to-face herringbone T-motif (dipole–quadrupole interaction, energy 1–2 kcal mol^{-1}), and parallel-stacked arrangement of phenyl rings with face-to-face interaction between π-electron clouds (quadrupole–quadrupole interaction, energy 1 kcal mol^{-1}). Possible variations in these geometries are the vertex-to-face approach, and the presence of offset or slight inclination between p stacked rings.

Host–Guest Compound

The inclusion of small guest molecules in the open framework of a host molecule constitutes a host–guest compound. They are of two major types: cavitands, or molecular host compounds with intramolecular cavities. The cavity is an intrinsic property of the molecule and exists in solution and in the solid state, e.g., calixarenes, cyclodextrins. Clathrands are hosts with extramolecular cavities that result from the aggregation of two or more molecules. Lattice inclusion hosts exist only in the crystalline or solid state, e.g., hydroquinone and urea. The corresponding host–guest adducts are referred to as cavitates and clathrates.

Isomorphism and Isostructurality

Isomorphism is similarity of crystal shape, unit-cell dimensions, and structure between substances of similar chemical composition. Ideally, the substances are so closely similar that they can generally form a continuous series of solid solutions. The degree of similarity between the crystals can be calculated using Kálmán's parameters [1.23]: the unit cell similarity index, Π, and isostructurality index I_i(n):

$$\prod = \left| \frac{a+b+c}{a'+b'+c'} \right| - 1$$

where a, b, c and a', b', c' are the orthogonalized lattice parameters of related crystals.

$$I_i(n) = \left[1 - \left(\frac{\sum \Delta R_i^2}{n} \right)^{1/2} \right] \times 100$$

where n is the number of distance differences (ΔR_i) between the absolute coordinates of identical nonhydrogen atoms within the same section of the asymmetric units of related structures. For an isostructural pair of crystals, Π must be close to 0, and $I_i(n)$ should approach 100%. These parameters were derived in the context of steroid crystals but are now used for all classes of molecules.

Polymorphism

A solid crystalline phase of a compound resulting from the possibility of at least two different arrangements of the molecules of that compound in the solid state is called polymorphism [1.24]. Theoretically, the packing of a molecule can be arranged in many ways in the crystal of a given symmetry and polymorphism is a reflection of the alternative ways in which molecules in a crystal strive towards a free energy minimum. Polymorphs are like supramolecular isomers in the spontaneous organization from molecule→nucleus→crystal. Polymorphism is said to be the antithesis of crystal engineering. This phenomenon is of fundamental and commercial importance, because polymorphs have different physical and chemical properties. About 10% of compounds are estimated to be polymorphic. When polymorphs occur, kinetic factors are deemed to be dominant during crystallization.

Some related terms are concomitant polymorphs [1.25] (crystals from the same flask under identical crystal growth and solvent conditions), conformational polymorphs (different conformations of the same molecule in different crystals) [1.24], conformational isomorphs (multiple conformations of the same molecule in the same crystal) [1.24], configurational polymorphs (different configurations of the same molecule, e.g., Z, E, in different crystals) [1.24], and pseudopolymorphs (crystals formed

by the same substance crystallized with different amounts or types of solvent molecules) [1.26].

Site Occupancy Factor (SOF)

The SOF is the partial occupancy of a given site by a particular atom. It is most frequently used to describe disorder in a portion of a molecule or for describing nonstoichiometric situations, e.g., in solid solutions.

Supramolecular Chemistry

Supramolecular chemistry [1.27] is the chemistry of molecular assemblies, intermolecular bonds, noncovalent interactions, and hydrogen bonds. The original meaning of "supramolecular" is "beyond the molecule". "Supramolecular" currently has three different meanings: intermolecular interactions, coordination chemistry, and a strategy for the controlled organization of multiple components. Supramolecular chemistry is a philosophy and strategy for the controlled grand assembly of complex matter.

Supramolecular Synthon

Structural units within supermolecules (crystals) that can be formed and/or assembled by known or conceivable synthetic operations involving intermolecular interactions, most often hydrogen bonds, are supramolecular synthons [1.13]. The goal of crystal engineering is to design robust synthons that can be exchanged from one structure to another and then incorporate recurring synthons in retrosynthesis to anticipate (predict) the one-, two-, or three-dimensional structure of novel target architectures. Desiraju suggested that this exercise may be referred to as crystal synthesis in analogy with target molecule synthesis [1.13]. However, because hydrogen bonds are an order of magnitude weaker than covalent bonds, the robustness of a synthon is reliably derived from statistical trends, i.e., the probability of occurrence of a particular structural motif in the Cambridge Structural Database (CSD). The prediction of crystal packing through such an empirical-cum-chemical intuition approach was reasonably successful [1.28a].

This is distinct from crystal structure prediction [1.28b–e], i.e., to know the unit cell and space group of a given molecule without any experimental data. Synthon interchange is the exchange of one functional group with another (e.g., halogen, ethynyl, hydroxy) to generate topologically identical structures.

Twinned Crystal

This is a composite crystal built from two or more crystal specimens that grow together in a specific manner, so that there is at least one plane and a direction perpendicular to it that are related in the same manner to the crystallographic axes of both parts of the twin.

1.4.2 Mechanical Metallurgy

Mechanical metallurgy [1.18] is the area of knowledge which deals with the behaviour and response of metals to applied forces. Since it is not a precisely defined area, it has different meanings. This field includes the study of mechanical properties of metals or mechanical testing, theoretical mechanical aspects of metals which merges metal physics and physical metallurgy. It also includes applied mathematics and applied mechanics. Fundamentals in mechanophysical aspects are described briefly in this section.

Mechanical stability of solids is due to the existence of balanced forces between their constituent atoms [1.18]. Attractive forces cause the atoms to cohere to one another while short-range repulsive forces prevent the atoms from approaching each other too closely. Normally atoms occupy positions where these forces are balanced, but when an external force is applied this balance is disturbed. To restore equilibrium the atoms move slightly to nearby positions where there is a balance among the attractive, repulsive and external force.

Stress and Strain

Figure 1 illustrates the change in dimensions of a solid on the application of a mechanical force. In Figure 1a, a cylinder is stretched. In Figure 1b a cylinder is

deformed by a force perpendicular to its axis, i.e. it is sheared. What the two deformation types have in common is that a stress, or deforming force per unit area, produces a strain, or unit deformation. The force in Figure 1a leads to a tensile stress and the one in Figure 1b to a shear stress.

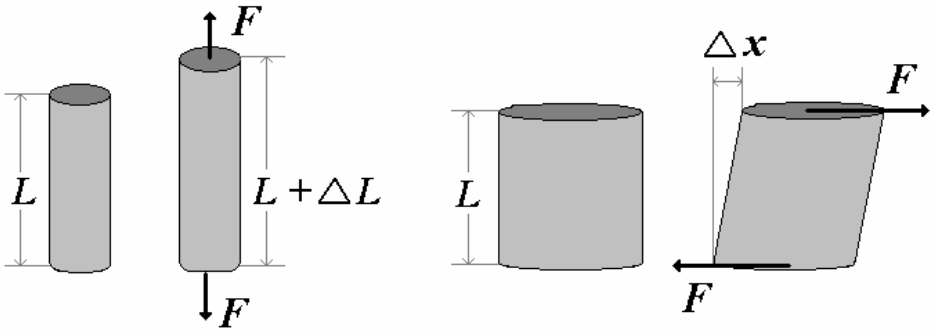

Figure 1. (a) A cylinder subjected to a *tensile stress* stretches by an amount Δ*L*. (b) A cylinder subjected to a *shear stress* deforms by an amount Δ*x*, which is somewhat like a movement in a pack of playing cards. This figure is reproduced from reference [1.29].

Figure 2 illustrates some basic terms used in the deformation and fracture of a body on the application of a mechanical stress [1.18].

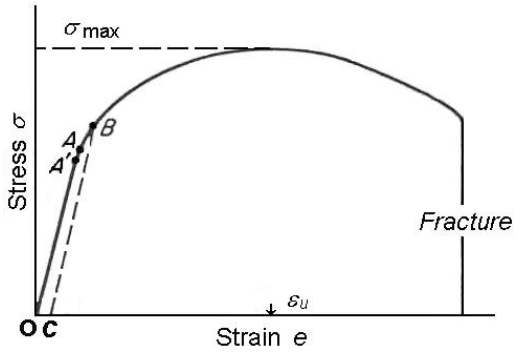

A = elastic limit

A' = proportional limit

B = yield strength (usually at an offset of 0.2% strain)

σ_{max} = *maximum stress*

ε_u = *maximum uniform strain*

Figure 2. Typical stress-strain curve in tension. This figure is adapted from reference [1.18a].

Elastic and Plastic Deformation

If an increasing load is applied to a metal wire suspended from a fixed point, initially an extension will take place, which is completely recoverable when the load is removed [1.18a]. Then the deformation is referred to as *elastic deformation*. However, beyond a certain load, complete recovery of the strain is not present on unloading because the metal has deformed permanently and this is known as *plastic deformation*. The transition between the elastic and the plastic deformation processes is defined in terms of the *yield stress*/*yield strength* or the *initial flow stress*.

Hooke's Law and Young's Modulus

In elastic deformation, below the elastic limit, the stress (σ) applied to stretch or compress a body is proportional to the strain (e) or to the change in length. This is known as Hooke's law [1.18a]. Here, the linear relationship between stress and strain is a constant $E = \sigma/e$. Thus, at any given load the ratio of the stress to the elastic strain is a constant E, known as Young's modulus in the case of a uniaxial tensile stress.

Creep

Progressive deformation of a material at constant stress is called *creep* [1.18a]. Creep is often studied in metals engineering by the application of a constant load to a tensile specimen of a given grain size maintained at a constant temperature. The strain (extension) suffered by the specimen is determined as a function of time. Further details of creep are given in Chapter 4.

Hardness

Hardness (H) is defined as the ability of a metal to resist plastic deformation. The greater the hardness of a material, the greater is its resistance to deformation [1.18]. Hardness is usually treated as a composite property of a material including yield strength, work hardening, true tensile strength and modulus of elasticity.

Dislocation

A dislocation is a linear defect that is responsible for nearly all aspects of the plastic deformation of metals, particularly at low temperatures [1.18]. The experimental techniques that are used for detecting the presence of dislocations and their activity are generally of two types: (1) those involving chemical reactions with the dislocations; (2) those utilizing the physical changes at the site of a dislocation. Chemical methods include etch-pit techniques and precipitation methods. Methods based on the physical structure at a dislocation site include transmission electron microscopy (TEM) of thin films, in situ microscopy using the transmission and the scanning electron microscopy techniques and X-ray diffraction.

Work Hardening

An ability of a material to become stronger as it deforms is known as work hardening [1.18a]. Work hardening arises when dislocations are hindered in their movement through crystals, so that a higher stress must be imposed to continue deformation.

CHAPTER 2

SHEARING, TWINNING AND ANISOTROPY IN LAYERED MOLECULAR STRUCTURES

2.1 Introduction

The forces that bind atoms into crystalline solids are electrical in nature, and in the broadest sense, can be termed as chemical bonds. There are five principal chemical bond types: metallic, ionic, covalent, hydrogen bond and van der Waals [2.1, 1.2]. Each bonding type is characterized by its particular strength and directionality characteristics. To a great extent, the bonding type determines the physical and chemical properties of a solid material at a given temperature [2.2]. For instance, hardness, cleavage, thermal and electrical conductivity are directly related to chemical bonds. Based on the directionality of chemical binding forces in crystalline state, solids are classified into 0D, 1D, 2D and 3D [2.3]. Among these types the 3D solids are well documented. Comparatively speaking, detailed studies of 2D solids are not so common [2.4]. Dimensionality is one of the most defining of material parameters: the same chemical compound can exhibit considerably different properties depending up on whether it is arranged in a 0D, 1D, 2D or 3D crystal structure [2.3, 2.4]. For example, the three allotropes of carbon—buckminsterfullerene, graphite and diamond—provide a potent example of how much the structure and properties of a system can vary with dimensionality [2.5b]. Buckminsterfullerene, a 0D molecular crystal, is very soft. In graphite, the weak van der Waals interactions that hold the trigonally bonded two-dimensional carbon layers together make it soft enough to cleave the material along these layers. In diamond, the carbon atoms are extended three-dimensionally by strong tetrahedrally directed covalent bonds of length 1.54 Å that makes it the hardest material in nature [2.3].

2.2 Overview of Two-Dimensional Structures

There are many kinds of layered structures in the literature with strong in-plane bonds and weak van der Waals interactions between layers. Sheets of layered crystals are

generally formed *via* metallic, ionic, covalent, hydrogen bonds and/or van der Waals interactions [2.3, 2.6]. The stacking of layers is simple, because of the small number of possibilities that exist. Other features like polytypism, polymorphism, disorder and cleavage of layers, occur due to variations in these basic stacking patterns such as the fcc (ABCABC) and hcp (ABAB) stackings. Variations in these simplest arrangements occur because of the weakness of the interlayer interactions [2.3].

2.2.1 Structure of Graphite and BN

The classic example for covalent crystals with a distinctive layered structure is carbon in graphite, wherein intralayer bonds are formed *via* sp^2 hybrids exactly as in benzene. In this structure, the layers are formed with atoms, connected to these three nearest neighbours with covalent bonds, Figure 1. π-Orbitals normal to the plane overlap to form π-molecular orbitals covering the entire layer. The layers are widely separated with a perpendicular distance of 3.35 Å and bonded by van der Waals forces only. Due to the weakness of interlayer interactions, graphite is readily cleaved and hence, used as a heavy-duty lubricant and 'lead' in pencil. Because of its interesting structural arrangement and the shearing behaviour of its layers, graphite has been investigated extensively and has been found to be useful in many ways [2.3].

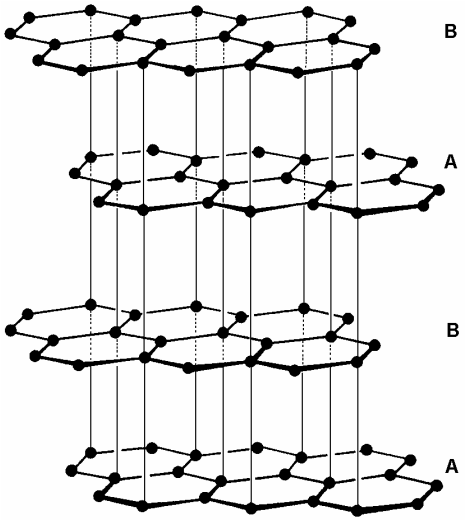

Figure 1. The layered structure of hexagonal graphite.

Any two graphite layers can be stacked in only one way, viz. with three alternating atoms of one ring above ring centres in the lower layer, Figure 1. The third layer can either be above the first (ABAB, giving hexagonal graphite) or displaced with respect to it (ABCABC, rhombohedral graphite). However, the ABC stacking is never found to extend throughout any one crystal; a complex form of disorder is present.

Planar layers of the same kind are also present in white BN, the isoelectronic solid which is dimorphic analogous to carbon [2.3]. Alternate boron and nitrogen atoms occur in graphite-like rings in BN but the layer stacking is not the same (Figure 2) and must result from weak directed bonding *via p*-orbitals normal to the layers. The higher electronegativity of nitrogen results in a greater delocalization of π-electrons than in graphite: consequently BN is an insulator. At high temperature and pressure (40 kbar) white BN transforms to a cubic form with the diamond structure and greater hardness.

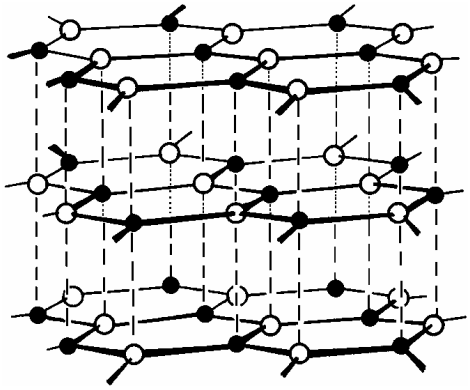

Figure 2. The layered structure of hexagonal BN.

Very recently, Novoselov *et al.* have reported free-standing atomic crystals that are strictly 2D and can be viewed as individual atomic planes pulled out of bulk crystals or as unrolled single-wall nanotubes [2.4]. They have taken several samples of layered materials with very strong intralayer bonds namely, graphite, BN, MoS_2, $NbSe_2$ and $Bi_2Sr_2CaCu_2O_x$, and obtained atomic 2D crystals by rubbing a fresh surface of the crystal against another solid surface, which left 2D atomic crystals along with a variety of other flakes. These atomic crystals were primarily identified by viewing the flakes on top of an oxidized Si wafer under the optical microscope and further investigated using scanning

tunneling, scanning electron, atomic force microscopy (AFM) and high resolution transmission electron microscopy (HRTEM). Electric field effects of few atomic thick carbon films were also studied by this group of scientists [2.7].

2.2.2 Structure of CdI_2

CdI_2 is termed a 'layer structure' because it consists of repeat units (sandwiches) I─Cd─I···I─Cd─I···I─Cd─I (where the symbols Cd and I represent layers of those atoms) with contact between adjacent iodine layers (Figure 3) [2.3]. CdI_2 is trimorphic. The known structures differ in the layer-stacking sequence (ABAB, ABCB or ABAC, and ABCACB). This is clearly not an ionic structure; bonds to the metal will be semi-ionic, but the I···I attraction is principally of the van der Waals type. Accordingly, the structure is easily cleaved between the I···I planes, which accounts for the flaky nature of the crystals. Much work has been done in the structural characterisation of the CdI_2 polytypes [2.8]. The related $CdCl_2$ structure has a cubic close packed stacking of layers (ABCABC) and the anisotropic properties are similar.

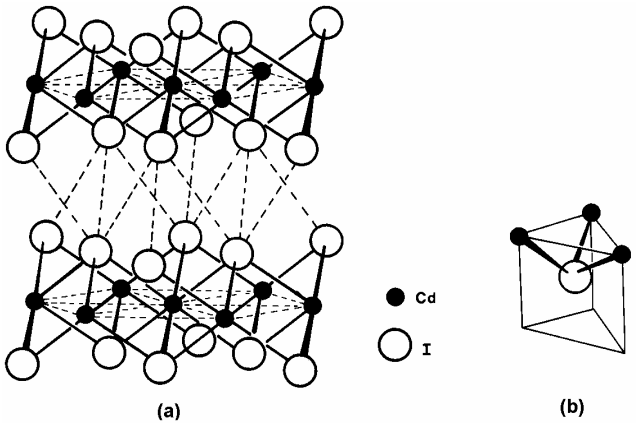

Figure 3. (a) The hexagonal CdI_2 structure. (b) The coordination around one I-atom.

2.2.3 Structure of $B(OH)_3$

Orthoboric acid is a dimorphic compound and both forms adopt layered packing [2.3]. In both the cases, the sheets are formed by the pseudo-hexagonal nearly perfect C_{3h} symmetrical $B(OH)_3$ molecules, which are connected *via* O─H···O hydrogen bonds to

three adjacent molecules (Figure 4). Hydrogen bond metrics in both forms are nearly the same. In both cases the sheets are connected *via* van der Waals interactions. However, the stacking sequences of the sheets differ between the two polymorphs. In H_3BO_3-3*T* (space group $P3_2$), the sheets are stacked with the repeating sequence ABCABC, whereas in H_3BO_3-2*A* (space group *P*-1), the sheets are stacked in the repeating sequence ABAB [2.9]. In effect, these structures are ccp and hcp variations of the same layer structure.

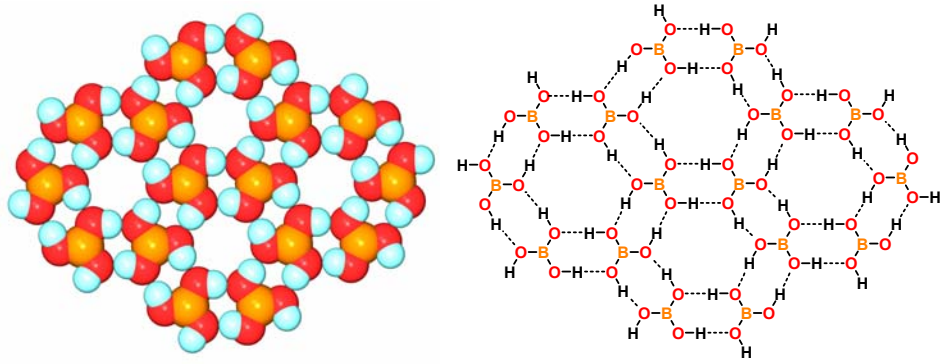

(a) **(b)**

Figure 4. Space filling model of pseudo-hexagonal sheet in $B(OH)_3$-3*T* formed *via* O─H···O hydrogen bonds (a) and molecular diagram of sheets (b). The sheet in the 2A polymorph is nearly identical.

2.2.4 2,4,6-Triethynyl-1,3,5-triazine

The crystal structure of 2,4,6-triethynyl-1,3,5-triazine, recently reported by Ohkita *et al.*, is a unique two-dimensional hexagonal network [2.10]. Weak C(sp)–H···N hydrogen bonds play a dominant role in stabilizing the layer structure, which is regarded as a supramolecular analogue of the hitherto unknown graphyne network. The network involves two types of short C(sp)–H···N contacts and has a head-to-tail polar tape using the first of these contacts. The tapes are connected to each other through the second of these contacts to form a polar network, which is stacked in an antiparallel fashion (Figure 5) at a separation 3.23 Å.

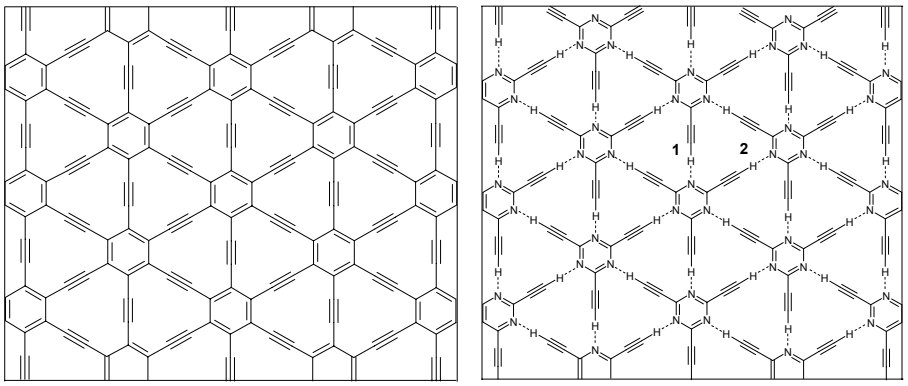

Figure 5. Two dimensional hexagonal network structures of (left) graphyne and (right) supramolecular graphyne. The two short C(sp)–H···N contact types are marked **1** (polar tape) and **2** (linker between polar tapes).

2.3 Shearing in Metal Single Crystals by Mechanical Stress

Mechanical shearing [1.11, 1.18] is often observed in metals because it is easy to slide one layer of the crystal over the next. Shearing caused by the sliding of layers held by non-specific interactions may be seen in single crystals of metallic Cu [2.11]. However, Cu is completely isotropic and the plane of shearing is immaterial. Shearing occurs if two layers of a crystal are subjected to a shear stress greater than the yield stress of the material, as shown in Figure 6a. Although it appears that the whole layer shifts over the hump one notch to the next, this does not happen in actuality. Shearing of a crystal in such a way would require much more force than what is normally applied. It is believed that the mechanism of such shearing is cooperative. One atom moves at a time; first, the atom on the left makes its jump, then the next, and so on, as indicated in Figure 6b. In effect it is the vacant space between two atoms that quickly travels to the right, with the net result that the whole second layer has moved over an atomic spacing. The slipping goes this way because it takes much less energy to lift one atom at a time over the hump than to lift a whole row. Once the force is enough to start the process, it goes the rest of the way very fast. In a real crystal, slippage will occur repeatedly at one plane, and then start at some other plane. Figure 6c shows a photograph of a tiny, thin copper crystal that has been thus sheared and stretched.

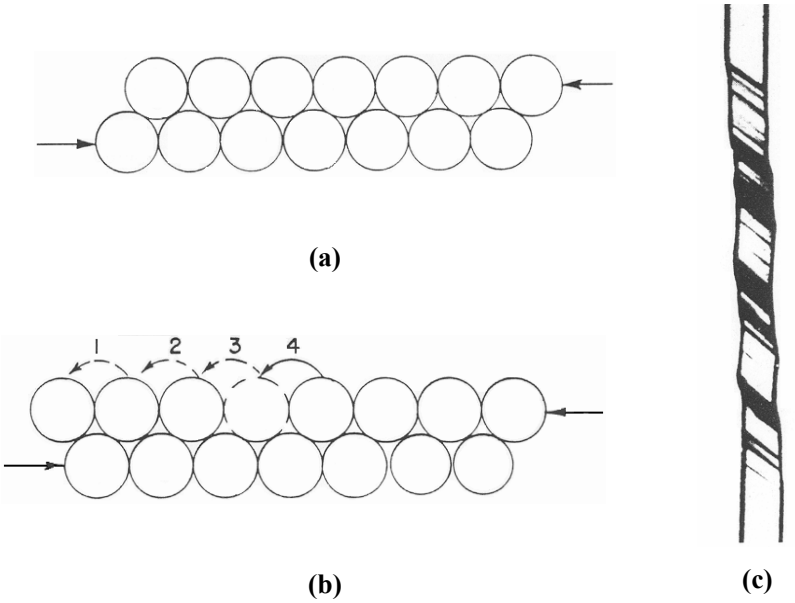

Figure 6. Shearing of layers. (a) Two layers of a crystal subjected to shear force (b) consecutive jumping of atoms in the shearing process. (c) A photograph of a small crystal of copper after shearing. Notice the striations on the crystal corresponding to the planes where slipping occurred. This figure is taken from reference [2.11].

2.4 Mechanically Induced Molecular Migrations in Layered Molecular Crystals

While dealing with solid state photochemical reactions, Schmidt proposed a topochemical hypothesis of 'minimal atomic and molecular movements' to explain the solid state reaction mechanism [1.7]. According to his hypothesis, molecules or atoms of the reactants have to move a minimum amount (at most 1.5 to 4.2 Å) to achieve the required topology (geometry, conformation and configuration) for the reaction to take place in the solid state. Schmidt's topochemistry hypothesis denies large scale molecular migrations both for homogeneous and heterogeneous solid-state reactions.

In connection with Schmidt's topochemical hypothesis, Kaupp *et al.* [2.12] have recently studied the action of mechanical stress [2.13] on two kinds of organic molecular crystals (layered and interlocked packing) by a new technique of nanoscratching at various faces in different directions in order to induce far-reaching anisotropic long-range molecular migrations. These workers have correlated their results with crystal packing and topochemical reactivity [2.12, 2.14]. In these experiments mechanical

scratching on the flat face of a crystal was done using a vertical cube corner indenter (Berkovich indenter). The three sided pyramidal tips were aligned with the sharp edge in front or back accordingly. In these experiments, chemically reactive crystals of thiohydantoin, anthracene, thiourea, tetraphenylethene and ninhydrin experience anisotropic long-range molecular migrations within the crystal because they exhibit cleavage planes between mono- or bi-layers along which migration occurs. For instance, thiohydantoin is an almost planar molecule with many hydrogen bonding acceptors and donors. It crystallizes in monolayer sheets that are 66º skew under the natural (110) face with cleavage planes between them. Scratching experiments in four different orthogonal directions on the skew cleavage planes of the crystal gave molecular migration (shift of debris) to different sides (Figure 7). The sketch in (a) and (d) of Figure 7 visualizes this situation more clearly. At 0º (along the long crystal edge [001]) molecular migration is to both sides and in front (b); the cracks indicate the direction of the cleavage planes. At 90º molecules migrate only to the right hand side (c). Only scratch (or abrasion) is detected at 180º as the tip moves against to the skew monolayers debris penetrate into the cleavage planes (e). At 270º molecules migrate only to the left hand side (f). The unusual piling-up of material only at one side of the scratch (Figure 7c, f) must be caused by the skew cleavage plane under the (110)-face. The geometric arrangement is such that the cleavage planes are open to the right side and blocked to the left side and vice versa as the scratching tip advances down in (b) and (d), respectively.

As there are multiple hydrogen bonds between the thiohydantoin molecules within a layer, single molecules cannot migrate, rather it appears likely that small molecular aggregates, such as almost planar hexamers that are present in the crystal structure as cyclic entities, may be small enough for the migration. On the other hand, scratching cannot induce molecular migrations in the case of chemically unreactive crystals of 2-benzylidenecyclopentanone or cis-1,2-dibenzoylethene which are packed with 3D-interlocking (Figure 8). Sometimes shift of debris in front or only abrasion is seen in these cases.

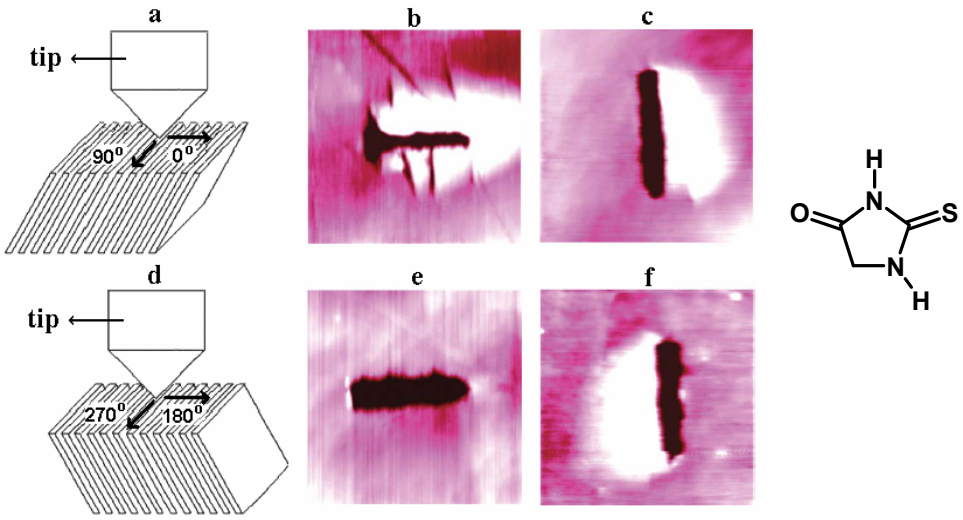

Figure 7. Nanoscratching on the (110) face of thiohydantoin crystals. Schemes (a) and (d) show the geometric conditions of the skew sheets sloping to the right and left respectively. AFM topographies of 5 mm nanoscratches with a cube corner at 250 mN in 60 s; (b) 0º, (c) 90º, (e) 180º, (f) 270º orientation with respect to the long crystal edge [001] or stacking direction. This figure is taken from reference [2.12a].

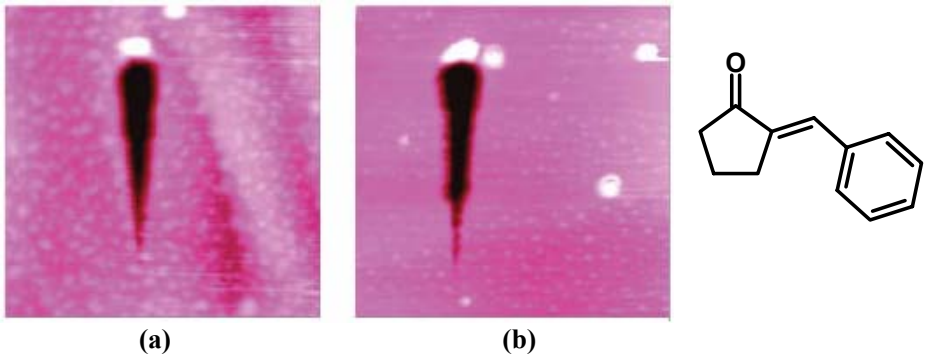

Figure 8. 2-benzylidenecyclopentanone (3D-interlocked packing); 15 mm AFM topography on (010) after ramp scratching with a cube corner indenter at 0–150 mN in parallel (a) and orthogonal (b) directions with respect to the long crystal edge [010], showing only abrasion and some debris collection in front. This figure is taken from reference [2.12a].

2.5 Results and Discussion

This chapter deals with the mechanical shearing, twinning and anisotropy of the layered structures **135B246I-T**, **135C246I**, **135B246M**, **135I246M**, and the molecular complexes **135C246I:135B246I**, **135C246I:135I246M**, **135C246I:135B246M**, **135B246I:135I246M**, as also 6-chloro-2,4-dinitroaniline **1** and 4-bromoacetophenone, **2** (Scheme 1).

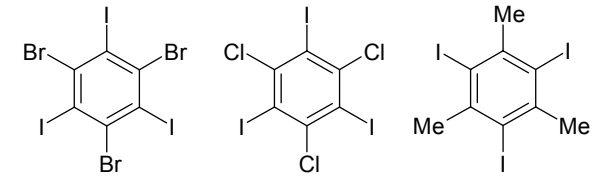

135B246I **135C246I** **135I246M**

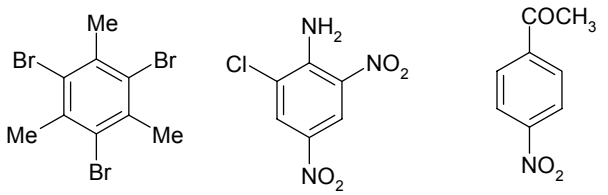

135B246M **1** **2**

Scheme 1

Crystals of 1,3,5-Trichloro-2,4,6-triiodobenzene, **135C246I** provides a good example for shearing crystals. **135C246I** crystallizes from THF in the triclinic, $P\bar{1}$ space group as long and thick blocks [2.15]. Molecules in its crystal structure are arranged in planar layers parallel to (100) and in a nearly hexagonal arrangement with clusters of three I-atoms from three neighboring molecules and correspondingly, clusters of three Cl-atoms (Figure 9). The I_3 clusters are formed with short I···I contacts within van der Waals distance. The Cl_3 clusters have Cl···Cl contacts somewhat loosely packed because of the bigger size of the I_3 clusters. These intralayer I···I interactions are chemically significant, because they are formed by polarization of I-atoms, which make the planar sheet strong. Successive planar layers are inversion related and stacked so that bumps in one layer fit into the hollows of the next. The interlayer interactions are non-specific in

that they are based on close packing of spheres in hollows. The planar layer structure in **135C246I** is reproduced in the corresponding bromo derivative **135B246I-T**, and in the methyl derivative **135I246M** [2.16], **135B246M** and **135C246M**. Mechanical properties of these crystals are discussed in this chapter while the detailed crystal structure analysis will be discussed in Chapter 5, noting the implications of these results on my understanding of the nature of halogen···halogen interactions.

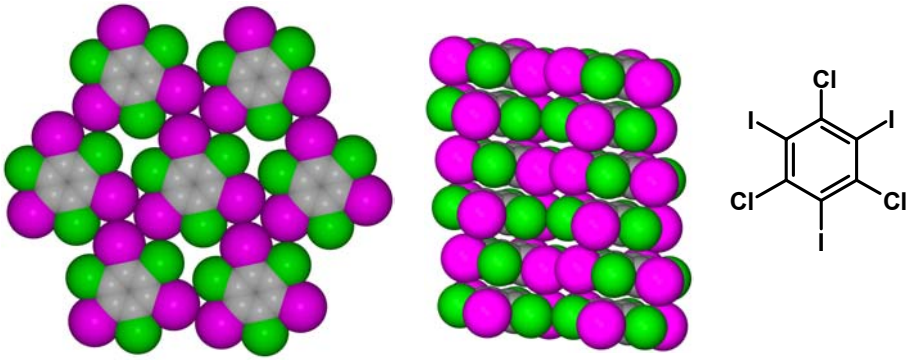

Figure 9. Crystal structure of **135C246I**. (a) Top view of a layer and (b) side view of layers.

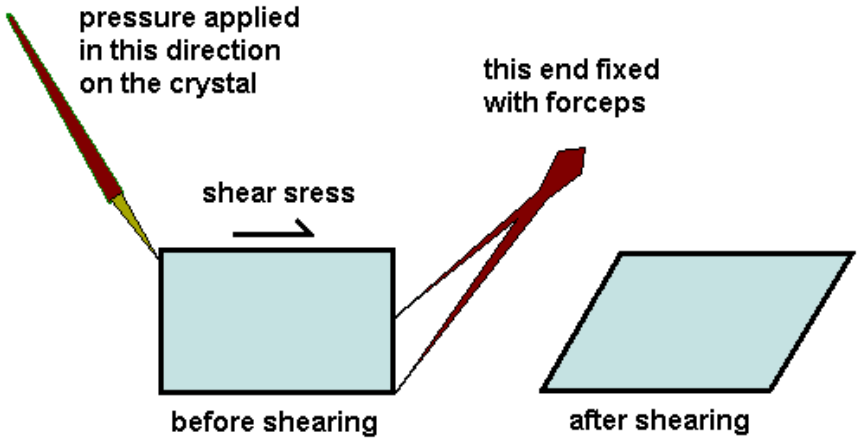

Scheme 2. Mechanical shearing of a layered structure using a needle and forceps.

Crystals of **135C246I**, grown from THF by slow evaporation, were found to be quite interesting being obtained as thick needles, some of which were boomerang-shaped. While examining these crystals under the microscope, it was also found that

some of them were curved and appeared with many striations nearly perpendicular to the crystal length (Scheme 2). These crystals were investigated to find out the reasons for the appearance of curvature, striations and boomerang-shapes.

Crystals of **135C246I** were separated carefully into normal, curved and V-shaped categories based on their appearance. Normal crystals were used to obtain the X-ray data and the V-shaped crystals which were found to be twinned will be discussed in the next section. Surprisingly, curvature was also observed when a normal (undeformed) crystal of **135C246I** or **135B246I-T** was pushed from opposite sides with metal needles roughly perpendicular to their length. Shearing occurred easily along (100) planes. Depending upon the direction and amount of stress applied on these crystals they transform into various shapes and/or cleave along the planes, as shown in Figure 10. This is similar to the shearing seen in single crystals of Cu (Figure 6c). This phenomenon, although not unprecedented, is certainly unusual in organic crystals, because usually organic crystals break when subject to a mechanical shear stress and generally do not shear in this manner.

After the shear deformation, crystals became curved and developed many striations at the regions where mechanical force was applied. Striations were also developed while separating the crystals from its mother liquor and handling at the microscope. A number of striations in Figure 11 show that they correspond to the shearing movement of (100) layers within a crystal of **135C246I**. The shearing direction corresponds to sliding of the (100) planes past one another. This deformation process has other parallels in the inorganic solid state and resembles the shearing of graphite [2.17a]. In contrast, when the crystal was attempted to shear or cut in other directions, the crystal broke. These directions would correspond to disrupting the layer structure—the difficulty in so doing confirms that the intralayer interactions are strong and directionally specific (synthon forming). When these crystals were subjected to a three-point bend test, they simply cleaved along the (100) planes.

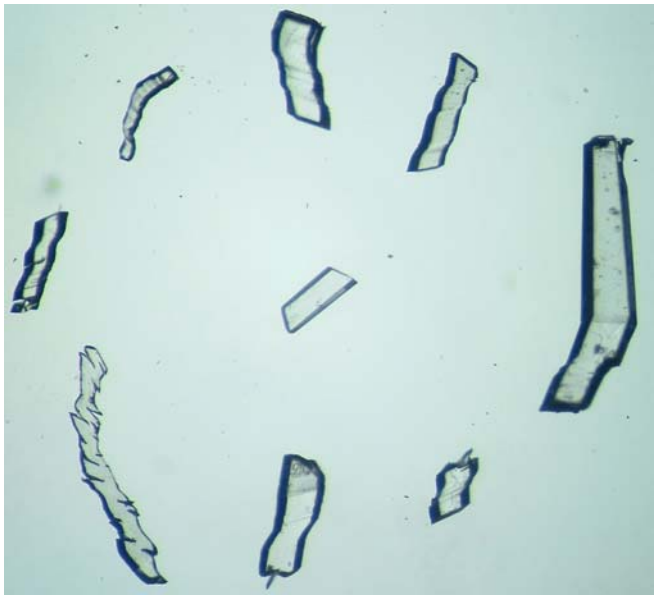

Figure 10. Crystals of **135C246I** sheared into different shapes by applying stress at various points. An undeformed crystal is shown in the middle. Notice the striations and slippage of planes in these crystals.

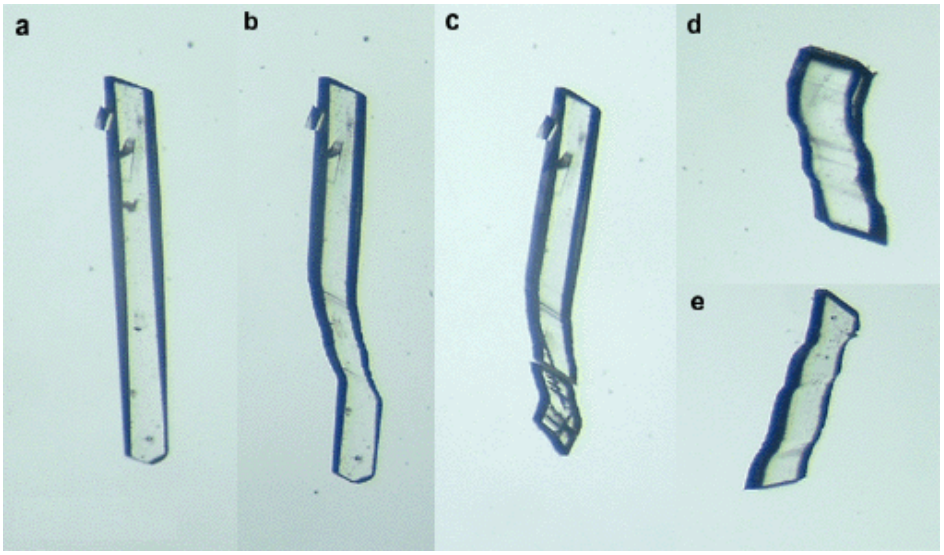

Figure 11. Shearing of crystals of **135C246I**: (a) unsheared specimen elongated along [100]; (b) after shearing. Notice the striations of slip along (100); (c) broken specimen after an attempt to cut it in a direction perpendicular to the shear plane; (d) and (e) multiple shearing. The similarity to Figure 8c may be noted.

A necessary condition for shearing is the presence of a layered structure. For example, **135I246M**, **135B246M, 135B246I:135C246I**, **135B246I:135I246M, 135C246I:135I246M** and **135C246I:135B246M** (see Chapter 5 for their crystal structures) also show this layered packing and shear just as easily. Compounds without layered packing do not show shearing on the application of a mechanical stress. They either break or bend. For instance, the monoclinic polymorph of **135B246I**, with a disordered corrugated layered structure, does not show shearing on application of a mechanical stress. In fact, it simply breaks down into pieces. There is a clear relationship between the appearance of a layered structure and susceptibility to mechanical shearing of layers. Such behaviour is often encountered in the study of plasticity of inorganic crystals. Such a relationship is mediated by dislocation movements within each layer, e.g., basal slip in hexagonal inorganic crystals like Zn, Cd and Mg. This deformation process has other parallels in the inorganic solid state and resembles the shearing of graphite [2.17], which has a layered structure, and polytypism in the layered CdI_2 [2.8, 2.18]. In the context of X···X interactions, the significant fact obtained from these experiments is that in **135C246I** the *intra*layer I···I interactions are much more important than the *inter*layer I···I and I···Cl interactions. To confirm the relationship between shearing and the appearance of a ~ 4 Å layered structure [2.19]. Similar experiments were carried out on molecular crystals of 6-chloro-2,4-dinitroaniline, **1** and 4-nitroacetophenone, **2**, which have completely different functional groups on the aromatic ring.

6-Chloro-2,4-dinitroaniline, 1

Form I of trimorphic 6-chloro-2,4-dinitroaniline, **1** has a layered structure in the monoclinic, $P2_1/c$ space group [2.5]. The short axis of the reported monoclinic form is 7.886 Å (nearly 2 × 4 Å) and the layers are stacked in an antiparallel fashion at separations of 3.057 Å and 3.209 Å (Figure 12). Layers are formed *via* N–H···O, C–H···O, C–H···Cl and C–Cl···O interactions. In this structure, intralayer C–H···O and C–H···Cl interactions are considered to be strong since the C–H groups are unusually activated by two nitro groups. The interlayer interactions are of the van der Waals type

and are non-specific. These crystals also underwent shearing on application of a mechanical stress and became irregular (Figure 13) as expected. This example makes it clear that shearing is not restricted only to the haloaromatics discussed above and that it is a widespread phenomenon among layered structures. The mechanical behaviour of the other two forms (Form II, corrugated layered structure and Form III, 3D-interlocked hydrogen bonded structure) will be discussed in Chapter 3.

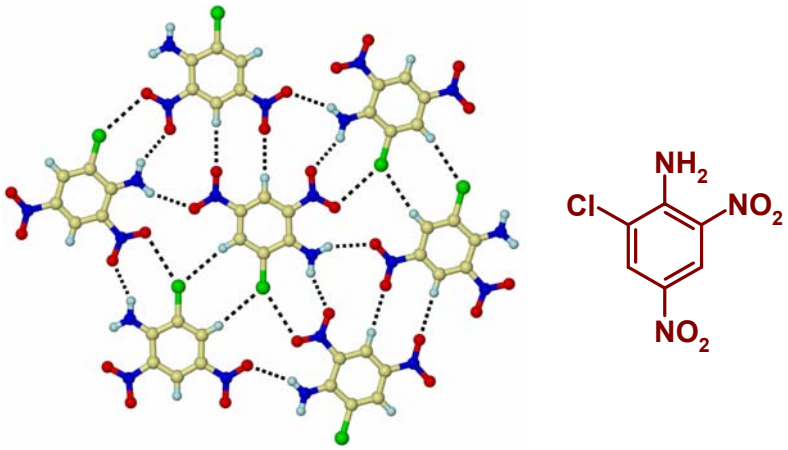

Figure 12. 6-Chloro-2,4-dinitroaniline, **1**. Layer structure to show N–H···O, C–H···O, C–H···Cl and C–Cl···O interactions.

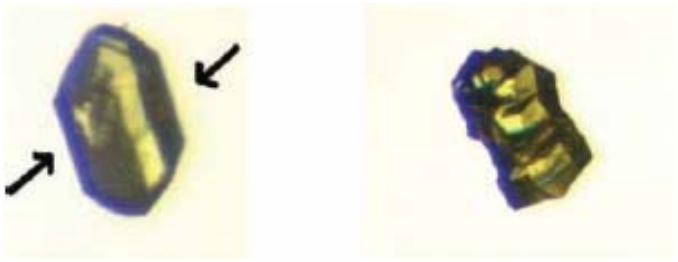

(a) **(b)**

Figure 13. Crystal of Form I (a) before and (b) after shearing. The arrows show the direction along which the shear stress was applied.

4-Nitroacetophenone, 2

In the crystal structure of 4-nitroacetophenone, **2**, molecules adopt a planar conformation in a 2D-layered packing (Figure 14) [2.20]. Layers are formed *via* C–H···O (*d*/Å, *θ*/º; 2.405, 136.78; 2.599, 140.01; 2.603, 162.78) interactions. Interlayer

interactions are of the weak van der Waals space filling type. The methyl hydrogen atoms of the acetyl group emerge into the interlayer space to form weak C–H···O (2.758 Å, 171.34 º) interlayer interactions.

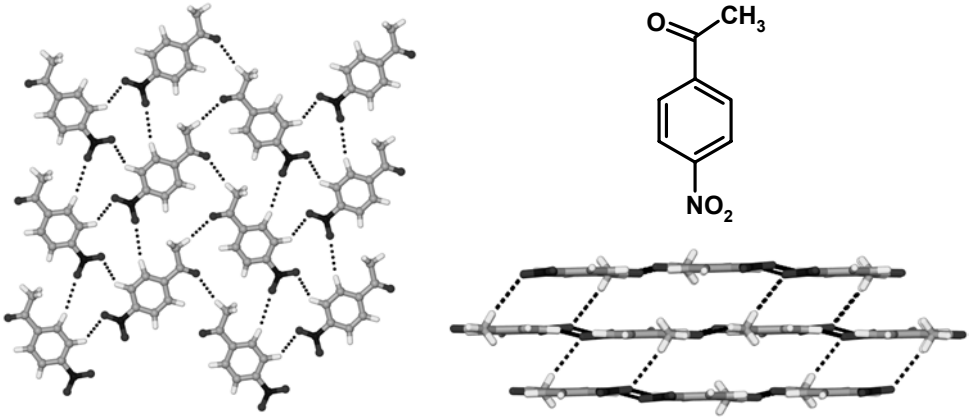

(a) **(b)**

Figure 14. 4-Nitroacetophenone, **2**. (a) Single planar layer (101) shows C–H···O interactions. (b) View down [010] shows stacking of parallel layers and a very weak interlayer C–H···O (2.758 Å) interaction.

Mechanical experiments on these crystals revealed that the shearing is not possible as seen in crystals of **135C246I**. However, layers of these crystals cleave easily and break down into slices on application of a mechanical shear stress. Although the *inter*layer interactions are weak in this structure, the crystals do not show shearing which is an indication of some specificity in the interlayer interactions. It is possible that in the shearing process, sliding layers have to encounter unfavorable repulsive $C^{(\delta+)}=O^{(\delta-)}...^{(\delta-)}O=C^{(\delta+)}$ interactions and locking of methyl groups (bumps on bumps) from molecules in the adjacent layers. Since the structure cannot afford to have these unfavourable interactions, layers would prefer to cleave rather than shear. The similar behaviour is observed in metal crystals when the shear strength is greater than the cleavage stress. In general, shear strength of a crystal will be more when the interlayer interactions are directional. Shearing of these crystals was also tried at higher temperatures, indeed up to the melting point 80 ºC, but there was no evidence for shearing.

2.6 Twinning

That the non-specificity of the weak interlayer interactions is vital for shearing is further confirmed by the structure of the boomerang or V-shaped crystals of **135C246I** and **135B246I-T**. Crystals with these distinctive shapes were obtained for every compound for which shearing was possible. Boomerang-shaped crystals of **135B246I-T** were mounted as such on a goniometer tip and X-ray data were collected (Figure 15). It was confirmed that twinning occurs at the hinge plane and that the common plane between the twins is (100) which is also the shearing layer mentioned above. A plausible twinning model is one in which two consecutive inverted layers in the normal structure are twisted by 60° and layers across the twin boundary are packed in a bumps-in-hollows fashion (Figure 16). This is preferred to a model in which the twins are mirror related because in the latter case, layers across the twin boundary would be packed in a bumps-on-bumps fashion. In general, the stacking of layers across the twin boundary is not as satisfactory as for the inverted layers in the untwinned crystal.

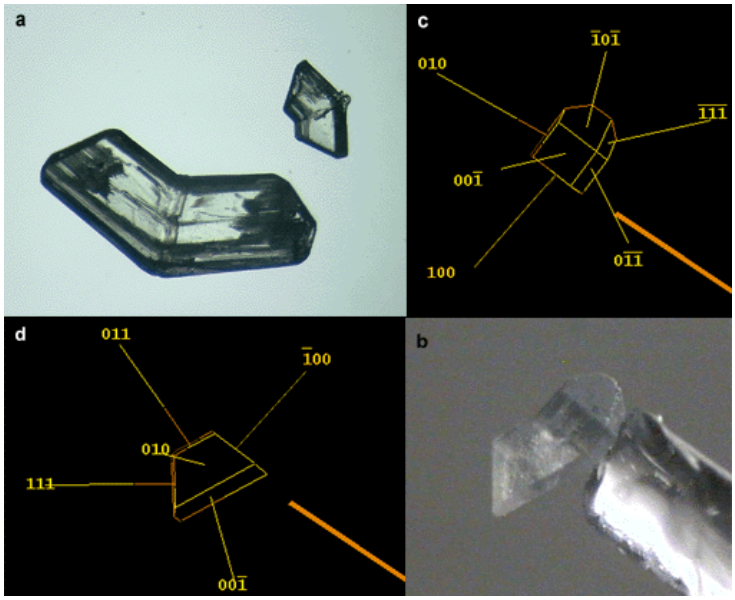

Figure 15. Twinning in **135B246I-T**: (a) twinned crystals; (b) twinned crystal as mounted on goniometer tip, used for X-ray measurements; (c) and (d) indexing of twin faces showing common plane (100). Notice that this is the plane that contains the structure determining I_3-supramolecular synthons.

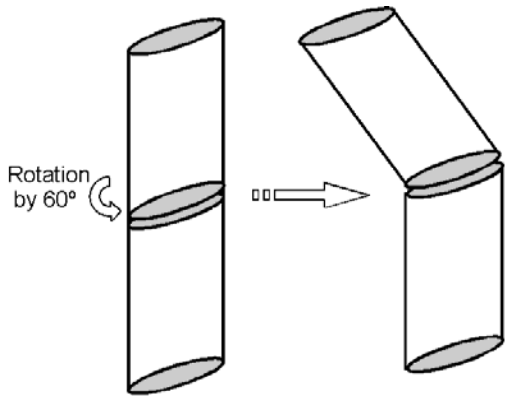

Figure 16. A schematic depiction of twinning shows that rotation by 60° achieves a boomerang shape.

Generally, bent or boomerang shaped crystals were obtained in all the structures that undergo shearing. However, in the 2:98 solid solution of **135B246M:135C246I**, grown from THF, multiple twinning was observed within the same crystal (Figure 17). In addition to the usual single hinged (V-shape) crystals, double hinged (N-shape), triple hinged (W-shape) and multiple hinged ("alkyl chain type zigzag") crystals were observed. All these crystals were grown as such from solution and obtained without mechanical deformation. The fact that twinning is easy and the twin boundaries always have a local minimum in free energy [2.21] suggests that normal and twinned stacking are energetically comparable. In other words, the interlayer I···I, Br···Br and I···Br interactions are non-specific, and this is important in the context of the shearing mechanism.

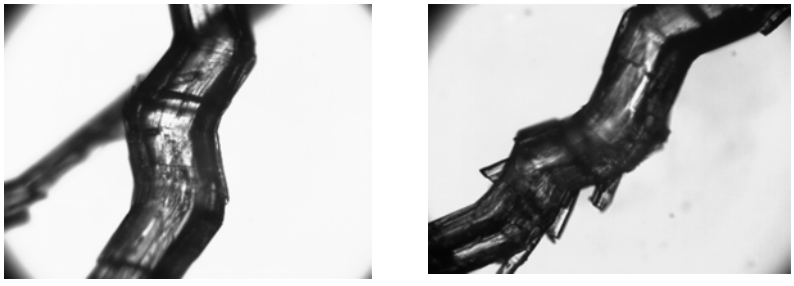

(a) **(b)**

Figure 17. Crystals of **135B246M:135C246I**: (a) triple hinged (w-type) crystal. (b) Multiple hinged (“alkyl chain” type) crystal.

2.7 Anisotropy in Molecular Crystals

The directional nature of thermal expansion can reveal some qualitative anisotropic features of the intermolecular forces in molecular crystals. In general, any direction in which intermolecular attraction is strong should have a relatively small coefficient of thermal expansion, while weak bond directions are expected to exhibit large expansion coefficients. To confirm the anisotropy of intermolecular interactions in the 1,3,5-substituted compounds, the cell parameters of **135B246I-T** and **135C246I** were determined at six different temperatures between 100 K and 300 K (Figure 18). The *a*-axis length (short axis) increases markedly with temperature compared to the other parameters (Table 1).

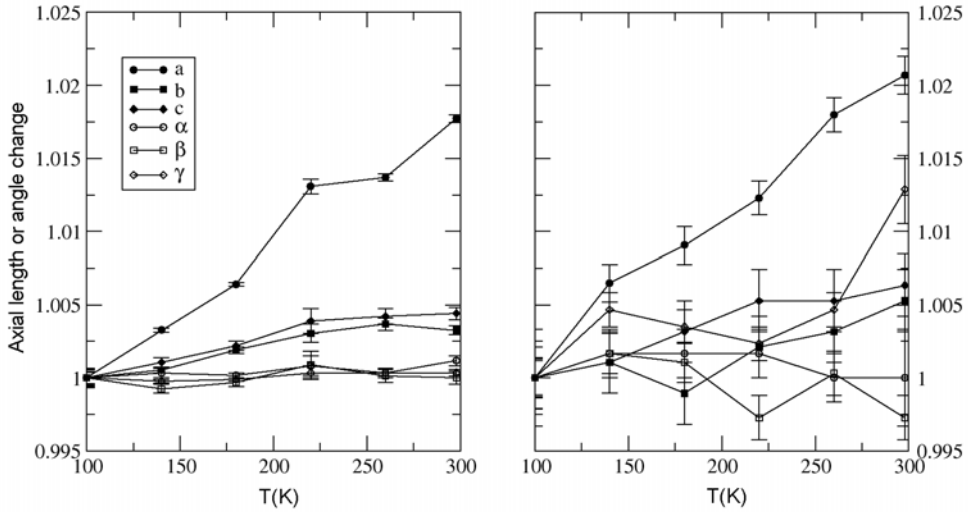

Figure 18. Variation of cell parameters with respect to temperature for compounds **135C246I** (left) and **135B246I-T** (right). Notice that the *a*-axis length increases markedly with temperature compared with the other parameters.

However, the change in the cell parameters cannot be directly correlated to the strength of the intermolecular interactions because the expansion coefficients also mirror the relative amount of expandable "empty" space in that direction [2.22]. Thus, directions corresponding to the longest molecular axis or the shortest intermolecular contacts will exhibit minimal expansion from purely geometrical reasons. The three cell lengths in these crystals are comparable but the expandable empty space is more in the *a*-

direction. Even after considering all these geometrical factors, the large difference in the expansion of the *a*-axis cell edge gives an indication that the interlayer interactions are weaker than the intralayer ones. An analogous situation in inorganic crystals is the anisotropic thermal expansion in metals like Zn and U.

Table 1. Variable temperature cell parameters (*d*/Å; *θ*/º) of **135B246I-T** and **135C246I**

135B246I-T

T/K	*a*	*b*	*c*	*α*	*β*	*γ*
100	7.953(3)	9.500(4)	9.512(5)	60.14(4)	66.21(4)	85.54(5)
140	7.979(1)	9.505(2)	9.522(3)	60.16(2)	66.16(2)	85.52(1)
180	8.004(1)	9.518(2)	9.533(3)	60.15(1)	66.19(2)	85.53(1)
220	8.057(4)	9.529(6)	9.549(8)	60.19(4)	66.27(6)	85.57(4)
260	8.062(2)	9.535(4)	9.552(5)	60.16(2)	66.22(3)	85.57(2)
298	8.094(2)	9.531(3)	9.554(4)	60.21(2)	66.21(3)	85.57(2)

135C246I

T/K	*a*	*b*	*c*	*α*	*β*	*γ*
100	7.73(1)	9.45(2)	9.46(2)	60.3(2)	65.78(9)	85.5(1)
140	7.78(1)	9.46(2)	9.47(2)	60.4(1)	65.89(9)	85.9(1)
180	7.80(1)	9.44(2)	9.49(2)	90.4(1)	65.85(9)	85.8(1)
220	7.825(9)	9.47(2)	9.51(2)	60.4(1)	65.6(1)	85.7(1)
260	7.869(9)	9.48(2)	9.51(2)	60.3(1)	65.8(1)	85.9(1)
298	7.89(1)	9.50(2)	9.52(2)	60.3(2)	65.6(1)	86.6(2)

2.8 Conclusions

To conclude, shearing of organic crystals is a common phenomenon and occurs in layered structures wherein the intralayer interactions are strong and specific, and the interlayer interactions are non-specific and weak. The intralayer interactions are directionally specific and form synthons in a planar layer, the structure of which is conserved in the normal, sheared and twinned specimens. In contrast, the interlayer

interactions are shape based and non-specific. This combination of specific intralayer interactions and non-specific interlayer interactions leads to shearing. Accordingly it may be concluded that X···X interactions (X = Cl, Br, I) are of several types and that it is sometimes difficult to characterize them using only geometrical criteria. The use of an independent technique, like observation of the mechanical behaviour of the crystal, offers a much clearer insight into their nature. The softness of the halogenated crystals is reminiscent of CdI_2 wherein layers of I-atoms form a close packed array and which shows similar anisotropic behavior. Whether or not these layered structures would exhibit polytypism like CdI_2 is still an open question but stacking faults are undoubtedly present. Mechanical experiments provide an excellent opportunity to study the nature of $\pi\cdot\cdot\pi$ interactions and the anisotropic behaviour of interactions in molecular crystals. From the present study it is clear that shearing is not possible in all layered molecular crystals, and that the required chemical and geometrical conditions, strength and specificity or otherwise of interlayer interactions and extent of anisotropy, if present, between *inter*layer and *intra*layer interactions for shearing are yet to be investigated for deeper understanding.

The effects of geometrical factors (available empty space) on the thermal expansion of cell parameters make it difficult to estimate the anisotropy of intermolecular interactions in most molecular crystals. But my experiments on these crystals hint that these crystals are highly anisotropic and that variable temperature X-ray data may be used as a qualitative supporting technique to confirm the same.

The mechanical response of these molecular crystals resembles in some respects that of certain types of inorganic crystals like graphite, which shows shearing. It is also well known in mechanical metallurgy that in most metals, the planes on which slip or shearing takes place are usually those with closest atomic packing, while the slip direction is always the closest-packed direction in the slip plane, which is similar to that of the layered structures discussed in this chapter. As the latter class of crystals has been investigated extensively, I conclude that there is scope for understanding the mechanical behaviour of these two different classes of crystals on a common basis.

2.9 Experimental Section

Materials: Samples of 6-chloro-2,4-dinitroaniline, 4-nitroacetophenone and all reagents and solvents employed were commercially available (Lancaster) and were used as supplied without further purification. All these compounds were characterized with NMR and IR spectra. The 1H NMR spectra were recorded on Bruker Avance at 400 MHz instrument. IR spectra were recorded on a Jasco 5300 spectrometer. All melting points were measured in Fisher-Johns melting point instrument.

Synthesis: All the mixed halogenated compounds were synthesized by either bromination or iodination of the corresponding halogenated starting materials. The general bromination and iodination procedures used to prepare these compounds are given for **135B246C** and **135C246I** [2.23].

Bromination: A mixture of 1,3,5-trichlorobenzene (3 mmol, 556 mg) and electrolytic Fe powder (19 mmol, 1 g) was taken in a round bottomed flask and Br_2 (0.23 mol, 6 mL) was added dropwise at 273 K after which the mixture was heated at 408-413 K for 1 h. The resulting mixture was poured into 500 mL of saturated $NaHSO_3$ solution, the precipitate filtered off and crystallized from THF to give 900 mg of **135B246C**. IR (KBr, cm^{-1}): 1317, 1271, 623; MS (70 eV): m/z (%): 414 (M^+), 416 ($M^+ + 2$), 418 ($M^+ + 4$), 420 ($M^+ + 6$), 422 ($M^+ + 8$), 424 ($M^+ + 10$), 335, 258, 107 and 77.

Iodination: H_5IO_6 (1.66 mmol, 380 mg) was dissolved in conc. H_2SO_4 (6 mL) and crushed I_2 (5 mmol, 1.27 g) was added followed by stirring for 0.5 h. Then 1,3,5-trichlorobenzene (1 mmol, 186 mg) was added to the reaction mixture, followed by stirring for 24 h at room temperature and then for 36 h at 333 K. The reaction mixture was cooled and poured onto crushed ice. The solid was filtered and recrystallized from THF to yield 390 mg of **135C246I**. IR (KBr, cm^{-1}): 1647, 1292, 559, 416; MS (70 eV): m/z (%): 558 (M^+), 560 ($M^+ + 2$), 562 ($M^+ + 4$), 431, 304, 234, 179, 142, 127, 107 and 72.

1H NMR: (400 MHz, [D_6]DMSO, 25 ºC, TMS): No peaks were found in the spectrum for all the hexahalogenated compounds.

Crystallization: All the compounds were crystallized from either CCl_4, THF or 1,4-dioxane by slow evaporation at ambient temperature.

X-Ray Crystallography: Face indexing was done on a Bruker Nonius Smart Apex CCD with graphite monochromated Mo-Kα radiation. For twinned crystals reflections were sorted out using program RLAT version 3.0 and obtained the cell values for both the twinned regions. Full data collection details are discussed in Chapter 5.

CHAPTER 3

STRUCTURAL BASIS FOR BENDING OF ORGANIC CRYSTALS: STRUCTURE-PROPERTY CORRELATION

3.1 Introduction

The study of molecular crystals subjected to mechanical stress has long been a subject of considerable interest to both chemists and mechanochemists [1.9]. In this process, breaking and making of covalent and noncovalent bonds takes place [3.1], i.e. chemical and supramolecular reactions take place [3.2]. In the pharmaceutical industry, bulk properties of a drug like hardness, strain rate sensitivity, granularity and flowability depend on its mechanical properties [3.3]. These properties play an important role in formulation and tableting. Controlling the mechanical properties demands a good understanding of structure-property relationships. But the mechanical properties of molecular crystals are poorly understood except for some generalisations [3.4]. For example, it is known that the typical organic molecular crystal is not mechanically tough and is susceptible to deformation or breakage on the application of mechanical stress. No systematic studies on the mechanical behaviour of molecular crystals have been reported in the literature [2.5b].

Although molecular crystals with unusually deformed morphologies have been noticed by crystallographers over the years, such observations have been generally ignored, due to the fact that crystallographers tend to choose high-quality single crystals for their X-ray diffraction studies [3.4]. For this reason, the examination of any given batch of crystals normally ends when a crystallographer finds a suitable single crystal for analysis and further attention is not paid to strange or differently shaped crystals from the same batch. The studies reported in this chapter are focused on the mechanical bending phenomenon of some organic molecular crystals and the correlation of such bending with crystal packing.

3.2 Bending in Metals

Bending is the process by which a straight length is transformed into a curved length [1.18]. Bending is a common process for changing metal sheet or plate into channels, drums, tanks and is part of the deformation in many other forming operations. The bending process of metal crystals at the atomic level is explained using the theory of dislocations [1.11]. The conventional definitions of the terms used in bending are illustrated in Figure 1 [3.5]. The bend radius *R* is defined as the radius of curvature on the concave or inside, surface of the bend. The neutral axis is an axis along which there will not be any change in the length in the deformation process. For elastic bending, that is below the elastic limit, the strain passes through zero halfway through the thickness of the sheet at the neutral axis. In plastic bending, that is beyond the elastic limit, the neutral axis moves closer to the inside surface of the bend as the bending proceeds. Since the plastic strain is proportional to the distance from the neutral axis, fibers on the outer surface are strained more than fibers on the inner surface which are contracted. Since the average fiber at the mid-thickness is stretched, there will be a decrease in thickness (radial direction) at the bend to preserve the constancy of volume. The smaller the radius of curvature, the greater will be the decrease in thickness on bending.

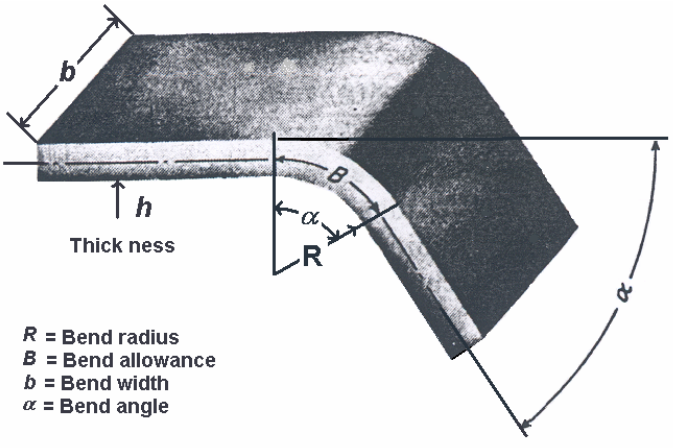

Figure 1. Bending of a metal sheet and definition of terms used in bending in mechanical metallurgy. This figure is reproduced from reference [3.5].

According to the theory of bending [3.6] the strain increases with decrease in radius of curvature. For a given bending operation the bend radius cannot be made smaller than a certain value or the metal will crack on the outer tensile surface. The minimum bend radius is usually expressed in multiples of the sheet thickness (*h* or *t*). Thus, a 3*t* bend radius indicates that the metal can be bent without cracking through a radius equal to three times the sheet thickness. The bend radius varies considerably from metal to metal and always increases with cold-working (deforming at lower temperature). Some very ductile metals have the minimum bend radius of zero, indicating that they can be flattened upon themselves. For high-strength sheet alloys the minimum bend radius may be 5*t* or higher. The minimum bend radius also depends on the geometry of the bending conditions.

3.3 Results and Discussion

After observing shearing in layered structures (Chapter 2), the mechanical experiments were also extended to a few other molecular crystals. In this process, the bending phenomenon was first observed in crystals of hexachlorobenzene which crystallizes in the monoclinic space group $P2_1/n$ with a *ca*. 4 Å short axis [3.7]. At first, the bending phenomenon in the C_6Cl_6 crystals seemed like an inexplicable property. In the search for reasons for the bending, an extensive survey of 60 (Table 2) molecular crystals was carried out to discover some more similar examples and to then establish a correlation between such bending and the crystal packing. The survey was begun with crystals that have a similar short crystallographic axis of *ca*. 4 Å [2.18] and then moved on to other types of compounds like 1D to 3D, isostructural to polymorphic, stacked to interlocked and co-crystals to solvates. At the end of the survey, it was found that around 17 of them could be bent (Table 1), while the rest (43 out of 60) could not be bent plastically (Table 2) in any direction on application of a mechanical stress. The 60 compounds were selected more or less randomly based on easy availability in our laboratory.

A model for bending was proposed using the information obtained from the mechanical bending experiments, X-ray diffraction and face indexing on both bending

and non-bending (brittle) crystals. Mechanical properties of both the bending and brittle crystals and a correlation of such mechanical properties with crystal packing are discussed in this chapter. Bending crystals will be discussed in Section 3.3.1, and the brittle crystals in the Section 3.3.7.

Table 1. List and details of bending crystals

No.	Name of Compound	M.P. /K	Crystallogr. Short Axis	CSD Refcode/ CCDC No.
1	2-(Methylthio)nicotinic acid	488	3.9834(10)	KAMQIZ
2	Hexachlorobenzene	491	3.8861(1)	HCLBEN11
3	Hexabromobenzene	598	4.007(1)	HBRBEN01
4	1,3,5-Trichlorobenzene	336	3.921(1)	TCHLBZ
5	1,3,5-Tribromobenzene	394	4.080(10)	TBRMBZ
6	Pyrazine-2-carboxamide	463	3.750(10)	PYRZIN14
7	6-Chloro-2,4-dinitroaniline	432	3.6646(8)	250456
8	Venlafaxine hydrochloride	484	5.797(6)	WOBMUV01
9	4-Nitrobenzoic acid	513	5.153(2)	NBZOAC02
10	4-Chlorobenzonitrile	364	4.038(1)	CLBZNT02
11	3,4-Dichlorophenol	339	3.859(5)	DCLPHM
12	Benzamide:pentafluorobenzamide (1:1)	377	7.355(1)	ESATOH
13	1,3,5-Trifluoro-2,4,6-triiodobenzene	425	4.7931(20)	261303
14	4-Fluorobenzonitrile	308	3.869(1)	PFBZCY
15	2-Nitrobenzaldehyde	316	3.960	NIBZAL
16	1,3-Dinitrobenzene	361	3.677(1)	DNBENZ11
17	3,4,5-Trimethoxybenzaldehyde	346	4.6649(12)	RAJKOC

3.3.1 Bending Model: 2-(Methylthio)nicotinic acid, 1

A good example for the bending model is provided by 2-(methylthio)nicotinic acid, **1** [3.8]. Plate-like long crystals of **1** were obtained from THF solvent at ambient temperature by the slow evaporation method. In the crystal structure, nearly planar

molecules form centrosymmetric acid dimers *via* strong O–H···O hydrogen bonds (1.85(5) Å and 169(5)°) and these dimers are stacked down the needle direction [100], which is also the short axis. The dimers are arranged laterally along [001] with C–H···O interactions (*d*/Å, *θ*/°; 2.63, 141; 2.70, 157). Along the third direction, namely [010], adjacent dimers are close packed in a zigzag fashion with Me···Me contacts (Figure 2).

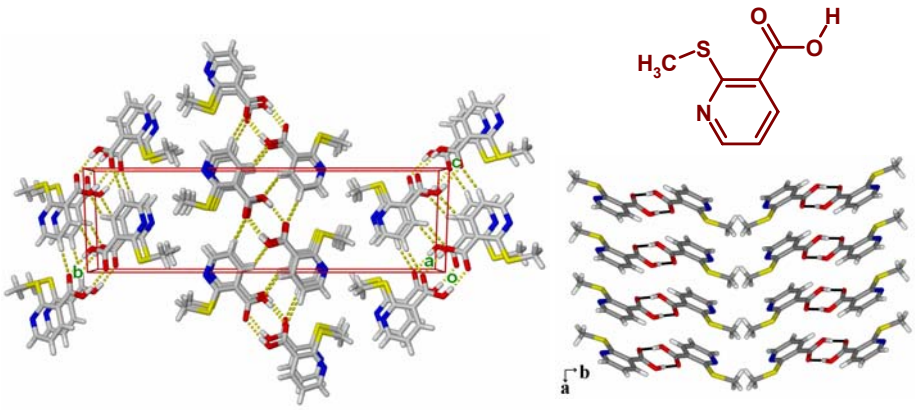

(a) **(b)**

Figure 2. 2-(Methylthio)nicotinic acid, **1**. (a) The zig-zag arrangement of molecules showing O–H···O and C–H···O hydrogen bonds parallel to the $(\bar{2}\,72)$ plane. (b) Stacking of dimers along crystal length. Notice the weak Me···Me interactions and $\pi\cdots\pi$ molecular stacking.

In search of a structural correlation for the bending phenomenon, faces of a plate like crystal of **1** were indexed (Figure 3). The same crystal was then used for the mechanical bending experiments. The crystal was viewed under microscope and the bending and non-bending faces of the crystal were determined [3.9]. In the bending process the crystal was taken with the (001) face on top and was prevented from movement at its ends by a pair of forceps that gripped the $(0\,\bar{1}\,0)$ planes. Pressure was then applied with a needle from the other side of the crystal, i.e. on (010), and in the middle. The crystal bent easily as seen in Figure 3c. The bending was continued till the crystal assumed a hairpin shape (Figure 3d). In the bending process the overall volume of the crystal remains nearly constant with permanent deformation of the crystal (the elastic

component of the total deformation is extremely small and is usually ignored). This is termed as *plastic bending* in the language of mechanical metallurgy. The bent crystal could also be 'straightened out' somewhat with the sites of the tools reversed (forceps ↔ needle) but it did not regain its pristine condition, i.e., some permanent deformation/strain was introduced in the crystal: mainly, it did not show diffraction characteristic of a single crystal anymore. Bending is strongly anisotropic in the type of crystals under consideration. When another crystal of **1** was placed with the (010) face upwards and subjected to mechanical stress as before but with the needle and forceps coming in on the (001) and (00 $\bar{1}$) faces, it cracked and eventually broke.

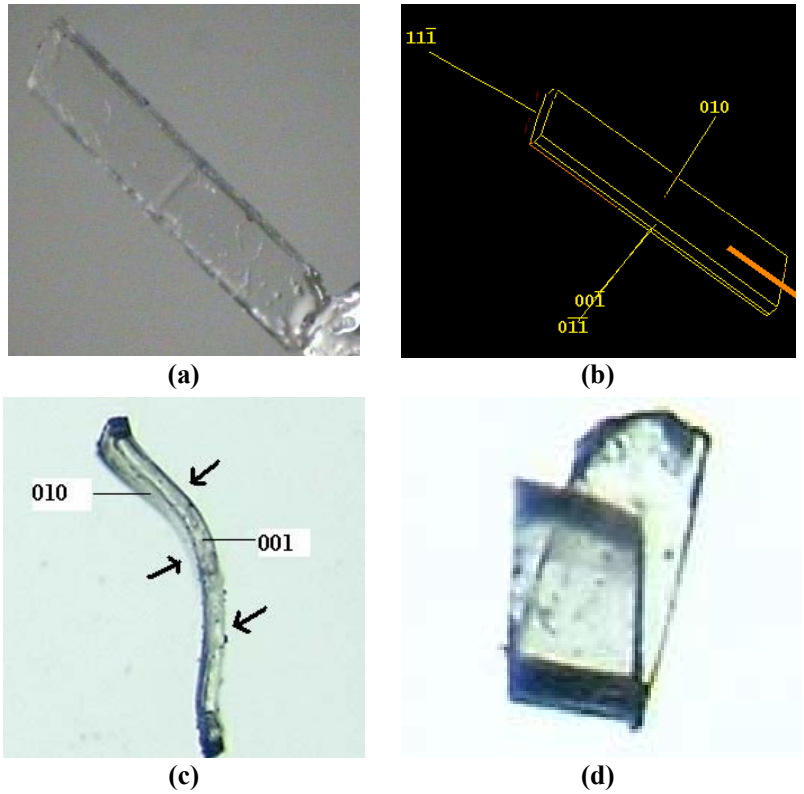

Figure 3. 2-(Methylthio)nicotinic acid, **1**. (a) Crystal as mounted for face indexing. (b) SMART face indexing graphic. (c) The same crystal bent on the (010) face; arrows show the point of impact of forceps and needle. Crystal packing shown in the Figure 2b is in the same orientation. (d) Crystal bent into hairpin shape.

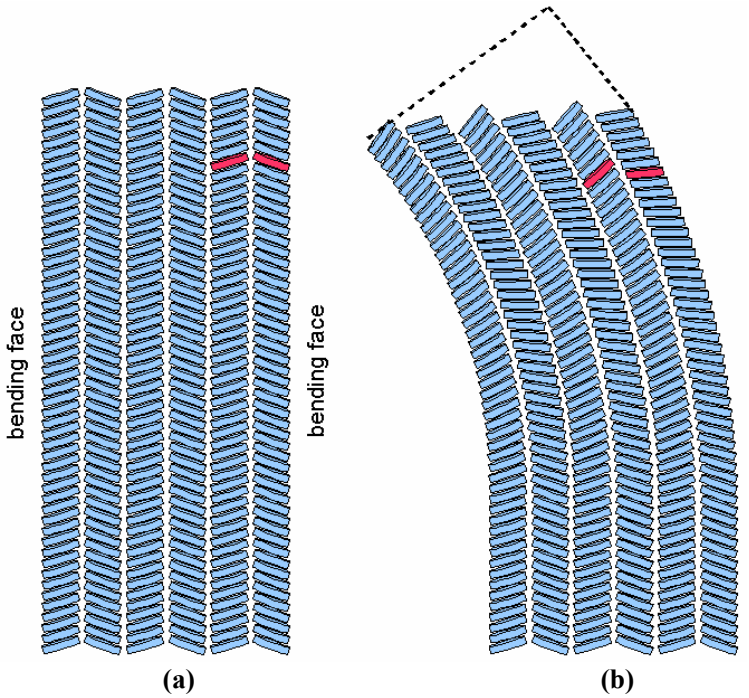

Figure 4. A model for bending (half sectional view). (a) Undeformed crystal. The white spaces between rows of stacks represent the weakest interactions. (b) Bent crystal. Note the pronounced deformation in some of the interfacial angles.

Close examination of both the crystal packing and the anisotropic bending behaviour of the crystals provided useful information related to the bending phenomenon. A schematic depiction of these events is given in Figure 4, which shows the crystal structure as viewed on the (001) face (similar to Figure 2b). The acid dimers in the undeformed crystal (Figure 4a) are shown as stacked disks, and the white regions between the molecular stacks correspond to Me···Me close packing. For bending of the kind observed to take place, one set of interactions ($\pi\cdots\pi$ stacking) should be substantially stronger than another (Me···Me van der Waals) in a nearly perpendicular direction. Application of a mechanical stress would then lead to the situation shown in Figure 4b. The disks are able to assume their distorted orientations in the bent crystal either by sliding along the molecular planes or by splaying (see the change in orientation between the red coloured disks in Figure 4). The dotted lines in Figure 4 show the

imaginary interfacial angles which were present in the undeformed shape (before bending).

As discussed before, in plastic bending of metals (beyond the elastic limit), the outer radius of the fibre increases while the inner radius decreases. The thickness of the bent portion decreases slightly to maintain the constancy of the overall volume. As a result, the outer length of the arc increases while the inner length of the arc decreases. In the case of elastic bending, there will be a change in volume below its elastic limit [3.5]. In contrast, in plastic bending of molecular crystals within the accuracy of present measurements the volume and thickness of the crystal remains nearly the same (the elastic component constitutes a very small fraction of the total strain). It is interesting to note that the interfacial angles of the crystal ends have changed markedly (Figure 4b) to keep the volume constant and lengths of the inner and outer arcs of the crystal the same. Such an observation has not been reported in metals. In fact, this is the clinching clue that suggests that the plastic bending of molecular crystals is not identical to the bending of metal crystals. This is the basis for the bending model proposed for molecular crystals.

3.3.2 Isostructural Compounds

Comparing isostructural compounds is advantageous because in these structures the crystal packing is kept constant and variations in properties can be directly correlated to the small differences present in the structures. In general, isostructural compounds [1.23] contain topologically similar supramolecular synthons [1.13] in their crystal structures. This allows one to compare the synthon energies.

Hexachlorobenzene, 2

The planar molecules of **2** form π···π stacks along the crystal length; within these stacks, the molecules are 3.44 Å apart (perpendicular distance) and tilted 63.3º to the stack direction so that π···π interactions are optimized (Figure 5a) [3.7a]. There are two categories of Cl···Cl interaction in the overall distance range of 3.44-3.67 Å. No Cl···Cl interaction appears to be particularly important and *π*···*π* stacking dominates the packing. The bending face is (001) from which the weak and non-specific Cl···Cl contacts emerge

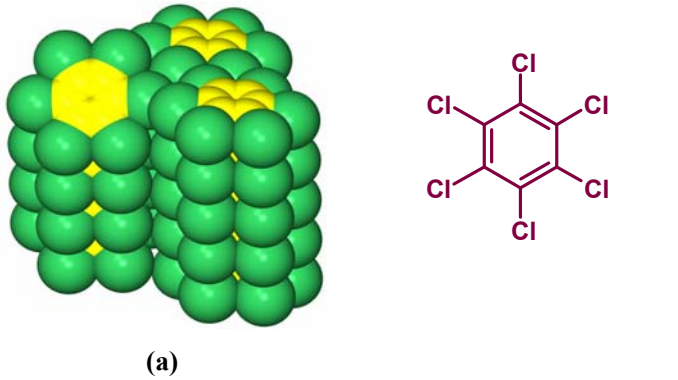

(a)

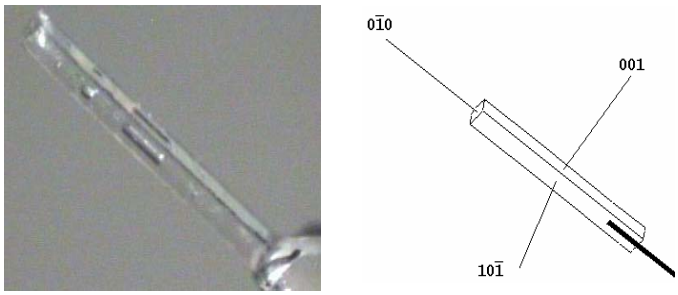

(b) **(c)**

Figure 5. Hexachlorobenzene, **2**. (a) Packing shows the rows of stacks along the crystal length. (b) Crystal as mounted for face indexing. (c) SMART face indexing graphic.

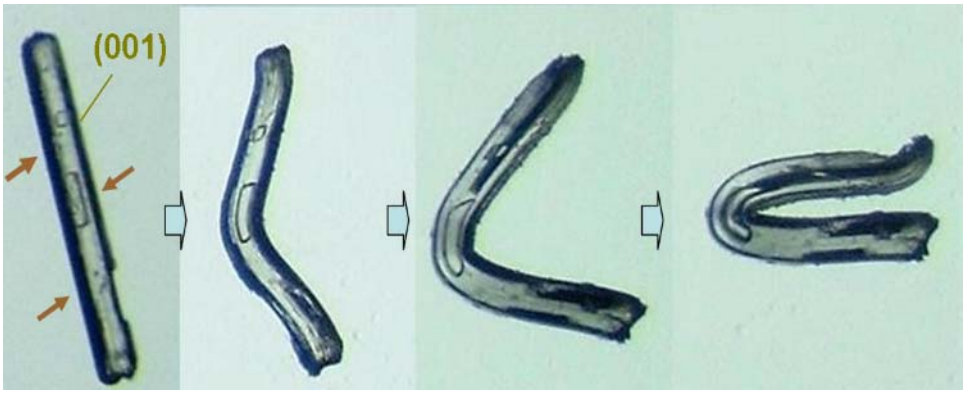

(a) **(b)** **(c)** **(d)**

Figure 6. Bending of the same face indexed crystal seen in Figure 5. (a) Before bending. Arrows show the point and direction of the stress applied. (b), (c) and (d) show different snapshots in the bending process. Notice the very low bend radius (close to zero) in figure (d).

(Figure 5b, 5c). Bending experiments were also carried out at 273 K by cooling the sample and it was found that the crystal bends as easily as it does at room temperature. This clearly shows the weakness and the non-specificity of the Cl···Cl interactions. Interestingly, these crystals can be deformed into various shapes depending upon the direction and the point of stress application on the crystals (Figures 6 to 8). In extreme cases, they can be even flattened upon themselves (Figure 6d). That is, the bend radius of the crystal approaches zero, if care is taken to prevent buckling.

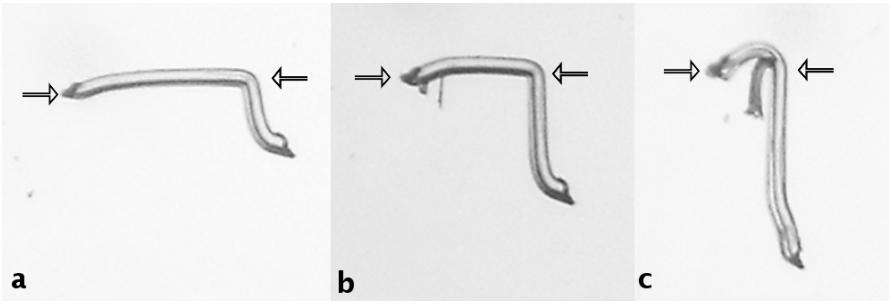

Figure 7. (a), (b) And (c) show the propagation of the bend through the crystal on continuous stress application. Arrows show the point and direction of the stress applied.

An interesting aside here is that when a crystal of C_6Cl_6 (m.p. 500 K) is compressed along its needle length, that is, [010], a bending deformation takes place, which on further compression propagates in a consecutive manner through the crystal (Figure 7). Inspection of Figure 4 will show why this is the case.

The feeble nature of the Cl···Cl interactions in C_6Cl_6 is further indicated by the variation in the shape of the bent specimens as a function of the mode of application of force. Figure 8a would result from a compressive force applied at both ends, parallel to the longitudinal axis. Figure 8b shows the situation when the crystal volume remains unchanged, as in plastic bending, if care is taken to prevent buckling [3.5]. Crystals also were subjected to three-point bending to obtain a bent shape, the schematic of which is shown in Figure 8c [3.5]. The cartoon depictions in Figure 8 show that the sliding of molecules past each other is very easy, and that the internal stresses between molecules in the stacks are dissipated with these kinds of deformation. Again, the conclusion is clear: interactions between halogen atoms between stacks are weaker and/or less specific than the $\pi\cdots\pi$ interactions within a stack.

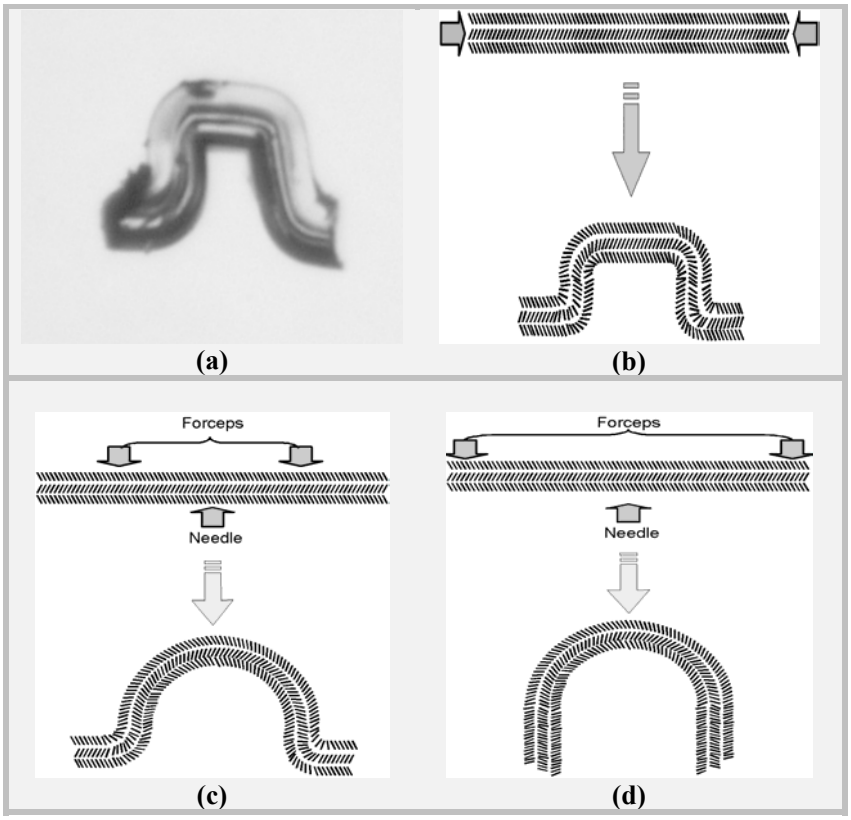

Figure 8. Bending of a normal C_6Cl_6 crystal into different shapes. (a) A crystal bent in four regions by a compressive force applied at both ends, parallel to the longitudinal axis; (b) schematic depiction of the process described in (a); (c) bending into an Ω-shape. The two bends in the flat portion of the crystal occurred without additional anchoring—the forceps tips were enough; (d) bending into a ∩-shape by changing the points of anchoring. Arrows indicate the point and direction of force applied.

Bending experiments on C_6Cl_6 crystals were also done using a nanoindenter. The crystal, with the bending face (001) upwards, was placed on a small iron washer which had a hole in the middle as shown in Figure 9a. The middle part of the crystal was unsupported. The indenter tip was used to press the crystal in the middle portion by applying a load of 10 g (a force of 98 mN). The direction of motion of the indenter tip was parallel to the [001] direction of the crystal. The rate of displacement of the tip was constant. The crystal underwent deformation as shown in Figure 9b. Two crystals that were used in this experiment had almost the same thickness (0.3 mm) and the

displacement (measured using a graduated optical microscope) was *ca*. 1 mm for both. Notably, when a crystal of C_6Cl_6 was placed on the washer with the (100) face pointing upwards, indentation led to immediate breakage. This reveals the strongly anisotropic nature of the plastic bending present/inherent in these molecular crystals.

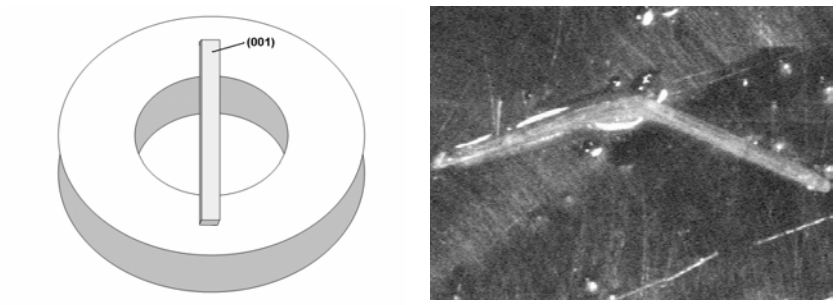

(a) **(b)**

Figure 9. Bending of C_6Cl_6 crystal using a nanoindenter tip. (a) Schematic depiction of crystal as mounted on iron sample holder. (b) Photograph of the crystal after bending.

Hexabromobenzene, 3

Hexabromobenzene, **3**, [3.10] is isostructural to C_6Cl_6 and was expected to bend. Surprisingly it did not. However, using the well known idea that the correct way of comparing the mechanical response of materials is in terms of similar/identical homologous temperature [3.10, 3.11] (equal to T/T_m where T is the temperature of deformation and T_m is the melting temperature are on the absolute scale), the bending experiments were repeated at 403 K. Bending took place at this elevated temperature, as it did for C_6Cl_6 at room temperature (Figure 10). The higher melting point of C_6Br_6 (T_m = 598 K) when compared to C_6Cl_6 (T_m = 491 K) is surely of enthalpic origin because the entropic change upon melting is expected to be very similar for both the compounds. This experiment incidentally can provide a comparison of Cl···Cl and Br···Br interactions in the two crystals of **2** and **3** and it may be concluded that the Br···Br interactions are stronger than the Cl···Cl interactions in these compounds. This conclusion is also apparent from their melting points (Table 1). This view is also compatible with their dispersive nature. Crystals of **3** deformed at a higher temperature did not show any elastic recovery ("spring back" to the original shape) upon cooling down to room

temperature. It also appeared as hard as the original single crystals at room temperature. Experiments were also done on the isostructural mixed halogenated compound 1,3,5-tribromo-2,4,6-trichlorobenzene (**135B246C**) which is an intermediate type (Br/Cl) to compounds **2** and **3**. This sample also did not bend at room temperature, but bends at the higher temperature of 403 K (T_m = 546 K).

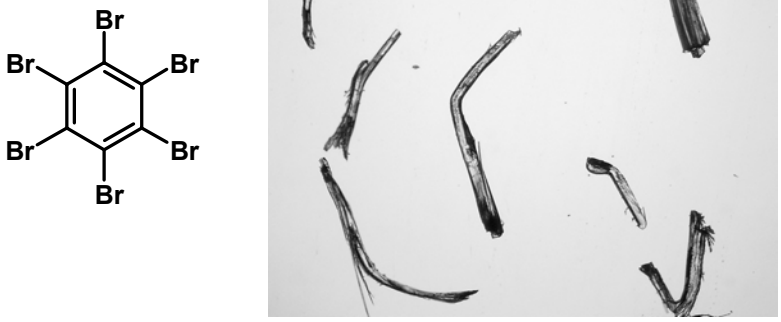

Figure 10. Hexabromobenzene, **3**. Crystals bent into different shapes at 403 K. Photograph was taken after cooling the crystals down to room temperature.

1,3,5-Trichlorobenzene, 4 and 1,3,5-Tribromobenzene, 5

Isomorphous compounds, **4** and **5** pack in the orthorhombic space group $P2_12_12_1$ [3.12]. The packing of these compounds is dominated by $\pi\cdots\pi$ stacking interactions in the [001] direction. Rows of the stacks are connected *via* weak C–H···X interactions in the other two directions. In compound **4**, the C–H···Cl interactions are 2.960, 149.8; 2.965, 156.3 and 2.984 Å, 154.8° but there are no significant Cl···Cl interactions present in the structure (Figure 11). In compound **5**, C–H···Br (*d*/Å, *θ*/°; 3.01, 151.6; 3.08, 156.2 and 3.09, 158.2) and weak C–Br···Br (*d*/Å, *θ*/°; 3.762, 117.9, 155.5; 3.765, 111.6, 151.8) interactions are present. Although the C–Br···Br interactions are present in **5**, it bends as easily as **4**, because the Br···Br interactions in this structure are non-directional and of the van der Waals type. They do not extend into the third dimension. But the Br···Br interactions in C_6Br_6 do extend in all the three dimensions and hence bending occurs at a higher temperature.

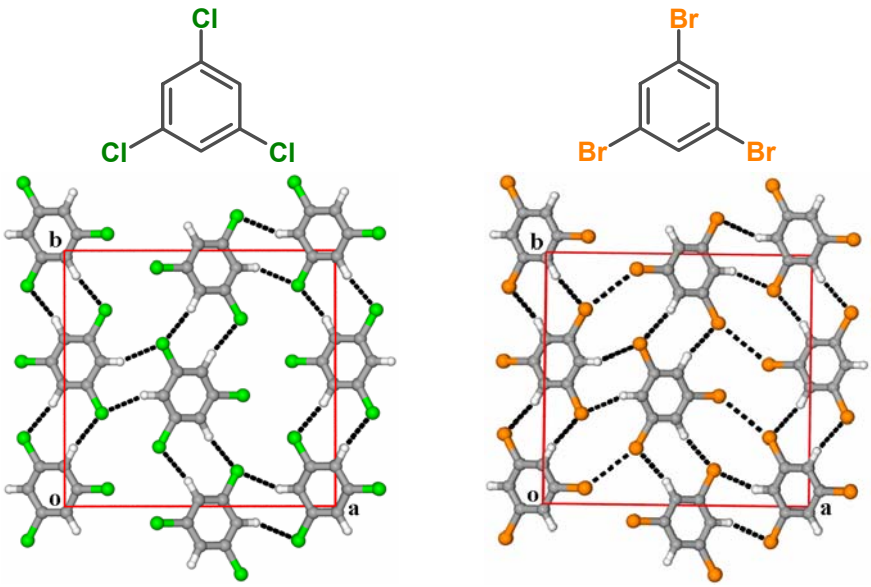

(a) **(b)**

Figure 11. Crystal packing in (a) 1,3,5-trichlorobenzene, **4**, shows the C–H···Cl interactions, and (b) 3,5-tribromobenzene, **5**, shows C–H··Br and C–Br···Br interactions, between the stacks.

3.3.3 Polymorphic Compounds

One of the main goals in crystal engineering is to understand the relationships between the crystal structure and the solid-state properties of materials at the molecular level. Polymorphism in molecular crystals—the ability of some molecules to crystallize into different structural forms—provides an excellent opportunity to study such relationships by preserving the same composition [3.5]. The polymorphic compounds in this study prove how the physical properties of a material can be influenced by its crystalline structure.

Pyrazine-2-carboxamide, 6

Pyrazine-2-carbaxamide, **6** is known to exist in five polymorphic forms [3.13]. Forms *α* (**6*α***) and *δ* (**6*δ***) could be crystallised in our laboratory. Bending experiments on form **6*α*** revealed some interesting facts related to the bending phenomena. A consequence of the bending model is that the angles between some of the faces would change markedly. This effect is observed very prominently in the bent crystal of **6*α***

(Figures 12a, 12b) which is also distinctive in that the thin face of the crystal, (100), is the bending face (Figures 12d to 12f). In the crystal of **6*α*** (Figure 12c) amide dimers are stacked along the short axis [001] (3.75 Å) and there are non-specific N–H···O (*d*/Å, *θ*/°; 2.32, 134.9) and C–H···O (2.24, 168.6) interactions between the phenyl rings along the other directions. Once again, one set of interactions (stacking) is significantly stronger than another (Ph···Ph) in a perpendicular direction. The bending face of these crystals is (100) which is the thickest crystal face. In the bending process, cracking always starts in the region of maximum tensile stress as marked with an arrow in Figure 12. This example shows that it is not that the largest area faces of a crystal are the bending faces (as in **1**). The bending face depends on the crystal structure. When bending was attempted on a crystal of **6*α*** along the prominent face say, (2 $\bar{1}$ 0), it cracked rather than bend. This clearly shows that the bending is a consequence of the crystal packing and does not depend on morphology.

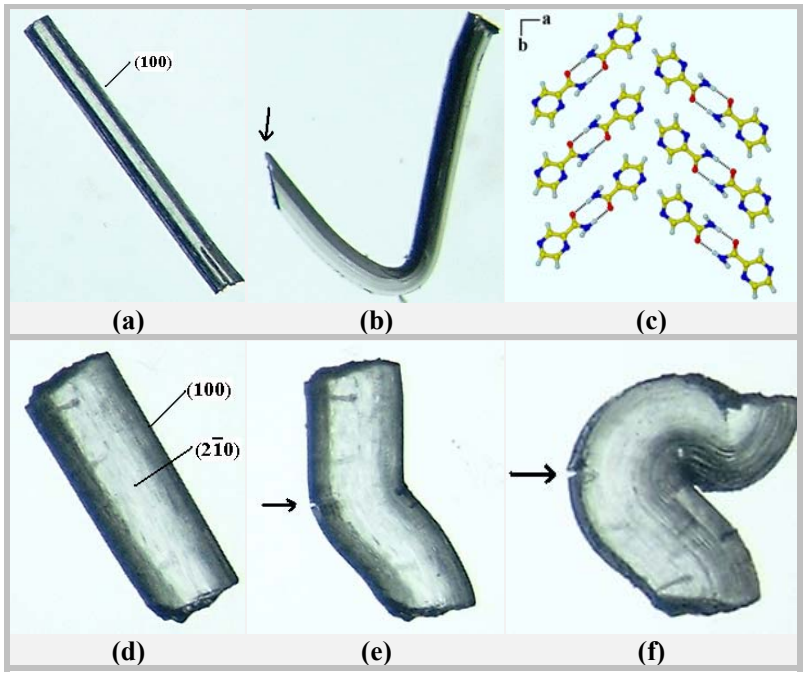

Figure 12. Pyrazine-2-carboxamide, **6*α***. (a) Before bending. (b) After bending. The arrow shows the acute interfacial angle. (c) Crystal packing. (d), (e) and (f) show the stages of bending on (100) plane on another crystal. Arrows in (e) and (f) indicate points of breakage.

Crystals of the other form, **6*δ***, could not be bent under similar conditions because the crystal packing does not fall into the bending model. In this structure, molecules are arranged in 2D planar sheets with weak C–H···N (2.50 to 2.70 Å) intralayer interactions (Figure 13) and stacking interactions between the layers. The crystal does not show either shearing or bending on application of a mechanical stress. This indicates that there is directionality in the interlayer interactions.

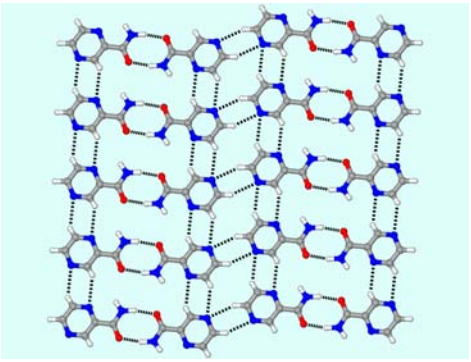

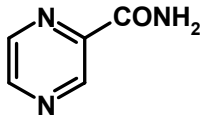

Figure 13. Pyrazine-2-carboxamide, **6*δ***. Planar layer in (012) shows the dimers in layer connected with weak C–H···N interactions.

6-Chloro-2,4-dinitroaniline, 7

6-Chloro-2,4-dinitroaniline, **7**, is a trimorphic compound which crystallizes concomitantly from CH_2Cl_2 solvent at ambient temperature [2.5]. Crystals of all the three forms are yellow in colour. Form I (blocks) is a layered structure which undergoes shearing on application of a mechanical stress. This was discussed in detail in Chapter 2. Crystals of Form II are very thin needles. These crystals undergo bending on application of a mechanical stress. In the crystal structure, molecules are arranged as corrugated tapes along [100] *via* strong N–H···O (*d*/Å, *θ*/°; 2.21, 141.6; 2.33, 139.7) interactions and the tapes are stacked along the *b*-axis (Figure 14). These tapes are connected by C–H···O (*d*/Å, *θ*/°; 2.51, 155.3) and C–Cl···Cl (*d*/Å, *θ*/°; 3.39, 153.7) interactions which are responsible for the bending. In fact, it was very difficult to get a single crystal from any batch of the crystallization for X-ray diffraction studies. Although the face indexing for this form was not successful, based on the bending model, it is predicted that the bending face would be (001) for these crystals (Figure 14).

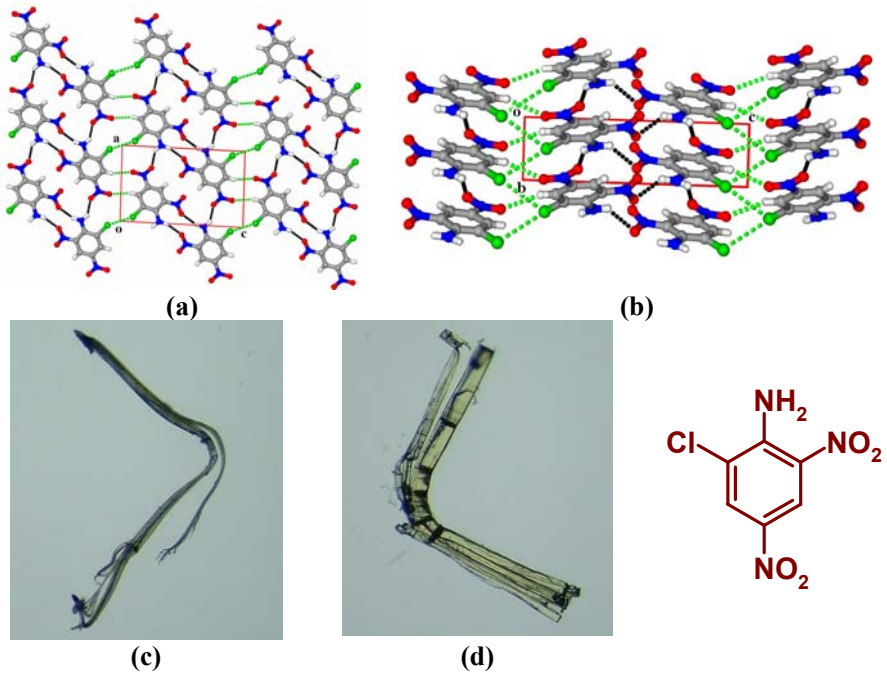

Figure 14. 6-Chloro-2,4-dinitroaniline, **7**, Form II. Crystal packing shows the tapes connected *via* strong N–H···O (black), weak C–Cl···Cl and C–H···O interactions (green) between tapes in (a) view down *b*-axis and (b) view down *a*-axis. (c) And (d) shows the two different bent crystals.

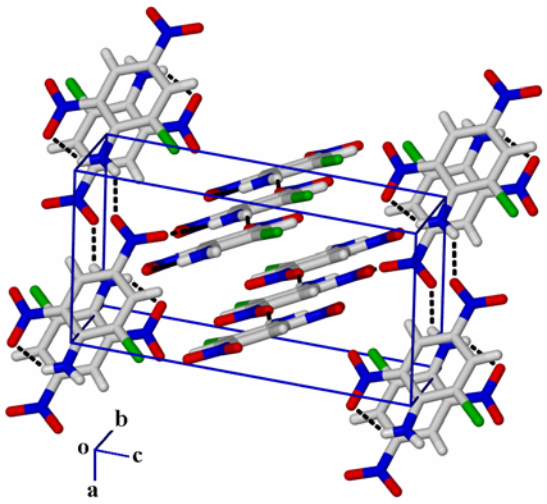

Figure 15. Crystal structure of Form III to show the perpendicular tapes.

Form III (blocks) crystallizes in the triclinic $P\bar{1}$ space group. There are two symmetry independent molecules in the asymmetric unit and each of them extends as an independent tape through the translation related molecules *via* strong N–H···O (*d*/Å, *θ*/°; 2.214, 141.08; 2.213, 143.38) interactions. These tapes run perpendicularly as shown in Figure 15. The tapes are interconnected *via* N–H···O (*d*/Å, *θ*/°; 2.43, 144.0) interactions in the third direction. The stronger N–H···O interactions in all the three directions prevents the bending and the crystals simply break into pieces on application of a mechanical stress.

In the packing of the three forms of **7**, the strong hydrogen bonding group NH is always involved in N–H···O hydrogen bonding. But the extension of these interactions in the crystal packing is completely different for the three forms, and hence, they show different mechanical properties. The mechanical behaviour of the three forms of molecular crystals **7** resembles the well known example of carbon allotropes, fullerene, graphite and diamond, where also the structure property correlation is noticed.

Venlafaxine hydrochloride, 8

Venlafaxine hydrochloride, **8**, exists in two crystalline polymorphic modifications (Forms 1 and 2) [3.14]. Form 2 crystallizes in the monoclinic $P2_1/n$ space group and has a one-dimensional packing (1D-tapes) with N^+–H···Cl^- (*d*/Å, *θ*/°; 2.128, 169.15) and O–H···Cl^- (*d*/Å, *θ*/°; 2.332, 164.16) ionic interactions in the [100] direction i.e. along the crystal length. Only van der Waals interactions are present elsewhere (Figure 16) [3.14]. These crystals bend on the expected (010) face. This example is not a 4 Å structure and shows that aromatic ring stacking is not mandatory for crystal bending. Here, the 1D-tapes are formed *via* strong interactions along the crystal length, and this does the job of the stronger $\pi\cdots\pi$ stacking interactions seen in the 4 Å structures. In this structure, there are no short contacts present between the 1D-tapes within the van der Waals radii.

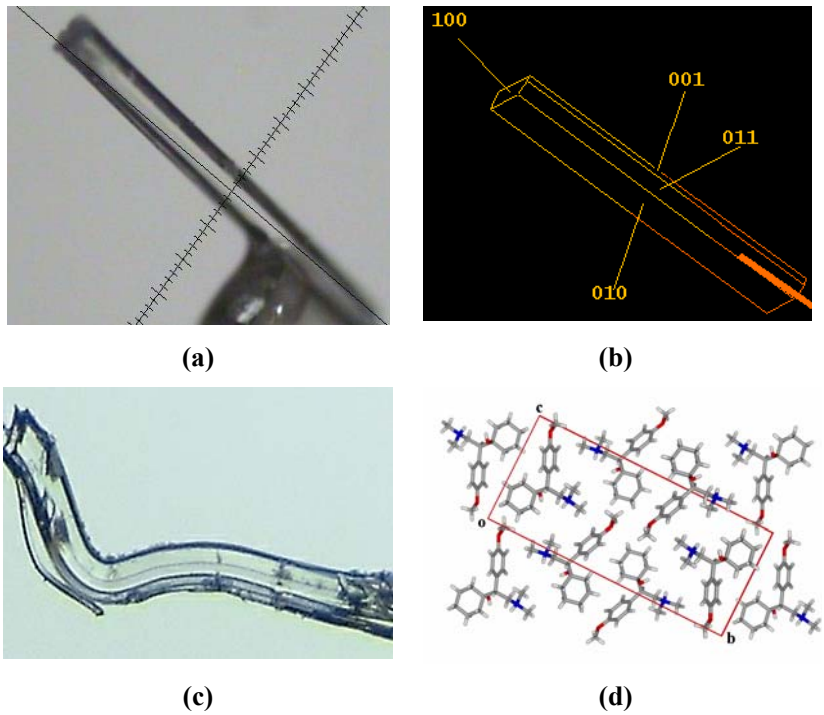

Figure 16. Venlafaxine hydrochloride, **8**, Form 2. (a) Crystal as mounted for face indexing. (b) SMART face indexing graphic. (c) Crystal bent on (010) face. (d) Packing diagram.

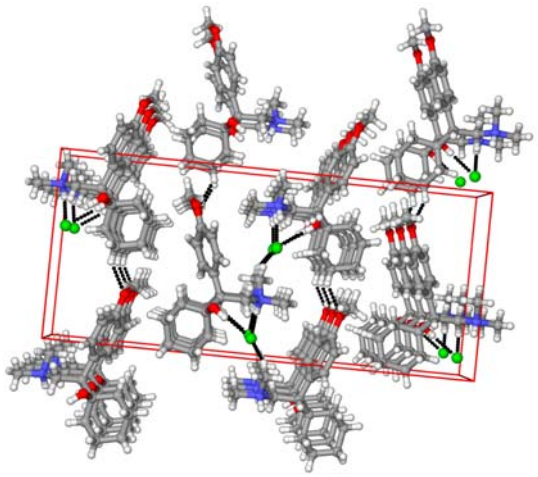

Figure 17. Perspective view along *b*-axis shows the O–H···Cl⁻, N–H···Cl⁻, C–H···O and C–H···Cl⁻ interactions in Forms 1.

Form 1 (orthorhombic, $Pca2_1$) is the harder (brittle) form and has a similar 1D-tape packing in the crystal structure with the same kind of N^+–H···Cl^- (d/Å, θ/°; 2.142, 173.09) and O–H···Cl (d/Å, θ/°; 2.330, 179.93) interactions along [010] (Figure 17) as the softer Form 2. But the arrangement of the adjacent tapes is slightly different. The tapes are connected *via* weak C–H···O (d/Å, θ/°; 2.614, 142.9) and C–H···Cl (2.945, 150.9) interactions along [001]. These crystals break on application of a mechanical stress instead of bending, i.e. these crystals are less plastic than Form 2. From the view point of structure-property correlation, this is an interesting observation. Normally, in metals, ductility increases with an increase in the crystal symmetry. This is because the nature of the metallic bonds remains the same in all the structural forms of a particular metal while the number of available slip-systems (shear planes) increases. In contrast, in molecular crystal **8**, the higher symmetry Form 1 (orthorhombic) is less ductile than the lower symmetry Form 2 (monoclinic). This is because the weak C–H···O interactions in the Form 1 increases specificity in the crystal packing. As a result, the shear strength of the crystal nearly equals the fracture strength, i.e. the crystal breaks instead of bending.

Drug molecule **8** is a currently important block buster in the pharmaceutical industry and is used as an antidepressant. The mechanical experiments on both the forms suggest that the softer form (Form 2) would create more problems than the harder form (Form 1) because it has a lower hardness, strain rate sensitivity (which affects the high speed tableting process), low flowability and poor granularity in the formulation. Recent experiments of Roy *et al.* [3.14a] on drug **8** revealed that the crystal lattice energy of Form 2 is lower than that of Form 1 by 2.0 kcal mol^{-1}. However, Form 1 is stable in ball-mill grinding, whereas Form 2 partially transforms to the hydrate phase, suggesting that Form 1 is perhaps more suitable for pharmaceutical formulations. All these observations underline the importance of mechanical properties and their understanding in the pharmaceutical industry.

4-Nitrobenzoic acid, 9

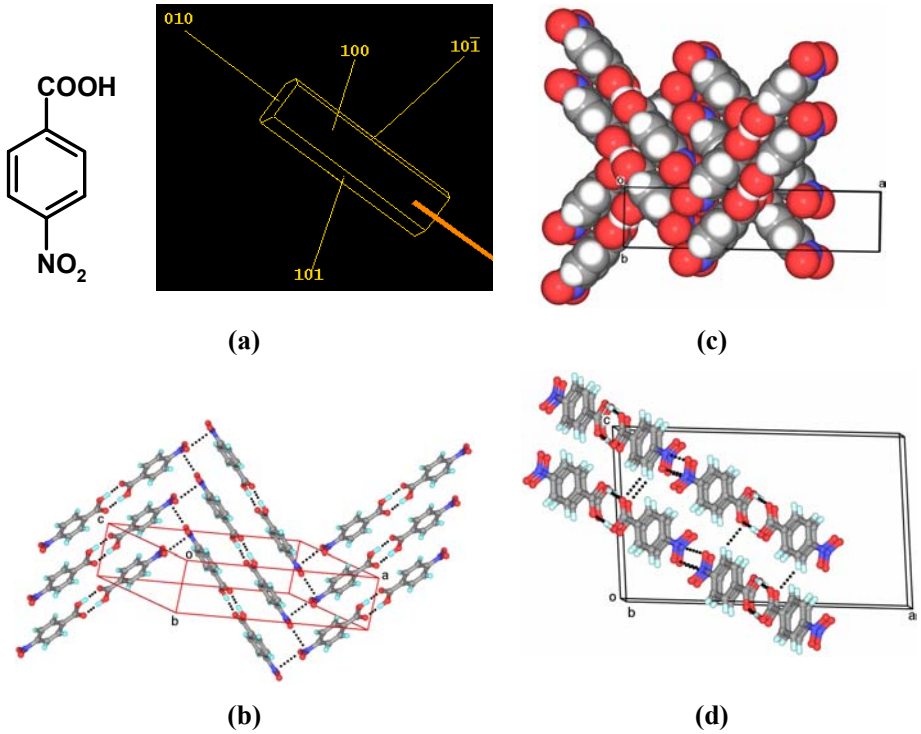

Figure 18. 4-Nitrobenzoic acid, **9**. (a) SMART face indexing graphic. (b) Stacking of the dimers along [010] in a zigzag fashion. (c) Space filling model shows the antiparallel arrangement of the adjacent dimer stacks (view down [001]). (d) The adjacent antiparallel dimers are connected *via* weak C–H···O interactions which are not visible in (c).

4-Nitrobenzoic acid, **9**, is a dimorphic compound [3.15]. The monoclinic *C*2/*c* (*Z*′ = 1) form which is reported in the literature was crystallized and the structure redetermined. The molecules aggregate *via* the carboxylic acid dimer synthons which are stacked along [010] in a zigzag fashion (Figure 18). Nitro groups of these dimers are arranged in a herringbone fashion to stabilize *via* $O^{(\delta-)}\cdots N^{(\delta+)}$ interactions along [101] direction as seen in Figure 18b. In the [101] direction, there are only weak C–H···O interactions (*d*/Å, *θ*/°; 2.659, 133.7; 2.619, 162.8) between the adjacent dimers which are arranged in an antiparallel fashion (Figure 18c). The bending face for these crystals is determined as (101) and this is the thickest face along which the weak C–H···O

interactions emerge. The prominent face is (100) which is the thinnest face but bending on theses faces leads to breakage of the crystal. This example shows that the thinnest face is not always the bending face and is reminiscent of Form *α* of pyrazine-2-carboxamide (**6α**).

4-Chlorobenzonitrile, 10

4-Chlorobenzonitrile, **10**, is a dimorphic compound [3.16] and the noncentrosymmetric monoclinic (*Pc*) form was recrystallized. In this structure, molecules are stacked along [100]. The molecules from the adjacent stacks are connected *via* weak C–Cl···N (3.37, 168.3) and C–H···N (2.71, 151.1) interactions to form a corrugated sheet in the (102) plane (Figure 19). There are only weak van der Waals interactions between the corrugated sheets and hence the crystals of **10** bends on application of a mechanical stress. In their original report on this structure, Desiraju and Harlow [3.16] noted that some of these crystals had a curved morphology. However, the basis for such curvature was not understood till now.

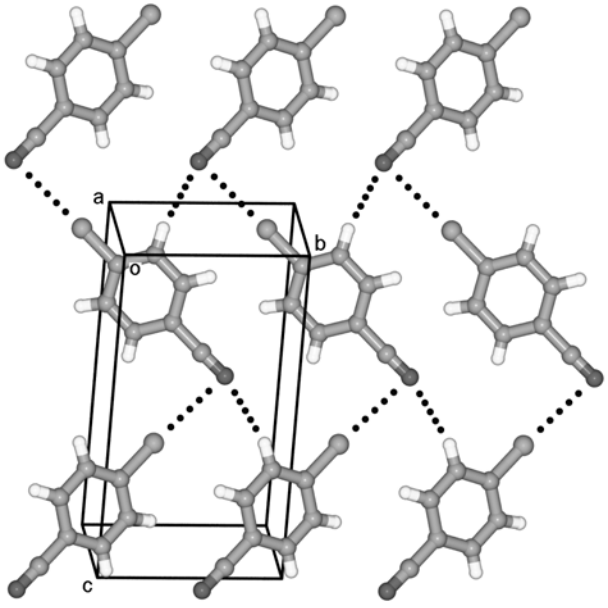

Figure 19. Packing diagram shows the layer formed *via* C–Cl···N and C–H···N interactions. View down *a*-axis.

3.3.4 Tetragonal crystal, 3,4-dichlorophenol, 11

In the process of confirming the bending model, crystallographically different examples were considered for detailed experiments. 3,4-Dichlorophenol, **11**, is a tetragonal crystal with a 4 Å short axis along the unique direction. Molecules are stacked along the short axis [001] i.e. crystal length. In the same direction strong O–H···O interactions are extended as a helical chain (Figure 20c) [3.17]. The much weaker Cl···Cl directions are equivalent along the two other perpendicular directions because of crystal symmetry. Therefore, **11** bends with equal ease on its both equivalent faces (010) and (100) into a variety of shapes (Figure 20a). For such high symmetry crystals, more than one pairs of faces are the bending faces. In fact, it was very difficult to find an undeformed crystal for X-ray diffraction studies from the commercially available sample (Figure 20d); the crystals in the bottle appeared as if they were thin earthworms.

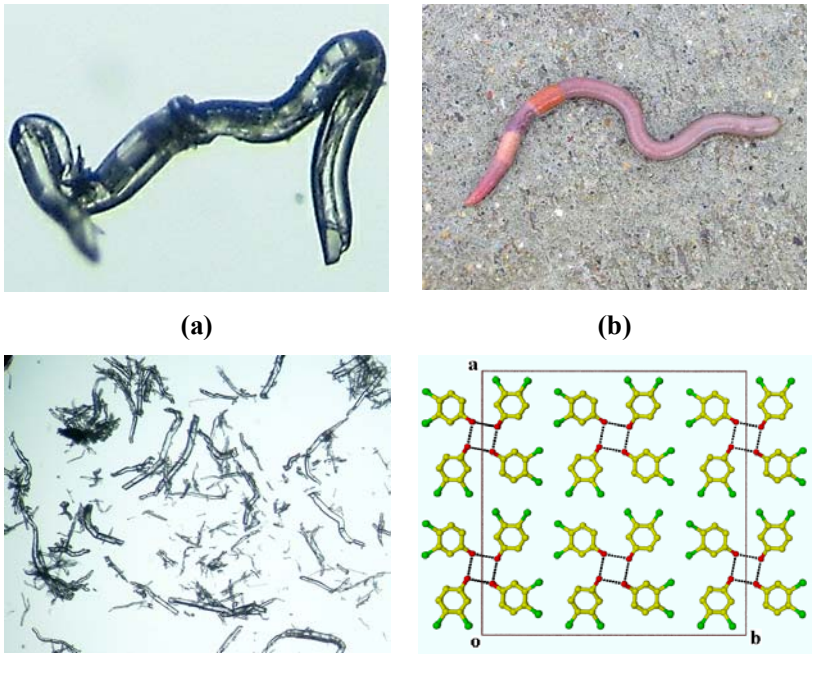

Figure 20. 3,4-Dichlorophenol, **11**. (a) Crystal bent in all directions. (b) Earthworm. (c) Packing diagram. (d) Bent crystals from the commercial sample to show the mechanical sensitivity of the crystals.

3.3.5 Molecular Complex

Benzamide:Pentafluorobenzamide (1:1), 12

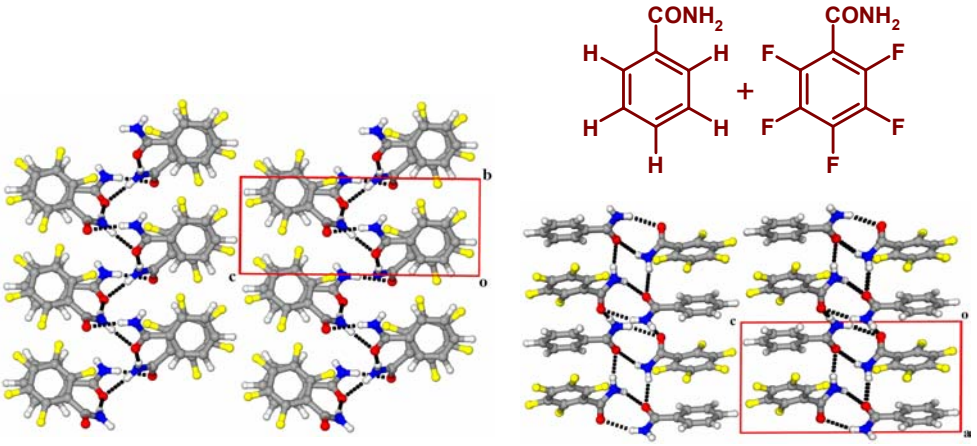

(a) **(b)**

Figure 21. Benzamide:pentafluorobenzamide (1:1), **12.** Crystal packing shows the rows of stacks connected as catemers *via* strong N–H···O interactions and the weak C–H···F interaction region between the catemers in (a) and (b).

The molecular complex **12** which was recently reported by Reddy *et al.* [3.18] crystallizes in the polar space group $P2_1$ ($Z' = 1$) with one molecule of each residue in the asymmetric unit. In this molecular complex, amide groups of both benzamide (**BAm**) and pentafluorobenzamide (**PFBAm**) molecules are twisted with respect to their aromatic rings. The **BAm** and **PFBAm** molecules are stacked along the [100] direction to stabilize *via* phenyl–perfluorophenyl interactions (Figure 21). Two adjacent stacks are connected *via* N–H···O helical chains along [110] and [$1\,\bar{1}\,0$] directions. These helical chains are formed by the twisted amide groups from each of a **BAm** and **PFBAm** molecule from the adjacent stacks. There are only weak C–H···F interactions present between the helical chains (Figure 21). Because these are the weakest interactions present in [001], the bending face for these crystals is the (001) face.

3.3.6 Miscellaneous Structures

1,3,5-Trifluoro-2,4,6-triiodobenzene, 13

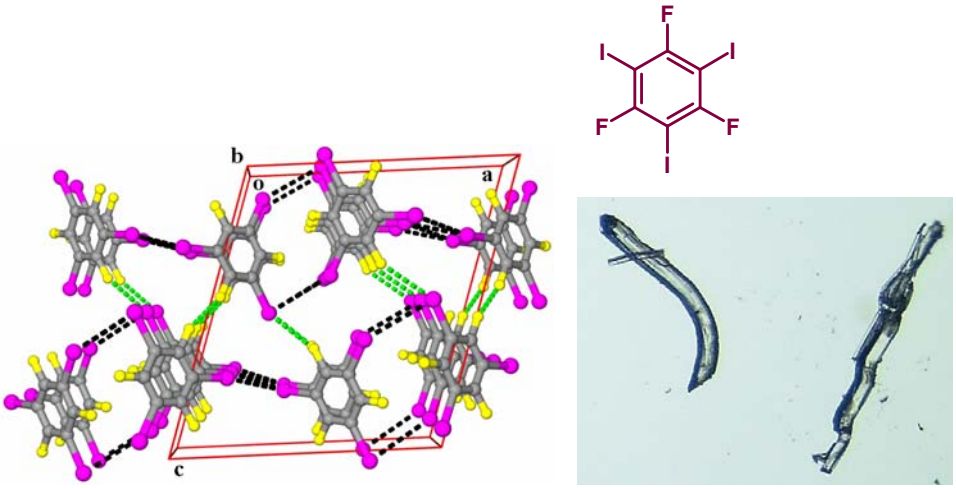

(a) **(b)**

Figure 22. 1,3,5-Trifluoro-2,4,6-triiodobenzene, **13**. (a) Tapes formed *via* I···I interactions (black) are stronger than F···F and F···I interactions (green) between tapes. (b) Bent crystals.

1,3,5-Trifluoro-2,4,6-triiodobenzene, **13**, crystallizes in the monoclinic space group $P2_1/n$ [2.15]. In the crystal, molecules are stacked along the *b*-axis and these stacks are extended as tapes through I···I (*d*/Å, *θ*/°; 3.774, 100.7, 171.1; 3.957, 80.0, 146.8) interactions along the [100] direction. Between these tapes there are weak contacts, F···F (*d*/Å, *θ*/°; 2.853, 157.4, 157.4) and F···I (*d*/Å, *θ*/°; 3.58, 126.0, 145.5) as seen in Figure 22a. The weak and (comparatively) strong interactions are arranged perpendicularly. Thus bending is possible on application of mechanical stress (Figure 22b).

4-Fluorobenzonitrile, 14

4-Fluorobenzonitrile, **14**, crystallizes in the triclinic space group $P\bar{1}$ with a short crystallographic axis of 3.87 Å [3.19]. In this structure, molecules are slightly tilted and thus form corrugated layers parallel to (101) plane (Figure 23). In fact, the layer arrangement in this structure is in between the planar and corrugated layer structure

types. Molecules within the layers are connected *via* weak C–H···N (*d*/Å, *θ*/°; 2.623, 156.8; 2.699, 153.5) and C–H···F (*d*/Å, *θ*/°; 2.66, 153.0) interactions. There are only weak van der Waals interactions between the corrugated layers. Crystals of this compound bend on the (010) face through which C–H···F interactions emerge (Figure 23a). The interactions within the corrugated layers are weak. These crystals also show bending, but the shape of the resulting bent portion is different from the crystals discussed earlier. In this case, the bent portion of the crystal is angular (Figure 23c, marked with arrows) instead of being a smoothed curvature. This could be because of the intermediate type arrangement of the layers, i.e. between planar and corrugated layer structure types.

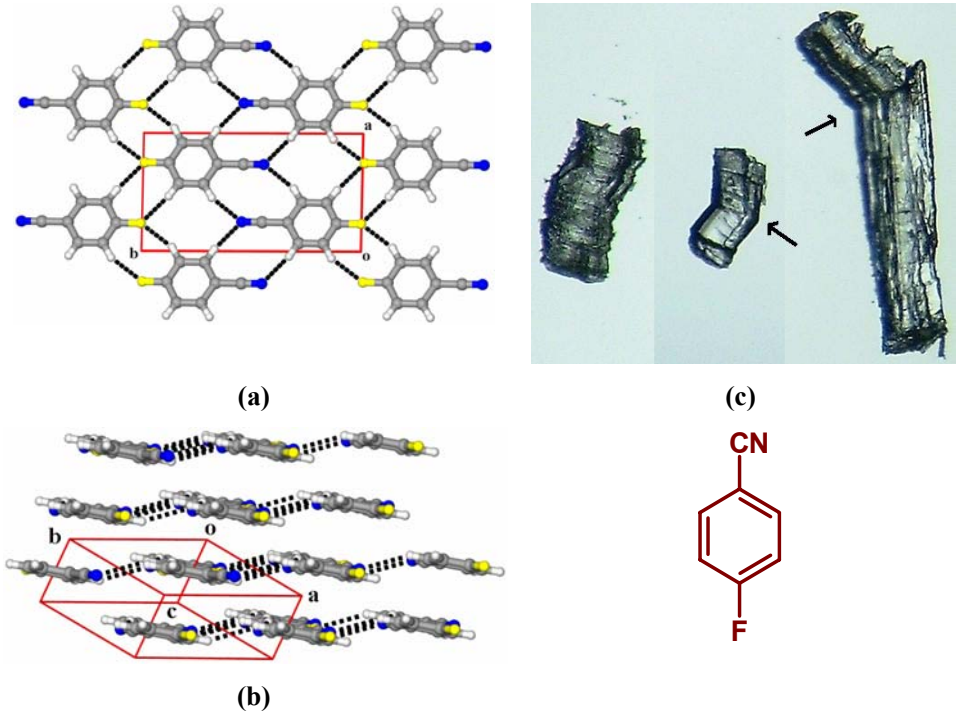

Figure 23. 4-Fluorobenzonitrile, **14**. (a) Packing diagram of a single layer view down *c*. (b) Shows the corrugation of layers. (c) A photograph of bent crystals. The arrows show the bent portion with a corner shape.

2-Nitrobenzaldehyde, 15

2-Nitrobenzaldehyde, **15** crystallizes in the monoclinic polar space group $P2_1$ [3.20]. In its crystal structure, molecules are stacked down the *b*-axis. Weak C–H···O (*d*/Å, *θ*/°; 2.37, 143.3; 2.55, 156.9; 2.56, 160.4; 2.68, 122.8) interactions are present in the two other directions (Figure 24). These crystals also bend on application of a mechanical stress.

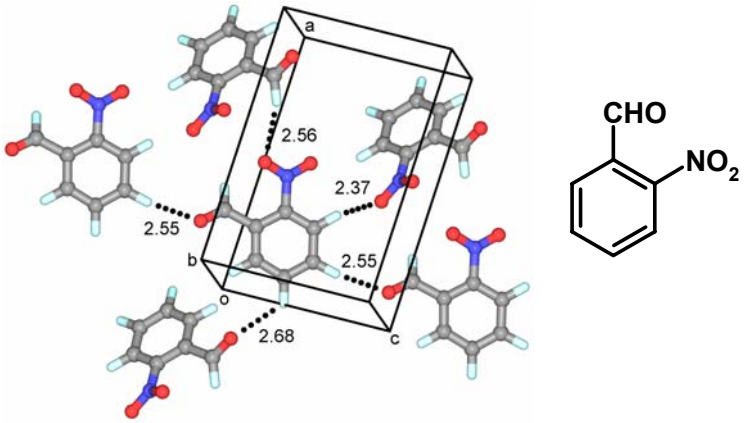

Figure 24. Packing diagram shows the weak C–H···O interactions (view down *b*-axis) in 2-nitrobenzaldehyde.

1,3-Dinitrobenzene, 16

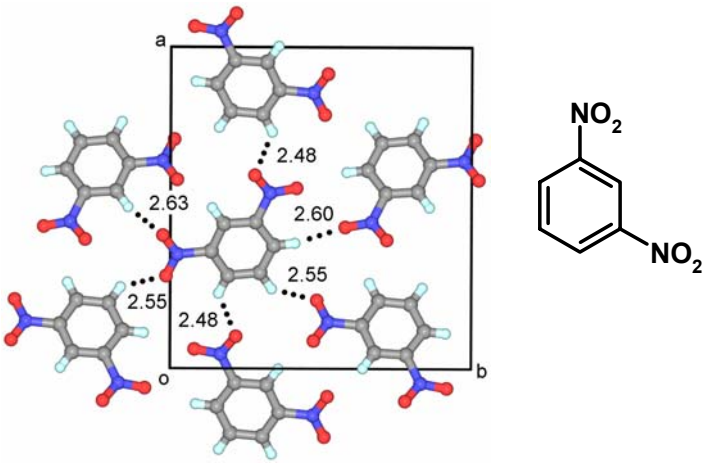

Figure 25. Packing diagram shows the weak C–H···O interactions (view down *c*-axis).

1,3-Dinitrobenzene, **16**, crystallizes in the orthorhombic space group $Pna2_1$ with a short crystallographic axis of 3.68 Å (*c*-axis) along which translation related molecules are stacked in a zigzag fashion [3.21]. In the other two directions, molecules are connected *via* weak C–H···O (*d*/Å, *θ*/°; 2.48, 132.7; 2.55, 141.2; 2.60, 153.5; 2.63, 132.7) interactions (Figure 25). These crystals also bend on application of a mechanical stress, but the bending faces could not be determined experimentally. From the crystal packing, it may be predicted that the bending face is (010).

3,4,5-Trimethoxybenzaldehyde, 17

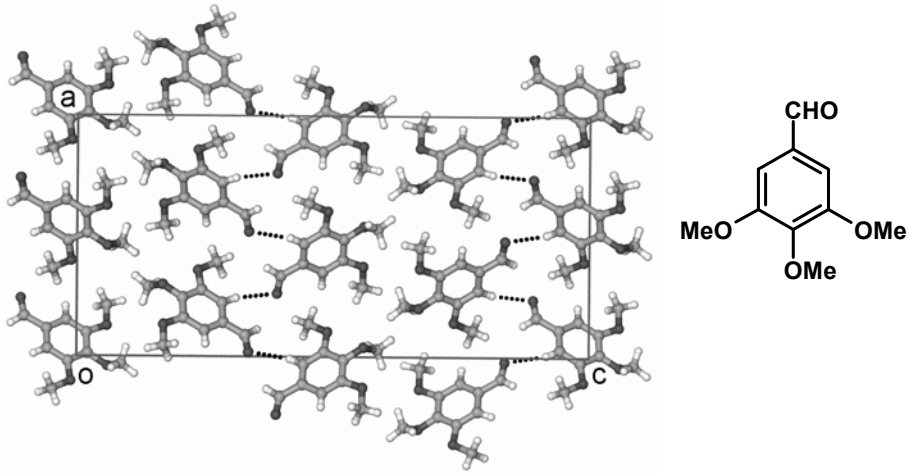

Figure 26. Packing diagram shows both the weak C–H···O and Me···Me contacts emerging from the (001) face.

3,4,5-Trimethoxybenzaldehyde, **17**, crystallizes in the orthorhombic space group $Pca2_1$ and has a short crystallographic axis of 4.66 Å [3.22]. There are two molecules in the asymmetric unit. Molecules are stacked along [010]. Except weak C–H···O (*d*/Å, *θ*/°; 2.50, 160.0; 2.55, 166.4) interactions, there are no significant short contacts present in this structure as seen in Figure 26. Although the faces of these crystals were not determined due to a limitation on the time available on the diffractometer, it can be suggested that the bending face for these crystals would be (001), because the weakest van der Waals type Me···Me contacts emerge from this plane.

3.3.7 3D Interlocked crystals (Brittle Crystals)

Most of the molecular crystals (43 out of 60) in the survey did not bend in any direction on application of a mechanical stress. Analysis of these crystal structures reveal that they have some kind of interlocking like strong hydrogen bonding, zigzag or herringbone packing of molecules in all the three dimensions. Crystal packing of some typical structures is now discussed. For all these crystals, the molecular diagram, CSD refcode and hydrogen bonding details are presented in Table 2.

Table 2. List of the hard (brittle) crystals (**18-60**) found in the survey.

No.	Molecular Structure	CSD Refcode	Hydrogen Bonding/ Packing Pattern
18	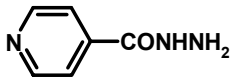	INICAC01	N–H···N 3D interlocked
19	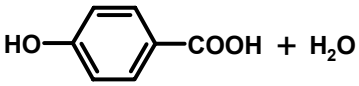	PHBZAC02	O–H···O 3D interlocked
20	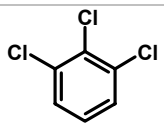	TCBENZ TCBENZ01	Cl···π anti-parallel packing of molecules.
21	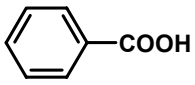	BENZAC01	O–H···O herringbone type arrangement of acid dimers
22	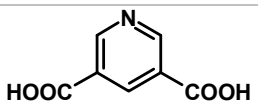	DINICA10	O–H···N and O–H···O 2D sheet
23	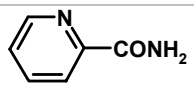	PICAMD	N–H···O zigzag 2D amide dimer tapes
24	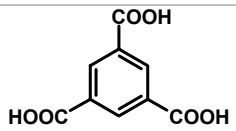	BTCOAC	O–H···O 3D interpenetrated

Table 2. *Continued…*

No.	Molecular Structure	CSD Refcode	Hydrogen Bonding/ Packing Pattern
25	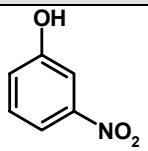	MNPHOL02 MNPHOL03	O–H···O tape
26	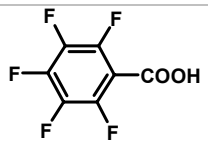	PFBZAC01	C–H···O and F···F layered
27	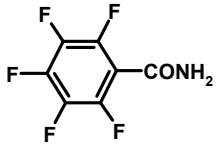	VATNOU	N–H···O tape
28	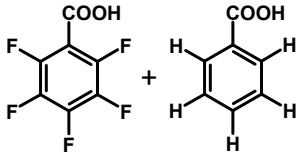	UKOKIO01	O–H···O and C–F···π
29	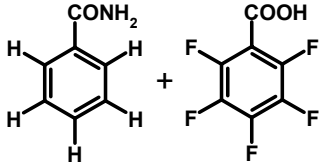	ESATUN	N–H···O 2D helical chain
30	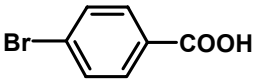	BRBZAP01	O–H···O corrugated sheet
31	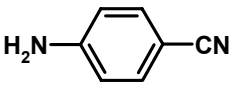	BERTOH01 BERTOH02	N–H···N and N–H···π zigzag tapes
32	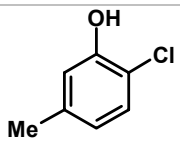	EKENUD	O–H···O parallel tapes

Table 2. *Continued…*

No.	Molecular Structure	CSD Refcode	Hydrogen Bonding/ Packing Pattern
33	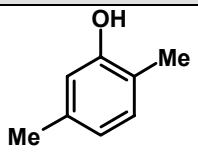	DMPHOL11	O–H···O parallel tapes
34	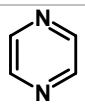	PYRAZI/ PYRAZI01	C–H···N 3D interlocked
35	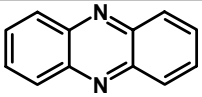	PHENAZ11 HENAZ01	C–H···N herringbone
36	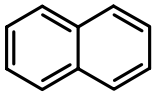	NAPHTA	C–H···π herringbone
37	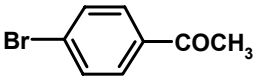	BRACPH01	Br···O parallel tapes
38	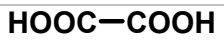	OXALAC	O–H···O catemer corrugated layers
39	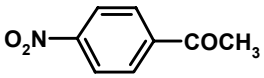	NACPON10	C–H···O layered
40	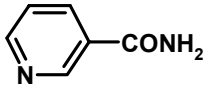	NICOAM01	N–H···O and N–H···N in 2D interlocked
41	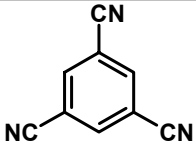	ZEXQAU	C–H···N helical chains/ 3D interlocked

Table 2. *Continued…*

No.	Molecular Structure	CSD Refcode	Hydrogen Bonding/ Packing Pattern
42	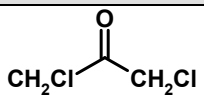	DCACON	C–H···O 2D sheet
43	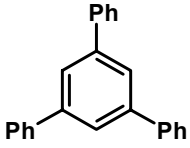	TPHBEN01	C–H···π 3D interlocked
44	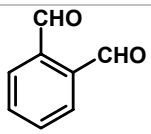	IHEMAJ	C–H···O
45	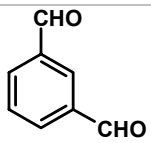	IHEMIR	C–H···O
46		JULJAR	C–H···O
47	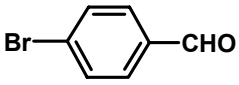	YICFEV	C–H···O and Br···Br
48	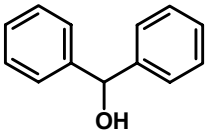	YUHHUE YUHHUE01	O–H···O Parallel tapes
49	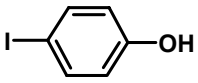	QQQBNJ	No 3D coordinates

Table 2. *Continued…*

Unreported Compounds			
No.	**Molecular Structure**	**No.**	**Molecular Structure**
50	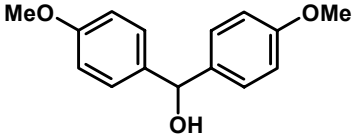	56	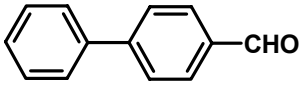
51	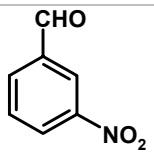	57	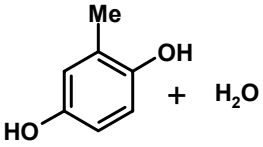
52	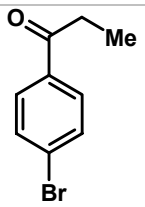	58	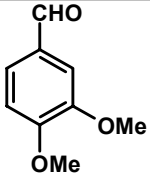
53	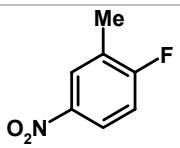	59	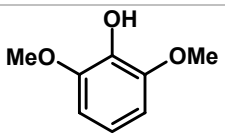
54	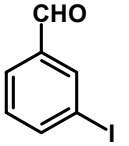	60	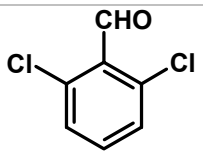
55	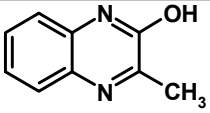		

Isonicotinic acid hydrazide, 18

Isonicotinic acid hydrazide, **18**, crystallizes in the orthorhombic space group $P2_12_12_1$ with a short axis of *ca*. 4 Å [3.23]. In this structure, molecules are stacked down along the [001] direction and form helical chains *via* N–H···N interactions in the same direction (Figure 27). Molecules from adjacent helical chains are connected with N–H···$N_{(pyridyl\ ring)}$ interactions in the two other directions to form a three-dimensional interlocked structure. These crystals were found to be hard and do not bend on

application of a mechanical stress in any direction because of N–H···N interactions in all three crystal directions.

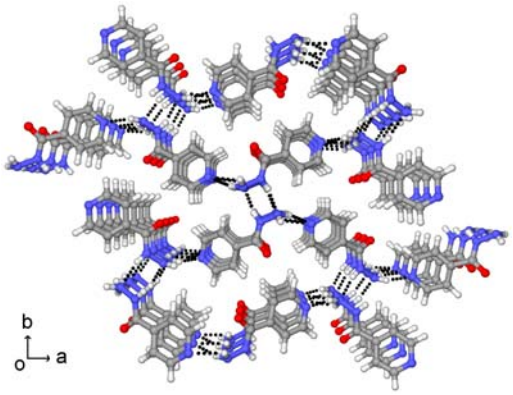

Figure 27. Isonicotinic acid hydrazide, **18**. Perspective view of packing along the *c*-axis shows the helical chains and connections between them *via* N–H···N interactions.

4-Hydroxybenzoic acid-monohydrate, 19

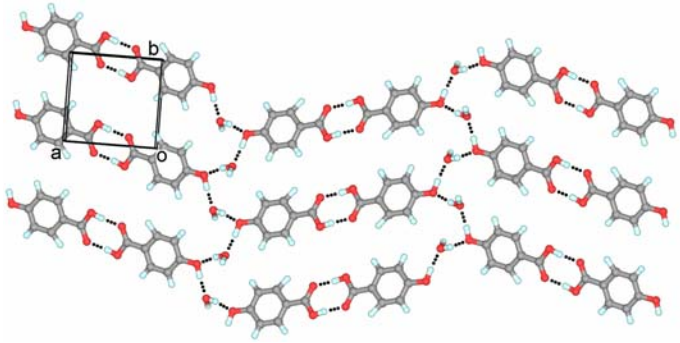

(a)

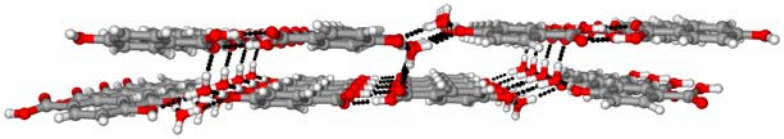

(b)

Figure 28. 4-Hydroxybenzoic acid-monohydrate, **19**. Packing shows (a) the interlayer O–H···O hydrogen bonding in the 2D-sheet; (b) the O–H···O hydrogen bonds between the layers, view down [010].

4-Hydroxybenzoic acid-monohydrate, **19**, crystallizes in the monoclinic space group $P2_1/n$ [3.24]. In this structure molecules form carboxylic acid dimer synthons *via* O–H···O (*d*/Å, *θ*/°; 1.76, 174.4) hydrogen bonds. The leftover phenolic OH groups of the adjacent dimer molecules are connected through the H_2O molecules *via* $O_{(ph)}$–H···$O_{(w)}$–H···$O_{(ph)}$ (*d*/Å, *θ*/°; 1.71, 172.8; 1.95, 170.1) interactions thus forming a sheet in the $(\bar{1}05)$ or $(10\bar{5})$ planes as shown in Figure 28a. The second OH group of the H_2O molecule forms an O–H···O (*d*/Å, *θ*/°; 1.95, 169.0) interaction with the carbonyl oxygen of the next layer, which interlocks the structure in the third dimension (Figure 28). As expected, these crystals do not undergo plastic bending deformation i.e. they broke on application of mechanical stress.

1,2,3-Trichlorobenzene, 20

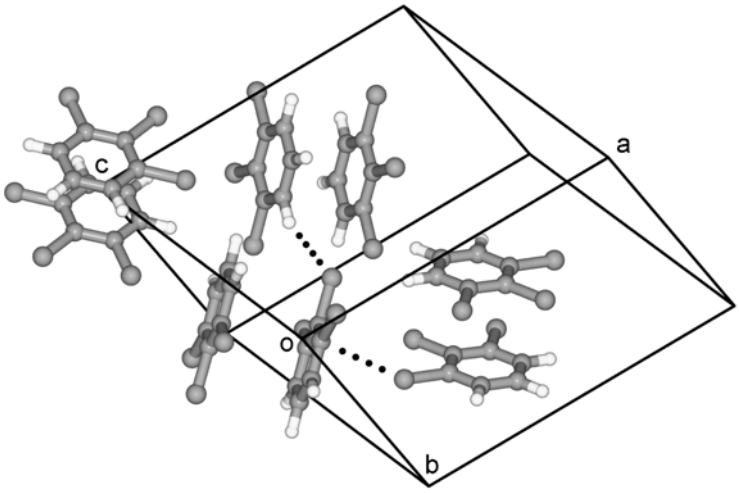

Figure 29. 1,2,3-Trichlorobenzene, **20**. Packing diagram shows the anti-parallel stacking of the dipoles of the molecules and Cl···π and C–H···Cl interactions. View down [101].

1,2,3-Trichlorobenzene, **20**, crystallizes in the monoclinic space group $P2_1/c$ with two molecules in the asymmetric unit [1.2, 3.25]. Molecule **20** has a significant permanent dipole moment. In its crystal structure, molecules show anti-parallel stacking of dipoles which results in a doubling of the short axis to *ca*. 8 Å. Adjacent anti-parallel dimers are packed perpendicularly with weak Cl···π and C–H···Cl interactions (Figure

29). These crystals are hard and do not bend on application of a mechanical stress because of the herringbone type of packing in the crystal structure. The same kind of packing with weak interactions is also seen in pyrazine, phenazine, anthracene and naphthalene, which also do not bend on application of a mechanical stress under similar conditions.

3.3.8 Anisotropy

Anisotropic behaviour of these crystals was examined by nanoindentation [3.26] and thermal expansion experiments which depend mainly on the internal packing of the crystals and intermolecular interactions in the three dimensions.

Nanoindentation

Nanoindentation experiments on the three different faces (100), (010) and (001) confirmed the anisotropic behaviour of crystal **1**. These tests revealed that the Young's modulus of crystal **1** (~15 GPa) was comparable to that of wood [3.27]. It could also be demonstrated that at room temperature, crystal **1** experienced steady state creep deformation (Figure 30-inset). In this experiment, the load was maintained constant; yet the depth of indenter penetration increased with the time of load application. This is constant load (~stress) indentation creep [3.5, 3.11]. Creep becomes significant in a material when the test temperature is greater than or equal to 0.5 T_m, where T_m is the melting point [3.5]. Here the test temperature was 298 K, while the T_m of **1** is 488 K. That the interactions in crystal **1** are quite anisotropic could also be demonstrated by the nanoindentation experiments in which the hardness of the crystal at different values of indenter penetration along the three crystal directions were determined. Figure 30 shows that the hardest face is the bending face (010). This is because application of a mechanical stress perpendicular to this face will cause the crystal to deform plastically.

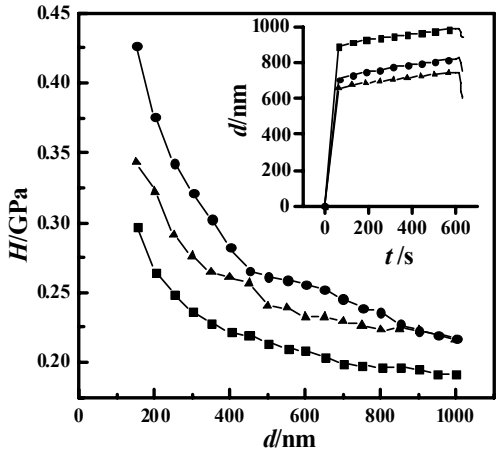

Figure 30. Nanoindentation experiments demonstrating anisotropy in acid **1**. Hardness (*H*) *vs* depth (*d*) of indenter penetration. Inset: Indenter penetration *vs* time of load application. ▲ (100), ● (010), ■ (001).

Variable Temperature Data

As mentioned in Chapter 2, the directional nature of thermal expansion can reveal some qualitative anisotropic features of the intermolecular forces in molecular crystals [2.22]. To examine the anisotropy of intermolecular interactions, the cell parameters of the bending compounds **1** and **2** were determined at six different temperatures between 100 K and 300 K (Figure 31).

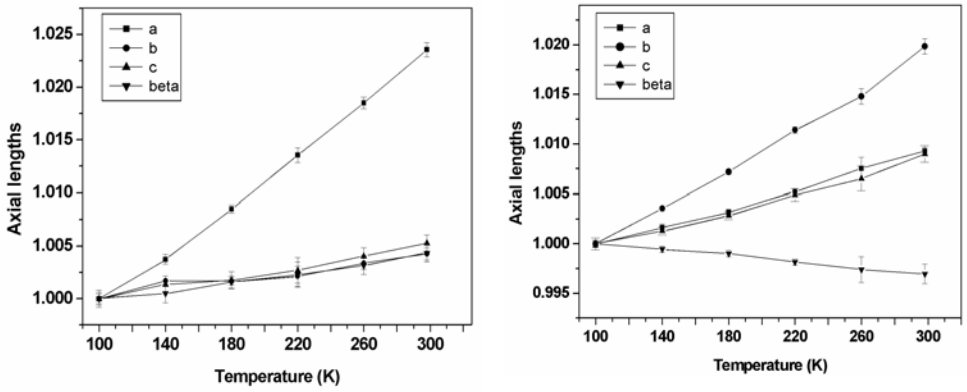

Figure 31. Variation of cell parameters with respect to temperature for compounds 2-(methylthio)nicotinic acid, **1** (left) and hexachlorobenzene, **2** (right). Notice that the short axis length increases sharply with temperature.

Table 3. Variable temperature cell parameters of **1** and **2**

2-(Methylthio)nicotinic acid, **1**

T/K	*a*	*b*	*c*	*α*	*β*	*γ*
100	3.8923(6)	25.276(5)	7.432(2)	90	101.01(2)	90
140	3.9068(6)	25.319(4)	7.442(2)	90	101.06(3)	90
180	3.9254(5)	25.318(3)	7.445(2)	90	101.17(2)	90
220	3.9450(9)	25.330(8)	7.452(3)	90	101.24(4)	90
260	3.9643(7)	25.361(5)	7.462(2)	90	101.33(3)	90
298	3.9840(9)	25.384(5)	7.471(2)	90	101.45(3)	90

Hexachlorobenzene, **2**

T/K	*a*	*b*	*c*	*α*	*β*	*γ*
100	7.972(1)	3.7613(4)	14.684(3)	90	92.44(1)	90
140	7.985(1)	3.7747(3)	14.703(2)	90	92.39(1)	90
180	7.9973(8)	3.7884(3)	14.726(2)	90	92.35(1)	90
220	8.0137(1)	3.8042(4)	14.756(3)	90	92.270(13)	90
260	8.032(3)	3.817(1)	14.780(6)	90	92.20(4)	90
298	8.046(1)	3.836 (1)	14.816(4)	90	92.16(3)	90

In compounds **1** and **2,** though the changes in the cell lengths are not very clear, there is an indication of anisotropy (Table 3). The ambiguity is due to purely geometrical reasons and a similar situation has been discussed in detail in Chapter 2.

3.4 Conclusions

Bending of organic crystals is a widespread phenomenon. Bending is possible when the packing is anisotropic in such a way that strong and weak interaction patterns occur in nearly perpendicular directions. Bending can be understood on the basis of a structural model that takes into account the highly anisotropic nature of these crystals. When a crystal bends, two parallel opposite faces become non-planar, i.e. curved. The bending phenomenon does not depend on the melting point of the crystal but the idea of homologous temperature is important. Bending depends completely upon the nature of

intermolecular interactions and crystal packing. An organic crystal which bends is not like plasticine, modelling clay or even a slab of metal. It cannot be mechanically deformed in any arbitrary manner. Interactions in such crystals are not uniform and similar in all directions. These crystals can be deformed into many shapes and in some cases they can even be flattened on to themselves without breakage, i.e. they are highly ductile. Crystals with comparable intermolecular interactions in all the three directions do not show bending and will be hard and brittle. Isotropic crystals, wherein the packing patterns are similar in the three dimensions, will often have highly cross-linked structures (naphthalene, benzoic acid, D-glucose). In the context of aromatic molecules, this is equivalent to herringbone packing. These crystals would break rather than bend when subjected to a mechanical stress. In contrast, metals which are isotropic but do not have cross-linking display excellent plasticity. Mechanical properties of molecular crystals are important because they have major implications for large scale processing and handling of materials in industry, especially the pharmaceutical industry. Soft crystals become pasty upon grinding. Harder crystals are granular and can be handled more easily. Plastic deformation of a solid may also affect its chemical properties [1.9].

In metallic crystals the length of the outer arc increases, while the length of the inner arc decreases. But the thickness decreases. Therefore, there will be no significant change in volume after plastic bending (apart from what is introduced during the initial elastic bending) [3.5a]. In contrast, molecular crystals practically show no change with respect to the volume, the lengths of the inner and the outer arcs and the sample thickness following plastic bending. This is why the shape of the plastically deformed molecular crystal appears to be different from that of metallic materials. This suggests that the plastic bending phenomenon in molecular crystals is somewhat different from that present in metals.

The bent molecular crystals easily lose their long range crystalline property while handling. Hence, they tend to create more problems to crystallographers in X-ray diffraction studies. The deformation processes seen in these molecular crystals may be used to deduce the mechanism for the transformation of crystalline materials into the amorphous state upon grinding, which is a very common problem encountered in the

pharmaceutical industry. A further assessment of these undoubtedly common but little understood properties is clearly desirable.

3.5 Experimental

Materials: Except **10** and **11**, all the compounds were available commercially. Molecular complex **10** was obtained by co-crystallization of a 1:1 mixture of benzamide and pentafluorobenzamide from EtOAc/hexane (1:1) solvent mixture at ambient temperature. Compound **11** was synthesized by iodination of 1,3,5-trifluorobenzene using the procedure mentioned in Chapter 2 and was then crystallized from THF solvent by slow evaporation. All the reagents and solvents employed were commercially available (Lancaster) and were used as supplied without further purification. Melting points were measured in a Fisher-Jones melting point instrument.

Crystallization: All the compounds were crystallized from either CCl_4, THF, EtOAc, hexane, 1,4-dioxane or solvent mixtures by slow evaporation at ambient temperature. For the mechanical bending experiments, the range of crystals thickness was between 0.2 to 0.6 mm^2 while the length was between 1 to 5 mm.

X-ray crystallography: Face indexing was done on a Bruker Nonius Smart Apex CCD with graphite monochromated Mo-Kα radiation.

Nanoindentaion: Nanoindentation experiments were performed by using a nanoindenter model XP, supplied by MTS Systems Corporation, USA. The diamond indenter had a Berkovich (three-sided) pyramidal geometry. The bending experiments were carried out at 293 K using the load control mode. The maximum allowed drift (thermally induced vibrations of the indenter tip) was set to 0.1 nms^{-1} and the indenter velocity was 10 nms^{-1}.

CHAPTER 4

NANOINDENTATION STUDY AND "NEAR-EXHAUSTION CREEP" BEHAVIOUR OF SOME MOLECULAR CRYSTALS

4.1 Introduction

Studying the mechanical response of materials at the nanoscale level has received considerable attention in recent years [4.1]. These studies have been motivated by the development of new nanostructured materials and the recent advances in nanotechnology [4.1]. Measurement of nanoscale mechanical properties of materials is very important in understanding the initiation of plastic deformation or fracture and the behavior of surfaces in tribology (the branch of engineering that deals with the interaction of surfaces in relative motion as in bearings or gears) [1.18]. Three different technical instruments have been developed for these studies: (1) the surface force apparatus (SFA) [4.2]; (2) the atomic force microscope (AFM) [4.3], and (3) the depth sensing nanoindentation technique [4.4]. The capabilities of these instruments cover a wide range of contact area (several mm^2 in the case of SFA; a few nm^2 in AFM) and displacement resolution. The SFA is mainly used for direct measurements of surfaces and intermolecular forces. The early use of the AFM was limited due to technical limitations to qualitative investigations of the elastic and plastic properties of materials at the nanoscale [4.5]. The recent developments in scanning probe microscopy, combining depth sensing nanoindentation with imaging capabilities [4.6] have reduced the problems associated with quantifying load-displacement data obtained using an AFM. Accurate determination of both contact area and displacement can be achieved by coupling depth sensing nanoindentation with force modulation [4.7] that allows quantitative measurement of nanoscale mechanical properties like hardness, modulus, viscoelasticity and creep. Nanoindentation is a useful technique for measuring the mechanical properties of small volumes of materials [4.8] and will be discussed in Section 4.4.

4.2 Hardness

The term hardness is variously defined depending upon the topic and level of understanding [4.8]. In general, it is taken as the resistance of a material to permanent or plastic deformation [1.18]. In mechanical metallurgy, hardness is defined as the ability of a metal to resist plastic deformation. The greater the hardness of the material, the greater is the resistance to deformation [1.18]. Hardness is generally treated as a composite property of a material including yield strength, work hardening, true tensile yield strength and modulus of elasticity. Hardness is usually measured by an indentation test, which is of major engineering interest for metals. In the indentation process, a pointed or rounded indenter is pressed into a surface under a nearly constant load. Hardness is defined as the indentation load divided by the projected contact area of the indentation.

Hardness measurements are classified as being on macro-, micro- and nano-scale based on the forces applied and displacements obtained [1.18]. Macro-hardness is generally measured by quick and simple methods to obtain mechanical property information from a small sample of a bulk material. This method is useful to test the bulk properties and quality of engineering materials. Macro-hardness measurements are highly variable and do not identify accurate features in case of fine microstructure, multi-phase or non-homogeneous structures [1.11, 1.18]. Here, micro-hardness measurements are appropriate [4.9c].

Micro-hardness [4.9c] of a material is generally determined by forcing an indenter, say Vickers or Knoop indenter, into the surface of the material by using loads varying from 15 to 1000 gf. In this process, the applied load, penetration depth and cycle time are measured continuously by pressing a tip of the micro-indenter into a sample. Usually the indentations are very small and are measured with a microscope. This is a good measurement to determine the hardness of different microconstituents within a structure, or measuring steep hardness gradients in case hardening. In nano-indentation tests, a very small indentation force in the range of a few nano-Newton to milli-Newton is used to determine the hardness and the depth of indenter penetration. New technology promises accurate measurement, control of the indenting forces and precise measurement of the indentation depths [4.3].

4.3 Hardness Measurement Methods

There are four common types of hardness measurement methods: (1) Brinell hardness test, (2) Rockwell hardness test, (3), Vickers hardness test, and (4) Knoop hardness test [1.18, 4.8]. These four hardness measurement methods are used to determine the resistance of a material to the penetration of a non-deformable ball or cone. Brinell and Rockwell hardness tests are generally used to measure the macro-hardness, while Knoop hardness test is used for measuring micro-hardness. The Vickers hardness test is a widely used method to measure the macro-, micro- and the nano-hardness of materials (depending on the size of the indenter used).

Brinell Hardness Test

The first widely accepted indentation-hardness measurement method was developed by Brinell in 1900 [1.18]. In this method a hard steel-ball of a known diameter is forced into the surface of a material by applying a specified load (Scheme 1). The load is usually applied for 10 to 15 seconds. The Brinell (hardness) number is obtained by dividing the applied load (kilograms) by the actual surface area (square millimeters) of the indentation.

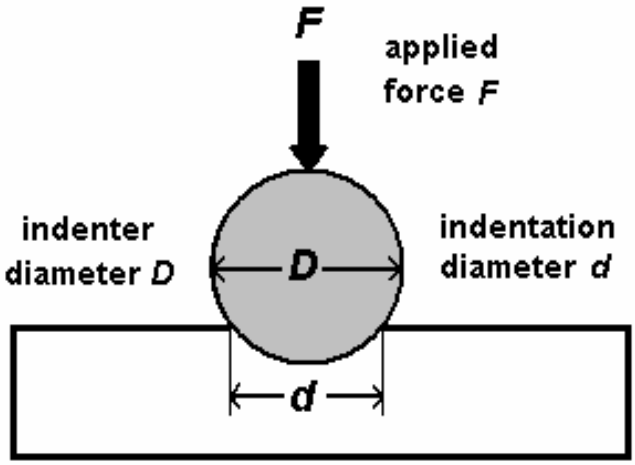

Scheme 1

Rockwell Hardness Test

The Rockwell hardness test is performed to measure the net increase in the depth of penetration of an indenter for an applied load [1.18]. Hardness numbers have no units, the higher the number means the harder the material. In the Rockwell test two (minor and major) loads are applied one after the other using a diamond-cone or steel ball indenter. For instance, a minor load of 5 kg is first applied which initiates the penetration and holds the indenter in place. Then, the reading is set to zero and the major load is applied for some time and removed. The depth reading is taken while the minor load is still on. The reading on the scale directly shows the difference in depth caused by the two different forces.

Vickers Hardness Test

The Vickers hardness test is a standard method for measuring the hardness of various materials using a diamond pyramid indenter [1.18]. In this method, the hardness of a material is calculated from the size of an impression produced under load by a pyramid-shaped diamond indenter. The Vickers test is somewhat similar to the Brinell test, but the pyramid-shaped diamond indenter is used in the former while a steel ball is used in the latter case. The square-based diamond cone of the Vickers indenter has an advantage over the other indenters because it does not deform over time and use.

Knoop Hardness Test

This test method was devised in 1939 by F. Knoop and colleagues at the National Bureau of Standards (United States), which is now known as National Institute of Standards and Technology (NIST). The relative micro-hardness of a material is determined by the Knoop indentation test [1.18]. In the Knoop test, the indentation pressures are lower than in the Vickers hardness test, which allows also the hardness testing of brittle materials such as glass and ceramics. The Knoop hardness number (KHN) is the applied load divided by the unrecovered projected area of the indentation. The hardness of the material is determined by the depth to which the Knoop indenter penetrates.

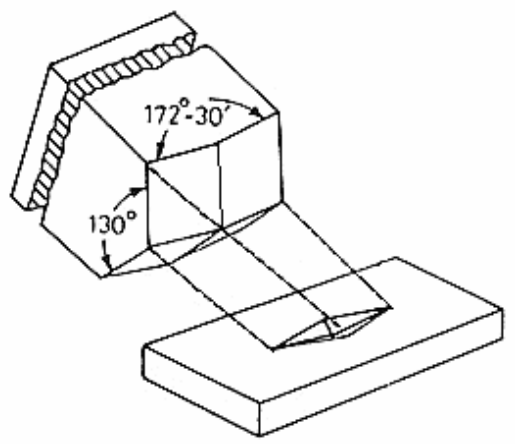

Scheme 2

The diamond indenter employed in the Knoop test is in the shape of an elongated four-sided pyramid, with the angle between two of the opposite faces being approximately 170º and the angle between the other two being 130º (Scheme 2) [1.18]. The loads used in this test are often less than one kilogram-force, and the indenter produces a four-sided impression of about 0.01 to 0.1 mm in size. The length of the impression is approximately seven times the width, and the depth is 1/30 the length. The area of the impression under the specified loads can be calculated after measuring the length of the longest side using a calibrated microscope. The final Knoop hardness (*H*K) = $14.229\times(F/D_2)$, where F is the applied load (in kilograms-force) and D_2 is the area of the indentation (in square millimetres). Knoop hardness numbers are often cited in conjunction with specific load values.

4.4 Nanoindentation Technique

Instrumented indentation, also known as depth-sensing indentation or nanoindentation, is a useful and well-established technique (Scheme 3) for measuring the mechanical properties of small volumes of samples ranging from metals, ceramics, polymeric and biological materials [4.8, 4.9]. In this technique, the Vickers test is performed with a Berkovich indenter tip which has the shape of a three-sided pyramid with triangular faces. In nanoindentation, a continuously increasing load is applied to the

indenter and the depth of penetration of the indenter or the displacement into the specimen is measured as a function of the applied load. From the unloading slope of the load-displacement data the contact stiffness, contact area and mechanical properties such as hardness and modulus of the material are calculated using standard models [4.8, 4.9]. The contact stiffness is calculated from the amplitude and phase shift using a dynamic model [4.7, 4.8]. The advantage of force modulation is that the contact stiffness can be directly obtained continuously during indentation. Because measurements are carried out at frequencies greater than 40 Hz, it is less sensitive to thermal drift, allowing accurate observation of creep in nanoscale contacts, when the hardness is measured as a function of time [4.10]. The ultimate sensitivity and useful frequency range of the technique depend on the mass, the damping coefficient, and stiffness of the indenter. A low mass, low damping coefficient and optimum stiffness of the indenter will significantly improve sensitivity.

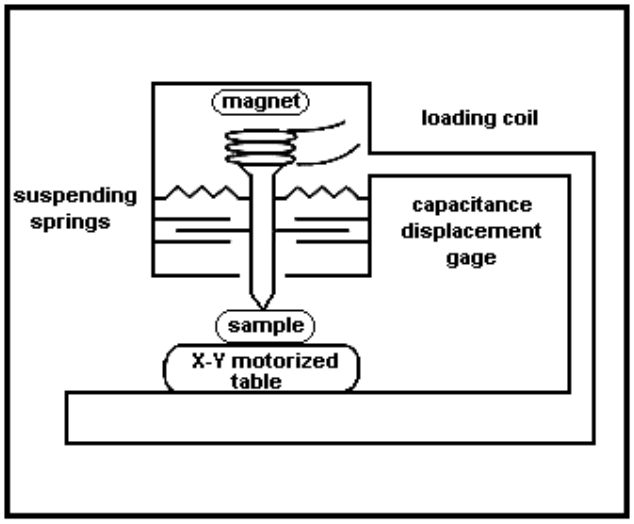

Scheme 3. A schematic model for a nanoindenter machine. This figure is reproduced based on [4.8a].

In general, there are two ways of measuring the hardness of a material by nanoindentation: (1) depth control method (continuous stiffness measurements), and (2) load control method [4.6, 4.8, 4.9]. In the depth control method hardness is measured over a defined range based on continuous stiffness measurement (CSM). Hardness is

calculated only during the loading cycle [4.8a, 4.11]. In load control method, the hardness is measured from the first few points of the unloading curve.

Techniques of Analysis

The analysis of force-displacement curves produced by instrumented indentation systems is often based on the works of Doerner and Nix [4.8c] and Oliver and Pharr [4.8b]. When an indenter is pressed into a sample, both elastic and plastic deformation takes place, which produces a hardness impression that depends on the shape of the indenter. During indenter withdrawal (unloading), only the elastic portion of the displacement is recovered, which facilitates the use of an elastic solution in modeling the contact process in this method [4.9a]. These elasticity-based analyses are normally applied to the unloading data of an indentation measurement. When creep is present in the material, the measured values from this method are not absolute as they are time-dependent, and hence they need to be compared at similar depths (at the same loading/unloading rate). Assuming the initial unloading part of deformation to be only elastic is reasonable, because in the early stages of unloading only the first few points are considered to record the hardness, and in this region the anelastic and plastic components are extremely small/negligible. Therefore, the very early unloading behavior of the material is assumed to be elastic recovery only. In general, the relationships between penetration depth, h, and force, P, during on unload can be represented by an equation of the form

$$P = \alpha(h - h_f)^m \qquad (1)$$

The parameter α contains geometric constants, the elastic modulus of the sample, E, the Poisson's ratio of the sample, v, the elastic modulus of the material of the indenter, E_i, and the Poisson's ratio of the material of the indenter, v_i. The parameter h_f is the final unloading depth and m is a power law exponent that is related to the geometry of the indenter. Once an appropriate nonlinear power law fit is obtained to the unloading data (where α, h_f, and m are the fitting parameters), a derivative, dP/dh, applied at the maximum loading point (h_{Max}, P_{Max}) gives the information about the state of contact at

that point (contact stiffness, S) (Scheme 4). The measured stiffness, S^*, is the slope of the tangent line to the unloading curve at the maximum loading point (P_{Max}) and is given by

$$S^* = \left(\frac{dP}{dH}\right)_{P_{max}} = am(h_{max} - h_f)^{m-1} \qquad (2)$$

In this equation, a is the contact radius of the indenter with the sample and H is the hardness of the sample ($H = P/A$). Here the cross section of the indenter is assumed to be circular.

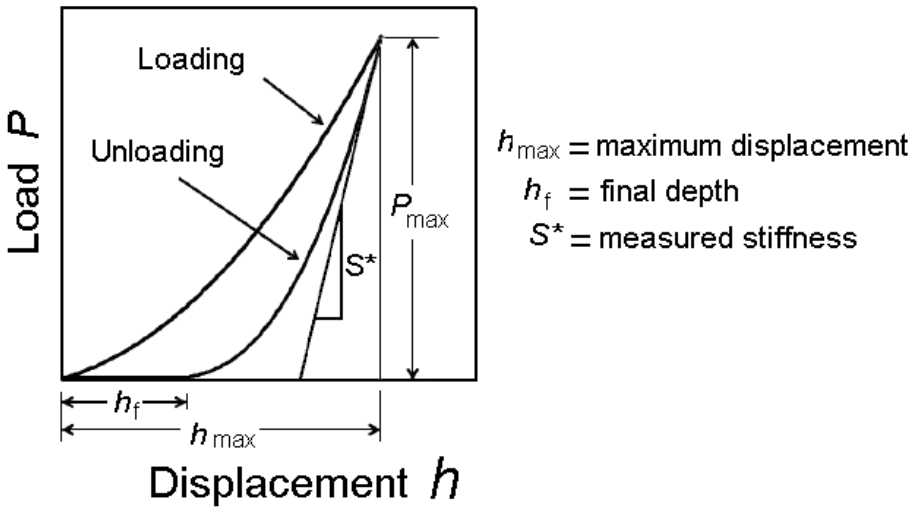

Scheme 4. An indentation force-displacement curve illustrates several important parameters used in the Oliver and Pharr analysis. The scheme is reproduced from reference [4.8a].

4.5 Stress-Strain Curves

The stress-strain relationship was introduced in Chapter 1 and the different possible shapes for this relationship are discussed now [4.12]. Which depend on the mechanical response of various materials (Scheme 5).

(a) It is found that the work-hardening of many metals approximates to a parabolic form. The stress-strain curve can then be represented by a simple power law

$$\sigma = B\varepsilon^m \qquad (3)$$

where B and m (strain-hardening exponent) are constants.

(b) For cold-worked metals with an initial yield stress Y, the curves are better represented by an equation of the form

$$\sigma = Y + B\varepsilon^m \qquad (4)$$

where Y is the initial yield stress. This ignores the elastic strain, which is very small.

(c) A further simplification is often made by assuming that the strain-hardening rate is uniform (and linear). That is,

$$\sigma = Y + B\varepsilon \qquad (5)$$

(d) When work-hardening is negligible in a material, then the yield stress is constant and independent of strain. Elastic strain is also ignored, and the stress-strain curve is reduced to the horizontal straight line—the so called "rigid plastic" behaviour.

$$\sigma = Y \qquad (6)$$

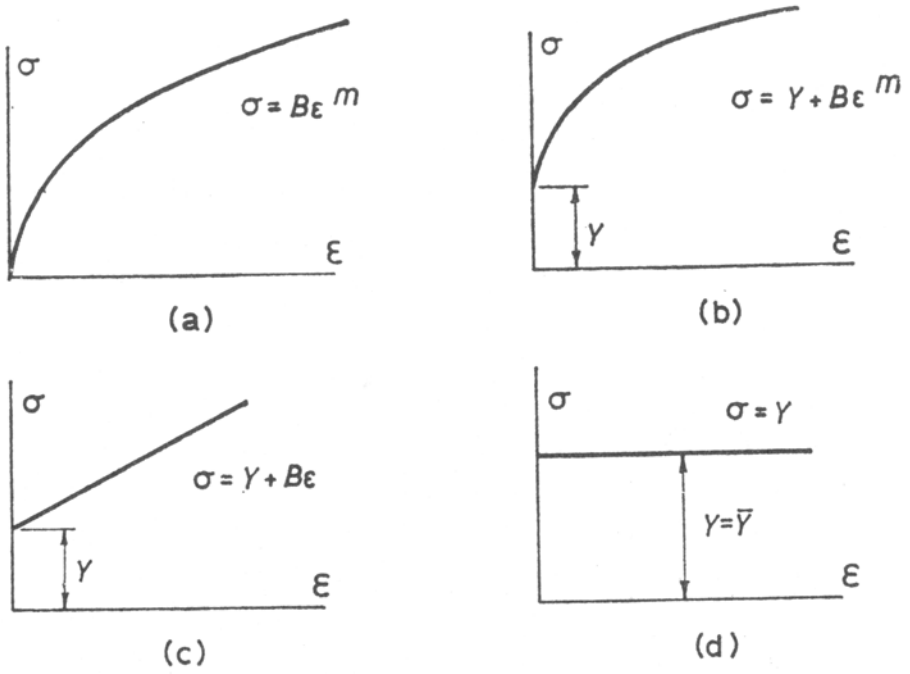

Scheme 5. Various approximate forms of stress-strain curves. This figure is taken from [4.12].

Hardness and displacement of a material can be derived from the expressions for stress and strain respectively, and thus the stress-strain curves are analogous to the hardness-displacement curves, discussed in the following sections.

4.6 Creep

The time-dependent/continuous deformation of a material at constant stress is called *creep*. Creep basically depends upon the temperature of the test and microstructure, and is significant at elevated temperatures in many metals [1.18c]. It has been reported extensively in metals at medium and elevated temperatures. Often, the creep curve of a material is determined by applying a constant tensile load to a specimen at a constant temperature. In this case, the strain suffered by the specimen is determined as a function of time. An ideal strain-time (creep) curve is illustrated in Figure 1. The slope of the curve gives the creep rate. Generally, the full creep curve is divided into three stages/regions, primary (I), secondary (II) and tertiary (III) creep. The strain increases rapidly in the initial stage when a constant load, P, is applied and this region is called the primary creep. Then, the creep rate decreases with time and reaches a nearly steady state, which is known as secondary creep. Finally the creep rate increases rapidly with time till fracture occurs, which is referred to as tertiary creep. In a material of a given microstructure, the appearance of the three stages in the creep curve largely depends on the applied stress and temperature. When a constant load is applied throughout the test, the thickness of the sample decreases as it elongates, thus the axial stress increases and follows the path shown till fracture. Had the stress remained constant, the path would how been along A indicated with dashed line in Figure 1. The mechanical properties of materials largely depend on test temperature, because the mobility of atoms increases rapidly with temperature (an exponential/Arrhenius relationship). The high-temperature mechanical properties also depend on the time scale. Generally, creep becomes of engineering significance in metals at a homologous temperature, T/T_m (where T is the test temperature and T_m is the melting temperature, both being presented on the absolute scale), greater than or equal to 0.3-0.5.

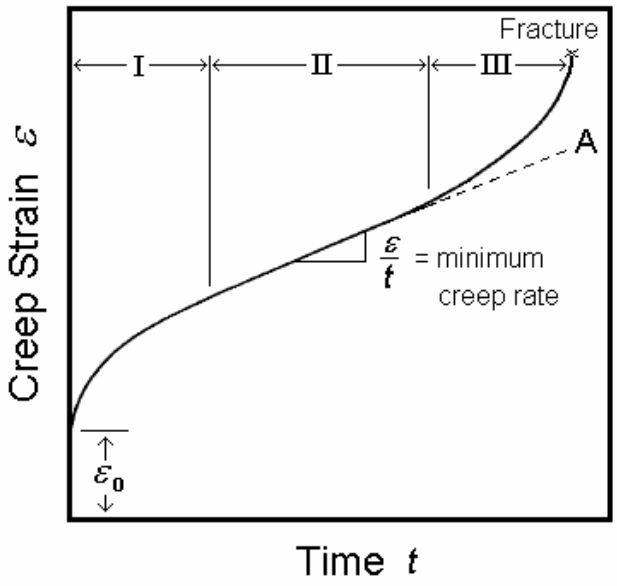

Figure 1. Typical creep curve shows the primary (I), secondary (II) and tertiary (III) stages of creep and fracture in a constant-load test. Curve *A* (dashed line) represents the constant-stress test. This figure is reproduced from reference [1.18c].

4.7 Results and Discussion

The mechanical properties of metals, ceramics, plastics and several other materials have been studied extensively in the recent past using nanoindentation experiments [4.1, 4.9], but the mechanical behaviour of molecular crystals at the molecular level is not yet understood. The experimental findings in this chapter constitute the first report on the mechanical deformation and creep behaviour of molecular single crystals studied using the nanoindentation technique. The results obtained could be interpreted using the well-known ideas on the mechanical behaviour of metals and other kinds of materials. Useful information on the intermolecular interactions present in the molecular crystals studied could be derived.

There are some reports on the mechanical deformation of organic layered thin films [4.13] and on molecular migrations upon nanoindentation scratching [2.12] of molecular single crystals. In this work, the mechanical behaviour of some molecular crystals (Scheme 6) has been investigated at the nanometer scale using the

nanoindentation technique on a nanoindenter (MTS make) equipped with a pyramidal (Berkovich) indenter tip. In this study, two types of crystals were taken: (1) bending crystals (samples **1** to **5**); (2) shearing crystal (sample **6**). The detailed mechanical properties and crystal packing of these crystals have been discussed in Chapters 2 and 3. Hardness (*H*) and creep behaviour were recorded in the depth control method using the continuous stiffness measurement (CSM) mode [4.8a]. Although approximately 10 indents were made on each sample, only 2 to 4 indentations on an average were successful. This was due to the unavoidable surface defects on the molecular crystals. In other words, molecular crystals are soft and develop surface defects while they are separated from the mother liquor. Thus, the indenter fails to find a flat surface at some locations. In the present experiments the thickness of the samples used was a minimum of 1 mm (10^6 nm) and the maximum depth of indenter penetration recorded was approximately 1600 nm. Therefore the thickness of the crystal is sufficiently greater than the total depth of indenter penetration and thus the entire deformation can be significantly considered to be confined only to the crystal interior, which ensured that the hardness and the elastic modulus obtained pertained to the crystal only, i.e. there were no artefacts.

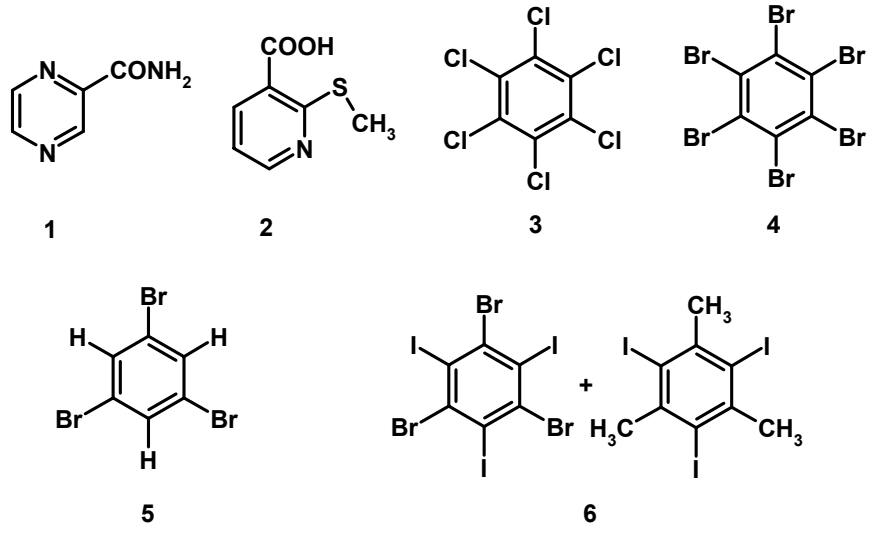

Scheme 6

4.7.1 Pyrazine-2-carboxamide, 1

Pyrazine-2-carboxamide, **1** is a polymorphic compound [3.13] and the nanoindentation experiments in this case were concerned with Forms *α* and *δ*. Nanoindentation experiments on these crystals are interesting, because Form *α* bends on application of a mechanical stress, while Form *δ* is brittle under similar conditions. The crystal packing and mechanical behaviour of these two forms are discussed in detail in Chapter 3, Section 3.3.3. Single crystals of the Forms *α* (**1A**, **1B**) and *δ* (**1C**, **1D**) of the molecular compound **1** were selected and mounted on the sample holder, as shown in Figure 2a. Two types of tests were done on each of these samples: (1) depth control method tests using the CSM mode from which hardness, *H*, and modulus, *E*, are obtained; (2) load control method tests with different loads on the indenter, but each time involving constant load application with a 600 s hold time. In the latter method, to achieve a particular depth (300, 500 or 1000 nm) in the specified time, the applied loads were estimated using the CSM data. In the CSM method all the indentations were made using constant $\dot{P}/P$ loading, while a constant $\dot{P}$ loading was used in the load control method ($\dot{P}$ is the rate of change of load with time). Since the hardness value of a sample is time dependent, it varies with the depth of penetration of the indenter and the two different methods gave comparable hardness at similar indenter penetration depth.

In the case of Form *α* (**1A**, **1B**) the indents were made with the tip approaching the (100) face of the crystal at 90º to that face with a velocity of 10 nm s^{-1}. The crystal packing shown in Figure 2b is a view along [100] direction along which the indentation was done.

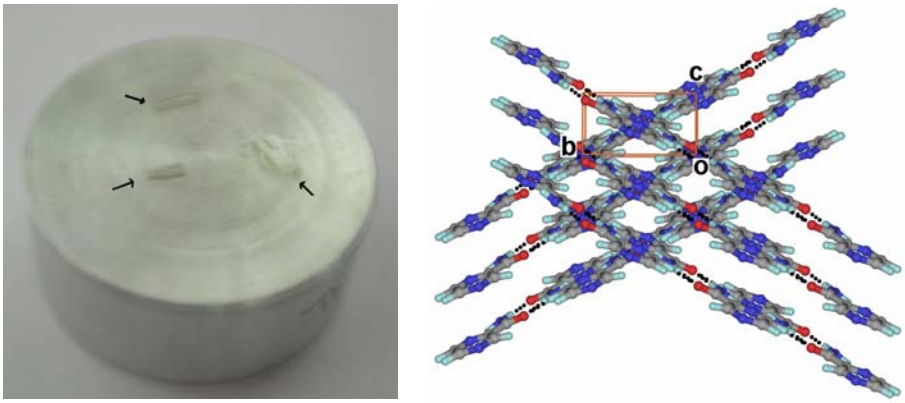

(a) **(b)**

Figure 2. (a) Crystals as mounted on sample holder. Arrows indicate the location of the crystals. (b) Crystal packing in Form *α* samples of **1A** and **1B**, viewed down [100] axis along which the indentation was made.

Nanoindentation data from the CSM tests are discussed here and the data from the load control method will be discussed in a later part of this section. The experimental data for all the tests on these samples are presented in Table 1. Two indentations were successful on each sample **1A**, **1B** and **1C**, while all the tests failed on **1D** in the CSM tests. The two successful tests on sample **1A** are coded as **1A-t01** and **1A-t02**, and similarly for the two tests on **1B** (**1B-t01**, **1B-t02**) and **1C** (**1C-t01**, **1C-t02**) (Table 1). The same method of coding is followed for the experiments on the other samples (**2** to **6**) also. In these experiments, the past experience in our laboratory has been that the nanoindentation data at lower depths, say up to 100-120 nm, are not reliable because of tip blunting and calibration errors and always the curve has to go through an initial transient state. This was also the case with some indentation experiments done in our laboratory on much stronger materials on the same machine. But, in the present study in all experiments "creep-like" behaviour was seen in the region below 120 nm depth also and hence, data in that region were also included to plot all the full curves. In addition, hardness-time curves pertaining to the region only above 100-120 nm depth were plotted separately for obtaining a really reliable analysis. The H average (H_{Ave}) and E average (E_{Ave}) values given in Table 1 were estimated at an indenter depth that ranged from 100 to 200 nm (automatic machine selection) as a default option by the instrument. (It was

possible to change the specified range of the depth to measure the H_{Ave} value, but it was not done as it did not give any additional information in this particular study.) The H at the beginning of a test is higher and it decreases with the time because of creep. H_{Ave} was always greater than the H value from unload (H_{Unl}) because the former was invariably measured at a lower depth (100 to 200 nm) than the latter, which was obtained from peak unload at maximum depth (see Table 1). This comment is valid in case of all the other samples examined in this thesis.

Table 1. Pyrazine-2-carboxamide, **1**. The indentation data obtained from depth control method with a depth limit of 1500 nm and 10 s hold time using the CSM mode. The error limit for each value is given in brackets, and this convention is followed through out the thesis.

Sample Code –Test No.	**H_{Ave} (GPa)**	**E_{Ave} (GPa)**	**E_{Unl} (GPa)**	**H_{Unl} (GPa)**
1A–t01	0.632(±0.09)	13.887 (±1.1)	10.193(±0.65)	0.29(±0.03)
1A–t02	0.76(±0.09)	15.443(±1.1)	11.118(±0.65)	0.33(±0.03)
1B–t01	0.585(±0.05)	15.191(±0.67)	12.897(±0.17)	0.264(±0.02)
1B–t02	0.593(±0.05)	16.141(±0.67)	13.142(±0.17)	0.29(±0.02)
1C–t01	0.823(±0.06)	11.814(±0.65)	6.689(±0.89)	0.335(±0.03)
1C–t02	0.912(±0.06)	12.732(±0.65)	7.95(±0.89)	0.293(±0.03)

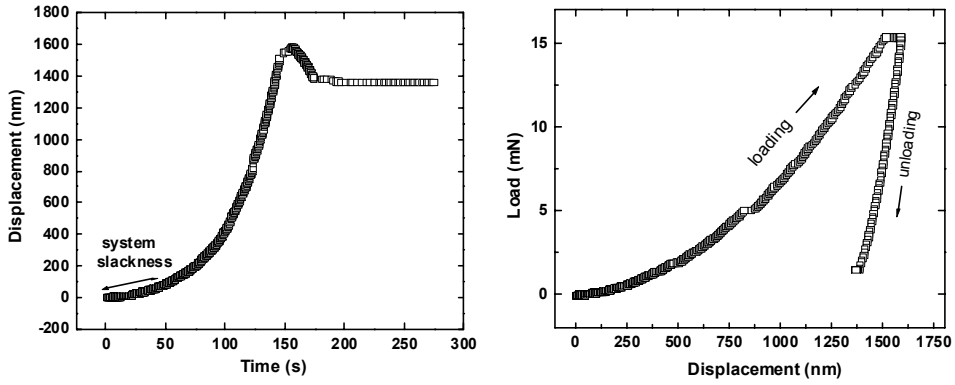

(a) **(b)**

Figure 3. Pyrazine-2-carboxamide, **1A**. (a) Variation of the depth of indenter penetration with time (displacement-time relationship). (b) Load-displacement curve including the 10s hold segment.

The displacement–time (*h–t*) and the load–displacement ((*P–h*)) curves obtained from sample **1A** by the CSM test are illustrated in Figure 3. There was no significant pop-in and discontinuity was found in the curve indicating that the crystal did not crack during the measurements. The initial portion in Figure 3a (indicated) where the displacement rate is very slow, is on account of the system (specimen-indenter combine) slackness arising out of a lack of proper contact between the specimen and the indenter. This is followed by a linear region of load increase (elastic region). Then, there is a displacement over-shoot before the displacement becomes practically independent of time (Figure 3a), i.e. creep is nearly exhausted. Before exhaustion, the total displacement decreases slightly paralleling the corresponding stress over-shoot, as the system gradually reaches a state of equilibrium. This phenomenon is also reported in metals during creep at relatively high strain rates, during hot working or during superplastic flow at higher than optimal strain rates [4.14]. In all these cases, microstructural changes/rearrangements/evolution that accompany time-dependent deformation are responsible for the shape of the displacement-time/load-time curves. Recovery of elastic/anelastic strains commences on unloading (see Figure 3). Recovery of strain is due to both elastic and viscous effects [1.18c]. This type of deformation is called *elastoviscous* or *anelastic deformation*. The elastoviscous deformation is different from elastic deformation in which strain is recovered immediately on stress removal. In the former, the strain recovery is time dependent and takes place over significant time. In metals this is common at high temperatures when continuous deformation occurs on tool (indenter) movement arrest. In short duration tests, from a macroscopic viewpoint creep deformation is treated as plastic deformation and the elastic and viscous deformation is neglected because the former contribution is much larger than the latter ones [1.18c].

The path of the unloading curve (Figure 3b) indicates (a) that there is mechanical hysteresis [1.18c], i.e. the unloading path is different from the loading path, and (b) that the material has suffered plastic deformation, i.e. some amount of strain cannot be recovered and is set permanently in the material. If the unloading curve is extrapolated to zero load, there is a residual depth of about 1250 nm.

The hardness-time curve (obtained using the full data, i.e., above about 20 nm depth) is from the same indentation on sample **1A** in the CSM mode, which is illustrated in Figure 4. In case of all the indentations, the hardness values obtained below 20 nm depth was always highly scattered, and hence were excluded. The hardness slowly decreases with time which indicates the strain softening behaviour of the material. Time dependent strain softening is indicative of viscous deformation, i.e. creep [4.15]. This is in contrast with work hardening in which hardness increases with time (i.e. strain hardening; see Scheme 5 in Section 4.5). As can be seen from the Figure 4, the deformation process in these molecular crystals can be treated as primary/exhaustion creep followed by a steady state, which has been discussed extensively in case of metals undergoing deformation at medium and elevated temperatures [1.18]. (It is well-known that hardness, H and the flow/yield stress, σ_y are directly related [2.2].) Initially, the hardness (analogous to flow stress) decreases rapidly with time, but tends to a near constant value after some time. The shape of the curve obtained from **1B** was similar to that of sample **1A**, but the absolute values were slightly different, which could be due to small local variations in the concentration of defects or experimental scatter or both.

The full curve in Figure 4a could be described accurately by

$$H = y_0 + A_1 e^{(-t/t_1)} + A_2 e^{(-t/t_2)} \qquad (7)$$

where y_0, A_1, A_2, t_1 and t_2 are unknown (fitting) constants.

The near-steady state portion (i.e. the curve above 55 s that corresponds to the data obtained from a depth above 100 nm) of the *H-t* curve is plotted separately (Figure 4b) and is fitted well by Equation (8), which was derived recently by Padmanabhan *et al.* [3.11] to understand micro-indentation creep in porous nanocrystalline Pd metallic compacts and Fe-63 vol% TiN and Ni-58 vol% TiN composites.

$$H = H_{\max} \cdot e^{-m \ln(C_1 t + 1)} \qquad (8)$$

where H is the hardness, H_{Max}, is a constant that matched the maximum H value at the start of the experiments described in reference [3.11], m is the *strain-rate sensitivity index*, t is the time of load application and C_1 is an unknown constant. The exponent m is

obtained as the slope of a plot of log stress vs. log strain rate (proportional to log H vs. $\log\left[-\left(\dot{H}/H\right)\right]$).

H_{Max}, m and C_1 in Equation (8) had to be considered as fitting constants devoid of physical meaning to fit the experimental data presented in Figure 4b. The H_{max} value also did not match the maximum H recorded in Figure 4b and it lay between the H_{max} values of the full curve and the steady state curve. It is conceivable that the near-steady state creep commenced where the hardness equals that constant value.

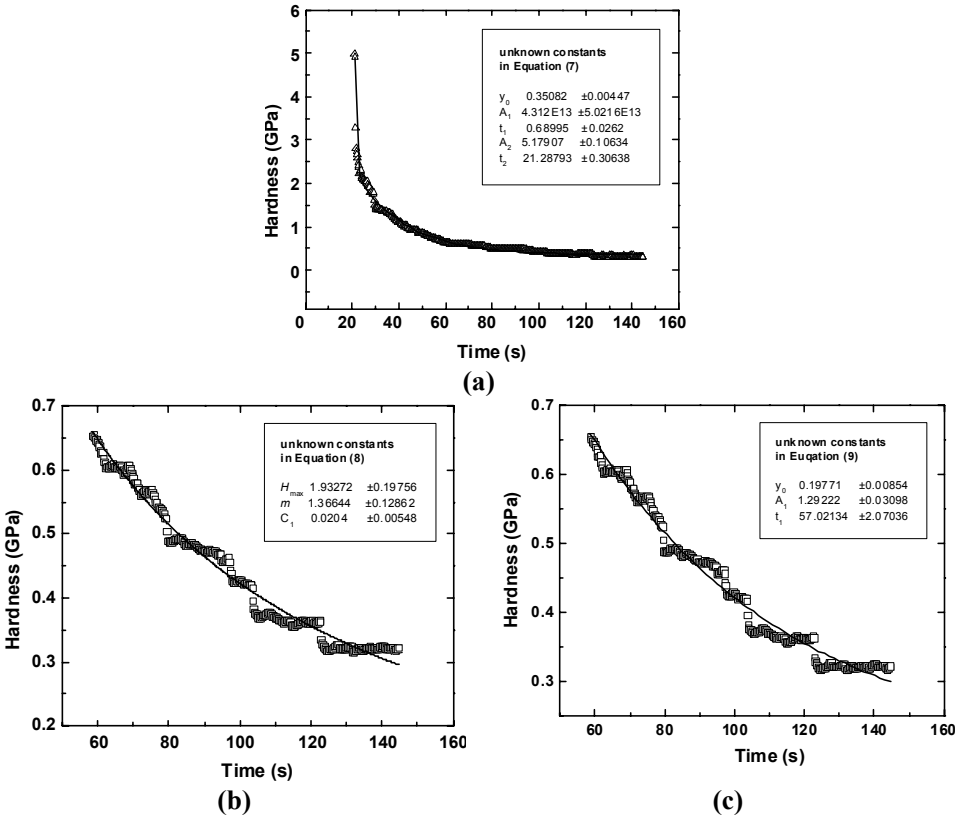

Figure 4. Nanoindentation experiments on pyrazine-2-carboxamide, **1A**. Hardness (H) – time (t) of load application relationship obtained in (a) using the full data; (b) and (c) by excluding the data below ~125 nm depth. Symbols represent experimental points. Line curves in (a), (b) and (c) are predictions based on Equations (7), (8) and (9) respectively (the corresponding constants in the three equations are given in boxes in respective figures).

This is interesting because molecular crystals have relatively low melting points (463 K; 394 K) compared with metals (Fe: 1808 K; Ni: 1726 K; Pd: 1825 K) and still the phenomenology of the creep behaviour is similar. This may be explained by comparing the homologous temperatures of deformation of the molecular (T = 298 K, T_m = 463 K, T/T_{m} = 0.64) and the metallic (T = 298 K, T_m (Pd) = 1825 K, T/T_{m} = 0.16) crystals involved. Exhaustion creep (primary/logarithmic creep) sets in first at around T/T_{m} = 0.05 – 0.3 and can also be present at higher homologous temperature, prior to the on set of steady state creep [1.18c]. The equation developed here gives a phenomenological explanation for the mechanical deformation of diverse classes of materials on a common basis.

The same near-steady state portion of the curve could also be fitted equally well with the equation

$$H = C_2 + C_3 e^{-\frac{t}{C_4}} \qquad (9)$$

where C_2, C_3 and C_4 are unknown constants (Figure 4c). This expression (first order exponential decay) is commonly used to understand many decay processes, but here it is to be viewed only as an empirical fit. Both the Equations (8) and (9) have three fitting parameters with comparable standard deviation and suggest that they are both equally good fits for the near-steady state portion of the curve determined in the present experiment. But it is emphasized that neither equation has a physical meaning in terms of the operating mechanics of deformation at the molecular level. This latter aspect will be examined in future investigation.

In addition, Padmanabhan *et al.* [3.11] have described the domain in which creep at a given stress present before it ceases in terms of the power-law by plotting the log H $- \log\left[-\left(\frac{\dot{H}}{H}\right)\right]$ relationship (the latter derived from the predicted $H - t$ curves obtained by fitting the experimental data using Equation (8); $\dot{H}$ is the time derivative of H). In all their experiments, a log – log plot of H (which is proportional to the uniaxial yield stress)

vs. ($-\dot{H}/H$) (which is proportional to the corresponding strain rate) relationship was linear over the one to two orders of magnitude change in strain rate obtained in microhardness tests. The same analytical procedure is adopted here to describe creep in the molecular crystals. The present creep results are interesting because the power law creep, so well-known in case of metallic and other inorganic crystalline materials, is seen in these molecular crystals also. Although the initial portion of the indentation data around up to 100-120 nm depth was not fully reliable (discussed earlier in this section), the full set of data (from 20 nm depth) was used to plot the log $H - log\left[-\left(\frac{\dot{H}}{H}\right)\right]$ curve (proportional to the log stress – log strain rate relationship). Interestingly, here it was possible to derive the full sigmoidol curve from a single nanoindentation test (see Figure 5) because of the very low strength and the high strain-rate sensitivity of these molecular crystals. This is in contrast with the limited linear region present over a strain rate range of 1-2.5 orders of magnitude in the ln H – ln$\left[\frac{\dot{H}}{H}\right]$ relationship pertaining to the much stronger and less strain-rate sensitive nanocrystalline Pd and two other ceramic nanocomposites studied earlier [3.11]. It is time consuming to generate the full sigmoidol curve by tension testing. Therefore, the present result constitutes an interesting observation, because producing molecular crystals in large sizes is extremely difficult and even if this were possible, tensile testing at different strain rates will take a very long time. In contrast, the size of the specimen required for nanoindentation testing is very small and it is heartening that the nanoindentation technique has proven so useful in case of molecular crystals.

The full curve in Figure 5a could be represented accurately by Equation (10), where $y = \log H$ and $x = \log\left[-\left(\frac{\dot{H}}{H}\right)\right]$. In this equation, A_1, A_2, x_1 and x_2 are unknown constants.

$$y = \frac{A_1 - A_2}{1 + e^{((x - x_1)/x_2)}} + A_2 \qquad (10)$$

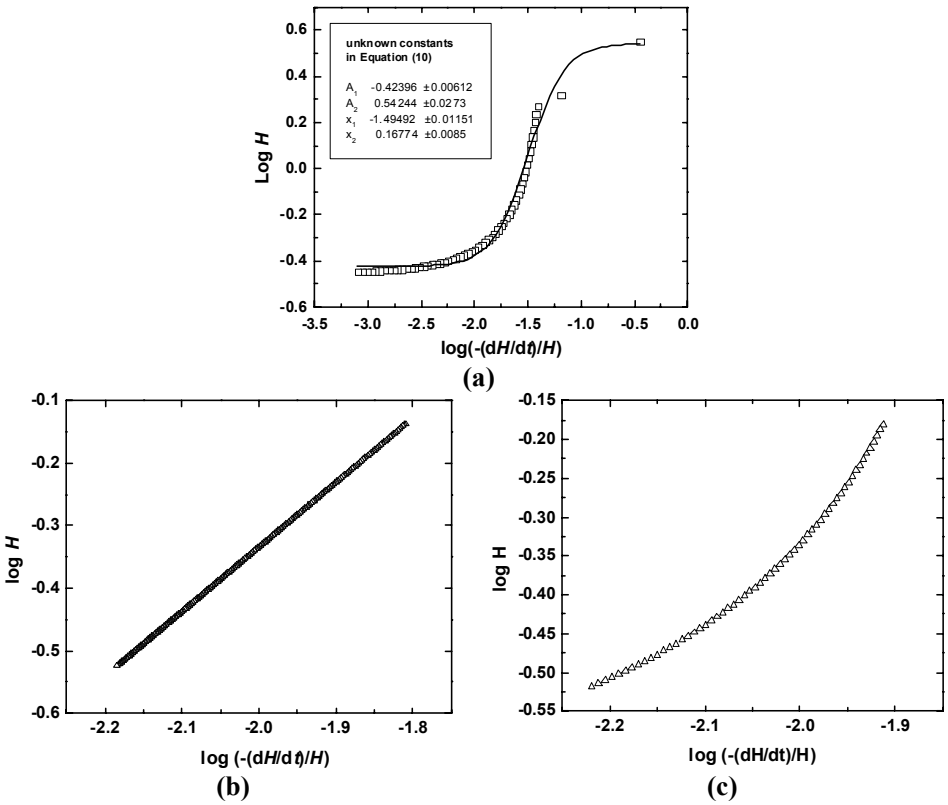

Figure 5. Nanoindentation experiments on pyrazine-2-carboxamide, **1A**. $H - \left[-\left(\frac{\dot{H}}{H}\right)\right]$ plots (a), (b)and (c) are derived from curves similar to that presented in Figures 4a (full curve), 4b and 4c (near-steady state portion, i.e. the data from above 100 nm depth) respectively. Symbols represent experimental points. Full curve in (a) is a prediction based on Equation (10) (see above).

The full curve in Figure 5a shows the three regions, also reported in superplasticity and during the deformation of hot polymers and bulk metallic glasses [4.16]. The point of inflection in the sigmoidol curve is found at log (– (dH/dt)/H) ~ – 1.5. Since molecular crystals are very soft, the three regions of creep covering a strain rate range of about 2.5 orders of magnitude is obtained in a short time, from a single nanoindentation test (see the full curve in Figure 5a). The curves in Figures 5b (linear) and 5c (nonlinear) are derived from curves similar to that presented in Figures 4b and 4c, which were predicted based on Equations (8) and (9) respectively. The nonlinearity of the curve presented in Figure 5c suggests that for that case

$$n = \frac{-(t + C_4 \ln H)}{C_4 \ln H} \qquad (11)$$

(this also follows from Equation (9)) where n is the inverse of the strain rate sensitivity index, m. As t tends to 0 in Equation (11), n becomes a constant. As log H in Figure 5c is negative, it is evident that n is positive.

It is emphasized that as these are empirical fits, it may be possible to describe the curves in Figures 4 and 5 in terms of other equations also. But, the present equations are easy to handle, as only exponential terms are involved and standard software are available to handle such equations. In a future investigation, an attempt will be made to describe the above curves in terms of constitutive equations based on physical mechanisms of deformation.

Nanoindentation data from load control method are discussed now. To examine the creep behaviour in detail, indentations were also made with different indenter penetration depths and hold times (time of constant load application) using the depth control mode on the nanoindenter. In these experiments, the required load to achieve some particular depth (e.g., 300, 500/600 and 1000 nm) was estimated using the CSM tests. The nanoindentation data obtained at maximum load (P_{Max}) on samples **1A** to **1D** at each estimated depth are given in Table 2. The presence of a positive slope (Figures 6a and 6c) in the displacement-time curves at constant load and continuing displacement at constant load (Figures 6b and 6d) are further evidence for creep.

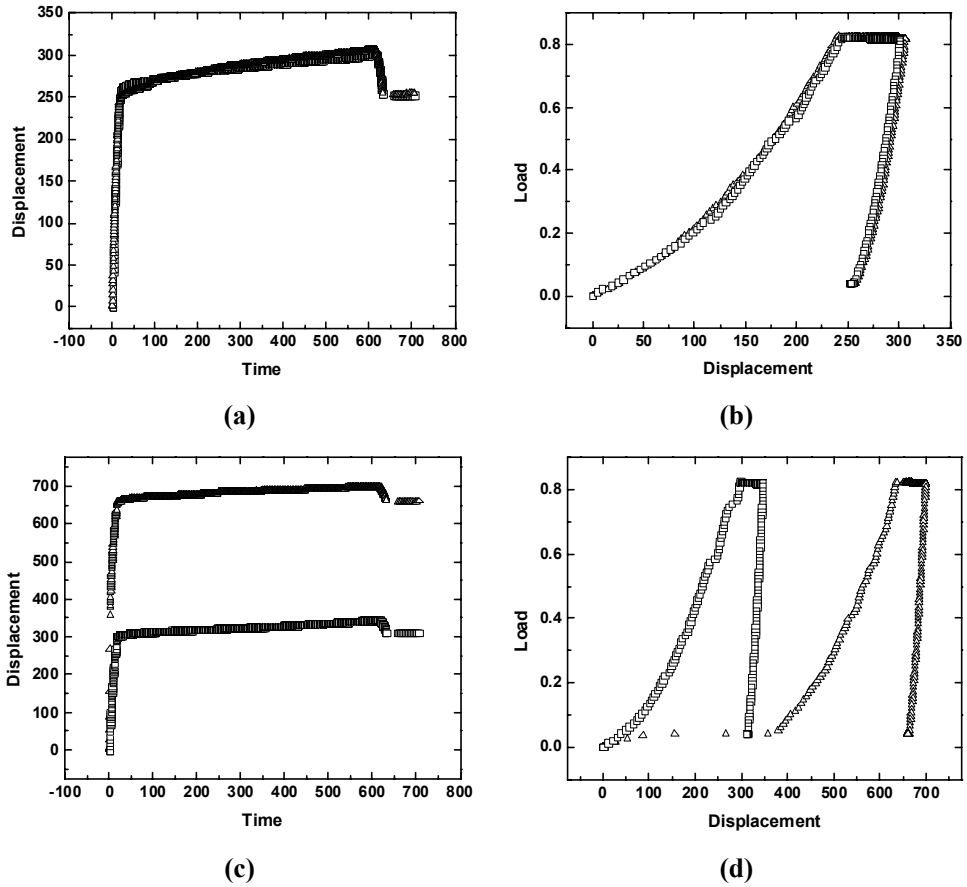

Figure 6. Pyrazine-2-carboxamide. (a) Displacement-time and the corresponding (b) load-displacement curves obtained from two different indentations (**1A-t01** and **1A-t02**) with penetration depths up to approximately 300nm on sample **1A**; (c) and (d) are from **1B-t01** and **1B-t02** with penetration depths up to approximately 300nm on sample **1B** (Table 2). In all the cases the hold time was 600 s. Note that the positive slope in the displacement-time curves at constant load indicates creep in (a) and (c) and continuing displacement at constant load is further indication of creep.

Comparison of the experimental results obtained from all the indentations on samples of Form α (**1A**, **1B**) and Form δ (**1C**, **1D**) (Table 2) gave important information related to the deformation and the local distribution of defects/dislocations. For instance, the data obtained from tests−01 and −02 on sample **1A** (see **1A−t01**, **1A−t02** in Table 2, estimated depths up to 300 nm) are considered to be similar, because E, H, h at P_{Max} are

similar for a given P_{Max} (0.81 mN). This suggests that the local concentration of defects at the two indentation positions is similar and hence, the deformation is similar. Whereas, although the applied load was similar in case of **1B−t01** and **1B−t02**, the achieved indenter penetration depths reached, *h*, were 698 and 345 nm respectively for a same P_{Max} 0.81 mN. The difference in the depths achieved in between the two tests is about 350 nm, i.e. one value is approximately one-half of the other. But, Figures 6d reveals that this difference is apparent because it is introduced almost at the beginning of the application of load, perhaps due to a lack of proper contact between the indenter and the sample. Once a proper contact is established, the indentation processes in the tow cases are similar (Figure 6d). When the initial portion of the **1A-t02** curve was adjusted to zero, the two curves nearly overlapped. This suggests that the local concentration of defects in the two positions of the sample is comparable. So, one has to be cautious while interpreting the indentation data as artefacts also are to be considered while calculating the *E* and *H* values. An apparent effect, similar to what was explained above was also found in case of tests **1A-t01** and **1A-t02** carried out to depths of about 500 nm. The data on samples **1C** and **1D** are discussed in a later part of this section where some different situations are discussed.

Now the nanoindentation data obtained on crystals of Form δ (brittle) are discussed. In this crystal packing, molecules are arranged as layers in the (012) planes (Figure 7). The layers are slightly tilted (slant) in the crystal when viewed perpendicular to the (100) face of the crystal (Figure 7b). Accordingly, the indentation direction is not parallel to the layers. Still, the overall creep behaviour of these crystals is similar to that of Form **1**α (Figure 8).

Table 2. Pyrazine-2-carboxamide, **1**. The experimental data obtained from indentations at different loads (applied to achieve some desired depth). 600 s hold time. Load control method.

Sample Code – Test No.	E at P_{Max} (GPa)	H at P_{Max} (GPa)	Displ. (h) at P_{Max} (nm)	P_{Max} (mN)
Estimated depths up to 300 nm				
1A–t01	13.052(±0.55)	0.411(±0.01)	306.452(±3.89)	0.817
1A–t02	13.759(±0.53)	0.423(±0.01)	300.944(±3.89)	0.814
1B–t01	6.948(±5.43)	0.071(±0.16)	698.187(±249.2)	0.81
1B–t02	14.631(±5.43)	0.304(±0.16)	345.7(±249.2)	0.811
1C–t01	9.311(±1.13)	0.468(±0.06)	337.316(±19.39)	1.02
1C–t02	10.911(±1.13)	0.553(±0.06)	309.896(±19.39)	1.018
1D–t01	4.317	0.084	735.172	1.012
Estimated depths up to 500 nm				
1A–t01	13.283(±1.43)	0.339(±0.08)	524.41(±75.81)	2.019(±0.05)
1A–t02	11.265(±1.43)	0.227(±0.08)	631.624(±75.81)	2.013(±0.05)
1B–t01	12.516(±1.11)	0.264(±0.03)	588.1(±32.95)	2.021(±0.05)
1B–t02	14.081(±1.11)	0.312(±0.03)	541.5(±32.95)	2.015(±0.05)
Estimated depths up to 650 nm				
1C–t01	10.227(±0.07)	0.367(±0.04)	687.155(±28.55)	3.545(±0.01)
1C–t02	10.323(±0.07)	0.425(±0.04)	646.776(±28.55)	3.534(±0.01)
1D–t01	9.305(±0.74)	0.263(±0.08)	797.132(±84.9)	3.548(±0.01)
1D–t02	10.358(±0.74)	0.378(±0.08)	676.955(±84.9)	3.533(±0.01)
Estimated depths up to 1000 nm				
1B–t01	13.384	0.265	1072.399	6.761
1C–t01	9.141(±2.55)	0.279(±0.05)	1139.18(±174)	7.59(±0.04)
1C–t02	3.454(±2.55)	0.183(±0.05)	1483.11(±174)	7.53(±0.04)
1C–t03	7.061(±2.55)	0.281(±0.05)	1157.99(±174)	7.51(±0.04)
1C–t04	8.518(±2.55)	0.295(±0.05)	1113.78(±174)	7.54(±0.04)
1D–t01	5.734(±3.04)	0.101(±0.13)	1827.349(±438)	7.56
1D–t02	9.539(±3.04)	0.275(±0.13)	1143.676(±438)	7.60

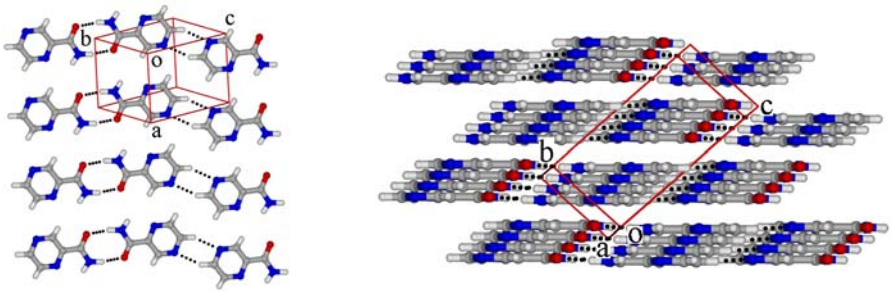

Figure 7. Pyrazine-2-carboxamide, Form *δ*. (a) A layer in the crystal packing. (b) Packing along the indentation direction, i.e. perpendicular to (100) face.

The serrations in the load–displacement curve (Figure 8) indicate the possibility of cracking or discontinuous yielding [1.18d] in the crystal at a molecular level during the measurement. As these crystals display limited ductility (brittle), this observation is very significant. When the indenter penetrates into the sample, the increase in the local concentration of defects will obstruct further indenter movement. As the load continuously increases on the indenter, the defects are moved away at some point, and then a sudden change in displacement takes place at a higher load. Further deformation will be easier and at a lower stress for a while, before obstruction causes into play once again. In brittle materials, the sudden movement away of defects may also lead to the

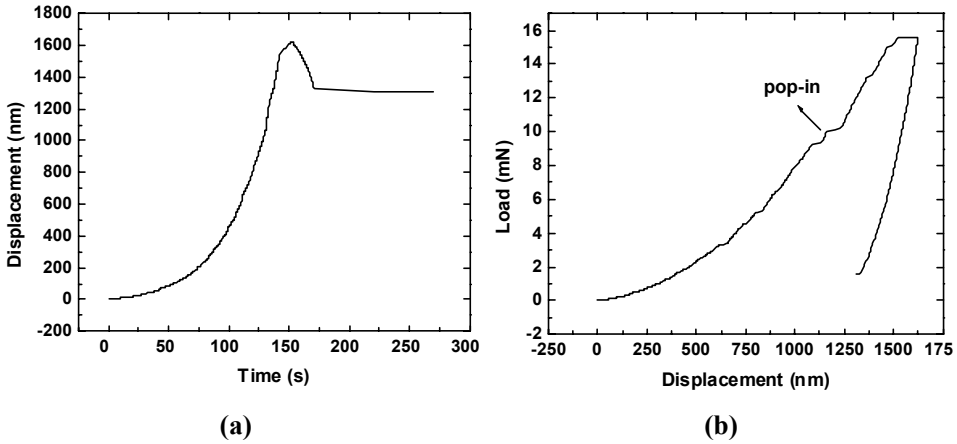

Figure 8. Pyrazine-2-carboxamide, Form *δ*, sample **1C** (see **1C-t01** in Table 1). (a) Variation of the depth of indenter penetration with time (displacement-time relationship). (b) Load-displacement curve including the 10s hold segment.

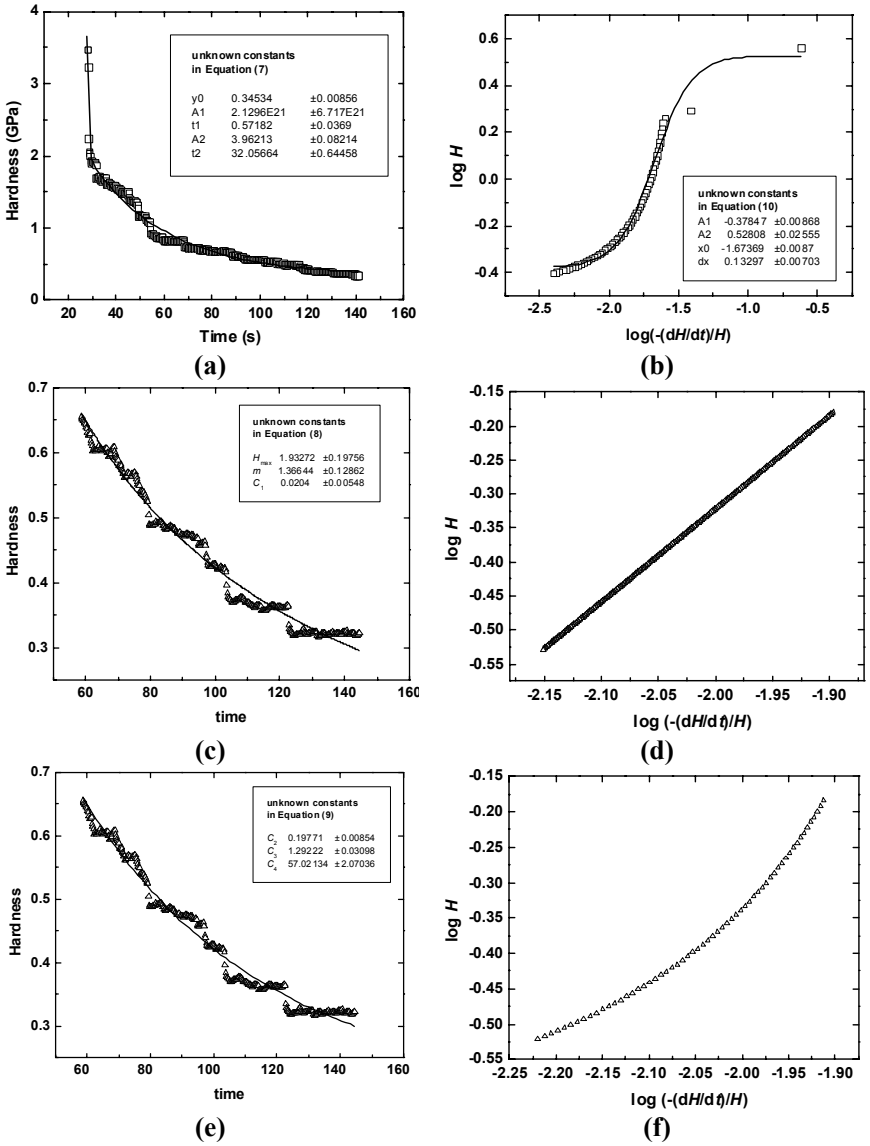

Figure 9. Pyrazine-2-carboxamide, Form δ, sample **1C**. Hardness-time relationship from CSM tests show (a) full curve; (c) and (e) obtained by excluding the data below 125 nm depths. (b), (d) and (f) are log H – log $\left[-\left(\dot{H}/H\right)\right]$ plots derived from curves similar to those presented in (a), (c) and (e) respectively. Symbols in (a), (c) and (e) represent experimental points while continuous curves are predictions based on Equations 7, 8 and 9 respectively.

creation of local nanoscale cracks. Both these alternatives will have to be examined quantitatively before a preference can be exercised for one or the other hypothesis/conjecture. The indentations on the (100) face of the crystals of Form **1***δ* (samples **1C** and **1D**) reveal that the hardness of these crystals is also close to that of the Form α (see Table 2) and Equations 7 to 9 fit the experimental data well (Figure 9).

In tests with estimated depths up to 300 nm, the data obtained from **1C-t01** and **1C-t02** are similar for a given P_{Max} value (1.02 mN) (see Table 2). But, in case of **1D-t01** the depth reached, *h*, is significantly greater than on **1C**, which again is only an apparent-effect due to the lack of proper contact between the indenter and sample **1D**. So, in such cases the *E* and *H* values can not be taken directly into account, as they are influenced by the error in the *h* values estimated. In tests with estimated depths up to 1000 nm, although the applied P_{Max} was nearly equal (7.5 mN), the achieved *h* in **1C-t02** (indicated in Figure 10b) was 1483 nm which is nearly 300 nm more than the *h* in **1C-t01**, **1C-t03** and **1C-t04** (see Table 2). Figure 10b suggests that this is not an artefact because the difference in depth was present at the beginning of load application. In fact it was accumulated gradually throughout the indentation process. This is indicative of the difference in the local concentration of defects in the crystal.

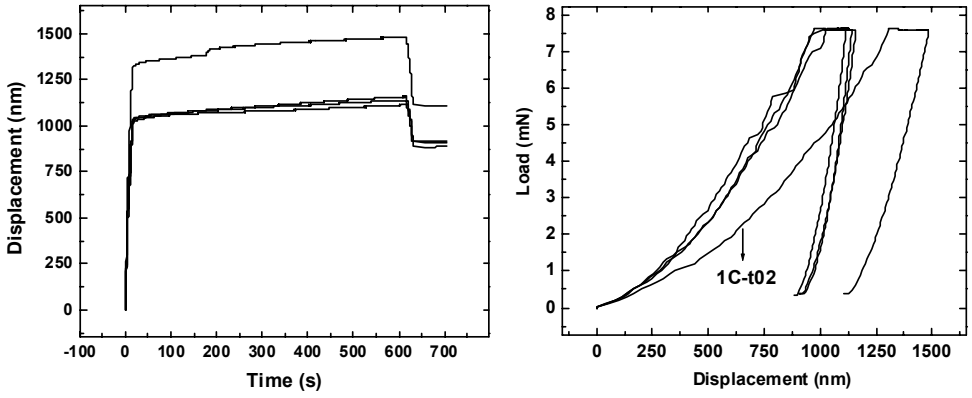

(a) **(b)**

Figure 10. Pyrazine-2-carboxamide, Form *δ*, sample **1C**. (a) Displacement–time, and (b) load-displacement curves, obtained at an estimated depth of 1000 nm with a peak hold time of 600 s from four different indentations on sample **1C**. Load control method (see Table 2).

The experiments on Form α (bending) were done on the bending face (100) along which molecules are arranged in a zigzag fashion (Figure 2b) and hence this face is expected to be hard compared to the other faces. Experiments on the other faces were difficult to perform due to the roughness of those faces. The indentation experiments on Form δ (limited ductility) were carried out perpendicular to the (100) face of the crystal along which molecular layers are present with a small slant. The packing along the indentation direction for the two crystal forms is not very different, and hence the hardness of the crystals is nearly the same. In this study, the indentations were made on only the (100) faces of both Form **1**α and Form **1**δ. The mechanical behaviour of the other two pairs of faces was not assessed, as that requires a large number of indentations to be made and analyzed and that is a time consuming process. Therefore, machine availability determined the number of experiments that could be performed.

4.7.2 2-(Methylthio)nicotinic Acid, 2

Indentations on 2-(methylthio)nicotinic acid samples, **2A** (one test) and **2B** (two tests) were made in the depth control method using the CSM mode. The indentations were made on these crystals with the tip approaching the (010) face, i.e. the bending face of the crystal was at 90º to the indenter, with a velocity of 10 nm s^{-1}. Figure 11 illustrates the indentation direction as well as crystal packing.

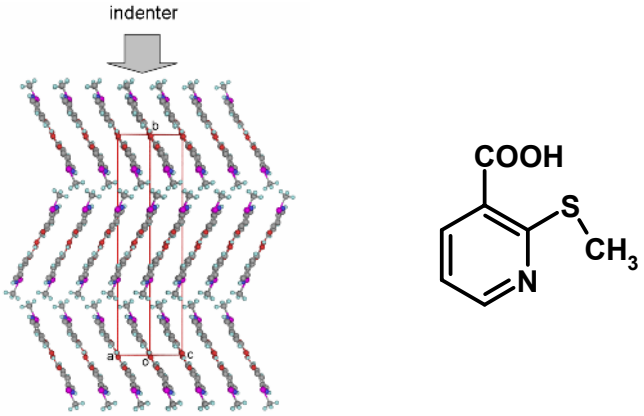

Figure 11. 2-(Methylthio)nicotinic acid, **2**. Packing diagram view down [101] shows the arrangement of molecules and the arrow shows the direction of indenter penetration through the (010) face of the crystal.

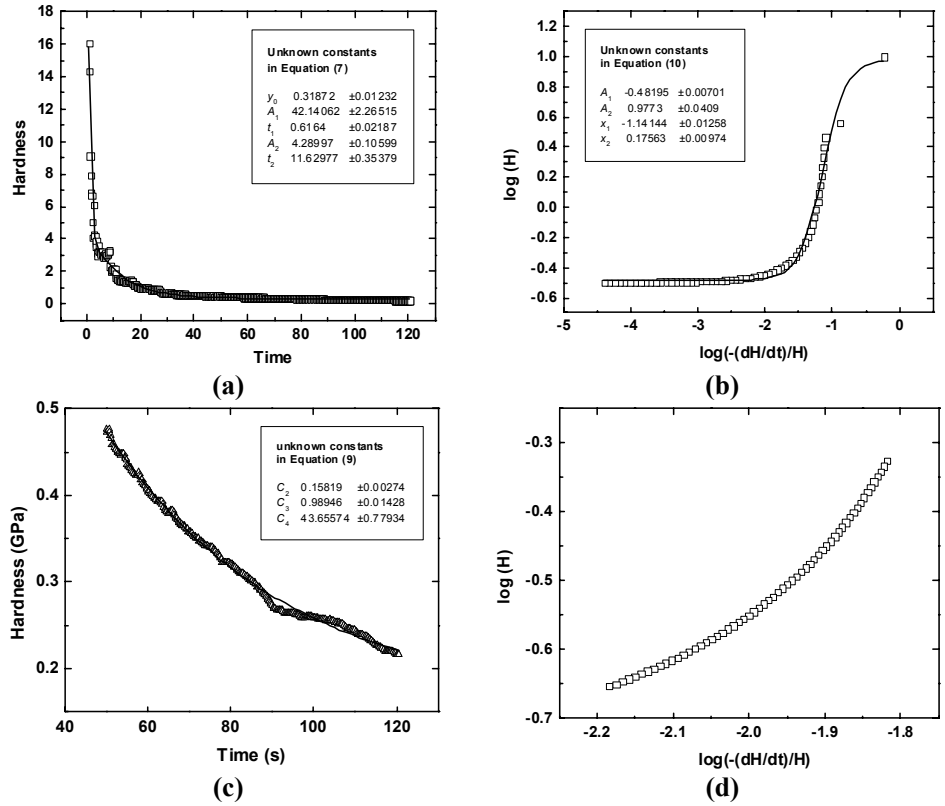

Figure 12. 2-(Methylthio)nicotinic acid, **2**. Hardness (H) – time (t) of load application relationship from (a) full set of data, and (c) near-steady state portion data obtained from crystals of **2B** (**test 02**) using the CSM mode. Symbols represent experimental points. Full curves (continuous line) in (a) and (c) are predictions based on Equations (7) and (9) respectively. (b) And (d) show log H – $\log\left[-\left(\dot{H}/H\right)\right]$ plots (symbols) derived from the curves presented in (a) and (c) respectively. Full curve (continuous line) in (b) is a prediction based on Equation (10).

In these crystals, the near-steady state was reached very rapidly after the initial linear portion as can be seen from the hardness-time or the displacement-time curves (Figures 12a and 13a). The measured average hardness value from the unloading curves was slightly lower for these crystals (~ 0.20 GPa) than for sample **1** (~ 0.29 GPa). The overall mechanical deformation and creep behaviour of these crystals was similar to that of sample **1** (Figures 4 and 5) and the full set of data could be fitted by Equations (7) and

(10) (Figures 12a, b). The hardness-time curve reaches a near-steady state approximately after 50 s of the commencement of the experiment, i.e. at a depth of about 125 nm of indenter penetration. This portion of the curve is fitted well by Equations (8) and (9), and only the latter one is depicted (see Figure 11c, 11d).

The creep behaviour is evident from the positive slope in the displacement-time curves present in the indentations made to different indenter penetration depths and different hold times using the depth control mode available on the nanoindenter (Figure 13). Nine indentations were successfully made with the maximum penetration depths ranging from 450 nm to 950 nm. The hardness values and the corresponding experimental details for samples **2A** and **2B** are given in Table 3. The appearance of the positive slope in the displacement-time curves at constant load and displacement at constant load, as function of time are evidence for creep (Figure 13).

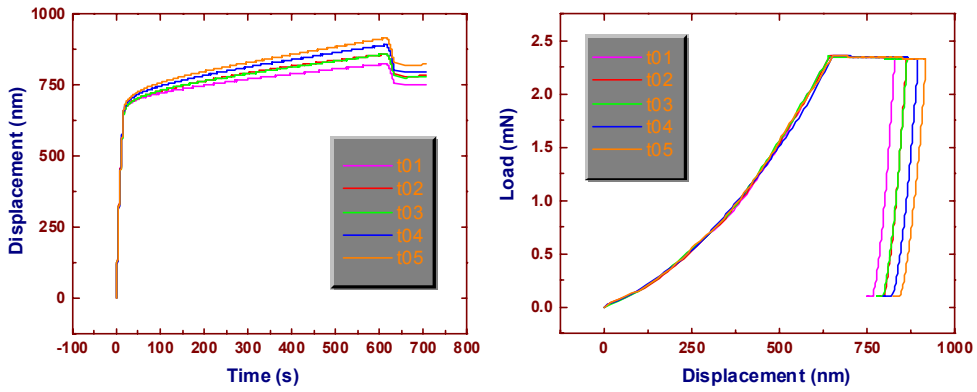

Figure 13. 2-(Methylthio)nicotinic acid. (a) Displacement–time and (b) the corresponding load–displacement curves obtained by load control method on sample **2B** (see **2B-t01** to **2B-t05** in Table 3b).

In the indentations produced in tests **2B-t01** to **2B-t05** (Table 3b), the indenter penetration depths practically fall on the same curve for all specimens in the loading part of the curve. Difference in *h* develops during the hold period (see Figure 13b), i.e. the creep resistance differs in different parts of the same sample. As a result, the *E* and *H*

values are different as they are measured from the peak unload at h_{Max}. Further work is necessary to understand this intriguing result, although location-dependent density gradient below 650 nm depth is a possible explanation. In the absence of a detailed study, other possibility cannot be ruled out.

Table 3. 2-(Methylthio)nicotinic acid. The nanoindentation data obtained on samples **2A** and **2B**

(a) with the depth limit of 1000 nm by depth control method using the CSM mode

Sample Code – Test No.	E_{Ave} (GPa)	H_{Ave} (GPa)	*E* from Unload (GPa)	*H* from Unload (GPa)
2A–t01	6.449	0.344	5.453	0.204
2B–t01	15.173	0.432	12.201	0.194
2B–t02	15.517	0.459	12.584	0.212

(b) with estimated depth limit of 650 nm and 600 s hold time by load control method

Sample Code – Test No.	*E* at P_{Max} (GPa)	*H* at P_{Max} (GPa)	Displacement (*h*) at P_{Max} (nm)	P_{Max} (mN)
2A-t01	5.473 (±0.15)	0.167(±0.17)	749.438(5.634)	1.968(±5.64)
2A-t02	5.683 (±0.15)	0.17 (±0.17)	741.47 (±5.63)	1.97 (±5.64)
2B-t01	10.683 (±3.76)	0.148 (±0.08)	827.063(±131)	2.331(±0.01)
2B-t02	10.018 (±3.76)	0.136 (±0.08)	860.577(±131)	2.322(±0.01)
2B-t03	9.218 (±3.76)	0.137 (±0.08)	861.889(±131)	2.316(±0.01)
2B-t04	8.757 (±3.76)	0.128 (±0.08)	893.348(±131)	2.332(±0.01)
2B-t05	8.723 (±3.76)	0.12 (±0.08)	917.055 (±131)	2.316(±0.01)

4.7.3 Hexachlorobenzene, 3 and Hexabromobenzene, 4

The nanoindentation tests on hexachlorobenzene, **3** and hexabromobenzene, **4** were made on the bending faces (001) of the crystals (Figure 14). These results on the isostructural compounds (Chapter 3) are interesting because the internal packing along the indentation direction is similar, while the strength of the Cl···Cl and Br···Br intermolecular interactions in the two compounds are different. The differences in the mechanical properties of these two compounds can be correlated directly to the Cl···Cl and the Br···Br interactions. Two types of tests were done on the bending face, i.e. (001),

of these crystals: tests in (1) the depth control (CSM), and (2) the load control modes. The crystal packing diagrams in Figure 14 show the direction of indenter penetration into the crystal.

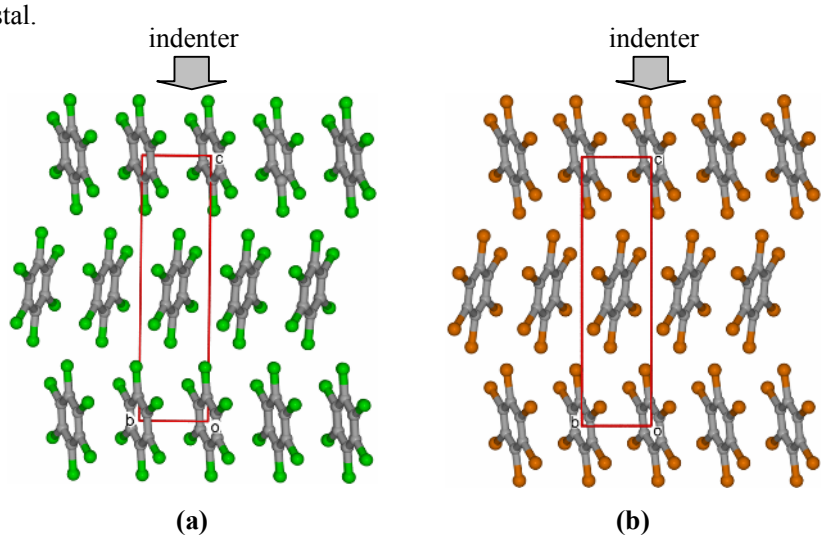

Figure 14. Packing diagram, a view along [100], in (a) hexachlorobenzene, **3**, (b) hexabromobenzene, **4**. The arrow mark indicates the indentation direction on the bending face (001) of the crystals.

The nanoindentation results obtained from these samples are given in Table 4. It is interesting to note that the hardness values obtained in the CSM mode for sample **3** (average H_{Unl} ~ 0.22 GPa) is clearly less than that of sample **4** (average H_{Unl} ~ 0.31 GPa). This difference in H_{Unl} accounts for the stronger Br···Br interactions in **4** compared with the weaker Cl···Cl interactions in sample **3**. The mechanical deformation and creep behaviour of these samples are similar to that of sample **1**. Equations (7) and (10) fit the hardness-time (Figures 15a and 15c) and the log H – log $(-(\dot{H}/H))$ (Figures 15b and 15d) curves well. In case of the two samples **3** and **4** also the H–t curve reaches a steady state nearly at around 100-120 nm depth and the set of data is fitted well by Equations (8) and (9), as in the case of samples **1** and **2**. Therefore, those figures are not shown here.

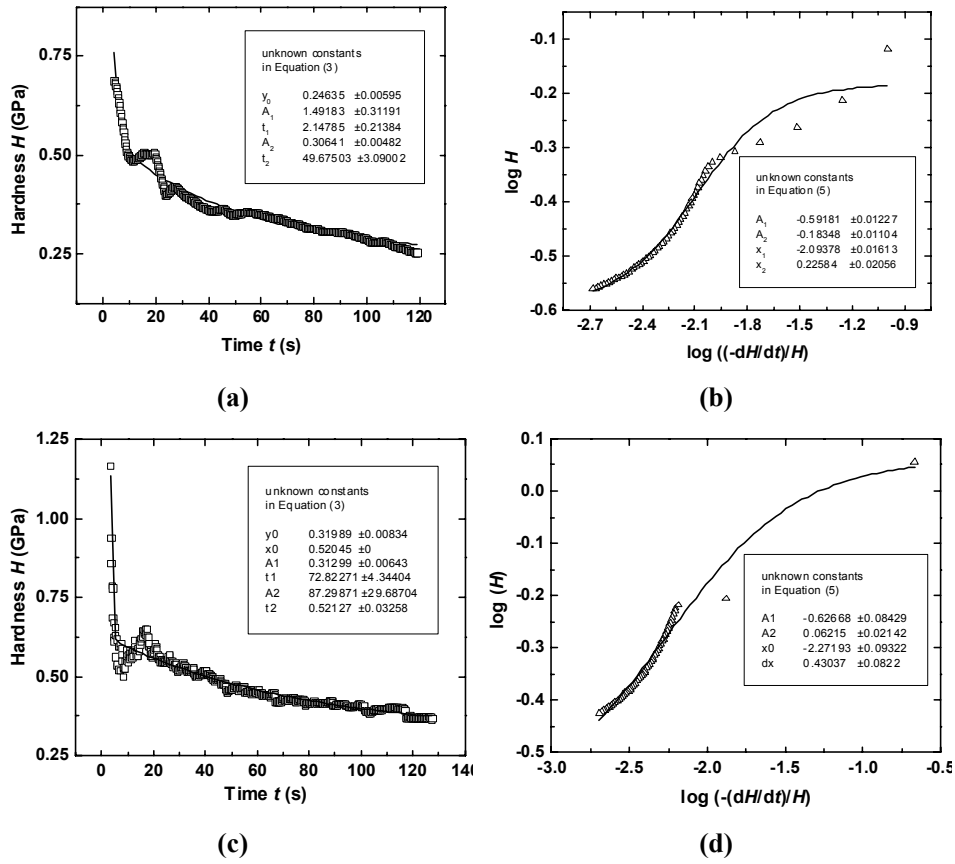

Figure 15. (a) and (c) show hardness (H) – time (t) relationships obtained from nanoindentations on crystals of **3A** (**test 01**) and **4A** (**test 02**) respectively using the CSM mode. Symbols represent experimental points. Full curves are predictions based on Equation (7). (b) and (d) are log H – $\log\left[-\left(\dot{H}/H\right)\right]$ plots (symbols) derived from (a) and (c) respectively. Full curve is a prediction based on Equation (10).

Table 4. The experimental data obtained from indentations on hexachlorobenzene, **3** (samples **3A**, **3B**), and hexabromobenzene, **4** (samples **4A**, **4B**)

(a) with maximum depth limit of 1000nm by depth control method using CSM module

Sample Code – Test No.	E_{Ave} (GPa)	H_{Ave} (GPa)	E_{Unl} (GPa)	H_{Unl} (GPa)
3A-t01	8.603 (±0.44)	±0.35 (0.02)	7.569(±1.49)	0.226(±0.02)
3A-t02	7.979 (±0.44)	±0.327 (0.02)	5.455(±1.49)	0.199(±0.02)
3B-t01	8.624	±0.353	7.927	0.246
4A-t01	12.226	±0.44	11.907	0.33
4A-t02	11.921	±0.44	11.907	0.33
4B-t01	12.596 (±1.01)	±0.332(0.04)	12.765(±0.44)	0.274(±0.01)
4B-t02	14.031 (±1.01)	±0.39(0.04)	13.388(±0.44)	0.291(±0.01)

(b) with maximum estimated depth of 650 nm with 600 s hold period by load control method

Sample Code – Test No.	E at P_{Max} (GPa)	H at P_{Max} (GPa)	Displacement (h) at P_{Max} (nm)	P_{Max} (mN)
3A-t01	7.569	0.193	731.321	2.841
3B-t02	7.428 (±0.01)	0.174	806.422 (±6.47)	2.726(±0.01)
3B-t01	7.416 (±0.01)	0.178	797.262 (±6.47)	2.716(±0.01)
4A-t01	12.233(±0.08)	0.299(±0.01)	717.4 (±7.2)	3.735
4A-t02	12.344(±0.08)	0.308(±0.01)	707.202 (±7.2)	3.735
4B-t01	13.054(±0.85)	0.246(±0.02)	724.689(±37.22)	3.225(±0.01)
4B-t02	11.357(±0.85)	0.21(±0.02)	789.515(±37.22)	3.243(±0.01)
4B-t03	12.18(±0.85)	0.248(±0.02)	725.399(±37.22)	3.236(±0.01)

4.7.4 1,3,5-Tribromobenzene, 5

The nanoindentation experiments on 1,3,5-tribromobenzene, **5**, were done on the (100) and (010) faces of the crystal. Figure 16a is a view of the crystal packing along [100], i.e. the longitudinal axis of the (needle shaped) crystal. The crystal packing along the indentation direction, i.e. a view down perpendicular to the (100) and (010) faces are

shown in Figures 16b and 16c respectively. In the nanoindentation experiments on these samples, both the hardness measurement and the creep tests were done by the depth control method using the CSM mode and a hold time of 600 s. The average hardness value from unload on the (100) face was 0.0588 GPa, while on the (010) face it was 0.0606 GPa, a difference of just 3.06 % (Table 5). Thus the difference in the hardness values of both the faces of the crystal is small and is less than the average error associated with the hardness value, 0.0157 GPa (given in brackets for each *H* value). So the *H* value for the two faces is similar. This is not surprising. Although the arrangement of the molecules along the [100] and [010] are different (Figures 16b, 16c), the intermolecular interactions (Br···Br and C−H···Br) in both the directions are comparable.

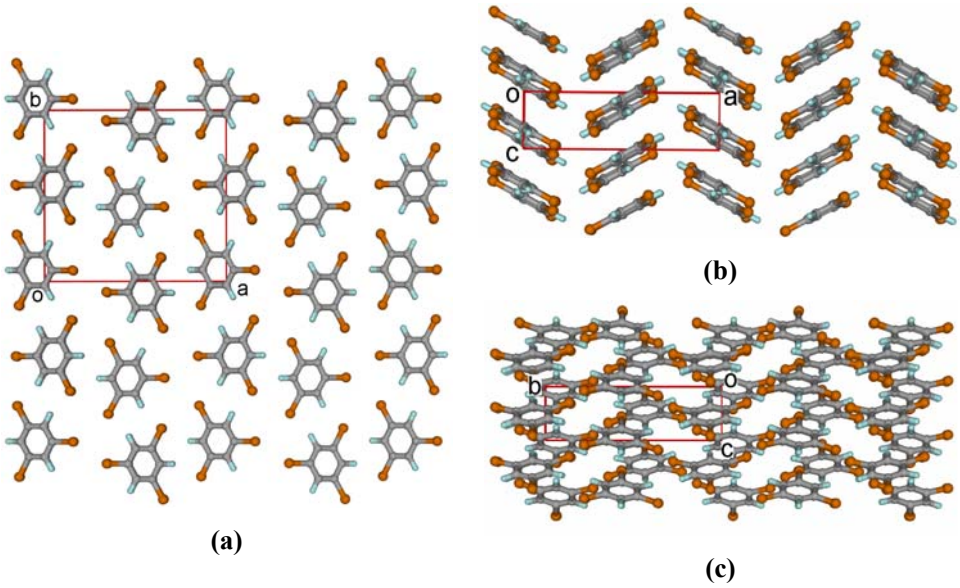

Figure 16. 1,3,5-Tribromobenzene, **5**. Crystal packing view along (a) [001], (b) [010] and (c) [100].

The indentation data for sample **5** are scattered (see Table 5), which was not because of lack of proper contact between the indenter and sample **5** in the initial stage of load application. In fact, the increase in displacement, *h*, was not similar throughout the experiment. This complex deformation process is evident from the *P*–*h* and *H*–*t*

curves in Figures 17a and 17b. Although there is pop-in in some of the *P–h* curves, the pop-in appears to be smooth or broad which suggests that the crystal did not break. The scatter therefore, may be due to an inhomogeneous distribution of imperfections in different locations of the crystal.

Table 5. The nanoindentation data obtained on 1,3,5-tribromobenzene, **5**, by depth control method (h_{Max} = 650 nm) using the CSM mode with 600 s hold time. The indentions on **5A**, **5B** correspond to the (100) face and **5C**, **5D**, **5E** to the (010) face.

Sample Code – Test No.	E_{Ave}	H_{Ave}	E_{Unl}	H_{Unl}
5A-t01	5.737(±1.29)	0.134(±0.08)	3.272(±1.54)	0.030(±0.04)
5A-t02*	8.203(±1.29)	0.28(±0.08)	6.117(±1.54)	0.080(±0.04)
5A-t03*	6.306(±1.29)	0.166(±0.08)	5.737(±1.54)	0.101(±0.04)
5B-t01	6.822(±2.65)	0.232(±0.14)	4.885(±1.11)	0.055(±0.02)
5B-t02	3.075(±2.65)	0.037(±0.14)	3.315(±1.11)	0.028(±0.02)
5C-t01	10.152(±2.06)	0.411(±0.12)	6.525(±0.28)	0.103(±0.01)
5C-t02	7.243(±2.06)	0.241(±0.12)	6.133(±0.28)	0.095(±0.01)
5D-t01	6.924(±0.17)	0.251(±0.03)	4.786(±0.81)	0.044(±0.01)
5D-t02	7.237(±0.17)	0.217(±0.03)	6.267(±0.81)	0.067(±0.01)
5D-t03	7.206(±0.17)	0.205(±0.03)	6.109(±0.81)	0.071(±0.01)
5E-t01	4.572(±3.03)	0.066(±0.09)	5.026(±0.72)	0.033(±0.02)
5E-t02	6.177(±3.03)	0.206(±0.09)	5.413(±0.72)	0.062(±0.02)

***** The inconsistency in the *E* and *H* values, i.e. less *E* value for a greater *H* and vise-versa, for tests **5A-t02** and **5A-t03** is not tenable. But, when the error limits are taken into account, rationalization is possible.

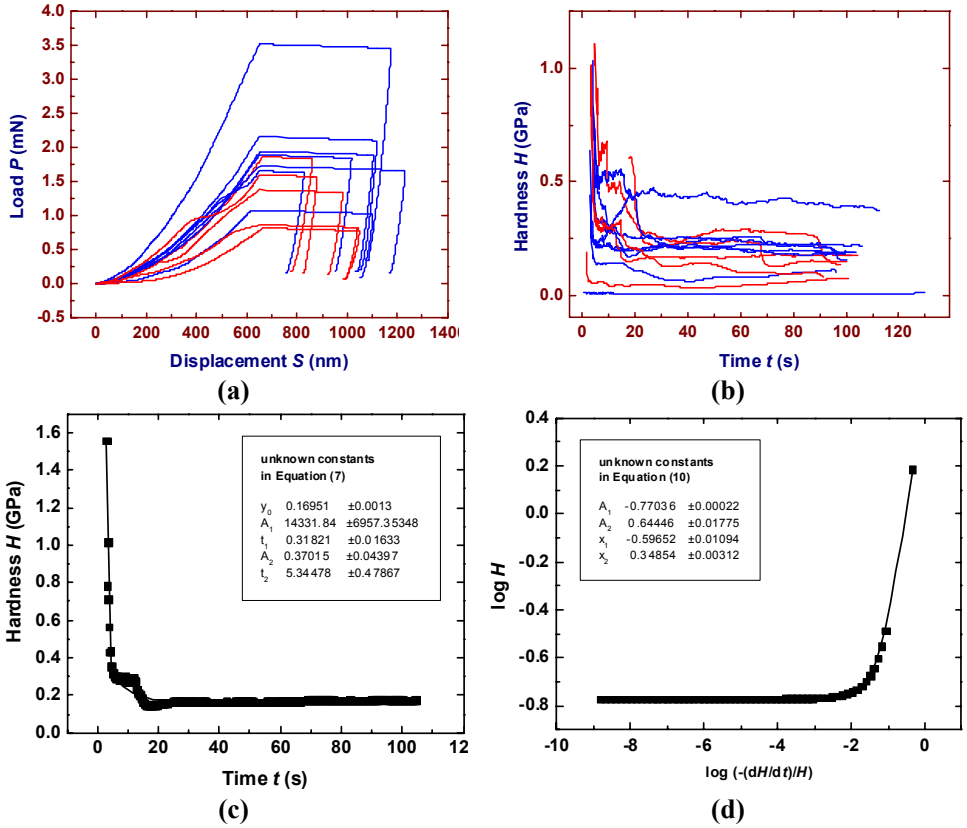

Figure 17. (a) Load-displacement curves from tests done on (100) (red) and (010) (blue) faces. (b) Hardness-time relationship obtained from test 2 on sample **5A** (**5A-t02**) by indentation on (100) face. (c) Hardness-time, and (d) $\log H - \log\left[-\left(\dot{H}/H\right)\right]$ relationship based on values presented in (c). Lines in (c) and (d) represent the predicted curves based on Equations (7) and (10) respectively and the symbols represent the experimental data.

The near-steady state portion of the *H-t* curves (starting around at 100-120 nm depth) was not smooth in most of the samples as can be seen from the curve in Figure 18a, which corresponds to the data from **5A-t01**. Therefore, Equations (8) and (9) were not useful. For **5B-t02** it was found that *H* increased slowly with the time after an indentation depth of 200 nm (i.e. after ~ 40 s) (Figure 18b) and the relationship could be fitted reasonably well by

$$H = A_3 + B_1 t + B_2 t^2 \qquad (12)$$

where A_3, B_1 and B_2 are unknown constants. This may be an indication of work hardening. The reason is unknown at this stage, particularly because another crystal of the same compound (Figure 18a) exhibited strain softening and creep effect. The H_{Ave} and H_{Unl} were found to be low in **5A-t01**, **5B-t02** and **5E-t01** compared to the other samples (see Table 5).

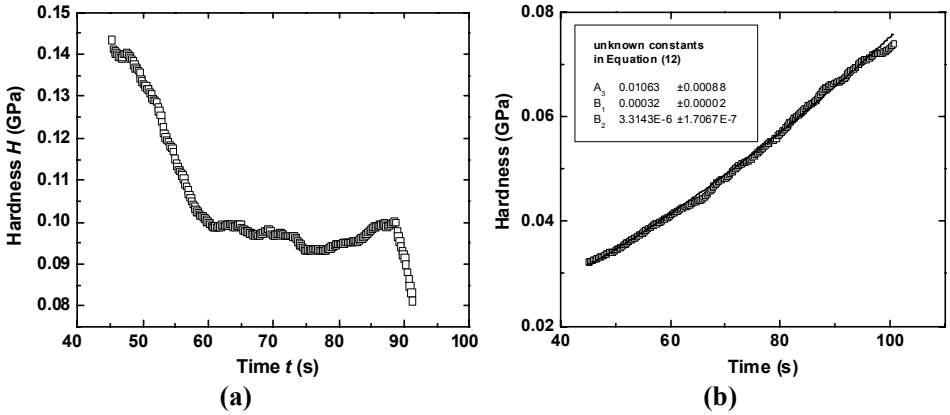

Figure 18. Hardness-time relationship after about 200 nm depth from the beginning of indentation on (a) sample 5A test 01 (**5A-t01**). Notice that this curve is not smooth; (b) sample **5B**, test 02 (**5B-t02**). Symbols represent the experimental data and the continuous curve in (b) is a prediction based on Equation (12).

4.7.5 Molecular Complex: 135B246I:135I246M, 6

135B246I:135I246M, **6**, is a molecular complex, which is obtained by dissolving the **135B246I** and **135I246M** compounds in a 1:1 ratio in tetrahydrofuron (THF) solvent and evaporating the solvent at ambient temperature. Crystal structure determination confirmed the 1:1 molecular complex **6**, in which the molecules are disordered statistically with approximately 50% occupancy. But it is always very difficult (or even impossible) to say from the X-ray data whether the molecular distribution in the crystals is homogeneous or heterogeneous. This aspect may be examined by nanoindentation experiments.

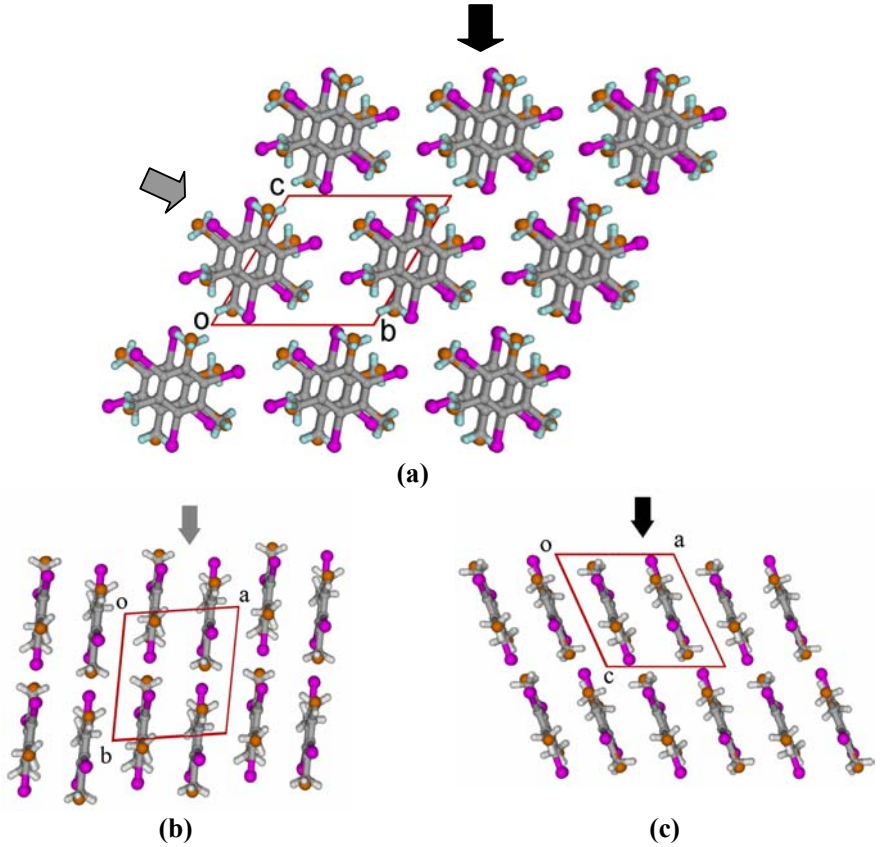

Figure 19. 135B246I:135I246M, 6. (a) Crystal packing view along [100]. The arrows indicate the indentation direction onto (or perpendicular to) the (001) (black) and (010) (grey) crystal faces respectively. (b) and (c) show the slight slant of the layers and the direction of indentation into the crystal.

Crystals of sample **6** are needle-shaped and the molecules form layers *via* I_3-synthons (Section 5.4.2). These layers are stacked along the crystal length, i.e. [100]. The (010) and (001) faces of the crystals are perpendicular to the crystal length and the indentations were made perpendicular to these faces (Figure 19). The layers are slightly slanted when viewed perpendicular to the (010) and the (001) faces. This means that the indenter penetration direction is not exactly parallel to the layers in the crystal as seen in Figure 19a. Although the two faces (010) and (001) are crystallographically different, the crystal packing is similar when viewed perpendicular to these faces (Figure 19b and 19c).

The deformation behaviour of these crystals was found to be different for different indentations made at different locations of the same sample (Figure 20). Two different types of hardness-time relations were found in this sample. In first case, hardness decreases initially from ~ 1.6 GPa to reach a steady state with a hardness in the range of ~0.60 – 0.23 GPa (Figure 20c), which is analogous to that of samples **1** to **5** and predictions could be made using Equations (7) and (10). In the second case, the hardness increased from ~ 0.05 GPa to ~ 0.23 GPa and reached a near-steady state (Figures 20a and 20b) which is in contrast with the observations made on samples **1** to **5**. The second case appears to be complicated, because the two *H-t* curves in Figures 20a and 20b follow two different paths to reach a near-steady state portion where absolute values are also different. The differing mechanical behaviour of these crystals at different locations indicates the complex mechanical deformation behaviour in this molecular complex **6**. The crystal packing in sample **6** is layered and is different from that of samples **1** to **5**. It is difficult to give a particular reason for the variation in the mechanical behaviour, because there are many variables in this case, say slanted layers in the crystal with respect to the front side corner of the pyramidal tip, differing local distribution of the two components/compounds and defect density. If the tip of the pyramidal indenter is along the direction of slant of the layers in the crystal (Figure 19), the initial hardness would be low and then slowly increase as the indenter penetrates into the sample. If the tip of the indenter and the slant of the crystal plane are directed in opposite direction, the initial hardness would be more and then slowly decrease as the indenter proceeds. But, the orientation of the slant of the layers with respect to the tip could not be taken into account while making the indentation and hence it is not possible to explain the effect. The other possibility for the variation in the deformation resistance at different locations is the heterogeneous distribution of the two compounds, **135B246I** and **135I246M**, in the crystals of solid solution **6**. Although the mechanical behaviour (hardness values) of the parent compounds was not determined because of non-availability of the machine, it may be noted that the deformation seen in **6A-t01** (Figure 20a) is possible when the softer component is present in the top portion of the crystal and the harder one below. In this case, the indenter has to penetrate into the softer part of the crystal first and then the

harder one, and hence the work hardening behaviour could be observed. If the harder component were present at the on top and the softer compound below, the material would show strain softening and appears as seen in Figure 20c. It is likely that the reason for the variation in the mechanical behaviour is the heterogeneous distribution of the two compounds in the crystal. Since the crystal packing is similar on the two faces (010) and (001) of **6**, they also have similar hardness values, as revealed by the nanoindentation measurements (Table 6).

Hardness – time relationship in these samples does not follow Equation (7) but agrees with Equations (12) and (13) (Figure 20).

$$H = \frac{a_1}{a_1 - a_2}\left(e^{-a_2 t} - e^{-a_1 t}\right) \qquad (13)$$

where a_1 and a_2 are unknown constants. The near-steady state portion in Figure 16c could be fitted by both Equations (8) and (9), and the deformation process appears to be similar to that of sample **1**.

Although the hardness values obtained from the unloading curves were similar for all the tests except **6D-t01**, the initial hardness-time relationship was not similar due to the possible reasons discussed above (Figure 20). This indicates that the distribution of the molecules **135B246I** and **135I246M** could be in domains of differing composition in the crystal. If the domains are large enough (>100 nm), then it may be possible to differentiate the domains by nanoindentation. So in a heterogeneous distribution, the different molecular domains display a difference in the deformation process during nanoindentation. To verify this idea, the deformation of the parent single component crystals of **135B246I** and **135I246M** needs to be examined and the results combined in different ways to generate the distinctly different hardness-time curves obtained.

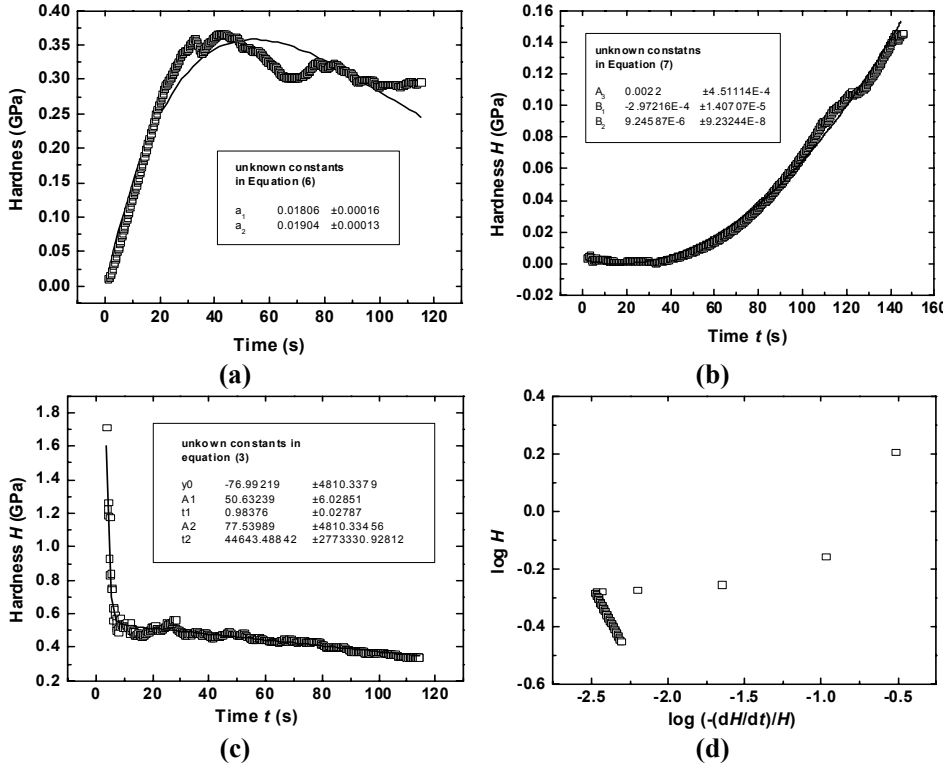

Figure 20. Hardness-time relationship in (a) sample **6A** test-01 (**6A-t01**) (b) sample **6C** test-02 (**6C-t02**) and, (c) sample **6B** test-01 (**6B-t01**). (d) log H – log$\left[-\left(\dot{H}/H\right)\right]$ plot derived from curve that presented in (c). Symbols represent experimental points. Full curve in (a), (b) and (c) are predictions based on Equations (13), (12) and (7) respectively.

Another possible reason for the variation in the $H - t$ curves may be due to the differences in the orientation of the layers with respect to the pyramid shaped diamond tip. (This is likely to be a less significant contribution than the reason advanced in the preceding paragraph). As the layer arrangement is not completely parallel to the indenter penetration direction, the initial hardness is expected to change depending on the orientation of the layers with respect to the direction of movement of the pyramid shaped indenter. Although the projection of the layers towards the indenter is nearly identical for a particular sample, variations are still observed in the $H - t$ curves. That perhaps indicates heterogeneous distribution of the component/compounds in the molecular solid

solution. Presence of small pop-ins in the load – displacement curves in these crystals indicates the disruption of layers at the molecular level. This is also evident from the discontinuity in the hardness – time curves (Figure 20a to 20c). The load – displacement curves of **6D-t01** in Figure 21 reveal the unusual deformation behaviour of these layered molecular crystals. But, in the curve **6C-t03** the initial large displacement at near-zero load is an artefact.

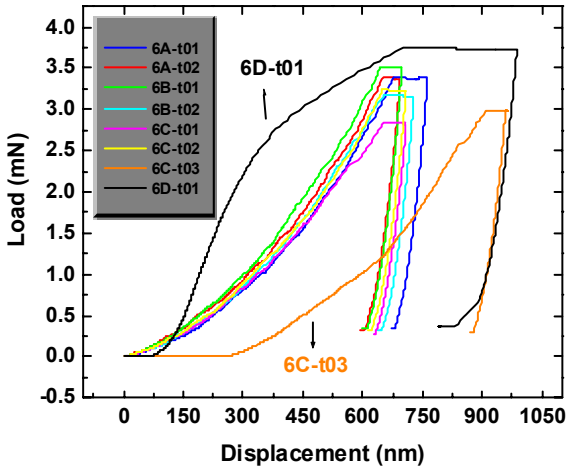

Figure 21. Load – displacement curves for the tests recorded on samples **6A** and **6B** on the (010) face and **6C**, **6D** into the (001) face. Test codes for the unusual curves are indicated in Table 6.

Table 6. Nanoindentation data obtained on **135B246I:135I246M**, **6** by the depth control method using the CSM mode. The indentations on **6A**, **6B** correspond to the (010) face and the ones on **6C**, **6D** to (001) face.

Sample Code – Test No.	E_{Ave}	H_{Ave}	E_{Unl}	H_{Unl}
6A-t01	12.895(±1.42)	0.318(±0.09)	12.185(±1.28)	0.235(±0.03)
6A-t02	14.909(±1.42)	0.452(±0.09)	14.003(±1.28)	0.282(±0.03)
6B-t01	14.852(±1.31)	0.440(±0.06)	14.602(±1.37)	0.289(±0.03)
6B-t02	13.044(±1.31)	0.357(±0.06)	12.661(±1.37)	0.239(±0.03)
6C-t01	12.859(±1.34)	0.368(±0.02)	12.145(±1.17)	0.224(±0.06)
6C-t02	13.278(±1.34)	0.388(±0.02)	12.709(±1.17)	0.259(±0.06)
6C-t03	0.367	0.001	8.699	0.131
6D-t01	27.315	0.498	9.43	0.158

4.8 Conclusions

Nanoindentation experiments on molecular crystals have been carried out for the first time. Experiments on bending (molecular crystals **1** to **5**) and shearing (molecular complex **6**) crystals revealed that the mechanical behaviour largely depends on the packing of molecules in the crystals. The crystals show near-exhaustion creep behaviour at room temperature on nanoindentation, which has been accounted for quantitatively in phenomenological terms. In these experiments it was tried to measure the difference in the mechanical properties of different faces of the crystals as was done in Section 3.3.8, but it was not successful due to the large experimental error. This is traceable to the poor quality of the surfaces of the crystals in this chapter. Polymorphic crystals of sample **1** are interesting because there was no pop-in or discontinuity in the $P - h$ curves of the bending crystals (Form **1**α). Pop-in is significant in the brittle crystals (Form **1**δ), and is an indication of molecular level cracking in the crystal. Characterization of such differences in the mechanical properties of polymorphic crystals is very advantageous, particularly for pharmaceutical formulation. In sample **3**, the $P - h$ curves are very smooth, which indicates that the crystals have high ductility. Indentation data from the isostructural samples **3** and **4** give a good estimate of the difference in the strength of the Cl···Cl and the Br···Br intermolecular interactions. Differences in the mechanical properties of these two compounds reveal the relative weakness of the Cl···Cl interactions compared with the stronger Br···Br interactions. The nanoindentation data on sample **5** are very scattered and indicate the presence of imperfections in the crystals. The results from the crystals of the molecular complex **6** (layered structure) are interesting, because the $H - t$ curves indicate the possibility of heterogeneous distribution of the two components, **135B246I** and **135I246M**, i.e. the **135B246I** and **135I246M** molecules occupy separate domains in the crystal. These results clearly demonstrate the advantages in measuring the mechanical properties of molecular crystals at this nm level with the aid of a nanoindenter.

The present state of development in the understanding of creep in molecular crystals is similar to the state of affairs that prevailed in the early days of experiments on creep in metallic materials [1.19]at the beginning of the last century, when useful

empirical equations to describe creep flow were developed. Detailed mechanistic models based on the dislocation theory assigned the earlier observations physical meaning at a later stage.

In general, creep deformation in metals is explained in terms of dislocation movement, diffusion and grain boundary sliding. It may be noted that in the deformation of molecular crystals by indentation, the molecules behave like atoms in metals and generally do not undergo any change in their chemical composition and the arrangement of covalent bonds. That is, only the intermolecular bonds are broken and rearranged by the deformation process, while the chemical bonds between the atoms within a molecule remain intact. But it is not possible to state unequivocally at this stage whether every individual molecule or a small group of molecules, say molecular aggregates, move around during deformation. It is possible that both types of motions are present at the same time. From the present experiments, it is also clear that the deformation of molecular crystals depends on the directionality of the intermolecular interactions and the crystal packing. It is more than likely that molecular movement during deformation is influenced by the anisotropy of the intermolecular interactions present along the three directions of crystal packing.

Further studies in greater depth are necessary to acquire a more accurate and detailed understanding of the mechanical properties of molecular crystals. The use of techniques like TEM, SEM, STEM and AFM will definitely help in the detailed characterization of the deformation process.

4.9 Experimental

Crystallization

Crystallization of the samples was done by dissolving the material in hot organic solvents like carbon tetrachloride (CCl_4), tetrahydrofuran (THF), ethyl acetate (EtOAc) or 1,4-dioxane followed by slow evaporation of the solvent at ambient temperature. The single crystals were obtained from the solution within a week and the crystals taken from the mother liquor were blotted dry on a filter paper.

Sample Preparation

Single crystals, with well grown smooth faces, were selected from the bulk samples for the nanoindentation experiments by viewing the crystals under a microscope to avoid samples with unwanted crystal imperfections. The dimensions of the selected crystals were approximately 0.2 to 0.5 mm thickness and 1 to 2 mm length. Araldite glue was spread (approximately to the crystal size) as a thin layer on a flat surface of an Al-sample holder and the selected crystal was slowly moved on to the glue with a metal needle and forceps. The crystal was then carefully adjusted on the glue to make sure that its top horizontal face was parallel to the surface of the sample holder. The fixing process of each crystal was finished before the glue got dry, i.e. within five to six minutes. Three to four crystals were fixed at different positions of a sample holder. The sample holders were carefully fixed on the X-Y motorized tray by adjusting the screws.

Nanoindentation

Nanoindentation experiments were done using a nanoindenter model XP, supplied by MTS Systems Corporation, USA. The diamond indenter had a Berkovich three-sided pyramidal geometry. Test positions were targeted using an optical imaging system with a 250X display. All the experiments were carried out at room temperature using either the load control mode or the depth control method. Poison's ratio was fed as 0.33 as input in these experiments, as the actual values for the crystals studied were not known. Indenter velocity was 10 nm s^{-1}.

CHAPTER 5

HALOGEN···HALOGEN INTERACTIONS IN HEXAHALOGENATED BENZENES

5.1 Introduction

Kitaigorodskii suggested in 1955 in "*The theory of close-packing of molecules*" [5.1], that organic molecules in crystals tend to close pack to fill spaces as tightly as possible. Accordingly, for a given molecule, the actual crystal structure is the one that corresponds to the most densely packed arrangement of all possible structures. The close-packing principle considers all organic molecules as spheres with characteristic atomic radii (geometrical fit). This assumption leads to a simple model applicable to a wide range of molecular crystals. In course of time, many exceptions to the model were found and the importance of intermolecular interactions in further understanding of the packing of molecular crystals was realized (chemical factors) [1.2]. In other words, the recognition between molecules during crystallization is governed by geometrical or chemical factors, that is because of shape complementarity and size compatibility (short range repulsion) [5.1, 5.2], or specific anisotropic interactions of electrostatic or polarization origin (long range attraction) [5.3, 5.4]. In the process of minimization of total free energy, a balance between these geometrical and chemical factors needs to be reached, i.e. the final structure is the result of the minimization of the internal energy, the entropy term and electrostatic, polarization and van der Waals interactions. But the nature of this balance between geometrical and chemical factors is poorly understood. Halogen···halogen intermolecular interactions appear to be particularly problematic [1.2, 1.14a].

5.2 Halogen···Halogen Interactions

The weak intermolecular interactions between halogen atoms have been a subject of interest and debate for many years because of their complexity in geometrical and chemical terms [5.5, 1.2]. Two hypotheses have been proposed to explain the

halogen···halogen interactions (Scheme 1). One explanation is that the shape of the atomic charge densities of halogen atoms is spherical and specifically attractive which produces short contacts in certain directions [5.6]. This view has been strengthened by Desiraju [5.5g] and Williams [5.5f] and variously referred to as a "donor-acceptor", or "charge-transfer" interaction, or "electrophilic and nucleophilic attack". The alternative model is the anisotropic repulsion hypothesis [5.5h, d]. According to this, shorter X···X contacts are observed in certain directions due to the nonspherical shape of the atomic charge densities which produce a decreased repulsion between the atoms. Based on theoretical investigations, Price *et al.* [5.5d] argued that the Cl···Cl interactions are best explained by the latter hypothesis. They predicted that the most important contributions to the X···X intermolecular interactions are the repulsion, electrostatic and dispersion terms and that the contributions from charge-transfer type interactions is negligible. Although an increase in the intermolecular attraction or a reduction in the repulsion can both account for short van der Waals contacts in certain directions, the two are not equivalent and have different implications.

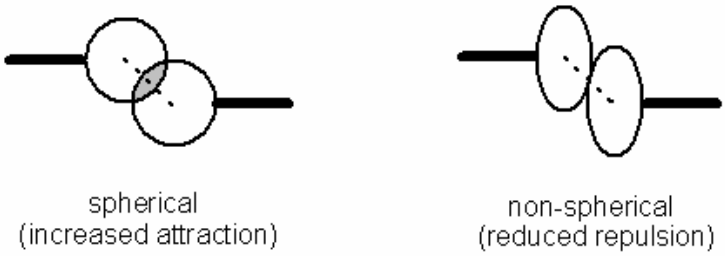

Scheme 1

According to the increased attraction force explanation, the C–X···X–C interactions (X = Cl, Br, I) are classified into two types based on the values of the two C–X···X angles, θ_1 and θ_2 [5.5i, 5.5e]. The type-I interactions ($\theta_1 \approx \theta_2$) represent close packing of X-atoms in a geometrical model because identical portions of the halogen atoms make the nearest approach. The type-II interactions ($\theta_1 \approx 180°$, $\theta_2 \approx 90°$) are understood based on the X-atom polarization, $X^{(\delta+)}\cdots X^{(\delta-)}$, and represent a chemical model with each halogen atom polarized positively in the polar region and negatively in the equatorial region (Scheme 2). Type-II interactions are included in a larger category

of $X^{(\delta+)}\cdots Y^{(\delta-)}$ "halogen bonds" in which electrophilic halogen is involved [5.7].

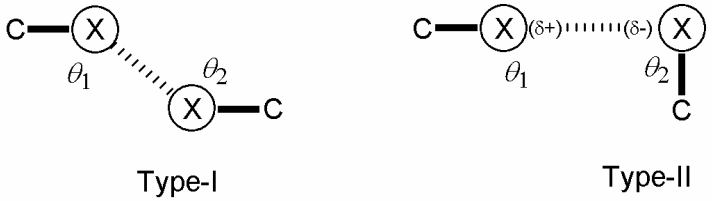

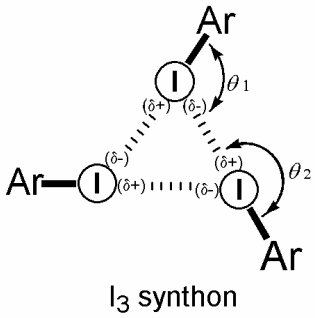

Scheme 2

One of the reasons for the difficulty in understanding the nature of X···X interactions arise from the fact that the halogens are of low to high electronegativity (I to F) and polarizability (F to I). They act, depending on the circumstances, as either electropositive or electronegative entities in an intermolecular interaction, or in some cases with no particular electrostatic character [5.8]. Iodine is somewhat easier to understand, in the context of halogen bonding, when compared to the other halogens because it is more readily polarized as $I^{(\delta+)}$. Accordingly, contacts such as I···Cl and I···Br may be represented as $I^{(\delta+)}\cdots Cl^{(\delta-)}$ and $I^{(\delta+)}\cdots Br^{(\delta-)}$ and they generally have the type-II geometry. Fluorine is very hard and non-polarisable, and it is still not really possible to deduce the nature of its interactions with other halogens [5.9]. Desiraju and co-workers have stated in their study that the F···F interaction is not really viable [5.10]. Perhaps the I···F interaction is polarization induced. Chlorine and bromine belong to an intermediate region and various workers analyzed them using one of the two models given above, and have attributed the observed geometries of X···X contacts to either a van der Waals (non-

spherical atoms) or polarization ($\delta^{+}\cdots\delta^{-}$) character of the interaction [5.5]. What is possible is that the type-I contacts formed by Cl and Br are of the van der Waals variety while the type-II contacts are polarization induced. If all contacts in a crystal were of the van der Waals type, one would expect a greater degree of isotropy in the packing—a Kitaigorodskii solid [5.1].

There are several reports on halogen interactions in the literature, and in some of the cases the discussion has been raised in the context of halogen···halogen interactions. Trihalomesitylene structures (**135X246M**, X = Cl, Br, I) [2.16] are isostructural with space group $P\bar{1}$ and Z = 2. In each structure, the molecules are arranged as layers of two-dimensional sheets which are formed *via* attractive trigonal X_3-synthons. Each halogen atom is part of the triangular X_3-synthons as shown in Figure 1.

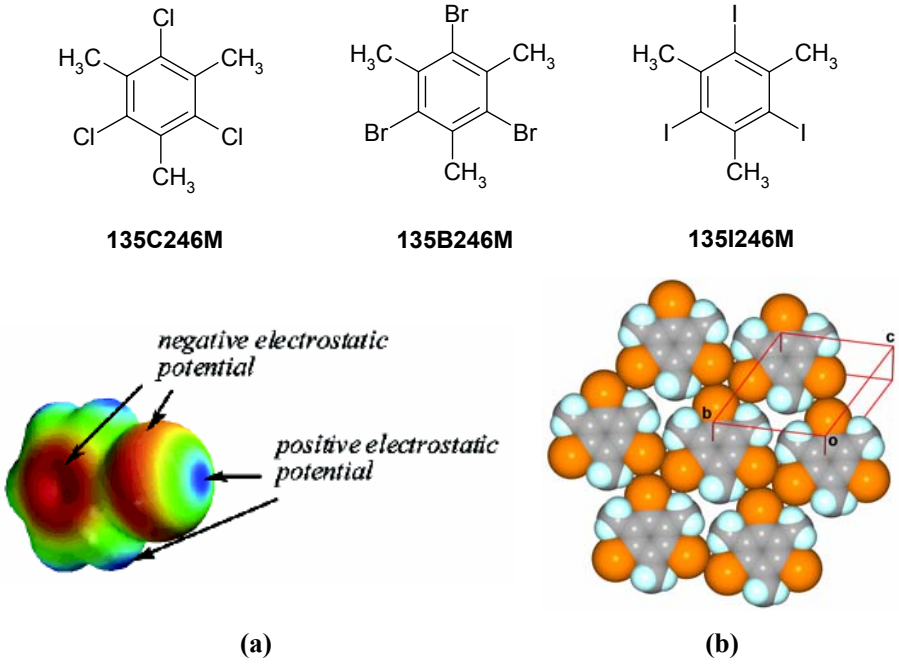

Figure 1. (a) Plot showing electrostatic potential in iodobenzene with maxima of negative and positive electrostatic potential indicated. This figure is reproduced from reference [2.16]. (b) Layer constituted of Br_3-synthons in **135B246M**.

Bosch *et al.* [2.16] analyzed the X_3-supramolecular synthons in their investigation on **135B246M**, **135I246M** and some other reported structures. Their

theoretical calculations on iodobenzene revealed the polarization of the iodo group in the molecule that supports the attractive donor-acceptor model (Figure 1). The nonspherical atomic charge distribution on the halogens results in the formation of donor-acceptor interactions in which each halogen atom is simultaneously a donor and an acceptor. In their investigation they strongly felt that the X···X interactions must be considered as being of the attractive donor-acceptor type as suggested by Desiraju and Williams [5.5g,f].

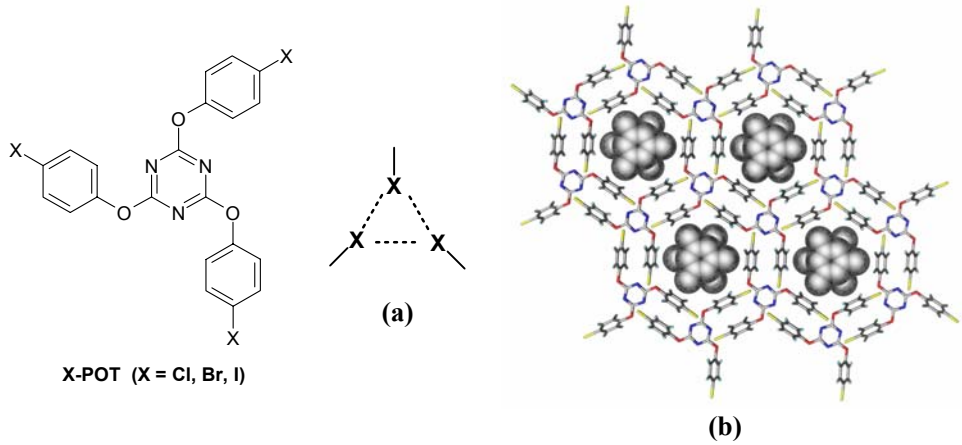

Figure 2. (a) Supramolecular X_3 synthon in the inclusion complexes of **X-POT**. (b) Hexagonal host framework formed through Br_3-synthons in the crystal structure of **Br-POT**•collidine. Disordered collidine molecules are shown in space filling model.

Nangia and co-workers [5.11] employed the halogen interactions for constructing hexagonal host frameworks in C_3 symmetric molecules, 2,4,6-tris(4-halophenoxy)-1,3,5-triazines (X-POT, X = Cl, Br, I)). The halogen groups on trigonal X-POT molecule, reproducibly self-assemble *via* the X···X trimer (X_3) synthon to form hexagonal cavities that include various aromatic guest molecules (Figure 2). The architectural isomerism from channel to cage framework and the persistent crystallization of trigonal X-POT molecule in high-symmetry host networks is exemplified in these host-guest complexes.

As the intermolecular contacts acquire some distinctiveness, anisotropy enters the crystal with a change in properties [1.2]. In a one-dimensional structure involving halogen atoms, molecules are held relatively strongly in this direction [5.12]. In a layered or two-dimensional crystal structure, the interactions within a layer (intralayer) are stronger and more directional than the interactions between layers (interlayer) [2.18]. Whether the layered structures arise on account of type-II halogen interactions or the ubiquitous π···π stacking interactions [5.13] is hard to say from the distance-angle criteria. However, there is a fundamental distinction between two-dimensional stacked (2D + 1D) and three-dimensional cross-linked (3D, Kitaigorodskii type) structures with respect to the nature of the intermolecular interactions. In general terms, the default packing for all organic molecular solids is the three-dimensional Kitaigorodskii packing. Therefore when a stacked structure is obtained, there must be specific reasons for its formation [1.2].

5.3 Halogen Bonding

Halogen bonding, D···X─Y, is the noncovalent interaction where X is the halogen atom (Lewis acid) and D is any electron donor (neutral or anionic Lewis bases) [5.7]. In general halogen bonds are formed between a halogen atom and more electronegative atoms like oxygen, nitrogen or sulfur. In recent years, Resnati and Pennington have extensively (and independently) used halogen bonding to engineer various crystal structures [5.7].

Resnati *et al.* [5.7c] used halogen bonding in the context of a co-crystal system to induce stereoselective photocyclization of olefins (Scheme 3). The pentaerythritol derivative, **I_4-PETol**, molecules (Scheme 3) co-crystallize with a dinitrogen spacer (reactant), *trans*-1,2-bis(4-pyridyl)ethylene (4,4'-bpe), in 1:2 ratio. The **I_4-PETol** behaves as a tetratopic halogen-bonding donor, while the dinitrogen spacer is ditopic acceptor. In this molecular complex, **I_4-PETol** molecules are connected to spacers through C─I···N halogen bonds (Scheme 3). The tetrafluorophenyl rings of **I_4-PETol** lying on the same side pair up in a quasi-parallel fashion due to face-to-face $\pi\cdots\pi$ intramolecular

interactions [5.7a] (distances ranging from 3.524 to 3.897 Å; cutoff distance is 3.915 Å). As a result, the double bonds of the spacers come closer into the allowable distance range for photochemical reactivity. These crystals on photoirradiation at 300 nm undergo a photochemical cycloaddition under topochemical control to produce tetrakis(4-pyridyl)cyclobutane. These experiments prove the robustness of halogen bonding in the use of solid state templated reactions.

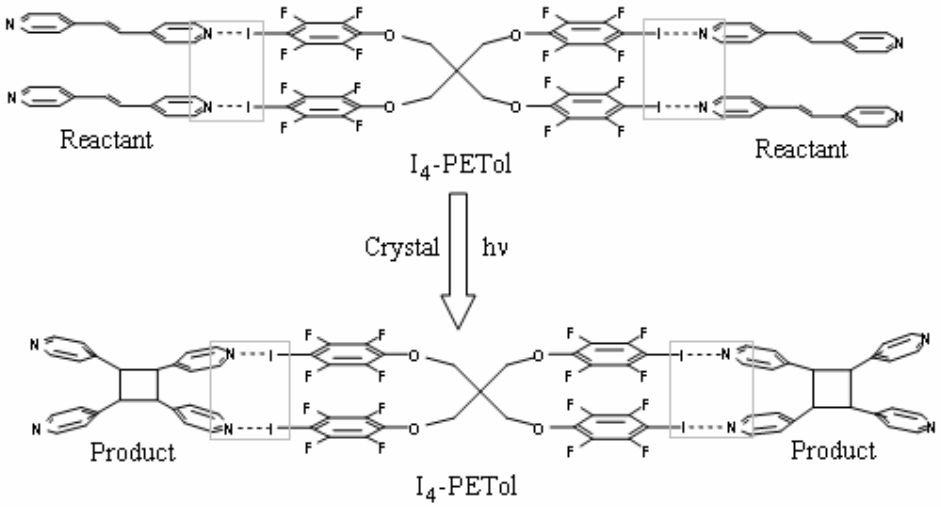

Scheme 3

Halogen bonds are also found in the biological molecules and are known to play an important role in natural systems. Thyroid hormones represent a class of naturally iodinated molecules for which halogen bonds appear to play a role in their recognition, as evident by the short I···O contacts between tetraiodothyroxine and its transport protein transthyretin [5.14]. In addition, more than 3,500 halogen-containing metabolites are currently known. In these systems, halogen atoms belonging to halogenated nucleotides or drugs, dominantly interact with the oxygen atoms that are present in the nucleic acids, proteins or ligands bound to nucleic acids or proteins. Recently Auffinger *et al.* [5.15] surveyed the PDB (Protein Data Bank) and calculated the electrostatic potentials for the different halogen atoms in various biological molecules. A clear trend of increasing

electropositive potential along the C─X bond was found when going from fluorine to iodine with the increasing polarizability of the halogen atoms. Fluorine atoms were found to remain entirely electronegative, whereas the other halogen atoms show the emergence of an electropositive charge along the C─X axis, which is surrounded by an electroneutral charge and, farther out, an electronegative charge. The size of the electropositive charge was found to be increased with the radius or polarizability of the halogen atoms. This suggests that iodines would form the strongest X···O halogen bonds.

The crystallographic and mechanical properties of some halogenenated benzenes and the relevance of these properties to the elucidation of the nature of halogen···halogen interactions is discussed in this chapter [2.15]. The results on these crystals enable us to identify the geometrical and the chemical features of the X···X interactions.

5.4 Results and Discussion

Table 1. IUPAC names and codes of the molecules.

IUPAC Name	**Code**
1,2,3,4,5-pentabromo-6-chlorobenzene	**12345B6C**
1,2,4-tribromo-3,5,6-trichlorobenzene	**124B356C**
1,2,4-trichloro-3,5,6-triiodobenzene	**124C356I**
1,2,4-tribromo-3,5,6-triiodobenzene	**124B356I**
1,3,5-trifluoro-2,4,6-triiodobenzene	**135F246I**
1,3,5-trichloro-2,4,6-tribromobenzene	**135B246C**
1,3,5-trichloro-2,4,6-triiodobenzene	**135C246I**
1,3,5-tribromo-2,4,6-triiodobenzene	**135B246I**
1,3,5-tribromo-2,4,6-trimethylbenzene	**135B246M**
1,3,5-triiodo-2,4,6-trimethylbenzene	**135I246M**
1,2,3-tribromo-4,5,6-trichlorobenzene	**123B456C**
1,2,3-trichloro-4,5,6-triiodobenzene	**123C456I**
1,4-dichloro-2,3,5,6-tetraiodobenzene	**14C2356I**
1,4-dibromo-2,3,5,6-tetraiodobenzene	**14B2356I**
1,4-dibromo-2,3,5,6-tetrachlorobenzene	**14B2356C**
1,4-dibromo-2,3,5,6-tetraiodobenzene	**14I2356C**

Several hexahalogenated benzenes $C_6Cl_{6-n}Br_n$, $C_6Cl_{6-n}I_n$, $C_6Br_{6-n}I_n$, were synthesized (Table 1, Scheme 4) and their crystal structures were examined (Appendix 2). These compounds adopt two broad packing modes, triclinic ($P\bar{1}$) and monoclinic ($P2_1/n$). Some of the compounds are polymorphic and some co-crystallize to form mixed crystals.

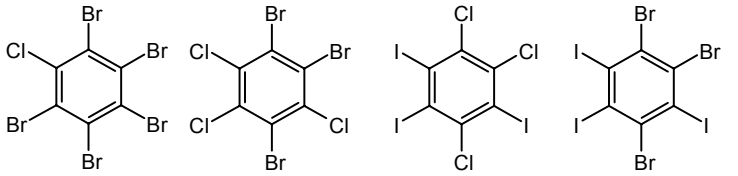

12345B6C **124B356C** **124C356I** **124B356I**

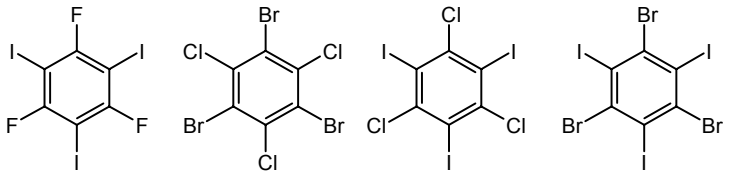

135F246I **135B246C** **135C246I** **135B246I**

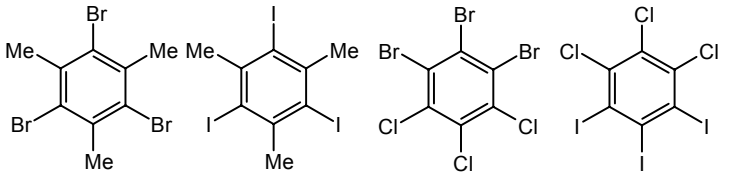

135B246M **135I246M** **123B456C** **123C456I**

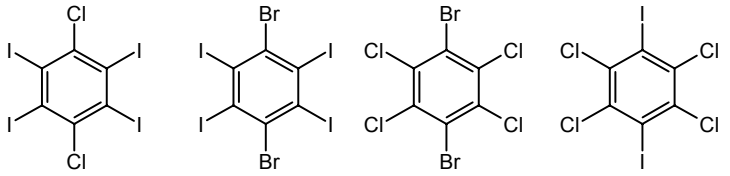

14C2356I **14B2356I** **14B2356C** **1245C36I**

Scheme 4

5.4.1 Monoclinic Structures: Hexachlorobenzene

Most of the hexahalogenated compounds in this study crystallize in the monoclinic crystal system and have a similar crystal packing to the classical hexachlorobenzene structure [3.7, 5.16]. The C_6Cl_6 structure has been introduced briefly in Chapter 3 to describe its mechanical behaviour, and full structural details and implications of these mechanical properties to the halogen interactions are discussed in this chapter.

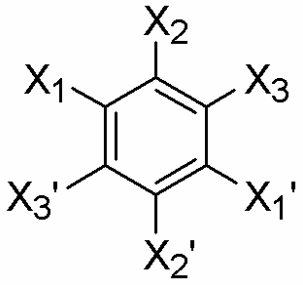

Scheme 5

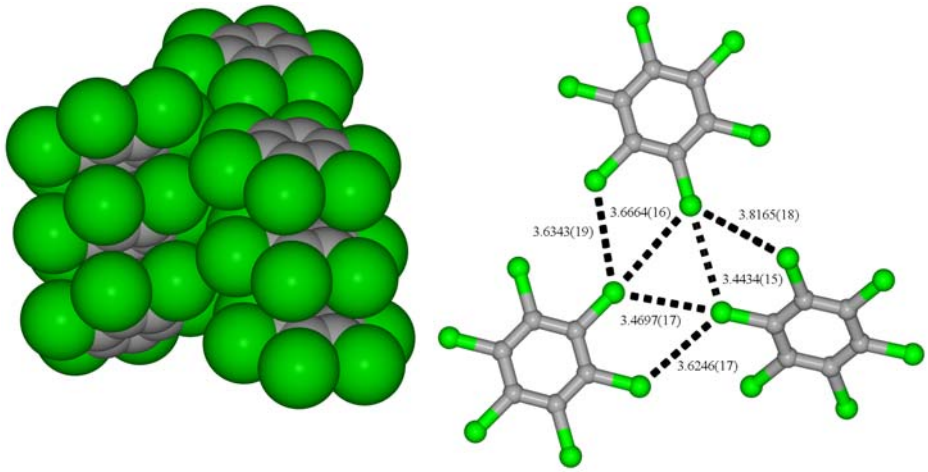

(a) **(b)**

Figure 3. Monoclinic form for hexahalogenated benzenes: (a) Corrugated layer in C_6Cl_6; (b) Cl···Cl distances between stacks in C_6Cl_6.

The unit cell of C_6Cl_6 at 100 K is a = 7.967(3), b = 3.7609(14), c = 14.670(5) Å, β = 92.459(6)º. The space group is $P2_1/n$, with two molecules in the unit cell. The molecule lies on an inversion centre in the crystal. The planar molecules form $\pi\cdots\pi$ stacks; within these stacks, the molecules are 3.44 Å apart (perpendicular distance) and tilted 63.3º to the stack direction so that $\pi\cdots\pi$ interactions are optimized (Figure 3a). The rest of the structure is close-packed in the usual way. In all the monoclinic structures, there are three distinct sites for the halogen atoms, which are referred to as X1, X2 and X3 (Scheme 5). There are two categories of Cl···Cl interaction in the overall distance range of 3.44-3.67 Å. The type-I contacts at sites X1, X2 and X3 (only the last lies on an inversion centre) have Cl···Cl distances of 3.8165(18) Å (107.48(13)°), 3.6246(17) Å (119.52(13)°) and 3.6343(19) Å (124.51(13)°) and are unremarkable. The second category does not appear to be type-I and the distances are in the van der Waals range (3.4434(15) Å, 175.05(15)°, 116.79(13)°; 3.4697(17) Å, 174.56(13)°, 124.47(13)°; 3.6664(16) Å, 171.25(13)°, 123.18(13)°) but the smaller angle θ_2 is not so close to 90°, which is more characteristic of type-II (Figure 3b). No Cl···Cl interaction appears to be particularly important and $\pi\cdots\pi$ stacking dominates this packing. C_6Br_6 and C_6I_6 also have a similar packing and hence are isostructural [5.17, 1.23] to C_6Cl_6. The unit cell volume increases uniformly in these three structures with the size of the halogen substituent (C_6Cl_6 439.2(3) Å^3 at 100 K, C_6Br_6 501.46(17) Å^3 at 100 K and C_6I_6 618.642 Å^3 at 298 K) which is not surprising. For molecules that lack inversion centre, and adoption of the monoclinic structure leads to crystallographic disorder.

The mechanical behaviour [1.18] of C_6Cl_6 crystals (Chapter 3) has implications to the nature of Cl···Cl interactions [1.28]. The direction of bending shows that the strong interaction in C_6Cl_6 is the $\pi\cdots\pi$ stacking. The fact that the crystal bends on (001) suggests that the Cl···Cl contacts that emerge from this face are weaker, and thus, they are expected to undergo some rearrangement (breaking and making) in the bending process. From the geometry of Cl···Cl interactions a question arises "are these contacts type-I or type-II?" Ideal type-I and type-II geometries are distinctive but these Cl···Cl geometries in C_6Cl_6 (3.4434(15) Å, 175.05(15)°, 116.79(13)°; 3.4697(17) Å, 174.56(13)°, 124.47(13)°) are intermediate and difficult to classify. The results on crystal bending

indicate, however, that these Cl···Cl interactions are weak and non-specific. They are easily deformed as the stacks of molecules slide against each other during bending. Distance and angle criteria are particularly poor indicators of the nature of Cl···Cl interactions especially when the geometry is ambiguous and does not correspond strictly to type-I or type-II. For a type-I interaction that lies on an inversion centre, a shortening below the van der Waals separation would be repulsive. For a type-II geometry, however, such shortening might be moderately attractive. By merely inspecting the crystal structure of C_6Cl_6 and noting the Cl···Cl distances and C–Cl···Cl angles, it would be very difficult to ascribe any particular chemical character to these quasi type-II interactions. In contrast, the bending results show that these interactions are weak and of low importance in the crystal packing. These results suggest that terminologies like type-I and type-II might permit some kind of classification but they cannot be used to draw definitive chemical inferences about the nature of the respective intermolecular interactions.

1,2,4-Trisubstituted Compounds

The 1,2,4 trisubstituted compounds **124B356C**, **124B356I** and **124C356I** also have the same monoclinic structure. These molecules lie on the inversion centre and as mentioned above, they must be disordered. However, the disorder is not statistical over the three positions; the site occupancy factors for Br at X1/X2/X3 are 0.76/0.34/0.40 in **124B356C**, for I in **124B356I** they are 0.76/0.35/0.39 and for I in **124C356I** they are 0.82/0.64/0.04. All three structures prefer to have the biggest atom in the X1-position where it can avoid a type-I contact with itself. There is a big increase in cell volume going from **124B356C** (473 $Å^3$) to **124C356I** (539 $Å^3$) while the exchange of Cl by Br in **124B356I** (544 $Å^3$) has only a small effect on the volume. This is distinct from the uniform volume increases in C_6Cl_6, C_6Br_6 and C_6I_6 and shows that in the 1,2,4 compounds the biggest substituent determines the cell volume. A fully statistical disorder would perhaps lead to more uniform cell volume increments in going from **124B356C** to **124C356I** to **124B356I**. Perhaps these structures have ordered domains of I-atom clusters that cannot be resolved in the X-ray experiment. It is clear that the 1,2,4

substitution pattern leads only to the monoclinic disordered packing in these structures irrespective of the substituent halogen atoms.

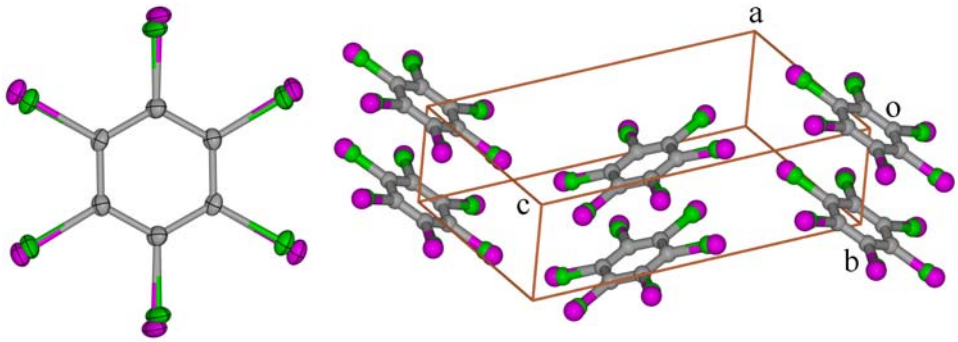

(a) **(b)**

Figure 4. 1,2,4-Trichloro-3,5,6-triiodobenzene, **124C356I**. (a) ORTEP diagram with 50% probability. (b) Disordered (I/Cl) molecules in the common monoclinic packing.

1,2,3-Trisubstituted Compounds

The 1,2,3 compounds also give the same monoclinic structure but the two disordered orientations in **123B456C** and **123C456I** are equally occupied as shown in Figure 5. This type of disorder could be linked to the molecular shape [5.18].

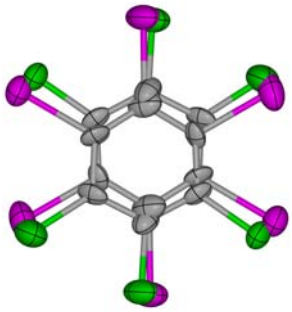

Figure 5. 1,2,3-Trichloro-4,5,6-triiodobenzene, **123C456I**. ORTEP diagram with 50 % probability. Notice the differences in the relative positions of halogens and ring C-atoms in **124C356I** and **123C456I**.

1,4-Disubstituted Compounds

The 1,4-disubstituted compounds **14B2356C**, **14C2356I**, **14B2356I** and **1245C36I** show a slightly different behaviour. The first is isostructural to C_6Cl_6 and (although the molecule has C_i symmetry) is disordered like the 1,2,4-trisubstituted

compounds The site occupancy factors for Br are 0.73/0.12/0.14 in positions X1/X2/X3 respectively. The position X1 is again favoured for the biggest substituent. (A refinement has been published but did not include the disorder [5.19]). The second and the third take a variant of the C_6Cl_6 structure but they are ordered (Figure 6). The Cl (or Br) and I positions might well have been disordered in this packing, but they are not. The reason for the ordering is suggested by the fact that the Cl···Cl (or Br···Br) interaction is exclusively type-I while the I···I interactions are both type-I and quasi type-II. So, even among these marginal X···X contacts, there seems then to be some preference for the Cl···Cl (or Br···Br) interactions to be more dispersive than the other interactions. There is just a hint therefore that Cl (or Br) and I are chemically distinguishable in these two structures. **1245C36I**, however, has two polymorphs. For the first, which occurs as needles, only a cell could be found that matches C_6Cl_6 (8.6484(6) Å, 4.1259(3) Å, 15.7424(11) Å, 90°, 92.1300(10)°, 90°) but the structure could not be solved adequately. The second crystallized from CCl_4 as monoclinic rhombs with cell dimensions of a = 6.5276(6), b = 5.9682(5), c = 13.3913(11) Å and β = 98.7720(10)°. The packing is not dominated by $\pi\cdots\pi$ stacks; instead there is a herringbone arrangement of molecules to form a zigzag chain of type-II I···I interactions (3.8957(3) Å, 170.52(6)º, 79.48(6)º; Figure 7). In this respect, **1245C36I-M2** is closer to 1,4-diiodobenzene rather than any of the other hexahalogenated benzenes. Specific bending properties for this last compound could not be distinguished from waxy flow. Here, it may be noted that the introduction of iodine group takes the lead in driving the crystal structure.

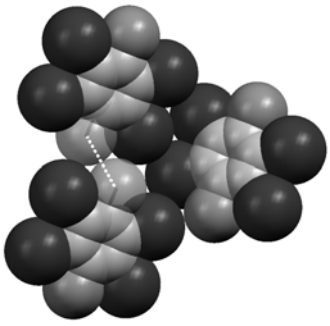

Figure 6. Ordered structure of 1,4-dichloro-2,3,5,6-tetraiodobenzene (**14C2356I**). Notice the type-I Cl···Cl interaction.

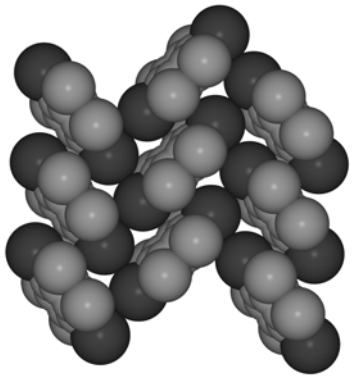

Figure 7. 1,2,4,5-Tetrachloro-3,6-diiodobenzene (**1245C36I**). Notice the herringbone arrangement of molecules to form a zig-zag chain of type-II I···I interactions.

In **14C2356I** there is a weak I···Cl (3.792 Å) type-II interaction in which the more electronegative Cl-atom is more acute (125°), while the less electronegative I-atom is less acute (168°) showing its correct polarization nature. Again, in **14B2356C** the interaction is acute more at the Cl-atom (117º) than at the Br-atom (173°). However, in **14B2356I** the more acute angle is at the less electronegative I-atom (118°) rather than at the Br-atom (162.5°). Perhaps with a larger electronegativity difference between the halogen atoms there would be a greater likelihood for a small angle (closer to 90º) at the more electronegative halogen, but the CSD (Cambridge Structural Database) is equivocal on this issue possibly because of lack of a sufficient number of examples.

The C_6Cl_6, C_6Br_6, C_6I_6 and the above mentioned mixed hexahalogenated benzenes adopt the same monoclinic structure, which indicates that there is a specific reason. It is known that when molecules with similar shape and size adopt the same crystal structure, geometrical factors operate [5.20]. When molecules of different sizes and shapes adopt the same crystal packing, chemical factors are supposedly more dominant. However, these generalizations are not very helpful here. Cl (18.1 Å^3), Br (24.4 Å^3) and I (33.0 Å^3) are clearly of different sizes. But, all the experimental observations on bending and crystallographic disorder in the monoclinic group seem to indicate that geometrical factors are more important. There is, however, a hint of the importance of chemical factors from the different site occupation factors and varying

volume increments and perhaps there are ordered domains, especially when iodine is introduced. The molecules **14C2356I** and **14B2356I** have an inversion centre and adopt the ordered structure of the C_6Cl_6 type. This suggests that there are definite chemical differences between Cl (or Br) and I. These chemical factors come out clearly when the geometrical arrangement of the halogen atoms (inversion centre or symmetrical arrangement of X atoms) permits the chemical factors to dominate. In the end, however, it is the bending experiments that provide the clinching evidence; they show that most of the X···X interactions in these structures are weak and non-specific.

5.4.2 The Triclinic Structure Type

1,3,5-Trisubstituted Compounds. Supramolecular Synthons

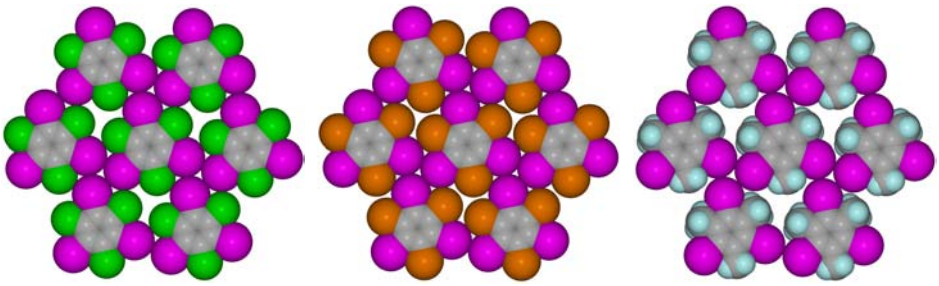

(a) **(b)** **(c)**

Figure 8. Planar layer in (a) **135C246I**; (b) **135B246I-T**; (c) **135I246M**. The three I-atoms in the I_3-synthon are in close contact in each case, but the Cl, Br and Me-groups are not. This indicates the structural importance of the I_3-synthons.

The crystal structure of **135C246I** has been introduced in Chapter 2 to elucidate the mechanical shearing of layers and twinning and now the full structural details of the similar triclinic compounds are discussed in this chapter in the context of the halogen interactions and rationalized the formation of supramolecular synthons. 1,3,5-Tribromo-2,4,6-triiodobenzene (**135B246I**) provides an excellent example for the triclinic compounds. **135B246I** crystallizes from THF concomitantly in the C_6Cl_6 monoclinic form **135B246I-M1** (thin needles) and a triclinic form, **135B246I-T**, which was obtained as thick blocks, some of which are boomerang shaped (twinned). A third polymorph was also obtained from THF and has the same structure as **14B2356I**, but quality of the X-ray data was poor. The molecules in the triclinic form are arranged in planar layers parallel

to (100) and in a nearly hexagonal arrangement with clusters of three I-atoms from three neighbouring molecules and correspondingly, clusters of three Br-atoms (Figure 8). The I_3 clusters are distinctive with particularly short I···I distances of 3.7548(4) Å (174.24(12)°, 119.68(13)°), 3.7762(4) Å (176.56(12)°, 119.68(12)°) and 3.7979(5) Å (170.06(12)°, 119.06(12)°) [5.11, 5.21]. The θ_2 values are all close to 120° and despite the short I···I distances, it would once again not be possible to say whether these contacts are type-II which ideally has $\theta_1 \approx 180^o$ and $\theta_2 \approx 90^o$. The I_3 cluster or synthon is supposedly stabilized cooperatively as $I^{(\delta+)}\cdots I^{(\delta-)}$. The Br_3 clusters have Br···Br distances of 4.0660(7), 4.0937(7) and 4.0946(7) Å and are somewhat loosely packed because of the bigger size of the I-atoms. Successive planar layers are inversion related and stacked so that bumps in one layer fit into the hollows of the next. The interlayer interactions are non-specific in that they are based on close-packing of spheres in hollows.

One may distinguish here between "synthon" and "cluster" [1.13]. The synthon has chemical relevance (short intermolecular distances, favorable geometries) and repeats in a number of related crystal structures. A cluster, as seen in these structures, is any association of atoms from different molecules in a crystal with no particular supramolecular significance.

An important aspect of chemically directed recognition is the repeated appearance of specific supramolecular synthons, which are sub-structural units containing directional interactions [1.13]. The planar layer structure in **135B246I-T** is reproduced in other related hexasubstituted benzenes. In the corresponding chloro derivative **135C246I**, the intralayer I···I distances are 3.7985(6), 3.8250(6) and 3.8646(8) Å (nearly the same as in **135B246I-T**). Because of this, the Cl···Cl distances are pushed apart as far as 4.3360(17), 4.3667(17) and 4.3697(18) Å (longer than the Br···Br distances in **135B246I-T**) and the Cl-atoms are not even in contact. In **135I246M** [2.16] the I···I distances in the I_3 synthon are 3.851, 3.897 and 3.933 Å and the Me-groups are well separated, a case of Cl/Me exchange [5.7a]. **135C246M** and **135B246M** wherein the Cl_3 and Br_3 synthons are, respectively, structure determining, are also isostructural. The I-atom is crucial in all these cases, and its size determines the overall layer structure. It may be suggested that the Br-clusters in **135B246I-T**, the Cl-clusters in

135C246I and the Me-clusters in **135I246M** are mere spectators in a layer structure that is determined by the robustness of the I_3 synthons. In **135F246I** a simple geometrical calculation showed that the F···F distances would need to be at an unrealistic distance of 5.01 Å if the layered structure of **135B246I-T** were adopted with the I_3 synthons conserved. Instead, the experimental structure is three-dimensionally corrugated and not layered, with I and F-atoms at van der Waals separation (I···F, 3.53, 3.59 Å).

A necessary (but not sufficient) condition for the appearance of the layered triclinic structure is the presence of the three halogen atoms in a 1,3,5 arrangement. For example, **135I246M** and **135B246M** also contain this pattern and form layered structures. Compounds that lack this substitution pattern take the monoclinic disordered structure and do not show layer packing. **135F246I** which has the same substitution pattern but takes a different (ordered) monoclinic structure (Appendix 2) which is not layered, also does not shear but bends (Chapter 3). From this, it is clear that the trigonal 1,3,5 arrangement of X-atoms favour the formation of X_3-supramolecular synthons. But **135B246C** is an exception to this generalization since it adopts the disordered monoclinic structure of C_6Cl_6.

Implications of Shearing and Twinning

The mechanical shearing behaviour of these crystals explicates the importance of the X_3-synthons in the triclinic structures (Chapter 2). As explained previously, these crystals undergo shearing by sliding of the *bc*-planes past one another on application of a mechanical stress in a direction perpendicular to the crystal length. In the context of X···X interactions, the key factor obtained from these experiments is that in **135B246I-T** the *intra*layer I···I interactions are much more important than the *inter*layer I···I and I···Br interactions, because these interactions hold the layers tightly and are preserved while shearing. Thus, the intralayer interactions are considered to be synthon forming and chemically significant, as they arise from the polarization of the I-atoms. The crystal breaks when it is attempted to shear or cut it in other directions. The difficulty in so doing is due to the disruption of the layers which confirms the fact that the intralayer interactions are strong and directionally specific and synthon forming.

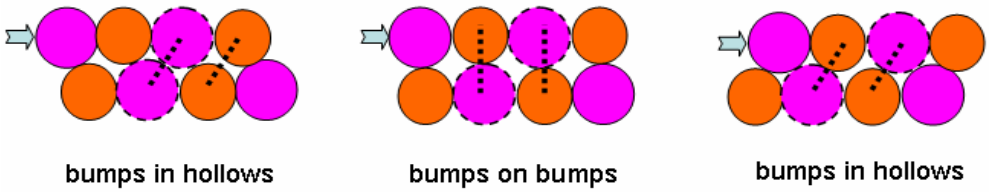

Scheme 6. Cross sectional view of the two layers in the triclinic structures shows the stages in the shearing process. Notice the rearrangement of the interactions between atoms from the two layers. Arrow indicates the direction of movement of the top layer over the bottom one.

In the shearing process, the X···X interactions between any two sliding layers undergo continuous rearrangement, i.e. breaking and making (Scheme 6). This indicates that the interactions between these layers are non-specific, and hence, they are stable (non-repulsive) in all the intermediate stages of the rearrangement. Twinning in the crystals of these layered structures gives the final confirmation for the non-specificity of the interlayer interactions (Chapter 2). X-ray data on these crystals confirmed that the twinning occurs due to the stacking faults of the (100) layers. In general, twinning is observed when the normal and twinned stacking energies are comparable. The twinning [5.22] in these structures suggests that the interlayer I···I, Br···Br and I···Br interactions are non-specific and comparable to the easily deformable Cl···Cl interactions in the bent crystals of C_6Cl_6. The variable cell measurements on these crystals also indicate that the interlayer interactions are weak when compared to the intralayer interactions (Chapter 2).

5.4.3 Solid Solutions

A series of solid solutions [5.23] was prepared to see whether the halogens exchange with each other and still preserve the layered structure. The solid solutions were prepared using equimolar concentrations in the crystallization solvent, 1,4-dioxane. All take the triclinic packing of **135B246I-T**, with the heavier atom forming the X_3 synthon. Molecules in these structures are disordered statistically (Figure 9). The solid solutions **135B246I:135C246I**, **135B246I:135I246M** and **135C246I:135I246M** are rather close to equimolarity in the solid state (57:43, 46:56 and 41:59, respectively) and have nearly the same cell volumes (553, 564 and 556 Å^3). With the same method, a solid

solution of **135C246I:135B246M** with a molar ratio of 8:92 was obtained. The crystallographically determined ratio was also confirmed by HPLC. Perhaps the lack of I-atoms in one of the constituents prevents a more equimolar crystallization product, once again hinting at the importance of I in forming these layered structures. The importance of I in this regard is also shown by the fact that **135B246C** adopts the disordered monoclinic structure of C_6Cl_6.

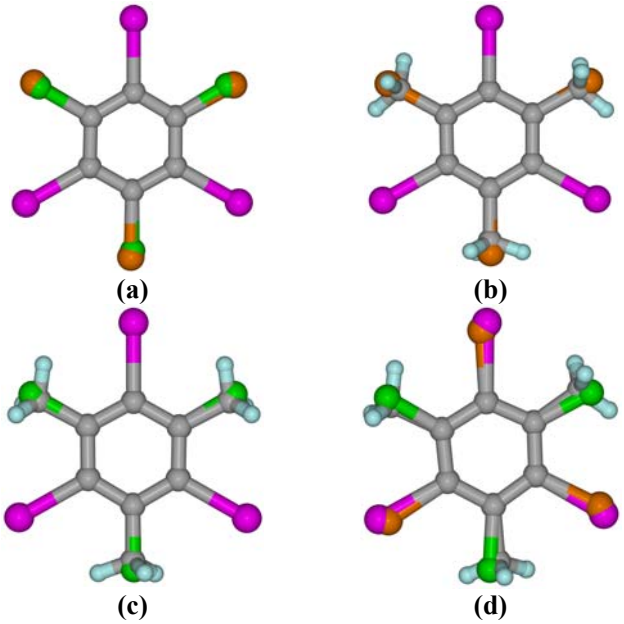

Figure 9. Disorder model of the molecules in the triclinic structures of solid solutions, (a) **135B246I:135C246I**; (b) **135B246I:135I246M**; (c) **135C246I:135I246M**; (d) **135C246I:135B246M**.

5.4.4 Polymorphism

Occurrence or non-occurrence of polymorphs in some of the 1,3,5/2,4,6 substituted compounds is in order. **135B246I** is trimorphic, with triclinic layered (**135B246I-T**), monoclinic C_6Cl_6 type (**135B246I-M1**) and monoclinic as in **14B2356I** (**135B246I-M2**) form. **135C246I** gives only the triclinic layered structure and **135B246C** only the C_6Cl_6 form. Despite repeated and exhaustive attempts the absent polymorphs **135B246C-T** and **135C246I-M** were never obtained. The monoclinic C_6Cl_6 structure (and the attendant disorder) is favoured when the two halogen atoms are similar in size

as Cl and Br are. The triclinic structure is tolerated even with large differences in halogen size as in Cl and I. In the combination Br/I both situations occur, but the cell volume of the triclinic form (563 Å^3) is higher than that of the monoclinic form (536 Å^3) because of the empty spaces in the Br_3 clusters in the former.

5.5 Conclusions

Halogen···halogen interactions (X···X) have been investigated in a series of hexahalogenated benzenes. These compounds occur in two broad structural groups. The more common one is a monoclinic packing that is isostructural with C_6Cl_6. The less common one is a layered triclinic packing that is exclusive, although not mandated, to compounds where different halogen atoms occupy the 1,3,5 and 2,4,6 positions respectively. Compounds $C_6Cl_{(6-n)}Br_n$ adopt the disordered monoclinic structure irrespective of their substitution pattern. For molecules that lack inversion symmetry, adoption of this monoclinic structure would necessarily lead to crystallographic disorder. The 1,3,5/2,4,6 arrangement of distinct halogen atoms is compatible with a threefold-symmetrical X_3-synthon based pseudo-hexagonal layer structure. X···X interactions have been traditionally classified using geometrical criteria as type-I and type-II. While there might be a general consensus that the symmetrical type-I interactions are of the van der Waals type and the unsymmetrical type-II contacts are polarization induced, some of the interactions in these structures do not lend themselves easily to this classification. Some of the monoclinic C_6Cl_6 type crystals undergo bending but only along certain planes: this can happen only when interactions in a direction orthogonal to these planes are particularly weak. Because it is the X···X interactions that emerge at the bending faces, it may be concluded that these interactions are weak and non-specific despite their geometry, which is more like type-II than type-I. The triclinic crystals shear along layers within which the X···X interactions, mostly I···I, are much stronger than X···X interactions between layers. The strong and specific intralayer I···I interactions assemble to form I_3 supramolecular synthons, which are the most important structural elements in the triclinic group. Accordingly from this study, it is clear that X···X interactions (X = Cl, Br, I) are of several types and that it is sometimes difficult to characterize them using

geometrical criteria only. The use of an independent technique, like observation of the mechanical behaviour of the crystal, offers a clearer insight into their nature. These results prove that both chemical and geometrical models need to be considered for X···X interactions in hexahalogenated benzenes.

5.6 Experimental Section

Materials: All reagents and solvents employed were commercially available (Lancaster) and were used as supplied without further purification. All these compounds were characterized with NMR and IR spectra. The ^{1}H NMR spectra were recorded on Bruker Avance at 400 MHz instrument. IR spectra were recorded on a Jasco 5300 spectrometer. All melting points were measured in Fisher-Jones melting point instrument.

Synthesis

All the mixed halogenated compounds were synthesized by either bromination or iodination of the corresponding halogenated starting materials. The general bromination and iodination procedures used to prepare these compounds are given for **135B246C** and **135C246I** in Section 2.9, Chapter 2 [2.23].

Characterization: ^{1}H NMR (400 MHz, [D_6]DMSO, 25 °C, TMS): No peaks were found in the spectrum for all the hexahalogenated compounds. IR (KBr, cm^{-1}): **135F246I:** 1560, 1404, 1323, 1049, 702, 652; **1245C36I:** 1309, 1282, 1246, 679, 582; **14B2356C:** 1325, 1286, 686, 623; **135B246I:**1263, 1224, 1028; **124C356I:** 1539, 1516, 1288, 1269, 632, 555; **135C246I:135B246I:** 1292, 1255, 1222, 1026; **135C246I:135B246M:** 2948, 1120, 1020, 949, 644, 559, 470.

Crystallization: All the compounds were crystallized from either CCl_4, THF or 1,4-dioxane by slow evaporation at ambient temperature.

X-ray crystallography

Intensity data were collected on a Bruker Nonius Smart Apex CCD with graphite monochromated Mo-K_α radiation. Gaussian face-indexed absorption corrections by Xprep were applied before empirical data correction by Sadabs 2.10. The structures were solved by direct methods and refined anisotropically by full-matrix least-squares method using the Shelxtl 6.14 software package. Crystal data are given in Appendix 2. Further details (CIF) are available *via* www.ccdc.cam.ac.uk/conts/retrieving.html.

APPENDIX 1

ENGINEERING OF A WEAK N–H···π INTERACTION AND CONTROLLING IT THROUGH GUEST SELECTION IN HOST 4-(TRIPHENYLMETHYL)BENZAMIDE

1. Introduction

Crystal engineering deals with the understanding of intermolecular interactions and the design of new solids with desired physical and chemical properties [1]. In this context, strong hydrogen bonds have been studied extensively in the past few decades while the importance of weak interactions for fine tuning of the crystal structures in crystal engineering is realized now [2]. The importance of weak C–H···O hydrogen bonds in protein–ligand binding has been demonstrated by Pierce *et al.* in a recent study of 200 liganded kinase structures [3]. Whereas the strong hydrogen bonds (energy 5-15 kcal/mol) are excellent tools for crystal design, the weak C–H···O and related interactions (energy 1-4 kcal/mol) too have been successfully used in recent years [4-6]. X–H···π (X = O, N, C, π = phenyl ring) is the interaction of a hydrogen atom with the π-system of an aromatic ring in either an intermolecular or an intramolecular fashion. X–H···π interactions are important not only in the stabilization of α-helix and β-sheet motifs of macromolecular proteins but also in the design of organic and organometallic crystal structures [4]. For example, weak N–H···π hydrogen bonds have been identified between (i+2) and (i+1) peptide residues when stronger O acceptors are not accessible [7]. Neutron diffraction crystal structure of vitamin B_{12} coenzyme shows a N–H···π interaction (2.58 Å) from amide donor to benzimidazole acceptor group [8]. The existence of these types of interaction has gained considerable attention in recent years.

The investigation of Malone *et al.* revealed the preferred geometry and interaction strength for O–H, N–H, $N–H^+$, S–H, sp^2 C–H and sp^1 C–H interactions with phenyl rings. This is done through searches of the Cambridge Structural Database (CSD), combined with semi-empirical and *ab initio* molecular orbital calculations. The database analyses [9] of small molecule organic and organometallic crystal structures shown that the T-shaped orientation, with the hydrogen bond donor pointing towards

phenyl ring centroid, is preferred in N–H···π interactions at short distance ($d_{H,\pi} \leq 3.0$ Å) whereas the H-atom interacts with a ring carbon at longer separation ($3.0 \leq d_{H,\pi} \leq 4.0$ Å) (Scheme 1). The calculated energy of N–H···π interaction is estimated to be 1-4 kcal/mol depending on the geometry of the interaction, it being stronger when the H atom is positioned above the ring centroid in a close to linear approach. The bond is much stronger with NH_4^+ donors (9-16 kcal/mol) [9b].

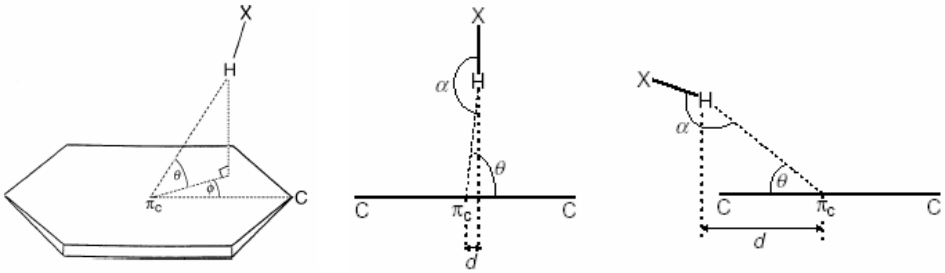

(a) **(b)** **(c)**

Scheme 1. (a) Definition of approach of interacting hydrogen atom to aromatic ring. (b) T-shaped orientation of N–H···π interaction to centroid (πc) at short distance ($d_{H,\pi} \leq 3.0$ Å). (c) Common geometry of N–H···π interaction to ring C atom at longer distance ($3.0 \leq d_{H,\pi} \leq 4.0$ Å).

2. Wheel-and-Axle Compounds

One of the rational approaches in host molecule design is to exploit the awkwardness in molecular shape to avoid close packing in a host material. Toda, Hart and others have employed this strategy to synthesize wheel-and-axle compounds [10]. Some examples of wheel-and-axle host compounds are shown in Scheme 2. Conventionally, a wheel-and-axle host molecule contains a long linear axle in the middle bearing large rigid substituent groups, the wheels being at both the ends [1.2]. The typical organic molecule has an unsymmetrical even irregular shape, but these molecules cross the normal bounds of shape irregularity and because of this, they are unable to pack properly as single component crystals. The wheels prevent the close packing of the axles and voids are created, there by promoting inclusion of guest molecules.

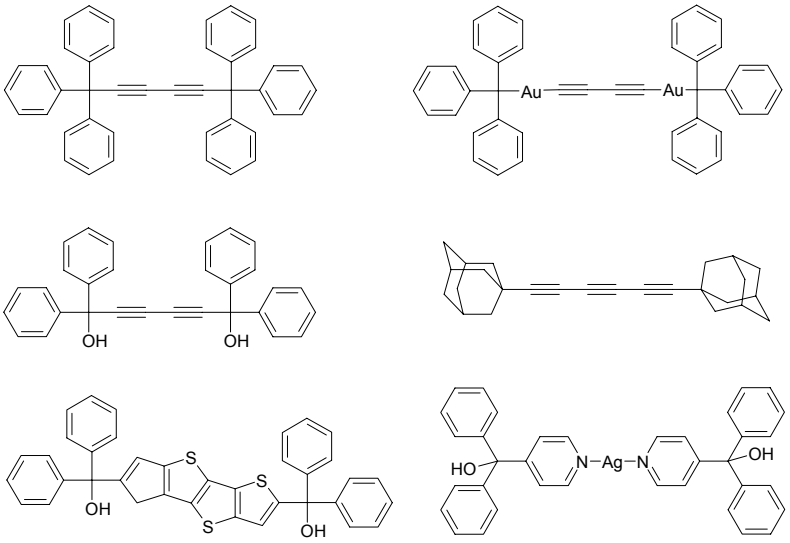

Scheme 2. Some examples of wheel-and-axle host compounds.

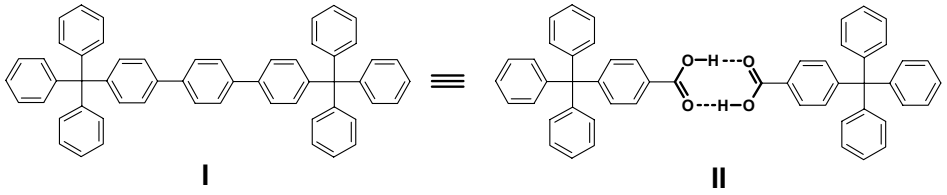

I **II**

Scheme 3. Host **II** is designed to resemble **I** at supramolecular level.

Synthesis of compound **I** is difficult and it is insoluble in common organic solvents, hence the compound 4-(Triphenylmethyl)benzoicacid, **II** (Scheme 3) was previously designed in our group to achieve the similar type of wheel-and-axle host framework through robust supramolecular acid dimer synthon (Scheme 4) [11]. Here, a molecular synthon (phenyl ring) in a wheel-and-axle host is replaced by an equivalent supramolecular synthon (acid dimer) to obtain a supramolecular host. Molecule **II** crystallizes *via* the carboxylic acid dimer supramolecular synthon to produce a wheel-and-axle host lattice (Scheme 4) that includes various aromatic solvents like PhCl, PhBr, $PhNO_2$, *o*-xylene, *m*-xylene, *p*-xylene and anisole in its microporus framework. Solvents like chlorobenzene, xylene and anisole are included with 2:1 host guest stoichiometry while mesitylene as 1:1 clathrate [11].

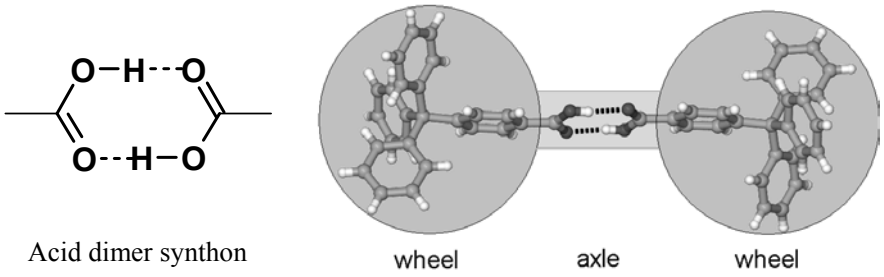

Acid dimer synthon

Scheme 4. Wheels and 'supramolecular axle' in host framework **II**.

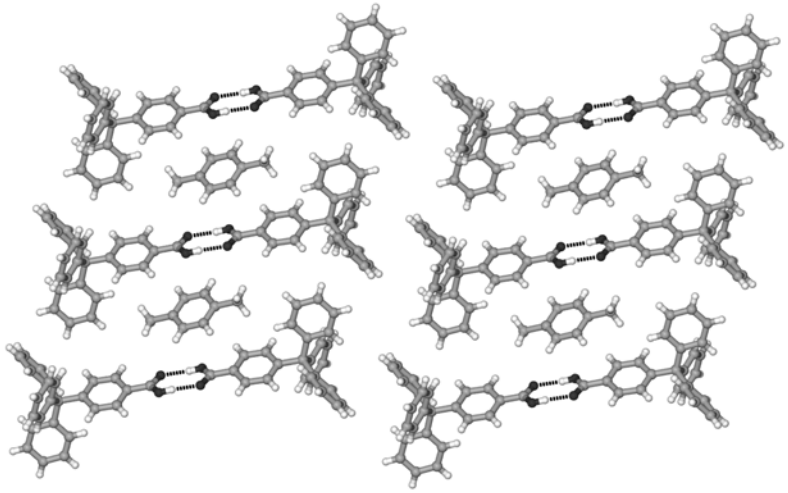

Figure 1. X-ray crystal structure of **II**•*p*-xylene (2:1). It shows the wheel and supra molecular axle host architecture and the inclusion of guest molecule in the void in (102) plane.

The crystal structure of acid **II**•*p*-xylene shows centrosymmetric carboxylic acid dimer synthon (Figure 1). These dimers are packed as zigzag tapes through phenyl-phenyl interactions. The dimer synthon and the phenyl-phenyl interactions produce the target wheel-and-axle architecture with the voids being occupied by guest molecules. The robust carboxy dimer supramolecular synthon produces an isomorphous series of clathrates for guests of similar size/shape, while the pore volume is adjusted by the multiple phenyl-phenyl motifs. This work showed that the supramolecular synthesis can be used in conjunction with molecular synthesis to gain rapid and convenient access to systems and functions that are often difficult and tedious to obtain with molecular synthesis alone.

3. Inclusion Complexes of 1

In continuation to the host **II**, the 4-(triphenylmethyl)benzamide, **1** was synthesized to employ the amide functional group to achieve the wheel-and-axle host framework [12]. In this structure, N–H···π interaction is expected to be present. Schemes 5 and 6 illustrate the design strategy of the N–H···π interaction. In general, primary amides form amide dimer synthon through the N–H···O interaction. And the second NH of the amide group forms another N–H···O interaction with the O atom of the adjacent (translation related) dimer, and hence extends as a tape (Scheme 5). In this tape, the distance between any two repeat atoms from adjacent translation related molecules will be *ca.* 5.1 Å (Scheme 5) which is the characteristic feature of the primary amides. The primary amide **1** with bulky triphenylmethyl groups, will hydrogen bond *via* the N–H···O dimer synthon but the second NH is unable to form the characteristic 5.1 Å axis tape structure [13] because of steric factors (Scheme 6). The large van der Waals radius of Ph_3C group (6.5 Å) [11] will prevent the formation of amide tape and the presence of adjacent phenyl ring acceptor should promote an intermolecular N–H···π(phenyl) interaction.

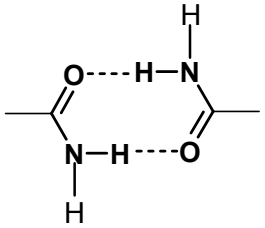

Amide dimer synthon

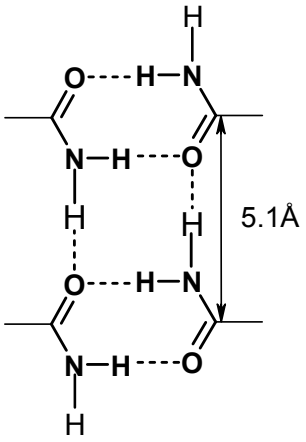

Characteristic 5.1 Å short axis of primary amides.

Scheme 5

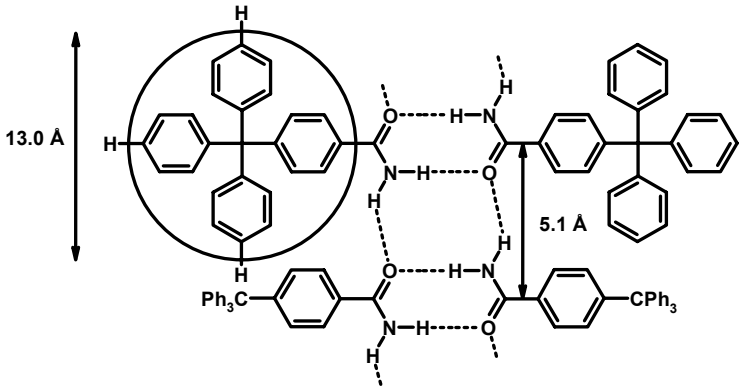

Scheme 6. The large size of trityl group (vdW diameter 13 Å) will sterically hinder formation of amide tape (repeat distance 5.1 Å), which should lead to the expected intermolecular N–H···π interaction with a neighboring phenyl ring.

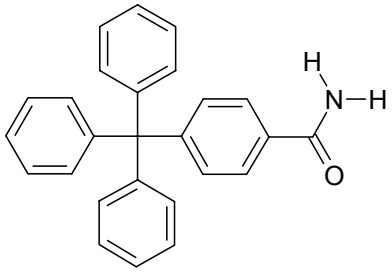

1

1.*p*-xylene
1.*m*-xylene
1.*p*-chlorotoluene
1.*p*-bromotoluene
1.CH_2Br_2
1.CH_2Cl_2
1.CH_3NO_2
1.CH_3COOEt
1.$CH_3COCH_2COCH_3$
1.anisole
1.CH_2I_2

The host compound **1** was prepared using the literature procedure and crystallized from *p*-xylene and *m*-xylene solvates. As anticipated, in the crystal structure of **1**•*p*-xylene ($P\bar{1}$), carboxamide molecules are N–H···O hydrogen bonded (1.90 Å, 175º, neutron-normalised geometry) as dimers. The triphenylmethyl groups of inversion-related molecules are interlocked through numerous edge-to-face and face-to-face aromatic–aromatic interactions (Figure 2a). The host molecules form zigzag tapes along [$11\bar{1}$] which are in turn packed along [010] to form voids of 42 $Å^2$. Ordered *p*-xylene molecules occupy the cavity. The second NH group of the primary amide approaches the phenyl ring of a translation-related molecule. Interestingly, the N–H···π geometry is shorter to the nearest ring C-atom (2.89 Å, 165º) compared with the centroid approach

(3.58 Å, 166º). Notwithstanding that the approach of donor hydrogen to the phenyl ring centroid is preferred in statistical distributions [14] a H atom pointing towards a C atom or a C≡C bond midpoint is not uncommon. For example, in the host–guest structure of 2,4,6-tris(4-chlorophenoxy)-1,3,5-triazine–1,3,5-tribromobenzene (1:1) determined by neutron diffraction, the C–H···π geometry is better to a C=C bond midpoint (2.81 Å, 174º) than to the phenyl ring centroid (3.46 Å, 164º) [15]. To complete the structure of **1**•*p*-xylene, guest molecules are bonded to the host carboxamide group by a C–H···O hydrogen bond (2.84 Å, 172º). The weak N–H···π (host–host) and C–H···O (guest–host) hydrogen bonds are displayed in Figure 2b.

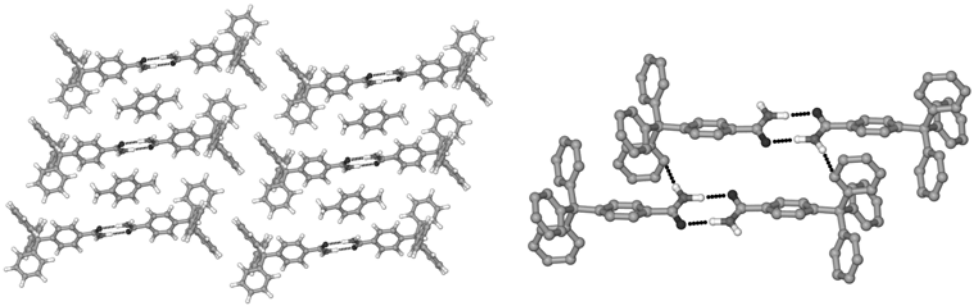

(a) **(b)**

Figure 2. Crystal structure of **1**•*p*-xylene (2:1). (a) Molecules shown are in (102) plane. Note the similarity with Figure 1 in the arrangement of host and guest molecules. Intermolecular N–H···π interaction approaching the phenyl C atom. Molecules shown are in (011) plane. H atoms bonded to C are omitted for clarity.

The crystal structure of **1**•*m*-xylene is isomorphous with the *p*-xylene clathrate except that the guest molecules are disordered. This is not surprising because *m*-xylene molecules do not have an inversion centre and guest disorder is one way to conform to the higher inversion symmetry of the host framework. Such behaviour is with precedent in host–guest systems [11, 16]. A perspective view of guest molecules included in the channels formed by the host lattice is shown in Figure 3. The N–H···π geometry in this structure is long (3.19 Å, 169º), presumably because the cavity is enlarged by the alternate orientations of disordered guest molecules, but what is significant from a design viewpoint is that this crystal is isomorphous with the *p*-xylene solvate. It may be noted

that N–H···π contacts up to 4 Å were considered in a detailed statistical analysis of these interactions in the CSD [9].

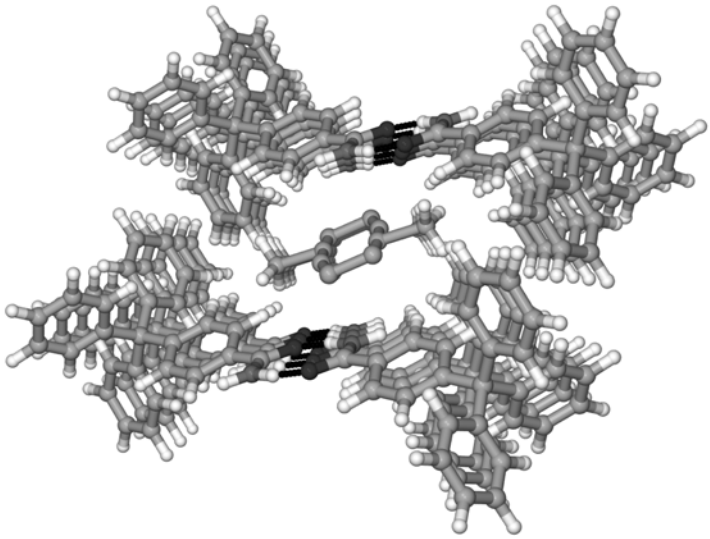

Figure 3. Perspective view of the channel down [100] in **1**•*m*-xylene. Guest molecules are disordered about the inversion centre. The N–H···O bond geometry is 1.90 Å, 171º.

And then, crystallization studies of host system **1** with several guest species were carried out to find out: (1) if the weak interaction persists in other inclusion structures; (2) whether the N–H···π geometry is within the accepted range of $d_{H,\pi}$ = 2.4-3.0 Å; [9, 17] (3) the effect of guest structure on hydrogen bonding and crystal packing. The studies revealed that the engineered N–H···π interaction is present in structures with aromatic guests (*p*-xylene, *m*-xylene, *p*-chlorotoluene, *p*-bromotoluene) whereas it is absent for guest molecules that contain stronger C=O type acceptor groups (EtOAc, acetylacetone, $MeNO_2$) because of preferential N–H···O_{guest} hydrogen bonding. Inclusion crystal structure of the host **1** with anisole contains two symmetry-independent amide dimers, one that engages in N–H···π interaction and the other forms conventional N–H···O_{host} hydrogen bond. These results show that the designed N–H···π interaction may be controlled by the nature of included guest within the robust wheel-and-axle framework [18] of 4-(triphenylmethyl)benzamide, **1** [12].

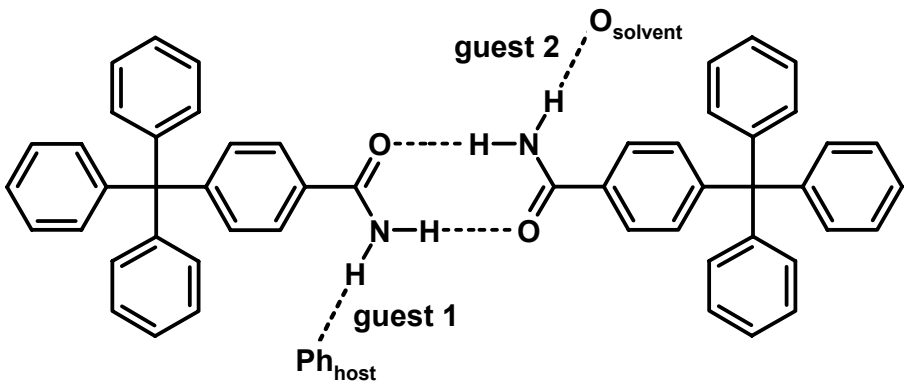

N–H···π present: **guest 1** = *p*-xylene, *m*-xylene, *p*-chlorotolune, *p*-bromotolune, CH_2Br_2
N–H···π absent: **guest 2** = CH_3COEt, $CH_3COCH_2COCH_3$, CH_3NO_2, CH_2Cl_2
Both N–H···π and N–H···O: **guest 3** = anisole, CH_2I_2

Scheme 7. 4-(Triphenylmethyl)benzamide host **1**. The three categories of guest molecules control the engineered N–H···π interaction.

4-(Triphenylmethyl)benzamide **1** was crystallized from solvents of different types: xylenes and haloaromatics (hydrophobic); EtOAc, $MeNO_2$, $AcCH_2Ac$ (C=O type acceptor), and halogenated CH_2X_2 molecules (X = Cl, Br, I). Diffraction quality single crystals were obtained from the appropriate guest solvent at ambient temperature. Inclusion of these solvents in the host lattice gave three types of host•guest structures as summarized in Scheme 7. These crystals were generally found to be stable under ambient conditions except the CH_2Cl_2 adduct which was bathed in perfluoropolyether and sealed in a capillary tube. X-ray data were collected at low temperature to minimize guest disorder and decomposition of the host•guest adduct. Crystallographic data are listed in Appendix 2 and information about host•guest structures and hydrogen bonds is summarized in Table 1.

Table 1. Hydrogen bond distances (neutron normalized) in **1**•guest crystal structures. The e.s.d. of H-bond distances is 0.003-0.010 Å.

Entry	Guest	Guest type	Guest order/ disorder	N–H···O		N–H···π		X-ray data *T*/K
				H···O /Å	∠N–H···O /º	N–H···π /Å	∠N–H···π /º	
1	*p*-xylene	1	ordered	1.90	174.6	2.89	165.0	293
2	*m*-xylene	1	disordered	1.90	171.4	3.19	168.8	293
3	*m*-xylene	1	disordered	1.70	171.6	3.16	170.3	123
4	*p*-chlorotoluene	1	disordered	1.89	175.6	2.89	165.1	293
5	*p*-chlorotoluene	1	disordered	1.87	175.3	2.82	163.1	123
6	*p*-bromotoluene	1	disordered	1.88	175.4	2.86	163.7	203
7	CH_2Br_2	1	disordered	1.94	165.4	2.96	164.9	123
8	CH_2Cl_2	2	disordered	1.95	165.2	---	---	293
9	CH_2Cl_2	2	disordered	1.94	166.6	---	---	123
10	EtOAc	2	disordered	1.88	170.2	---	---	293
11	acetylacetone	2	disordered	1.88	166.9	---	---	123
12	CH_3NO_2	2	ordered	1.89	171.7	---	---	123
13	CH_2I_2	3	disordered	1.95 1.98	164.9 155.9	--- 2.97	--- 160.5	123
14	anisole	3	disordered	1.91 1.89	171.6 173.1	--- 2.92	--- 173.2	123

3.1. Guest type 1

The crystal structure of **1**•(*p*-chlorotoluene)$_{0.5}$ (2:1, $P\bar{1}$, 123 K data) (Figure 4a) is similar to that of **1**•(*p*-xylene)$_{0.5}$ and shows the supramolecular axle of amide dimer (N–H···O: 1.87 Å, 175.3º) and trityl group wheels flank both sides to form cavities of *ca.* 40 Å^2 area. Disordered C_7H_7Cl guest molecules occupy channels along the *a*-axis to complete the close packing. The second NH donor participates in the designed N–H···π interaction (2.82 Å, 163.1º) with a phenyl ring of translation-related molecule. The N–H···π interaction is shorter and more linear to a phenyl carbon atom (Figure 4b) compared to the ring centroid, as noted in the CSD trend [9]. Even though approach of donor NH away from the phenyl ring centroid is energetically less favored, there are examples of N–H···π hydrogen bonds being directed towards a C atom or the C=C bond midpoint of phenyl ring [9b, 19]. Entries 2-6 in Table 1 (guest 1 in Scheme 7) have near identical arrangement of host molecules and 2:1 stoichiometry as observed in the fully ordered structure of **1**•(*p*-xylene)$_{0.5}$. [12]. The N–H···π interaction is present in seven entries given in Table 1. Structures of CH_2X_2 type (X = Cl, Br, I) lattice inclusion adducts will be discussed later in this chapter.

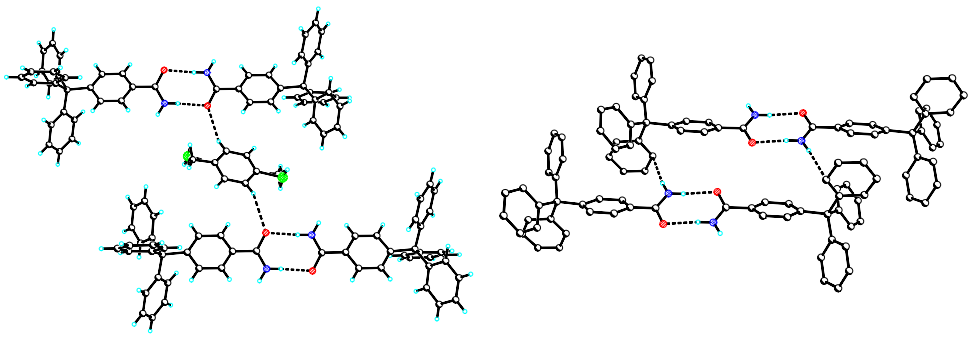

(a) **(b)**

Figure 4. Crystal structure of **1**•(*p*-chlorotoluene)$_{0.5}$. (a) Disordered guest molecule bonded to the host *via* C–H···O interaction (2.76 Å, 160.8°). (b) Intermolecular N–H···π interaction approaching the phenyl C atom of **1**. H atoms bonded to C are omitted for clarity.

3.2. Guest Type 2

Non-aromatic guests with C=O type acceptor group (entries 10-12, guest 2) have an isomorphous triclinic cell and similar packing of host molecules compared to guest 1. However, the conformation of amide group is different, in that the second NH points into the cavity (Figure 5a) and not towards another phenyl ring as in Figure 5b. Figures 5b and 5a may be viewed as the ON and OFF structures of the engineered N–H···π interaction. Now the intermolecular N–H···π interaction is absent because of strong N–H···O_{guest} hydrogen bonding (N···O: 3.0-3.3 Å). A remarkable feature in the crystal structure of **1**•(acetylacetone)$_{0.5}$ is the *anti* conformation of guest dicarbonyl groups.

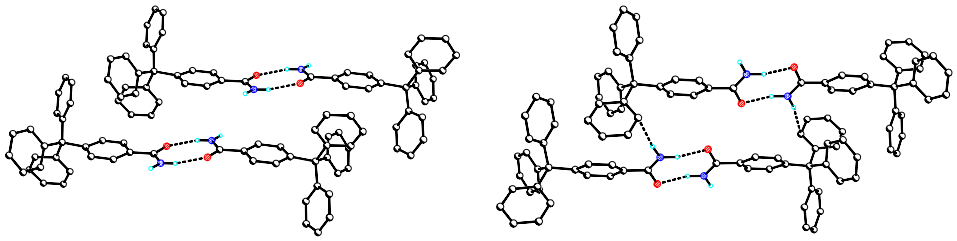

(a) **(b)**

Figure 5. (a) N–H···π OFF (**1**•CH_3NO_2)$_{0.5}$. (b) N–H···π ON (**1**•*p*-xylene)$_{0.5}$. Notice the difference in the orientation of the NH group of amide dimers in (a) and (b).

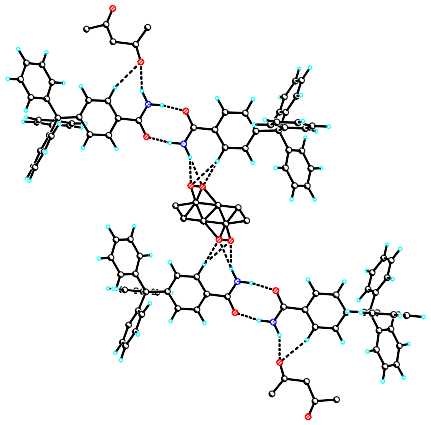

Figure 6. Crystal structure of **1**•(acetylacetone)$_{0.5}$. The orientation of the $CONH_2$ group is different from Figure 5b because of N–H···O_{guest} hydrogen bonding. *Anti* conformation of the disordered guest stabilized by N–H···O and C–H···O hydrogen bonds with different host molecules. Only one orientation of the disordered guest is shown (below and above) for clarity.

Notwithstanding the stabilization from N–H···O (1.96 Å, 155.3º; 2.25 Å, 169.8º) and C–H···O (2.25 Å, 171.0º) hydrogen bonds with different host molecules; and the fact that reflections are collected at 123 K, the guest species is disordered with 50% site occupancy factor (Figure 6). This is the first isolation of acetylacetone in its less stable *anti* diketone tautomer in the solid state [20]. The energy difference between *anti* diketone and keto-enol forms of acetylacetone is 5.0 kcal/mol from DFT calculations performed in DMol3 [21]. The presence of N–H···π interaction in **1**•(guest 1)$_{0.5}$ is similar to the observation with short peptides [7]: the weak interaction is formed only when it is impossible to engage the NH donor in bonding with stronger, conventional acceptors. This is achieved in the present system by the bulky Ph_3C wheel groups.

3.3. Guest Type 3

The dual structure type of host **1** is obtained with anisole guest (guest 3), which has two symmetry independent molecules whose amide group conformations resemble those in the structure types discussed above. Crystallographically distinct amide dimers are connected *via* N–H···O, N–H···π and C–H···O hydrogen bonds (Figure 7, Table 1). In contrast to guest 2, the second N–H···O hydrogen bond is long (*ca*. 2.50 Å) and with another host molecule instead of anisole guest.

Thus, guest-induced self-assembly [22] leads to three different host–guest structure types of **1** in which the designed N–H···π interaction is present (ON), absent (OFF), or shows dual behavior. A view down the uninterrupted channel axis in the three structure types shows near identical arrangement of host and guest molecules (Figure 8), except for differences in amide group conformations of **1**, which determine the three categories of structures. Attempts to obtain single crystals of guest-free amide host **1** were not successful whereas the solvent-free form of 4-tritylbenzoic acid was characterized by X-ray diffraction [11].

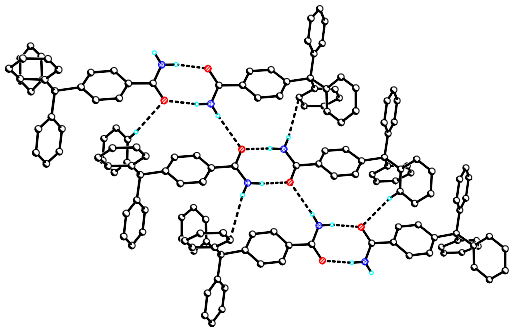

Figure 7. Crystal structure of **1**•(anisole)$_{0.5}$ in which symmetry independent amide dimers participate in N–H···O, N–H···π and C–H···O hydrogen bonds. Guest molecules are not shown for clarity.

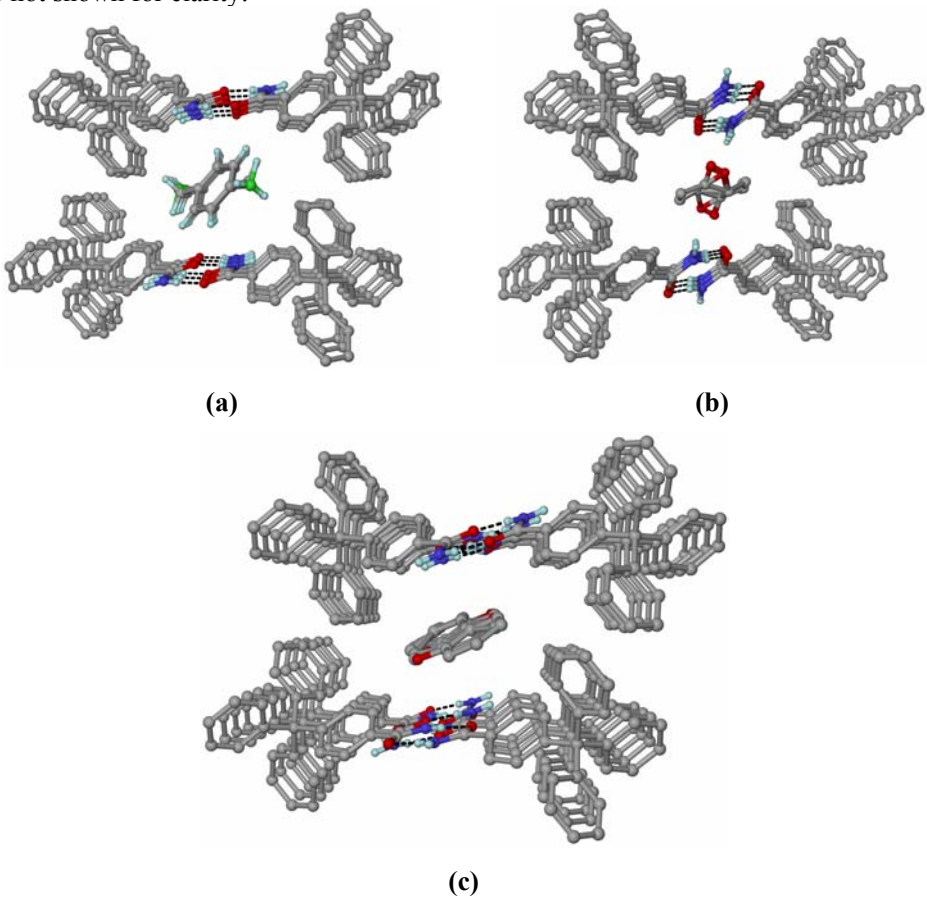

Figure 8. Perspective view of the uninterrupted channel axis in (a) **1**•(*p*-chlorotoluene)$_{0.5}$ down [100], (b) **1**•(acetylacetone)$_{0.5}$ down [100], and (c) **1**•(anisole)$_{0.5}$ down [110].

3.4. Dihalomethane (CH_2X_2) Guests

The CH_2X_2 guests, in effect, cover the three structure types observed with aromatic species, highlighting the role of solvent in guiding the N–H···π interaction as well as the final adduct structure. Electron density in the host cavity is diffuse for CH_2X_2 type guests because guest atoms are disordered and conatin much heavier halogens in a small molecule. It is therefore difficult to reliably determine the host•guest stoichiometry from X-ray data alone. The *R* factors for these channel inclusion structures are slightly higher because of heavy guest disorder. However, host atoms are well-ordered and the position of N–H···π interaction can be ascertained in CH_2Br_2 (entry 7, type 1) and CH_2I_2 (entry 13, type 3) inclusion structures whereas the interaction is absent in CH_2Cl_2 adduct (entry 9, type 2). The packing in these structures is otherwise identical to that described above except for CH_2Cl_2 inclusion adduct, which is now discussed. The structure of **1**•$(CH_2Cl_2)_{1.5}$ (space group C_2/c) is different from other structures in that: (1) host•guest stoichiometry is 1:1.5 instead of 1:0.5, (2) CH_2Cl_2 guest (one molecule, ordered) resides in channels between supramolecular axles and the other (half molecule, disordered) occupies channels between trityl groups of inversion-related host molecules (Figure 9) [23]. The higher electronegativity of Cl compared to Br and I means that it is able to activate N–H···Cl (2.84 Å, 120.3º) interaction with a guest molecule, thereby engaging the hydrogen that could have participated in the N–H···π interaction. Ordered CH_2Cl_2 guest molecules in the wider channel are connected *via* C–H···Cl interactions in the shape of a linearly fused supramolecular polycyclohexane (Scheme 8). This is the first occurrence of CH_2Cl_2 molecules assembled in an infinite linear tape [24]. Inclusion of CH_2Cl_2 in hydrophobic channels between Ph_3C groups could be due to the small size of guest and weak C–H···Cl interactions (2.9-3.2 Å).

CH_2Br_2 behaves like an aromatic, hydrophobic guest because of less electronegative and softer bromine atom, and the N–H···π interaction is present in this structure. Large size and hydrophobic nature of the iodo groups of CH_2I_2 result in dual nature of the NH interaction (N–H···π, N–H···O) in its crystal structure which is similar to the **1**•$(anisole)_{0.5}$ structure.

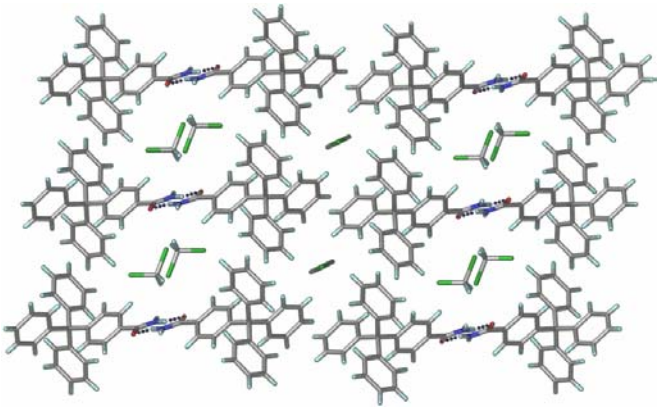

Figure 9. Crystal structure of **1**•$(CH_2Cl_2)_{1.5}$ down [010] to show two types of channels. Ordered guest molecules are present in the voids between amide dimer axles and disordered molecules are included in the smaller cavity between aromatic residues. CH_2Cl_2 molecules in the larger channel extend along the *b*-axis *via* C–H···Cl interactions to form the infinite tape of supramolecular cyclohexane rings shown in Scheme 8.

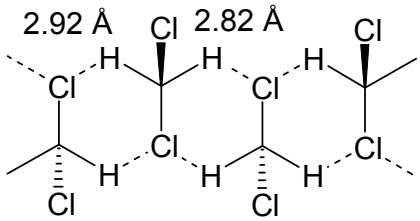

Scheme 8. Linearly fused supramolecular polycyclohexane of C–H···Cl interactions in the channel framework of **1**•$(CH_2Cl_2)_{1.5}$. This is the first occurrence of tape motif in the solid state.

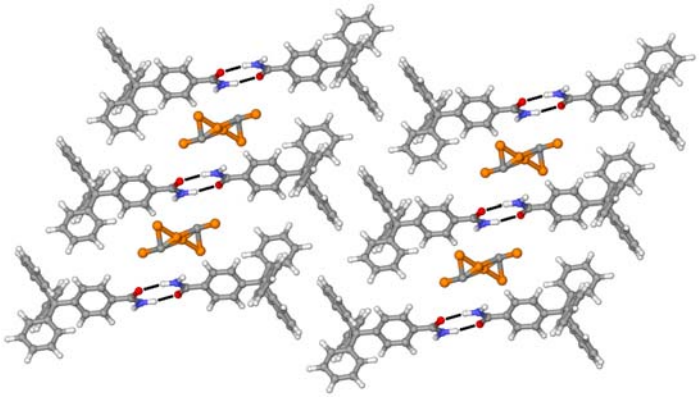

Figure 10. Crystal structure of **1**•$(CH_2Br_2)_{0.5}$. Molecules shown are in (102) plane.

4. Lattice Energy Calculations

The presence of both amide group conformations as symmetry-independent molecules in anisole and CH_2I_2 inclusion compounds, showing N–H···π and N–H···O interactions in the same structure, suggested that the energies of these host•guest crystals should be compared. Miminized crystal lattice energies (Cerius[2], Dreiding 2.21 force field) [25] for the host portion of crystal structure are listed in Table 2. The total energy, per molecule of **1** in the crystal, is in the range −76 to −89 kcal/mol. Crystal lattice energy of host•guest structure type 3 < type 2 < type 1, in accordance with fewer number of strong hydrogen bonds and this trend is reflected in the hydrogen bond and electrostatic energy components also.

Table 2. Minimized crystal lattice energy of **1** (kcal/mol) per host molecule. Guest molecules are excluded from the calculation.

Inclusion Compound	Total	van der Waals	Electrostatic	Hydrogen bond
1•(anisole)$_{0.5}$	–89.27	–63.30	–17.95	–8.03
1•(*p*-xylene)$_{0.5}$	–76.84	–57.09	–13.28	–6.45
1•(*p*-Cl-toluene)$_{0.5}$	–81.67	–63.20	–11.10	–7.36
1•(acetyl-acetone)$_{0.5}$	–86.19	–63.46	–15.69	–7.03
1•(EtOAc)$_{0.5}$	–88.52	–64.90	–16.05	–7.56
1•(CH_3NO_2)$_{0.5}$	–87.85	–64.61	–16.07	–7.16

5. Conformations of Host Molecule

An overlay diagram of amide group conformations in crystal structures of **1** shows that C=O and NH_2 fragments adopt different orientations (Figure 6). The robust synthon in the persistent wheel-and-axle framework is the strong N–H···O hydrogen bond dimer between amide groups and numerous aromatic edge-to-face and offset face-to-face interactions between phenyl rings [11], whereas host···guest interactions and amide group orientation control ON, OFF and DUAL structures of the engineered N–H···π hydrogen bond.

There have been a few reports on characterization of weak N–H···π hydrogen but these are mostly single structure examples [6, 17]. Short C–H···O interactions were identified in phosphonium aryloxide salts [5]. The stronger N^+–H···π hydrogen bond (energy 16 kcal/mol) is persistent in ammonium tetraphenylborate. This study is the first report on the designed recurrence and tuning of N–H···π interaction in a family of host·guest crystal structures making it possible to analyze structure correlation trends.

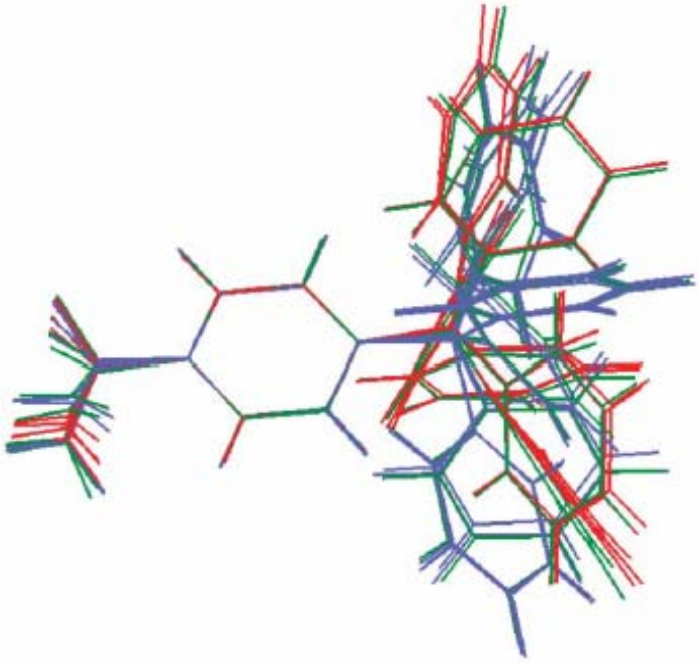

Figure 11. Overlay diagram of 4-(triphenylmethyl)benzamide host **1** to show $CONH_2$ and trityl group conformations in its inclusion structures with different guest molecules. Blue = guest type 1, N–H···π, red = guest type 2, N–H···O_{guest}; green = guest type 3, both N–H···π and N–H···O_{host}.

6. FT-IR Spectroscopy

Strong N–H···O and weak N–H···π hydrogen bonds have been studied by infrared spectroscopy [19]. The stronger the hydrogen bond, the greater is the bathochromic shift in solid state IR spectrum compared to stretching frequency in CCl_4 solution. Infrared N–H stretching frequencies for selected **1**•$(guest)_{0.5}$ compounds are listed in Table 3. Two intense bands correspond to the strong and weak hydrogen-bonded

NH groups corresponding to *syn* NH and *anti* NH groups, with the former being red shifted because of weaker N–H bond. The bathochromic shift in IR spectrum and shorter N–H···π hydrogen bond distance in **1**•(*p*-chlorotoluene)$_{0.5}$ and **1**•(*m*-xylene)$_{0.5}$ when crystal data are collected at 123 K compared to 293 K (Table 1) is consistent with the hydrogen bond nature of this interaction.

Table 3. IR stretching frequency (cm^{-1}) of amide NH groups in the solid state.

Sample	**N–H···π**	**N–H···O**
1•(anisole)$_{0.5}$	3478	3418
1•(*p*-xylene)$_{0.5}$	3476	3150
1•(*p*-Cl-toluene)$_{0.5}$	3474	3150
1•(acetylacetone)$_{0.5}$	3447	3169
1•(CH_3NO_2)	3462	3171
1•(CH_2Br_2)$_{0.5}$	3468	3159

7. TGA and DSC Measurements

Thermochemical data provide valuable information about the robustness of the host lattice and the strength of host···guest interactions [26]. In cases of heavy guest disorder (e.g. CH_2X_2 type guests), TGA measurements give an independent and accurate estimate of host·guest ratio in addition to the X-ray structure. DSC confirms the phase purity of solid adducts and quantifies the energy change associated with guest release and melting of host compound. TGA and DSC trace for selected guest inclusion adducts of **1** are shown in Figure 12 and T_{onset} values for guest release are listed in Table 4. The host•guest ratio determined from X-ray structures is in agreement with weight loss for guest release in TGA measurements, within experimental error. The second endotherm in DSC corresponds to melting of host **1**. The strength of host lattice **1** in trapping volatile guest species is evident from T_{onset} values for CH_2Cl_2 and CH_2Br_2, which are well above their respective boiling points. Two types of CH_2Cl_2 guests are released from the host structure at different stages: first disordered solvent molecules between triphenyl groups

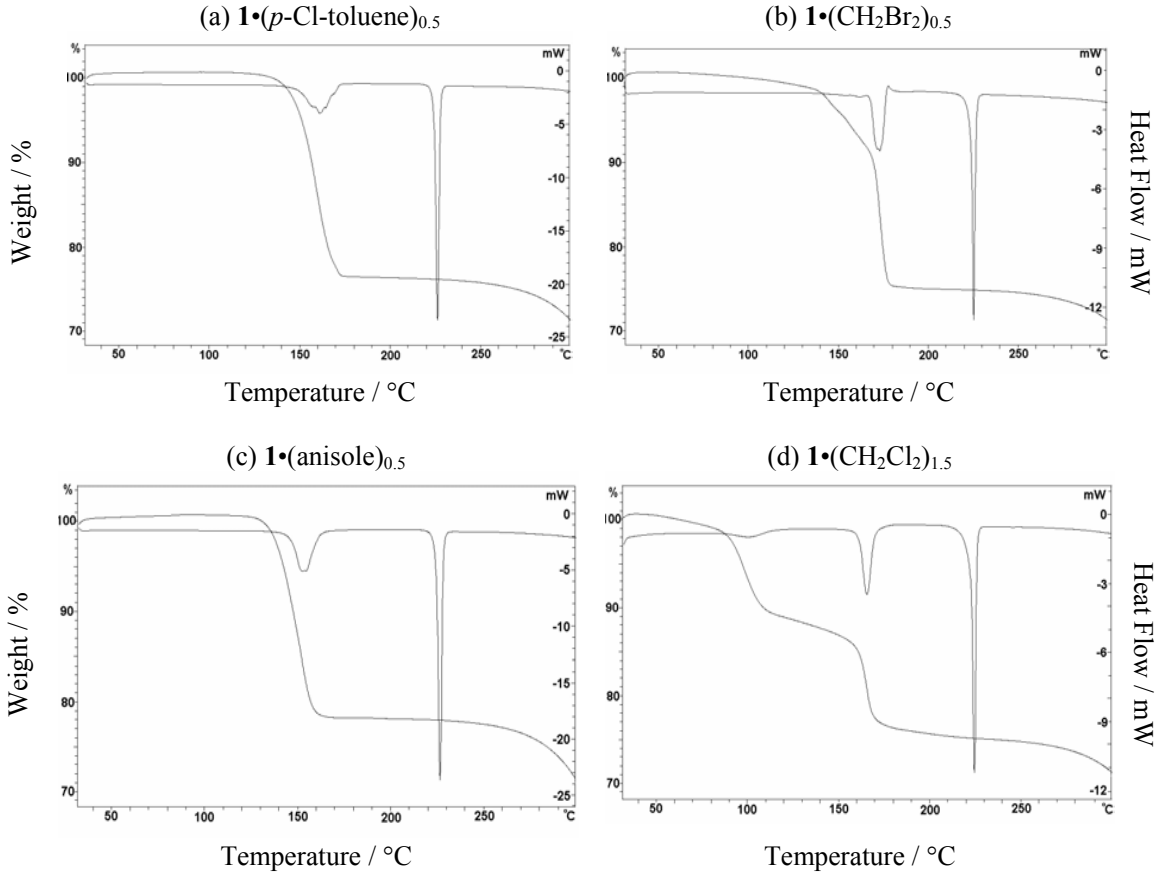

Figure 12. TGA/DSC trace for inclusion compounds. The first endotherm corresponds to guest loss and the second endotherm is melting of **1**. Weight loss in TGA is consistent with host·guest stoichiometry from X-ray structures.

are evolved and then ordered hydrogen-bonded tape of solvent molecules (connected *via* C–H···Cl interactions) is released from the channel between amide dimers. The overall weight loss corresponds to 1.5 solvent molecules as determined from the X-ray structure. Enthalpy change during guest release (ΔH values listed in Table 4) is difficult to determine accurately because it depends on particle size distribution and several other factors [26].

Table 4. Thermal analysis (TGA and DSC) on some inclusion compounds of **1**.

Inclusion complex	Observed weight loss from TG (%)	Calculated weight loss from X-ray	Guest release T_{on} / °C	Boiling point of guest (°C)	ΔH (J g^{-1}) (for guest release)
1•(*p*-Cl-toluene)$_{0.5}$	14.65	12.92 (1:0.5)	153	162	–65.79
1•(*p*-xylene)$_{0.5}$	12.26	11.3 (1:0.5)	130	138	–66.05
1•(*p*-Br-toluene)$_{0.5}$	19.16	16.01 (1:0.5)	146	184	–64.24
1•(anisole)$_{0.5}$	12.67	11.4 (1:0.5)	146	154	–56.54
1•(CH_2Cl_2)$_{1.5}$	24.53	28.46 (1:1.5)	85-160	40	–56.73
1•(CH_2Br_2)$_{0.5}$	16.56	16.20 (1:0.5)	168	97	–43.68

8. Conclusions

Crystal engineering is concerned with the study of intermolecular interactions, the design of new solids and architectures, and the development of functional materials. The present study combines all these aspects in the title host system **1**. While there are several examples of wheel-and-axle architectures, the present study is the first report on using strong host···host recognition to provide a robust framework within which the occurrence of a weak interaction is directed through host···guest hydrogen bonding. Three categories of host·guest structures are observed for a wide selection of guest molecules. The interplay of strong N–H···O and weak N–H···π hydrogen bonds is important in the stabilization of protein and drug·enzyme structures. The weak N–H···π hydrogen bond has been introduced in the persistent N–H···O framework of **1** through

deliberate design rather than observed as a serendipitous result. The presence of two symmetry-independent amide groups in anisole and CH_2I_2 inclusion compounds means that the energies of these conformations and host·guest adducts are comparable and so the guest is important in directing the final crystal structure. Two types of host channels, one hydrophilic and another hydrophobic include ordered and disordered CH_2Cl_2 guest molecules, respectively. The high T_{onset} temperature in TGA for CH_2Cl_2 and CH_2Br_2 confirms the ability of host channels surrounded by hydrogen bonding donor/acceptor groups to trap guest molecules tightly in the crystal lattice. The presence and absence of N–H$\cdots\pi$ interaction is shown to be related to the conformation of the amide group in isomorphous crystal structures having comparable lattice energies. DSC and TGA measurements confirm the functional behavior of host **1**.

9. Experimental Section

Synthesis and Crystallization

4-(Triphenylmethyl)benzamide **1**: A mixture of 4-(triphenylmethyl)benzoic acid [11] (37 mg, 0.1 mmol) and $SOCl_2$ (1 mL, 1 mmol) was refluxed under nitrogen for 1.5 h, excess $SOCl_2$ was removed at reduced pressure. Dry ether (1 mL) was added and the reaction mixture treated with 2 mL of 25% aq. NH_3 at 0 ºC and then stirred at ambient temperature for 45 min. The precipitated solid was collected by filtration and dried in vacuum to give amide **1** (30 mg, 80%), which was purified by column chromatography. The amide was crystallized from CH_2Cl_2. M.p. 224-225 ºC. ^{1}H NMR ($CDCl_3$, δ): 8.08 (d, J 7 Hz, 2 H), 7.46 (d, J 7 Hz, 2 H), 7.31-7.28 (m, 15 H), 6.00 (br s, 2 H, NH_2). Crystalline adducts were grown by dissolving **1** in the corresponding pure solvent and slow evaporation at ambient temperature. All crystals are needle shaped and melt at 223-225 ºC. IR (KBr, cm^{-1}): **1**•*p*-xylene: 3476, 3283, 3157, 1670, 1612, 1489, 1440, 1033, 893, 846, 750, 702, 630, 493; **1**•*p*-chlorotoluene: 3474, 3150, 1674, 1612, 1491, 1440, 1381, 1018, 746, 700, 630, 486; **1**•CH_2Br_2: 3468, 3159, 1668, 1610, 1489, 1440, 1381, 1016, 746, 700, 630; **1**•anisole: 3477, 3418, 1674, 1606, 1491, 1385, 746, 700, 630; **1**•acetylacetone: 3447, 3169, 1670, 1616, 1491, 1388, 746, 700, 630; **1**•CH_3NO_2: 3462,

3171, 1670, 1614, 1558, 1489, 1440, 1381, 1082, 746, 700, 628, 522; **1**•CH_2Cl_2: 3438, 3350, 3210, 1670, 1649, 1616, 1558, 1489, 1386, 1033, 846, 750, 702, 630, 520.

X-ray Crystallography

Reflections were collected on single crystals of **1** with *p*-xylene, *m*-xylene, *p*-chlorotoluene, CH_2Cl_2 and EtOAc guests included on Bruker SMART 1000 CCD diffractometer using Mo-Kα radiation (λ = 0.71073 Å) at 293(2) K. Structure solution and refinement were carried out with SHELX-97 [27]. Refinement of coordinates and anisotropic thermal parameters of non-hydrogen atoms were carried out by the full-matrix least-squares refinement. All H-atoms except methyl protons of *p*-xylene, *p*-chlorotoluene and EtOAc, and methylene protons on EtOAc and CH_2Cl_2 were located experimentally from the electron density difference maps. Methyl and methylene protons were generated geometrically (C–H distance fixed at 0.96 Å) and allowed to ride on their parent atoms. *m*-xylene, EtOAc, *p*-chlorotoluene and CH_2Cl_2 molecules reside on the special position and are disordered about the inversion centre; these atoms have an occupancy of 0.5.

X-ray intensity for **1** with *m*-xylene, *p*-chlorotoluene, CH_2Br_2 and anisole at 123(2) K and *p*-bromotoluene at 203(2) K were measured on Bruker SMART CCD area-detector diffractometer equipped with graphite monochromator and Mo-Kα radiation (λ = 0.71073 Å). Intensities were corrected for absorption effects using the multi-scan technique SADABS [28]. All or some hydrogen atoms on disordered guest molecules could not be located and these are omitted from the refinement. The methyl protons of the *m*-xylene, *p*-chlorotoluene and *p*-bromotoluene were generated geometrically (C–H distance fixed at 0.96 Å) and allowed to ride on their parent atoms and the guest disorder in these cases is mentioned as above.

Reflections were collected for single crystals of **1** with CH_2Cl_2, CH_2I_2, CH_3NO_2 and acetylacetone guests at 123(1) K on Bruker SMART APEX CCD area detector system equipped with graphite monochromator and Mo-Kα fine-focus sealed tube (λ = 0.71073 Å). Intensities were corrected for absorption effects using the multi-scan technique SADABS [28]. Structures were solved and refined using Bruker SHELXTL

(version 6.14) [29]. All H-atoms except protons of guest molecules were located experimentally from electron density difference maps. Methyl and methylene protons of acetylacetone, CH_3NO_2 and CH_2Cl_2 were generated geometrically (C–H distance fixed at 0.96 Å) and allowed to ride on their parent atoms. Acetylacetone and CH_2Cl_2 molecules reside on the special position and are disordered about the inversion centre; these atoms have occupancy of 0.5.

Hydrogen atoms on host molecules are fully ordered in all crystal structures. Crystallographic details are summarized in Appendix 2.

Thermal Analysis

Differential scanning calorimetry (DSC) was performed on Mettler Toledo DSC 822e module and thermal gravimetry (TG) was performed on Mettler Toledo TGA/SDTA 851e module. Crystals taken from the mother liquor were blotted dry on filter paper and placed in open alumina pans for TG experiment and in crimped but vented aluminum sample pans for DSC experiment. Sample size in each case was 5-7 mg. The sample was heated from 30-300 °C at a rate of 10 °C/min. The samples were purged with a flow of dry nitrogen at 150 ml/min for DSC and 50 ml/min for TG runs.

FT-IR Spectra

Recorded on JASCO 5300 spectrophotometer using KBr pellet.

REFERENCES

CHAPTER 1

[1.1] (a) P.J. Langley and J. Hulliger, *Chem. Soc. Rev.*, **1999**, *28*, 279. (b) M. Ohring, *Engineering Materials Science*, Elsevier, New York, **1995**. (c) V. Ramamurthy and D.F. Eaton, *Chem. Mater.*, **1994**, *6*, 1128.

[1.2] G.R. Desiraju, *Crystal Engineering: The Design of Organic Solids*, Elsevier, New York, **1989**.

[1.3] *Organic Solid State Chemistry*, Ed.: G.R. Desiraju, Elsevier, Amsterdam, **1987**.

[1.4] (a) L.S. Reddy, N.J. Babu and A. Nangia, *Chem. Commun.*, **2006**, 1369. (b) Ö. Almarsson and M.J. Zaworotko, *Chem. Commun.*, **2004**, 1889. (c) R.D.B. Walsh, M.W. Bradner, S.G. Fleischman, L.A. Morales, B. Moulton, N. Rodríguez-Hornendo and M.J. Zaworotko, *Chem. Commun.*, **2003**, 186.

[1.5] (a) A.W.K. de Jong, *Ber. Dtsch. Chem. Ges.*, **1923**, *56*, 818. (b) H. Stobbe and F.K. Steinberger, *Ber. Dtsch. Chem. Ges.*, **1922**, *55*, 2225. (c) A. Senier and F.G. Shephard, *J. Chem. Soc.*, **1909**, *95*, 1943. (d) G. Ciamician and P. Silber, *Ber. Dtsch. Chem. Ges.*, **1901**, *34*, 2040. (e) W. Marckwald, *Z. Phys. Chem.*, **1899**, *30*, 140.

[1.6] (a) D.Y. Curtin and I.C. Paul, *Chem. Rev.*, **1981**, *81*, 525. (b) D.Y. Curtin and I.C. Paul, *Science*, **1975**, *187*, 19. (c) J.M. Thomas, *Philos. Transac. R. Soc. London*, **1974**, *A277*, 251. (d) I.C. Paul and D.Y. Curtin, *Acc. Chem. Res.*, **1973**, *7*, 223.

[1.7] (a) G.M.J. Schmidt, *Pure Appl. Chem.*, **1971**, *27*, 647. (b) D. Rabinovich, G.M.J. Schmidt and Z. Shaked, *J. Chem. Soc.*, **1970**, 17.

[1.8] H.W. Kohlschutter, *Z. Anorg. Allg. Chem.*, **1918**, *105*, 121.

[1.9] V.V. Boldyrev, *Reactivity of Solids: Past, Present and Future*, Blackwell, Oxford, **1996**.

[1.10] R. Pepinsky, *Phys. Rev.*, **1955**, *100*, 971.

[1.11] A.H. Cottrell, *Dislocations and Plastic Flow*, Claredon, Oxford, London, **1953**.

[1.12] (a) *Crystal Engineering: From Molecules and Crystals to Materials*; Eds.: D. Braga and A.G. Orpen, NATO ASI Series, Netherlands, **1999**. (b) *Design of Organic Solids*, Ed.: E. Weber, Springer, New York, **1998**.

[1.13] (a) G.R. Desiraju, in *Stimulating Concepts in Chemistry*, Eds.: F. Vögtle, J.F. Stoddart and M. Shibasaki, Wiley-VCH, Weinheim, **2002**, p. 293. (b) A. Nangia and G.R. Desiraju, *Top. Curr. Chem.*, **1998**, *198*, 57. (c) G.R. Desiraju, *Angew. Chem. Int. Ed. Engl.*, **1995**, *34*, 2311.

[1.14] (a) G.R. Desiraju and T. Steiner, *The Weak Hydrogen Bond in Structural Chemistry and Biology*, Oxford University Press, Oxford, UK, **1999**. (b) D. Das, R.K.R. Jetti, R. Boese and G.R. Desiraju, *Cryst. Growth Des.*, **2003**, *3(5)*, 675. (b) V.A. Russell and M.D. Ward, *J. Mater. Chem.,* **1997**, *7*, 1123.

[1.15] G.R. Desiraju, *Chem. Commun.*, **2005**, 2995.

[1.16] Crystal engineering: Selected references include: (a) *Frontiers in Crystal Engineering*, Eds.: E.R.T. Tiekink and J.J. Vittal, John Wiley and Sons, Chichester, **2006**. (b) S. Aitipamula and A. Nangia, *Chem. Eur. J.*, **2005**, *11*, 6727. (c) B.K. Saha, R.K.R. Jetti, L.S. Reddy, S. Aitipamula and A. Nangia, *Cryst. Growth Des.*, **2005**, *5*, 887. (d) P.M. Bhatt, N.V. Ravindra, R. Banerjee and G.R. Desiraju, *Chem. Commun.*, **2005**, 1073. (e) G.M. Whitesides, J.P. Mathias and C.T. Seto, *Science*, **1991**, *254*, 1312. (f) D.H. Bush, *Acc. Chem. Res.*, **1978**, *11*, 392.

[1.17] Metallurgy references: (a) A.H. Cottrell, *An Introduction to Metallurgy*, Edward Arnold, London, **1975**. (b) N. Sevryukou, B. Kuzmin, Y. Chelishchev, (Translated from the Russian by B. Kuzetsov), *General Metallurgy*, Pease Publishers, Moscow, (Published year was not mentioned in the book, but first it appeared in the Indian market in **1964**). (c) R.G. Ward, *An Introduction to the Physical Chemistry of Iron and Steel Making*, ELBS and Edward Arnold, London, **1962**.

[1.18] (a) G.E. Dieter (adapted by D. Bacon), *Mechanical Metallurgy*, SI Metric Edition, McGraw-Hill, Singapore, **1988**. (b) R.W.K. Honeycombe, *The Plastic Deformation of Metals*, Edward Arnold, London, **1968**. (c) F. Garofalo,

Fundamentals of Creep and Creep-Rupture in Metals, The MacMillan Company, New York, **1965**. (d) A.H. Cottrell, *The Mechanical Properties of Matter*, John Wiley & Sons, Inc. New York, **1964**.

[1.19] (a) E.N. da C. Andrade, *Creep and Recovery*, Cleveland American Society for Metals, **1957**, 176. (b) E.N. da C. Andrade, *Proc. Roy. Soc.*, **1914**, *A 90*, 329. (c) E.N. da C. Andrade, *Proc. Roy. Soc.*, *A*, **1910**, *84*, 1.

[1.20] A.H. Cottrell, *Theoretical Structural Metallurgy*, Edward Arnold, London, **1964**.

[1.21] (a) M. Polanyi, *Z. Phys.*, **1934**, *89*, 660. (b) E. Orowan, *Z. Phys.*, **1934**, *89*, 605. (c) G.I. Taylor, *Proc. R. Soc.*, **1934**, *A145*, 362.

[1.22] A. Nangia, *Ency. Supramol. Chem.*, Eds.: J.L. Atwood and J.W. Steed, Marcel Dekker, New York, **2004**, pp. 967–972.

[1.23] For a general discussion of isostructurality, see: L. Fábián and A. Kálmán, *Acta Crystallogr.*, **1999**, *B55*, 1099.

[1.24] J. Bernstein, *Polymorphism in Molecular Crystals*, Oxford Univ. Press, Oxford, **2002**.

[1.25] J. Bernstein, R.J. Davey and J.-O. Henck, *Angew. Chem. Int. Edn.*, **1999**, *38*, 3440.

[1.26] (a) A. Nangia, *Cryst. Growth Des.*, **2006**, *6*, 2. (b) J. Bernstein, *Cryst. Growth Des.*, **2005**, *5*, 661. (c) G.R. Desiraju, *Cryst. Growth Des.*, **2004**, *4*, 1089. (d) K.R. Seddon, *Cryst. Growth Des.*, **2004**, *4*, 1087.

[1.27] *Comprehensive Supramolecular Chemistry*, Eds.: J.-M. Lehn, J.L. Atwood, J.E.D. Davies, D.D. MacNicol and F. Vögtle, Pergamon, New York, **1996**.

[1.28] (a) A. Dey, M.T. Kirchner, V.R. Vangala, G.R. Desiraju, R. Mondal and J.A.K. Howard, *J. Am. Chem. Soc.*, **2005**, *127(30)*, 10545. (b) J.D. Dunitz and H.A. Scheraga, *Proc. Natl. Acad. Sci. U.S.A.*, **2004**, *101*, 14309. (c) S.L. Price, *Ency. Supramol. Chem.*, Eds.: J.L. Atwood and J. Steed, Marcel Dekker, New York, **2004**, 371. (d) J.D. Dunitz *Chem. Commun.,* **2003**, 545. (e) G.R.. Desiraju, *Nat. Mater.*, **2002**, *1*, 77.

[1.29] D. Halliday, R. Resnick and J. Walker, *Fundamentals of Physics*, John Wiley, New York, **1997**, p. 309.

CHAPTER 2

[2.1] L. Pauling, *The Nature of the Chemical Bond and the Structure of Molecular Crystals*, Cornell University Press, Ithaca, **1939**.

[2.2] A. Kelly, *Strong Solids*, Clarendon Press, Oxford, London, **1966**.

[2.3] (a) H. Krebs, *Fundamentals of Inorganic Crystal Chemistry*, McGraw-Hills Book Company, (UK), **1968**. (b) A.F. Wells, *Structural Inorganic Chemistry*, Claredon Press, Oxford, **1984**. (c) A.F. Wells, *Three-dimensional Nets and Polyhedra*, Wily-Interscience, New York, **1977**. (d) D.M. Adams, *Inorganic Solids: an Introduction to Concepts in Solid-State Structural Chemistry*, John Wiley & Sons, London, **1974**.

[2.4] K.S. Novoselov, A.K. Geim, S.V. Morozov, D. Jiang, Y. Zhang, S.V. Dubonos, I.V. Grigorieva and A.A. Firsov, *Science*, **2004**, *306*, 666.

[2.5] (a) C.M. Reddy, S. Basavoju and G.R. Desiraju, *Chem. Commun.*, **2005**, 2439. (b) J. Bernstein, *Nature Mater.*, **2005**, *4*, 427. (c) J.A.R.P. Sarma and A. Nagaraju, *J. Chem. Soc., Perkin Trans. 2*, **2000**, 1113.

[2.6] (a) K. Kobayashi, T. Shirasaka, E. Horn and N. Furukawa, *Tetrahedron Lett.*, **2000**, *41*, 89. (b) V.R. Thalladi, K. Panneerselvam, C.J. Carrell, H.L. Carrell and G.R. Desiraju, *J. Chem. Soc., Chem. Commun.*, **1995**, 341. (c) K. Xu, M. Douglas and R.A. Pascal, *J. Am. Chem. Soc.*, **1994**, *116*, 105 (d) D.S. Reddy, B.S. Goud, K. Panneerselvam and G.R. Desiraju, *J. Chem. Soc., Chem. Commun.*, **1993**, 663.

[2.7] K.S. Novoselov, A.K. Geim, S.V. Morozov, D. Jiang, Y. Zhang, S.V. Dubonos, I.V. Grigorieva and A.A. Firsov, *Science*, **2004**, *306*, 666.

[2.8] (a) B. Palosz, *Acta Cryst.*, **1982**, *B38*, 3001. (b) B. Palosz and S. Gierlotka, *Acta Cryst.*, **1985**, *C41*, 1407.

[2.9] R.R. Shuvalov and P.C. Burns, *Acta Crystallogr.*, **2003**, *C59*, i47.

[2.10] M. Ohkita, M. Kawano, T. Suzuki and T. Tsuji, *Chem. Commun.*, **2002**, 3054.

[2.11] R.P. Feynman, R.B. Leighton and M. Sands, *The Feynman Lectures on Physics, Vol. 2*, Addison-Wesley, USA, **1964**, pp.30-8.

[2.12] (a) G. Kaupp and M.R. Naimi-Jamal, *CrystEngComm*, **2005**, *7(66)*, 402. (b) G. Kaupp, J. Schmeyers and U.D. Hangen, *J. Phys. Org. Chem.*, **2002**, *15*, 307.

[2.13] Some reports related to mechanical properties of molecular crystals include: (a) J.N. Grima, J.J. Williams and K.E. Evans, *Chem.Commun.*, **2005**, 4065. (b) G.M. Day, S.L. Price and M. Leslie, *Cryst. Growth Des.* **2001**, *1*, 13. (c) P. Pavlides, D. Pugh and K.J. Roberts, *Acta Cryst.* **1991**, *A47*, 846.

[2.14] G. Kaupp and J. Schmeyers, *Angew. Chem. Int. Ed. Engl.*, **1993**, *32*, 1587.

[2.15] C.M. Reddy, M.T. Kirchner, R.C. Gundakaram, K.A. Padmanabhan and G.R. Desiraju, *Chem. Eur. J.*, **2005**, *12*, 2222.

[2.16] E. Bosch and C.L. Barnes, *Cryst. Growth Des.*, **2002**, *2*, 299.

[2.17] (a) V.A. Phillips and P. Cannon, *Nature*, **1960**, *187*, 313. (b) M.S. Dresselhaus and G. Dresselhaus, *Adv. Phys.*, **2002**, *51*, 1. (c) L.M. Viculis, J.J. Mack and R.B. Kaner, *Science*, **2003**, *299*, 1361.

[2.18] A.R. Verma and P. Krishna, *Polymorphism and Polytypism in Crystals*, Wiley, New York, **1966**, pp. 115.

[2.19] J.A.R.P. Sarma and G.R. Desiraju, *Acc. Chem. Res.*, **1986**, *19*, 222.

[2.20] J.K.S. Kim, E.R. Boyko and G.B. Carpenter, *Acta Crystallogr.*, **1973**, *B29*, 1141.

[2.21] G.A. Chadwick, D.A. Smith, *Grain Boundary Structure and Properties*, Academic Press, London, **1976**.

[2.22] (a) G.L. Wheeler and S.D. Colson, *J. Chem. Phys.*, **1976**, *85*, 1227. (b) I. Woodward, *Acta Crystallogr.*, **1958**, *11*, 441.

[2.23] D.L. Mattern, *J. Org. Chem.*, **1984**, *49*, 3051.

CHAPTER 3

[3.1] A.M. Dubinskaya, *Russ. Chem. Rev.*, **1999**, *68(8)*, 637.

[3.2] (a) H.K. Chan and E. Doelker, *Drug. Dev. Ind. Pharm.*, **1985**, *11*, 315. (b) N. Kaneniwa and O. Makoto, *Chem. Pharm. Bull.*, **1985**, *33*, 1660.

[3.3] S.R. Byrn, R.R. Pfeiffer and J.G. Stowell, "*Solid-State Chemistry of Drugs*" SSCI, Inc. West Lafayette, Indiana, USA, **1999**.

[3.4] (a) J.D. Wright, *Molecular Crystals*, Cambridge University Press, Cambridge, **1996**. (b) A.R. West, *Solid State Chemistry and its Applications*, Wiley, **1984**, pp. 347.

[3.5] G.E. Dieter (adapted by D. Bacon), *Mechanical Metallurgy*, SI Metric Edition, McGraw-Hill, Singapore, **1988**, pp. 8, 301, 433, 651-678. See p. 652 for the different curved shapes that can be produced by changing the method of support and location of anchor.

[3.6] (a) J.D. Lubahn and G. Sachs, *Trans. ASME*, **1950**, *72*, 201. (b) B.W. Shaffer and E.E. Unger, *Trans. ASME*, Ser. E: *J. Appl. Mech.*, **1960**, *27*, 34.

[3.7] (a) G.M. Brown and O.A.W. Strydom, *Acta Crystallogr.*, **1974**, *B30*, 801. (b) J.A.R.P. Sarma and G.R. Desiraju, *Chem. Phys. Lett.*, **1985**, *117*, 160.

[3.8] S. Basavoju, C.M. Reddy and G.R. Desiraju, *Acta Cryst.*, **2005**, *E61*, o822.

[3.9] C.M. Reddy, R.C.Gundakaram, S. Basavoju, M.T. Kirchner, K.A. Padmanabhan and G.R. Desiraju, *Chem. Commun.*, **2005**, 3945.

[3.10] E. Baharie and G.S. Pawley, *Acta Crystallogr.,* **1979**, *A35*, 233.

[3.11] K.A. Padmanabhan, P. Mondal and H. Hahn, *J. Mater. Science*, **2005**, *40*, 6113.

[3.12] H.J. Milledge and L.M. Pant, *Acta Crystallogr.*, **1960**, *13*, 285.

[3.13] (a) Y. Takaki, Y. Sasada and T. Watanabe, *Acta. Cryst.*, **1960**, *13*, 693. (b) G. Ro and H. Sorum, *Acta Cryst.*, **1972**, *B28*, 991. (c) G.R. Desiraju, *Science*, **1997**, *278*, 404.

[3.14] (a) S. Roy, S. Aitipamula and A. Nangia, *Cryst. Growth Des.*, **2005**, *5*, 2269. (b) A. Sivalakshmidevi, K. Vyas, S.M. Rao and G.O. Reddy, *Acta Crystallogr.,* **2002**, *E58*, o1072. (c) D. Vega, D. Fernandez and G. Echeverria, *Acta Crystallogr.,* **2000**, *C56*, 1009.

[3.15] M. Tonogaki, T. Kawata, S. Ohba, Y. Iwata and I. Shibuya, *Acta Crystallogr.*, **1993**, *B49*, 1031.

[3.16] G.R. Desiraju and R.L. Harlow, *J. Am. Chem. Soc.*, **1989**, *111*, 6757.

[3.17] (a) N.W. Thomas and G.R. Desiraju, *Chem. Phys. Lett.*, **1984**, *110*, 99. (b) C. Bavoux, M. Perrin and A. Thozet, *Acta Cryst.*, **1980**, *B36*, 741.

[3.18] L.S. Reddy, A. Nangia and V.M. Lynch, *Cryst. Growth Des.*, **2004**, *4*, 89.

[3.19] D. Britton and W.B. Gleason, *Acta Cryst.*, **1977**, *B33*, 3926.

[3.20] (a) P. Coppens, *Acta Cryst.*, **1964**, *17*, 573. (b) P. Coppens and G.M.J. Schmidt, *Acta Cryst.*, **1964**, *17*, 222.

[3.21] G. Wojcik, I. Mossakowska, J. Holband and W. Bartkowiak, *Acta Cryst.*, **2002**, *B58*, 998.

[3.22] T.M. Krygowski, E. Pindelska, T. A-Ostrowska, S.J. Grabowski and A.T. Dubis, *J. Phys.Org. Chem.*, **2001**, *14*, 349.

[3.23] (a) T.N. Bhat, T.P. Singh and M. Vijayan, *Acta Cryst.*, **1974**, *30*, 2921. (b) L.H. Jensen, *J. Am. Chem. Soc.*, **1954**, *76*, 4663.

[3.24] S. Kashino, S. Tateno, H. Tanabe, M. Haisa and Y. Katsube, *Acta Cryst.*, **1991**, *C47*, 2236.

[3.25] R.G. Hazell, M.S. Lehmann and G.S. Pawley, *Acta Cryst.*, **1972**, *B28*, 1388.

[3.26] (a) B. Bhushan, A.V. Kulkarni, W. Bonin and J.T. Wyrobek, *Phil. Mag. A.*, **1996**, *74*, 1117. (b) A.J. Stephen and J.E. Houston, *Rev. Sci. Instrum.*, **1990**, *62*, 710.

[3.27] M.F. Ashby and D.R.H. Jones, *Engineering Materials*, Pergamon, Oxford, **1980**, p. 31.

CHAPTER 4

[4.1] (a) L.M. Grover, U. Gbureck, A.M. Young, A.J. Wright and J.E. Barraleta, *J. Mater. Chem.*, **2005**, *15*, 4955. (b) M.L. Gardel, J.H. Shin, F.C. MacKintosh, L. Mahadevan, P. Matsudaira and D.A. Weitz, *Science*, **2004**, *304*, 1301. (c) M. Sarikaya, C. Tamerler, A.-Y. Jen, K. Schulten and F. Bankeyx, *Nature Mater.*, **2003**, *2*, 577. (d) G. Bao and S. Suresh, *Nature Mater.*, **2003**, *2*, 715. (e) D.E. Discher, R. Winardi, P.O. Schischmanoff, M. Parra, J.G. Conboy and N. Mohandas, *J. Cell Biol.*, **1995**, *130*, 897.

[4.2] J.N. Israelachvili and D. Tabor, *Proc. R. Soc. London A*, **1972**, *331*, 19.

[4.3] G. Binnig, C.F. Quate, and Ch. Gerber, *Phys. Rev. Lett.*, **1986**, *56*, 930.

[4.4] J.B. Pethica, R. Hutchings and W.C. Oliver, *Phil.Mag. A,* **1983**, *48*, 593.

[4.5] (a) N.A. Burnham, R.J. Colton and H.M. Pollock, *Nanotechnology*, **1993**, *4*, 64. (b) N.A. Burnham and R.J. Colton, *J. Vac. Sci. Technol. A*, **1989**, *7*, 2906.

[4.6] (a) B. Bhushan, A.V. Kulkarni, W. Bonin and J.T. Wyrobek, *Phil. Mag. A.*, **1996**, *74*, 1117. (b) A.J. Stephen and J.E. Houston, *Rev. Sci. Instrum.*, **1990**, *62*, 710.

[4.7] J.B. Pethica and W.C. Oliver, *Phys. Scr. T.*, **1987**, *19*, 61.

[4.8] (a) M.R. VanLandingham, *J. Res. Natl. Inst. Stand. Technol.*, **2003**, *108*, 249. (b) D. Tabor, *Philos. Mag. A.*, **1996**, *74*, 1207. (c) W.C. Oliver and G.M. Pharr, *J. Mater. Res.*, **1992**, *7*, 1564. (d) M.F. Doerner and W.D. Nix, *J. Mater. Res.*, **1986**, *1(4)*, 601. (e) J.B. Pethica, R. Hutchings and W.C. Oliver, *Philos. Mag. A.*, **1983**, *48*, 593.

[4.9] (a) L. Xiaodong and B. Bhushan, *Mater. Character.*, **2002**, *48*, 11. (b) S.A.S. Asif, K.J. Wahl and R.J. Colton, *Rev. Sci. Instrum.*, **1999**, *70*, 2408. (c) For a review of microhardness testing see H. Buckle, *Metall. Rev.*, **1959**, *4*, 49.

[4.10] S.A.S. Asif and J.B. Pethica, *Phil. Mag. A*, **1997**, *76*, 1105.

[4.11] W.C. Oliver and G.M. Pharr, *J. Mater. Res.*, **1992**, *7(6)*, 1564.

[4.12] G.W. Rowe, *An Introduction to the Principles of Metalworking*, Edward Arnold, London, **1965**.

[4.13] J. Caro, J. Fraxedas, P. Gorostiza and F. Sanz, *J. Vac. Sci. Technol. A*, **2001**, *19(4)*, 1825.

[4.14] (a) R.K. Yadava and K.A. Padmanabhan, *Mater. Sci. Eng.*, **1979**, *37*, 127. (b) C.M. Sellars and W.J.McG. Tegart, *Int. Metall. Rev.*, **1972**, *17*, 1.

[4.15] K. A. Padmanabhan and G.J. Davies, *Metal Science*, **1997**, *11*, 1077.

[4.16] K.A. Padmanabhan and G.J. Davies, *Superplasticity*, Springer-Verlag, New York, **1980**.

CHAPTER 5

[5.1] (a) A.I. Kitaigorodskii, *Molecular Crystals and Molecules*, Academic Press, New York, **1973**. (b) A.I. Kitaigorodskii, *Organic Chemical Crystallography*, Consultants Bureau, New York, **1961**.

[5.2] J.L. Atwood, L.J. Barbour and A. Jerga, *Science*, **2002**, *296*, 2367.

[5.3] H.A. Bent, *Chem. Rev.*, **1968**, *68*, 587.

[5.4] A. Nangia and G.R. Desiraju, *Acta Crystallogr.*, **1998**, *A54*, 934.

[5.5] (a) J.D. Dunitz and A. Gavezzotti, *Angew. Chem. Int. Ed.*, **2005**, *44*, 1766. (b) O. Navon, J. Bernstein and V. Khodorkovsky, *Angew. Chem. Int. Ed. Engl.*, **1997**, *36*, 601. (c) V.R. Pedireddi, D.S. Reddy, B.S. Goud, D.C. Craig, A.D. Rae and G.R. Desiraju, *J. Chem. Soc. Perkin Trans. 2*, **1994**, 2353. (d) S.L. Price, A.L. Stone, J. Lucas, R.S. Rowland and A.E. Thornley, *J. Am. Chem. Soc.*, **1994**, *116*, 4910. (e) G.R. Desiraju, R. Parthasarathy, *J. Am. Chem. Soc.*, **1989**, *111*, 8725. (f) D.E. Williams and L.Y. Hsu, *Acta Crystallogr.*, **1985**, *A41*, 296. (g) W. Jones, C.R. Theocharis, J.M. Thomas and G.R. Desiraju, *Chem. Commun.*, **1983**, 1443. (h) S.C. Nyburg and W. Wong-Ng, *Proc. R. Soc.,* London, **1979**, *A367*, 29. (i) T. Sakurai, M. Sundaralingam and G.A. Jeffrey, *Acta Crystallogr.*, **1963**, *16*, 354.

[5.6] N. Ramasubbu, R. Parthasarathy and P. Murray-Rust, *J. Am. Chem. Soc.*, **1986**, *108*, 4308.

[5.7] (a) P. Metrangolo, G. Resnati, *Chem. Eur. J.*, **2001**, *7*, 2511. (b) E. Corradi, S.V. Meille, M.T. Messina, P. Metrangolo, G. Resnati, *Angew. Chem. Int. Ed.*, **2000**, *39*, 1782. (c) T. Caronna, R. Liantonio, T.A. Logothetis, P. Metrangolo, T. Pilati and G. Resnati, *J. Am. Chem. Soc.*, **2004**, *126*, 4500. (d) P. Metrangolo, H. Neukirch, T. Pilati and G. Resnati, *Acc. Chem. Res.*, **2005**, *38(5)*, 386.

[5.8] Selected recent references on halogen atom interaction in the crystal engineering context include: (a) F. Zordan, L. Brammer and P. Sherwood, *J. Am. Chem. Soc.*, **2005**, *127(16)*, 5979. (b) A.C.B. Lucassen, M. Vartanian, G. Leitus and M.E. van der Boom, *Cryst. Growth Des.*, **2005**, *5*, 1671. (c) H.L. Nguyen, P.N.

Horton, M.B. Hursthouse, A.C. Legon and D.W. Bruce, *J. Am. Chem. Soc.*, **2004**, *126*, 16. (d) R. Glaser, N. Chen, H. Wu, N. Knotts and M. Kaupp, *J. Am. Chem. Soc.*, **2004**, *126*, 4412. (e) S. Berski, Z. Ciunik, K. Drabent, Z. Latajka and J. Panek, *J. Phys. Chem. B*, **2004**, *108*, 12327. (f) A. Dey and G.R. Desiraju, *CrystEngComm*, **2004**, *6(104)*, 642. (g) A. Dey, R.K.R. Jetti, R. Boese and G.R. Desiraju, *CrystEngComm*, **2003**, *5(43)*, 248. (h) F. Neve and A. Crispini, *CrystEngComm*, **2003**, *5(46)*, 265. (i) D. Das, R.K.R. Jetti, R. Boese and G.R. Desiraju, *Cryst. Growth. Des.*, **2003**, *3*, 675. (j) A. Crihfield, J. Hartwell, D. Phelps, R.B. Walsh, J.L. Harris, J.F. Payne, W.T. Pennington and T. W. Hanks, *Cryst. Growth Des.*, **2003**, *3*, 313. (k) R. Liantonio, P. Metrangolo, T. Pilati, G. Resnati and A. Stevenazzi, *Cryst. Growth Des.*, **2003**, *3*, 799. (l) S.V. Lindeman, J. Hecht and J.K. Kochi, *J. Am. Chem. Soc.*, **2003**, *125(38)*, 11597. (m) R. Thaimattam, D.S. Reddy, F. Xue, T. C.W. Mak, A. Nangia and G.R. Desiraju, *New J. Chem.*, **1998**, 143.

[5.9] J.D. Dunitz and R. Taylor, *Chem. Eur. J.*, **1997**, *3*, 89.

[5.10] V.R. Thalladi, H.-C. Weiss, D. Bläser, R. Boese, A. Nangia and G.R. Desiraju, *J. Am. Chem. Soc.*, **1998**, *120*, 8702.

[5.11] R.K.R. Jetti, P.K. Thallapally, F. Xue, T.C.W. Mak and A. Nangia, *Tetrahedron*, **2000**, *56*, 6707.

[5.12] A.D. Bond, J. Griffiths, J.M. Rawson and J. Hulliger, *Chem. Commun.*, **2001**, 2488.

[5.13] (a) C. Janiak, *J. Chem. Soc., Dalton Trans.*, **2000**, 3885. (a) H.I. Süss and A. Neels and J. Hulliger, *CrystEngComm*, **2005**, *7*, 370.

[5.14] A. Wojtczak, V. Cody, J.R. Luft and W. Pangborn, *Acta Cryst.*, **2001**, *D57*, 1061.

[5.15] P. Auffinger, F.A. Hays, E. Westhof and P.S. Ho, *Proc. Natl. Acad. Sci. USA*, **2004**, *101(48)*, 16789.

[5.16] C_6Cl_6 has been reported to be dimorphic but has not been characterized as such. K. Schaum, K. Schäling and F. Klausing, *Lieb. Ann.*, **1916**, *411*, 161.

[5.17] (a) E. Baharie and G.S. Pawley, *Acta Cryst.*, **1979**, *A35*, 233. (b) R.J. Steer and

S.F. Watkins, P. Woodward, *J. Chem. Soc. C*, **1970**, 403.

[5.18] These observations may be explained on the basis of order-disorder changes as in metallic alloys which were discussed by Cottrell long back. See reference [1.20], pp. 191-202. The effects involved are the decrease in internal energy on ordering, and the increased importance of entropy at high homologous temperatures.

[5.19] T.L. Khotsyanova, T.A. Babushkina and G.K. Semin, *Zh. Strukt. Khim.* **1968**, *9*, 148.

[5.20] A. Dey, R.K.R. Jetti, R. Boese, G.R. Desiraju, *CrystEngComm*, **2003**, *5*, 248.

[5.21] (a) B.K. Saha, R.K.R. Jetti, L.S. Reddy, S. Aitipamula and A. Nangia, *Cryst. Growth. Des.* **2005**, *5*, 887. (b) J.M.A. Robinson, B.M. Kariuki, K.D.M. Harris and D. Philp, *J. Chem. Soc. Perkin Trans. 2*, **1998**, 2459. (c) M.B. Zaman, K.A. Udachin and J.A. Ripmeester, *Cryst. Growth Des.*, **2004**, *4*, 585.

[5.22] Twinning boundaries always have a local minimum in free energy. See G.A. Chadwick and D.A. Smith, *Grain Boundary Structure and Properties*, Academic Press, London, **1976**.

[5.23] A.I. Kitaigorodskii, *Mixed Crystals*, Springer, Berlin, **1984**.

APPENDIX 1

[1] (a) D. Braga, *Chem. Commun.*, **2003**, 2751. (b) D. Braga, G.R. Desiraju, J.S. Miller, A.G. Orpen and S.L. Price, *CrystEngComm*, **2002**, *4*, 500. (c) G.R. Desiraju, *Nature*, **2001**, *412*, 397. (d) M.D. Hollingsworth, *Science*, **2002**, *295*, 2410.

[2] G.R. Desiraju, *Chem. Commun.*, **2005**, 2995.

[3] A.C. Pierce, K.L. Sandretto and G.W. Bemis, *Proteins*, **2002**, *49*, 567.

[4] G.R. Desiraju and T. Steiner, *The Weak Hydrogen Bond in Structural Chemistry and Biology*, OUP, Oxford, **1999**.

[5] (a) C.K. Broder, M.G. Davidson, V.T. Forsyth, J.A.K. Howard, S. Lamb and S.A. Mason, *Cryst. Growth Des.*, **2002**, *2*, 163. (b) M.G. Davidson, A.E. Goeta, J.A.K. Howard, S. Lamb and S.A. Mason, *New J. Chem.*, **2000**, *24*, 477. (c)

B.M. Kariuki, K.D.M. Harris, D. Philip and J.M.A. Robinson, *J. Am. Chem. Soc.*, **1997**, *119*, 12679. (d) T. Steiner, J.H. van der Maas and B.T.G. Lutz, *J. Chem. Soc., Perkin Trans. 2*, **1997**, 1287.

[6] J.A. Cowan, J.A.C. Clyburne, M.G. Davidson, R.L.W. Harris, J.A.K. Howard, P. Küpper, M.A. Leech and S.P. Richards, *Angew. Chem. Int. Ed.*, **2002**, *41*, 1432.

[7] T. Steiner, *Acta Cryst.,* **1998**, *D54*, 584.

[8] E.B. Starikov and T. Steiner, *Acta Cryst.,* **1998**, *B54*, 94.

[9] (a) D. Braga, F. Grepioni and E. Tedesco, *Organometallics*, **1998**, *17*, 2669. (b) J.F. Malone, C.M. Murray, M.H. Charlton, R. Docherty, and A.J. Lavery, *J. Chem. Soc., Faraday Trans.*, **1997**, *93*, 3429.

[10] (a) M.R. Caira, L.R. Nassimbeni, F. Toda and D. Vujovic, *J. Chem. Soc., Perkin Trans. 2*, **1999**, 2681. (b) H. Hayashi, Y. Mazaki, K. Kobayashi, *J. Chem. Soc., Chem. Commun.*, **1994**, 2351. (c) H. Hart, H.-T. Lin and D.L. Ward, *J. Am. Chem. Soc.*, **1984**, *106*, 4043. (d) F. Toda and K. Akagi, *Tetrahedron Lett.*, **1968**, 3695.

[11] R.K.R. Jetti, F. Xue, T.C.W. Mak and A. Nangia, *J. Chem. Soc., Perkin Trans. 2*, **2000**, 1223.

[12] (a) C.M. Reddy, L.S. Reddy, S. Aitipamula, A. Nangia, C.-K. Lam and T.C.W. Mak, *CrystEngComm*, **2005**, *7(5)*, 44. (b) C.M. Reddy, A. Nangia, C.-K. Lam and T.C.W. Mak, *CrystEngComm*, **2002**, *4(58)*, 323.

[13] (a) P. Vishweshwar, A. Nangia and V.M. Lynch, *Acta Cryst.,* **2000**, *C56*, 1512. (b) G.T.R. Palmore and J.C. MacDonald, in *The Amide Linkage: Selected Structural Aspects in Chemistry, Biochemistry, and Materials Science*, Eds.: A. Greenberg, C.M. Breneman and J.F. Liebman, John Wiley, Chichester, **2000**, pp. 291-336. (c) L. Leiserowitz and G.M.J. Schmidt, *J. Chem. Soc. (A)*, **1969**, 2372.

[14] Z. Ciunik and G. R. Desiraju, *Chem. Commun.*, **2001**, 703.

[15] C.K. Broder, J.A.K. Howard, D.A. Keen, C.C. Wilson, F.H. Allen, R.K.R. Jetti, A. Nangia and G.R. Desiraju, *Acta Crystallogr.*, **2000**, *B56*, 1080.

[16] (a) A.J. Matzger, M. Shim and K.P.C. Vollhardt, *Chem. Commun.*, **1999**, 1871. (b) T. Imakubo, T. Matuyama, H. Sawa and K. Kobayashi, *Chem. Commun.*, **1998**, 2021.

[17] (a) S. George, A. Nangia and V.M. Lynch, *Acta Cryst.,* **2001**, *C57*, 777. (b) T. Steiner and S. Mason, *Acta Cryst.*, **2000**, *B56*, 254.

[18] (a) A. Bacchi, E. Bosetti, M. Carcelli, P. Pelagatti and D. Rogolino, *CrystEngComm*, **2004**, *6*, 177. (b) D.V. Soldatov, I.L. Moudrakovski, C.I. Ratcliffe, R. Dutrisac and J.A. Ripmester, *Chem. Mater.*, **2003**, *15*, 4810. (c) Z. Dominguez, H. Dang, M.J. Strouse and M.A. Garcia-Garibay, *J. Am. Chem. Soc.*, **2002**, *124*, 7719. (d) J. Overgaard, B.B. Iverson, S.P. Palii, G.A. Timco, N.V. Gerbeleu and F.K. Larsen, *Chem. Eur. J.*, **2002**, *8*, 2775. (e) T. Müller, J. Hulliger, W. Seichter, E. Weber, T. Weber and M.A. Wübbenjorst, *Chem. Eur. J.*, **2000**, *6*, 54.

[19] B.T.G. Lutz, J. Jacob and J.H. van der Maas, *Vibrational Spectroscopy*, **1996**, *12*, 197.

[20] July 2004 update of the Cambridge Structural Database recorded 18 hits of acetylacetone diketone tautomer. The *syn* conformation is present in metal chelates. www.ccdc.cam.ac.uk.

[21] Quantum mechanical calculations using generalized gradient approximation (GGA) in PBE potential and 'fine' basis set. See http://www.accelrys.com/references/dmol3.html for details.

[22] K. Uemura, S. Kitagawa, M. Kondo, K. Fukui, R. Kitaura, H.-C. Chang and T. Mizutani, *Chem. Eur. J.*, **2002**, *8*, 3587.

[23] For recent examples of host showing guest inclusion in different cavities, see: (a) R. Bishop, A.N.M.M. Rahman, J. Ashmore, D.C. Craig and M.L. Scudder, *CrystEngComm*, **2002**, *4*, 605. (b) S. Apel, M. Czugler, V.J. Griffith, L.R. Nassimbeni and E. Weber, *J. Chem. Soc., Perkin Trans. 2*, **1997**, 1949.

[24] There are *ca.* 10,000 hits of CH_2Cl_2 solvates in the CSD but none of these adopt the infinite tape motif. However, the finite dimer synthon of C–H···Cl interactions is quite commmon.

[25] Calculated in *Cerius*^{2}, www.accelrys.com. Single point lattice energies with no relaxation of atomic distances and angles compared to the crystal structure gave similar trends in energies. We prefer to compute optimized crystal energies.

[26] L.R. Nassimbeni, *Acc. Chem. Res.*, **2003**, *36*, 631.

[27] (a) *SHELXS-97*: G.M. Sheldrick, *Program for the Solution of Crystal Structures*, University of Göttingen, Germany, **1997**. (b) *SHELXL-97*: G.M. Sheldrick, *Program for Crystal Structure Refinement*, University of Göttingen, Germany, **1997**.

[28] (a) G.M. Sheldrick, *Program for Multi-Scan Absorption Correction of Area Detector Data*; Version 2.10, University of Göttingen, Germany, **2003**. (b) *SADABS*: G.M. Sheldrick, *Program for Empirical Absorption Correction of Area Detector Data*, University of Göttingen, Germany, **1996**.

[29] *SHELXTL (version 6.14)*: Bruker AXS, *Program for the Solution and Refinement of Crystal Structures*, Wisconsin, USA, **2000**.

APPENDIX 2

Table 1. Salient crystallographic details of the compounds discussed in this thesis.

Appendix 1				
	1.*p*-xylene	**1**.*m*-xylene	**1**.*m*-xylene	**1**.*p*-chloro-toluene
Empirical formula	$(C_{26}H_{21}NO)$ $0.5(C_8H_{10})$	$(C_{26}H_{21}NO)$ $0.5(C_8H_{10})$	$(C_{26}H_{21}NO)$ $0.5(C_8H_{10})$	$2(C_{26}H_{21}NO)$ (C_7H_7Cl)
Crystal system	Triclinic	Triclinic	Triclinic	Triclinic
Space group	$P\bar{1}$	$P\bar{1}$	$P\bar{1}$	$P\bar{1}$
T [K]	293(2)	123(2)	293(2)	123(2)
a [Å]	7.1811(9)	7.191(2)	7.2363(8)	7.0859(13)
b [Å]	9.0550(12)	8.904(2)	9.057(1)	8.9501(16)
c [Å]	18.990(3)	18.455(5)	18.701(2)	18.916(3)
α [deg]	85.197(3)	88.182(5)	88.480(2)	85.270(4)
β [deg]	88.438(3)	86.014(6)	86.264(2)	88.925(4)
γ [deg]	66.912(3)	68.243(6)	68.876(2)	67.076(3)
Volume [$Å^3$]	1131.9(3)	1094.8(5)	1140.8(2)	1101.0(3)
Z	2	2	2	1
D_{calc} [g/cm^3]	1.222	1.263	1.212	1.287
θ Range[deg]	1.08-26.04	2.21 - 22.50	1.09- 24.01	2.16 – 28.30
Range h	$-8 \le h \le 8$	$-7 \le h \le 7$	$-8 \le h \le 8$	$-9 \le h \le 9$
Range k	$-10 \le k \le 11$	$-8 \le k \le 9$	$-10 \le k \le 10$	$-11 \le k \le 11$
Range l	$-23 \le l \le 21$	$-17 \le l \le 19$	$-21 \le l \le 15$	$-25 \le l \le 25$
N-total	6923	5611	5941	14288
N-Unique	1994	1544	2089	3809
Parameters	375	325	326	298
R_1 [$I>2\sigma(I)$]	0.0628	0.0550	0.0514	0.0621
wR_2	0.1423	0.1160	0.1293	0.1512
GOF	0.892	1.010	0.973	1.061

APPENDIX 2

Table 1. *Continued…*

Appendix 1				
1.*p*-chloro-toluene	**1**.*p*-bromo-toluene	**1**.anisole	**1**.CH_2Cl_2	**1**.CH_2Cl_2
2($C_{26}H_{21}NO$) (C_7H_7Cl)	2($C_{26}H_{21}NO$) (C_7H_7Br)	2($C_{26}H_{21}NO$) 0.5($C_{14}H_{16}O_2$)	2($C_{26}H_{21}NO$) 3(CH_2Cl_2)	2($C_{26}H_{21}NO$) 3(CH_2Cl_2)
Triclinic	Triclinic	Triclinic	Monoclinic	Monoclinic
$P\bar{1}$	$P\bar{1}$	$P\bar{1}$	C_2/c	C_2/c
293(2)	203(2)	123(2)	123(2)	298(2)
7.1718(5)	7.110(3)	8.9167(6)	16.326(2)	16.554(2)
9.0439(6)	9.014(4)	13.6556(9)	7.2044(4)	7.3012(9)
19.0301(13)	19.008(7)	19.746(1)	40.212(2)	40.639(5)
85.179(2)	84.945(7)	104.198(1)	90	90
88.276(2)	88.467(8)	98.331(1)	96.288(2)	95.785(3)
66.8150(10)	66.981(7)	105.067(1)	90	90
1130.61(13)	1116.8(8)	2194.1(2)	4701.4(7)	4886.7(11)
1	1	2	4	4
1.253	1.335	1.264	1.401	1.332
1.07 - 26.03	2.15 - 25.50	2.18 - 28.30	2.04 – 27.13	1.01 - 24.02
$-8 \le h \le 8$	$-8 \le h \le 8$	$-11 \le h \le 11$	$-20 \le h \le 20$	$-18 \le h \le 17$
$-11 \le k \le 11$	$-10 \le k \le 10$	$-18 \le k \le 18$	$-9 \le k \le 9$	$-8 \le k \le 8$
$-20 \le l \le 23$	$-22 \le l \le 23$	$-25 \le l \le 26$	$-51 \le l \le 51$	$-42 \le l \le 46$
6947	11479	27001	36062	11538
2598	2986	5774	4161	2422
298	292	625	375	301
0.0505	0.0565	0.0676	0.0918	0.1077
0.1301	0.1377	0.1603	0.2452	0.3016
0.987	1.029	0.998	1.061	1.051

APPENDIX 2

Table 1. *Continued…*

Appendix 1				
1.CH_2Br_2	**1**.CH_2I_2	**1**.EtOAc	**1**.$MeNO_2$	**1**.acetylacetone
$2(C_{26}H_{21}NO)$ (CH_2Br_2)	$(C_{26}H_{21}NO)$ $0.112(C_2H_4I_4)$ $0.428(CH_2I_2)$	$(C_{26}H_{21}NO)$ $0.5(C_4H_8O_2$	$(C_{26}H_{21}NO)$ (CH_3NO_2)	$2(C_{26}H_{21}NO)$ $(C_5H_8O_2)$
Triclinic	Triclinic	Triclinic	Triclinic	Triclinic
$P\bar{1}$	$P\bar{1}$	$P\bar{1}$	$P\bar{1}$	$P\bar{1}$
123(2)	123(2)	298(2)	123(2)	123(2)
7.0754(17)	9.2416(11)	7.322(2)	7.3288(6)	7.291(1)
8.885(2)	13.3370(16)	8.895(2)	8.8318(7)	8.870(1)
18.643(4)	19.739(2)	18.468(4)	18.235(1)	18.337(3)
91.334(4)	105.381(2)	94.117(5)	94.864(1)	93.998(3)
91.807(5)	96.041(2)	90.902(5)	90.316(1)	90.416(3)
111.700(4)	104.497(2)	112.977(4)	114.166(1)	113.873(3)
1087.6(4)	2232.4(4)	1103.5(4)	1071.9(1)	1081.0(3)
1	4	2	2	1
1.375	1.874	1.226	1.315	1.270
2.74 - 25.0	1.65 – 26.09	1.11 - 25.01	2.24 - 25.66	2.23 – 26.37
$-8 \leq h \leq 8$	$-11 \leq h \leq 10$	$-8 \leq h \leq 8$	$-8 \leq h \leq 8$	$-9 \leq h \leq 8$
$-5 \leq k \leq 10$	$-16 \leq k \leq 16$	$-10 \leq h \leq 10$	$-10 \leq k \leq 10$	$-11 \leq k \leq 10$
$-20 \leq l \leq 18$	$-24 \leq l \leq 22$	$-21 \leq h \leq 16$	$-22 \leq l \leq 22$	$-18 \leq l \leq 22$
3447	15180	6262	15791	10301
1768	5589	2240	3508	3520
289	563	308	385	391
0.0940	0.0765	0.0493	0.0473	0.0521
0.2650	0.1740	0.1046	0.1103	0.1213
1.122	1.047	0.914	1.059	1.027

APPENDIX 2

Table 1. *Continued…*

Chapter 5				
	C_6Br_6	**C_6Cl_6**	**124B356I**	**124C356I**
Empirical formula	C_6Br_6	C_6Cl_6	$C_6Br_3I_3$	$C_6Cl_3I_3$
Crystal system	Monoclinic	Monoclinic	Monoclinic	Monoclinic
Space group	$P2_1/n$	$P2_1/n$	$P2_1/n$	$P2_1/n$
T [K]	100(2)	100(2)	100(2)	100(2)
a [Å]	8.3262(16)	7.967(3)	8.5007(6)	8.7025(7)
b [Å]	3.9491(8)	3.7609(14)	4.0812(3)	4.1087(3)
c [Å]	15.271(3)	14.670(5)	15.6911(10)	15.0989(12)
α [deg]	90	90	90	90
β [deg]	92.929(3)	92.459(6)	92.6560(10)	93.5890(10)
γ [deg]	90	90	90	90
Volume [Å^3]	501.46(17)	439.2(3)	543.79(7)	538.82(7)
Z	2	2	2	2
D_{calc} [g/cm^3]	3.653	2.153	4.229	3.446
F (000)	492	276	600	492
μ [mm^{-1}]	23.957	1.884	19.588	9.388
$2\theta_{max.}$	2.73–26.07	2.78–26.03	2.67–26.07	2.63–26.03
Range h	$-10 \le h \le 10$	$-9 \le h \le 9$	$-10 \le h \le 10$	$-10 \le h \le 10$
Range k	$-4 \le k \le 4$	$-4 \le k \le 4$	$-4 \le k \le 5$	$-5 \le k \le 4$
Range l	$-16 \le l \le 18$	$-18 \le l \le 18$	$-19 \le l \le 19$	$-18 \le l \le 18$
Parameters	56	55	68	68
N-total	4469	3112	5470	4377
N-independent	986	861	1059	1051
N-observed	913	812	1015	1033
R_1 [I>2σ(I)]	0.0218	0.0449	0.0199	0.0195
wR_2	0.0519	0.1097	0.0492	0.0469
R_{merge}	0.0317	0.0317	0.0253	0.0159
GOF	1.098	1.15	1.093	1.105

APPENDIX 2

Table 1. *Continued…*

Chapter 5				
124B356C	**123B456C**	**123C456I**	**14C2356I**	**14B2356I**
$C_6Br_3Cl_3$	$C_6Br_3Cl_3$	$C_6Cl_3I_3$	$C_6Cl_2I_4$	$C_6Br_2I_4$
Monoclinic	Monoclinic	Monoclinic	Monoclinic	Monoclinic
$P2_1/n$	$P2_1/n$	$P2_1/n$	$P2_1/n$	$P2_1/n$
100(2)	293(2)	293(2)	293(2)	293(2)
8.1454(8)	8.2578(17)	8.720(4)	8.7829(19)	9.3109(19)
3.8704(4)	3.9429(8)	4.1170(19)	4.2989(9)	4.2609(9)
15.0160(15)	15.137(3)	15.582(7)	15.320(3)	14.776(3)
90	90	90	90	90
92.385(2)	92.34(3)	92.667(7)	94.908(4)	93.33(3)
90	90	90	90	90
472.98(8)	492.46(17)	558.8(4)	576.3(2)	585.2(2)
2	2	2	2	2
2.936	2.82	3.323	3.749	4.197
384	384	492	564	636
13.575	13.038	9.053	11.225	17.426
2.72–26.03	2.69–28.13	2.73–25.97	2.58–27	2.52–29.06
$-10 \leq h \leq 10$	$-10 \leq h \leq 10$	$-7 \leq h \leq 10$	$-6 \leq h \leq 11$	$-12 \leq h \leq 12$
$-4 \leq k \leq 4$	$-4 \leq k \leq 4$	$-5 \leq k \leq 5$	$-5 \leq k \leq 5$	$0 \leq k \leq 5$
$-16 \leq l \leq 18$	$-19 \leq l \leq 9$	$-19 \leq l \leq 19$	$-19 \leq l \leq 19$	$-19 \leq l \leq 19$
67	73	74	56	41
6318	2542	2733	2977	2676
923	1075	1079	1243	1340
880	822	946	1168	1142
0.0162	0.0765	0.0536	0.0397	0.0401
0.0397	0.1994	0.1512	0.1055	0.1031
0.0301	0.0759	0.0721	0.0662	0.0462
1.09	1.013	1.108	1.099	1.084

APPENDIX 2

Table 1. *Continued…*

Chapter 5				
14B2356C	**1245C36I-M1**	**1245C36I-M2**	**12345B6C**	**135B246C**
$C_6Br_2Cl_4$	$C_6Cl_4I_2$	$C_6Cl_4I_2$	C_6Br_5Cl	$C_6Br_3Cl_3$
Monoclinic	Monoclinic	Monoclinic	Monoclinic	Monoclinic
$P2_1/n$	$P2_1/n$	$P2_1/n$	$P2_1/n$	$P2_1/n$
100(2)	100(2)	100(2)	100(2)	100(2)
8.0578(6)	8.6484(6)	6.5276(6)	8.2742(14)	8.1859(9)
3.8484(3)	4.1259(3)	5.9682(5)	3.9205(7)	3.8619(4)
14.9122(1)	15.7424(1)	13.3913(1)	15.196(3)	15.0355(1)
90	90	90	90	90
92.1900(1)	92.1300(1)	98.7720(1)	92.729(2)	92.766(2)
90	90	90	90	90
462.08(6)	561.34(7)	515.60(8)	492.39(15)	474.77(9)
2	2	2	2	2
2.686	2.767	3.012	3.42	2.925
348	420	420	465	384
9.86	6.499	7.076	20.613	13.524
2.73–26.20	2.59–26.01	3.08–26.03	2.68–26.04	2.78–26.01
$-9 \leq h \leq 9$	$-10 \leq h \leq 10$	$-8 \leq h \leq 8$	$-10 \leq h \leq 10$	$-10 \leq h \leq 10$
$-4 \leq k \leq 4$	$-5 \leq k \leq 5$	$-7 \leq k \leq 7$	$-4 \leq k \leq 4$	$-4 \leq k \leq 4$
$-17 \leq l \leq 18$	$-19 \leq l \leq 16$	$-16 \leq l \leq 16$	$-18 \leq l \leq 16$	$-18 \leq l \leq 18$
68	59	56	67	56
5435	5638	9332	4060	4781
919	1089	1007	965	932
896	1012	1000	904	891
0.0147	0.034	0.0136	0.0209	0.0172
0.037	0.0866	0.0324	0.0504	0.0409
0.0183	0.0204	0.0220	0.0319	0.0273
1.092	1.09	1.105	1.051	1.091

APPENDIX 2

Table 1. *Continued…*

Chapter 5				
135C246I	**135B246I-T**	**135B246I-M1**	**135B246I-M2**	**135F246I**
$C_6Cl_3I_3$	$C_6Br_3I_3$	$C_6Br_3I_3$	$C_6Br_3I_3$	$C_6F_3I_3$
Triclinic	Triclinic	Monoclinic	Monoclinic	Monoclinic
$P\bar{1}$	$P\bar{1}$	$P2_1/n$	$P2_1/n$	$P2_1/n$
100(2)	100(2)	100(2)	100(2)	298(2)
7.7131(11)	7.9452(3)	8.5045(16)	9.3129(50)	13.937(4)
9.4269(13)	9.4962(4)	4.0444(8)	4.1977(20)	4.7919(15)
9.4299(18)	9.5119(6)	15.608(3)	14.7054(80)	15.488(5)
60.213(2)	60.1370(10)	90	90	90
66.116(3)	66.202(2)	92.842(3)	93.296(6)	107.486(3)
85.575(2)	85.5120(10)	90	90	90
537.43(15)	562.61(5)	536.17(18)	573.9(5)	986.6(5)
2	2	2	2	4
3.455	4.088	4.289	4.007	3.432
492	600	600	600	888
9.413	18.933	19.866	18.56	9.493
2.52–26.01	2.50–26.00	2.61–26.03	2.52–26.02	1.73–26.03
$-9 \leq h \leq 9$	$-9 \leq h \leq 9$	$-10 \leq h \leq 9$	$-4 \leq h \leq 11$	$-17 \leq h \leq 15$
$-11 \leq k \leq 11$	$-11 \leq k \leq 11$	$-4 \leq k \leq 4$	$-5 \leq k \leq 5$	$-5 \leq k \leq 5$
$-11 \leq l \leq 11$	$-11 \leq l \leq 11$	$-19 \leq l \leq 19$	$-14 \leq l \leq 15$	$-19 \leq l \leq 18$
110	110	55	25	109
7213	8971	5041	1470	5283
2116	2195	1049	1000	1923
2091	2104	993	912	1642
0.0284	0.0213	0.0242	0.1455	0.0317
0.0754	0.0528	0.0687	0.3945	0.0799
0.0315	0.0297	0.0256	0.1369	0.0241
1.224	1.102	1.107	1.697	1.049

APPENDIX 2

Table 1. *Continued…*

Chapter 5			
135C246I: 135B246I	**135B246I: 135I246M**	**135C246I: 135B246M**	**135C246I: 135I246M**
0.863($C_6Cl_3I_3$)	0.922($C_6Br_3I_3$)	0.154($C_6Cl_3I_3$)	0.154($C_6Cl_3I_3$)
1.137($C_6Br_3I_3$)	1.078($C_9H_9I_3$)	1.846($C_9H_9Br_3$)	1.846 ($C_9H_9I_3$)
Triclinic	Triclinic	Triclinic	Triclinic
$P\bar{1}$	$P\bar{1}$	$P\bar{1}$	$P\bar{1}$
100(2)	100(2)	100(2)	100(2)
7.8534(8)	7.9146(5)	7.6549(9)	7.8342(8)
9.4683(9)	9.5156(6)	9.0787(10)	9.4966(10)
9.4810(9)	9.5282(6)	9.1025(10)	9.5031(10)
60.1420(10)	60.1830(10)	60.0510(10)	60.2820(10)
66.2530(10)	66.6090(10)	67.6180(10)	66.7010(10)
85.656(2)	85.9680(10)	85.0940(10)	86.2450(10)
552.69(9)	564.10(6)	502.49(10)	556.34(10)
1	1	1	1
3.814	3.458	2.461	3.12
553	516	348	463
14.887	13.147	11.837	8.666
2.51–26.04	2.50–26.03	2.61–26.04	2.50–26.12
$-9 \le h \le 9$	$-9 \le h \le 9$	$-9 \le h \le 9$	$-9 \le h \le 9$
$-11 \le k \le 11$	$-11 \le k \le 10$	$-11 \le k \le 11$	$-11 \le k \le 11$
$-11 \le l \le 10$	$-11 \le l \le 11$	$-11 \le l \le 11$	$-11 \le l \le 11$
120	123	131	123
7021	6198	7763	7617
2178	2216	1991	2211
2127	2150	1821	2178
0.0244	0.0173	0.0208	0.0177
0.0641	0.041	0.0518	0.0433
0.0283	0.0152	0.0242	0.0167
1.175	1.134	1.028	1.175

ABOUT THE AUTHOR

C. Malla Reddy, son of Narasimha Reddy and Anasuyamma, was born in Kothamolgara, a village in the Mahaboob Nagar district of Andhra Pradesh, India, in 1975. He received his primary education in Kothamolgara and completed his secondary school education in B.P.H.S, Mahaboob Nagar. He completed his intermediate from Boys Junior College, Mahaboob Nagar. After the completion of his B.Sc. (Silver Jubilee Degree College, Kurnool), B.Ed. and M.Sc. (Osmania University), he joined the School of Chemistry, University of Hyderabad to pursue the Ph.D. degree in 2001. He was awarded research fellowship by Council of Scientific and Industrial Research (JRF and SRF) for 2001-2006.

List of Publications

1. An engineered N–H···π interaction: crystal structure of 4-tritylbenzamide–*p*-xylene(2 :1)
   C.M. Reddy, A. Nangia, C-K. Lam and T.C.W. Mak
   CrystEngComm, **2002**, *4(58)*, 323–325.

2. Triphenyl(3,4,5-triiodophenyl)-methane.
   C.M. Reddy, A. Nangia, R.K.R. Jetti and R. Boese
   Acta Cryst., **2004**, *C60*, o331-o333.

3. Engineering the weak N–H···π hydrogen bond in 4-tritylbenzamide host and controlling the interaction through guest selection.
   C.M. Reddy, L.S. Reddy, S. Aitipamula, A. Nangia, C-K. Lam and T.C.W. Mak
   CrystEngComm, **2005**, *7(5)*, 44–52.

4. Sorting of polymorphs based on mechanical properties. Trimorphs of 6-chloro-2,4-dinitroaniline.
   C.M. Reddy, S. Basavoju and G.R. Desiraju
   Chem. Commun., **2005**, 2439-2441.

5. 2-(Methylsulfanyl)nicotinic acid.
   S. Basavoju, **C.M. Reddy** and G.R. Desiraju
   Acta Cryst. **2005**, *E61*, o822-823.

6. Structural basis for bending of organic crystals.
   C.M. Reddy, R.C. Gundakaram, S. Basavoju, M.T. Kirchner, K.A. Padmanabhan and G.R. Desiraju
   Chem. Commun., **2005**, 3945-3947.

7. Isostructurality, polymorphism and mechanical properties of some hexahalogenated benzenes. The nature of halogen···halogen interactions.
   C.M. Reddy, M.T. Kirchner, R.C. Gundakaram, K.A. Padmanabhan and G.R. Desiraju
   Chem. Eur. J., **2005**, *12*, 2222-2234.

8. Structu-property correlations in bending and shearing molecular crystals.
   C.M. Reddy, M.T. Kirchner, K.A. Padmanabhan and G.R. Desiraju
   (To be communicated).

9. Near-exhaustion creep behaviour of molecular crystals of 2-(methylthio)nicotinic acid, pyrazincarboxamide and hexachlorobenzene.
C.M. Reddy, R. Meenakshi, R.C. Gundakaram, K.A. Padmanabhan and G.R. Desiraju
(To be communicated).

10. Characterisation of deformation behaviour in molecular crystals of 2-(methylthio)nicotinic acid and hexachlorobenzene.
C.M. Reddy, K. Muraleedharan, K.A. Padmanabhan, and G.R. Desiraju
(To be communicated).

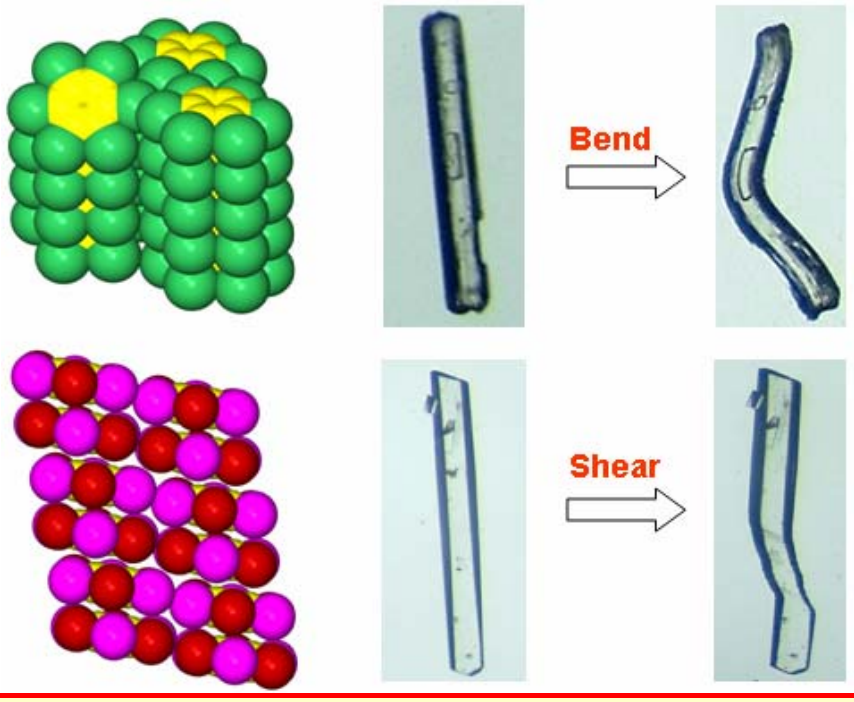

Arrangement of molecules and directionality of the intermolecular interactions in the lattice is a key factor for bending and shearing in molecular crystals.